

Università degli Studi del Piemonte Orientale “Amedeo Avogadro”

Dipartimento di Scienze ed Innovazione Tecnologica

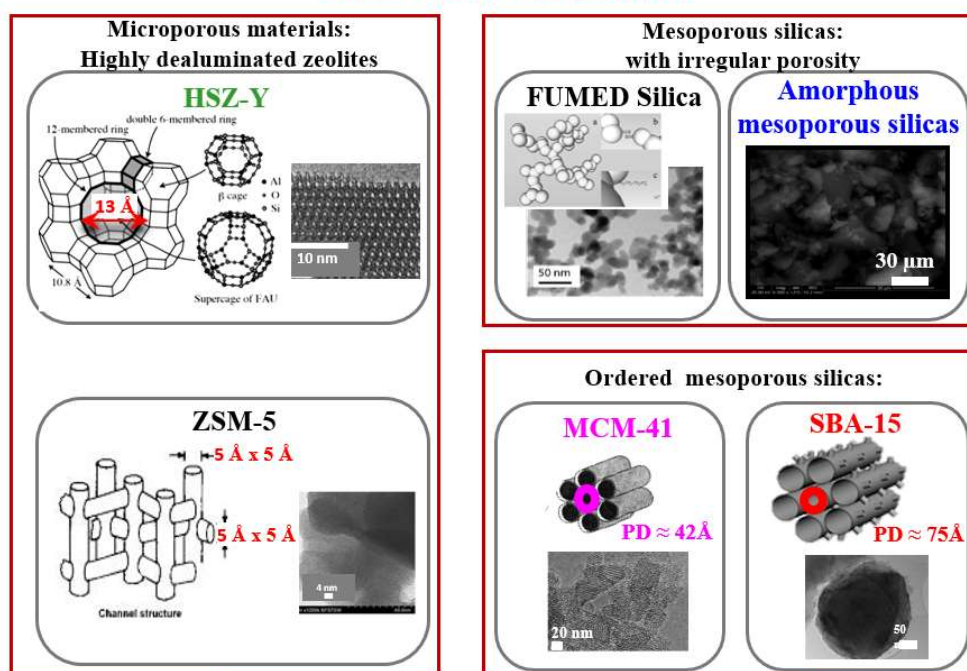
Dottorato di Ricerca in Chemistry & Biology

XXXI ciclo a.a. 2017-2018

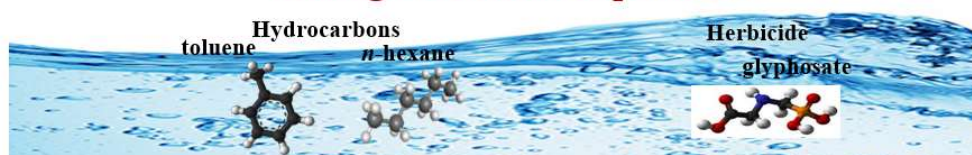
SSD: CHIM02

Silica Based Materials for Groundwater Depollution

Silica-based materials...



...for groundwater depollution



Diana Francia Olivas Olivera

Supervised by Prof. Chiara Bisio

Ph.D. program co-ordinator Prof. Guido Lingua

**Università degli Studi del Piemonte Orientale “Amedeo
Avogadro”**

Dipartimento di Scienze ed Innovazione Tecnologica


Dottorato di Ricerca in Chemistry & Biology

XXXI ciclo a.a. 2015-2018

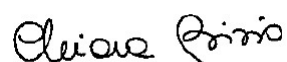
SSD: CHIM02

Silica Based Materials for Groundwater Depollution

Diana Francia Olivas Olivera



Supervised by Prof. Chiara Bisio



Ph.D. program co-ordinator Prof Guido Lingua



UNIVERSITÀ DEL PIEMONTE ORIENTALE
DOTTORATO DI RICERCA
IN CHEMISTRY & BIOLOGY

Via Duomo, 6
13100 – Vercelli (ITALY)

DECLARATION AND AUTHORISATION TO ANTIPLAGIARISM DETECTION

The undersigned Olivas Olivera Diana Francia student of the Chemistry & Biology Ph.D. course (XXXI Cycle)

declares:

- to be aware that the University has adopted a web-based service to detect plagiarism through a software system called “Turnit.in”,
- her Ph.D. thesis was submitted to Turnit.in scan and reasonably it resulted an original document, which correctly cites the literature;

acknowledges:

- her Ph.D. thesis can be verified by her Ph.D. tutor and/or Ph.D. Coordinator in order to confirm its originality.

Date: 14/11/2018

Signature:

A handwritten signature in black ink, appearing to read 'Diana Francia', is written over a horizontal line.

This Ph.D. is dedicated to my mother and father

Eva Olivera and Marco Olivas.

Thanks, mother and father, for giving me life, your endless love, support
and encouragement during this Ph.D.

Both of you have always inspired me to do my best!

I love you.

Contents

Chapter I: Polluted Water from Anthropogenic Activities and its Remediation.....	1
1.1 Environmental pollution from anthropogenic activities.....	1
1.2 Groundwater pollution.....	2
1.2.1 Organic pollution in groundwater.....	5
1.2.1.1 Hydrocarbons.....	6
1.2.1.2 Herbicides	8
1.3 Removal of pollutants from groundwater.....	9
1.3.1 Materials used as adsorbents for groundwater decontamination.....	12
1.3.1.1 Zeolites as adsorbents for hydrocarbons removal from groundwater.....	14
1.3.1.2 Hydrophobic zeolites as adsorbents for hydrocarbons removal from groundwater..	17
1.3.1.3 Ordered mesoporous silica as adsorbents for hydrocarbons removal from groundwater.....	26
1.3.1.3 Materials for herbicides removal from groundwater.....	29
References.....	33
Chapter II: Outline of The Thesis.....	43
Chapter III: Microporous Systems for Groundwater Depollution.....	47
3.1 Introduction.....	47
3.2 Structural, textural and surface properties of HSZ-Y and ZSM-5 zeolites.....	48
3.3 Adsorption of gaseous mixture of toluene and <i>n</i> -hexane on HSZ-Y and ZMS-5 zeolites.....	52
3.3.1 FTIR spectroscopy analysis.....	53
3.3.2 ¹ H MAS and ¹³ C CPMAS SS-NMR analysis.....	57
3.3.3 Determination of the amount of toluene and <i>n</i> -hexane adsorbed on HSZ-Y and ZSM-5 zeolites.....	65
3.4 Conclusions.....	69
References.....	71
Chapter IV: Experimental Determination of the Molar Absorption Coefficient of Toluene and <i>n</i>-hexane Adsorbed on Zeolites	73
4.1 Introduction.....	73
4.2 Determination of molar absorption coefficient of <i>n</i> -hexane adsorbed on HSZ-Y and ZSM-5 zeolites	74
4.2.1 Computational DFT study.....	83
4.3 Experimental determination of the molar absorption coefficients of adsorbed toluene on HSZ-Y and ZSM-5 zeolites	86
4.4 Conclusions.....	95
References.....	97

Chapter V: Silica-based Materials as Adsorbents for Groundwater Depollution	99
5.1 Experimental.....	99
5.2 Amorphous silicas with non regular porosity.....	100
5.2.1 Fumed silica.	100
5.2.1.1 Physico-chemical characterization of fumed silica.....	101
5.2.1.2 Toluene adsorption on FUMED silica.....	104
5.2.2 MSA-type silicas.....	106
5.2.2.1 Preparation and physico-chemical characterization of amorphous mesoporous silicas (AMS).....	106
5.2.2.2 Monitoring the hydrothermal stability of AMS samples.....	109
5.2.2.3 Toluene adsorption on AMS samples.....	115
5.2.2.4 Toluene adsorption on AMS samples treated under hydrothermal conditions.....	119
5.3 Monitoring the toluene adsorption capacities of ordered mesoporous silica.....	121
5.3.1 MCM-41 and SBA-15 silica samples.....	121
5.3.1.1 Preparation and physico-chemical characterization of ordered mesoporous silicas.....	122
5.3.2 Monitoring the toluene adsorption capacities of MCM-41 and SBA-15.....	126
5.4 Conclusions.....	128
References.....	130
Chapter VI: Experimental Determination of the Molar Absorption Coefficient of Toluene on Mesoporous Silicas	133
6.1 Introduction.....	133
6.2 Determination of molar absorption coefficient of toluene on mesoporous silica-based materials.....	133
6.2.1 Experimental determination of molar absorption coefficient of toluene on FUMED amorphous silica.....	134
6.2.2 Experimental determination of molar absorption coefficient of toluene on SBA-15 and MCM-41 order mesoporous silica.....	139
6.3 Conclusions.....	143
References.....	146
Chapter VII:	
Monitoring the Adsorption of Glyphosate on Porous Materials.....	147
7.1 Introduction.....	147
7.2 Physico-chemical properties of SBA-15 and SBA-15-PAPTS.....	147
7.3 Study of the adsorption of glyphosate from aqueous media.....	151
7.3.1 Derivatization procedure.....	152
7.3.2 Quantification of glyphosate by UV-vis analysis.....	153
7.4. Kinetic adsorption studies of glyphosate on SBA-15 silicas.....	154
7.4.1 Kinetic adsorption models.....	157
7.4.1.1 Pseudo-first order model (Lagergren's equation).....	157
7.4.1.2 Pseudo-second order model.....	158
7.4.1.3 Elovich model.....	158

7.4.1.4 Intraparticle diffusion model.....	159
7.4.2 Application of kinetic adsorption models to experimental data.....	159
7.5. Equilibrium adsorption studies of glyphosate on and SBA-15-PAPTS.....	163
7.5.1 Equilibrium adsorption models.....	164
7.5.1.1 Freundlich model	165
7.5.1.2 Langmuir model.....	166
7.5.1.3 Elovich model.....	166
7.5.1.4 Temkin model.....	166
7.5.1.5 Dubinin–Radushkevich model.....	167
7.5.2 Fitting the experimental adsorption data with models.....	168
7.6 Conclusions.....	170
References.....	171
General Conclusions.....	175
List of Publications.....	180
Acknowledgements.....	181
Appendix I:	
Microporous Materials: Introduction to Zeolites.....	183
Ordered Mesoporous Silicas.....	189
References.....	193
Appendix II: Instrumental Parameters.....	196

Chapter I

Polluted Water from Anthropogenic Activities and its Remediation

1.1 Environmental pollution from anthropogenic activities

In the last century, the development of industry has grown enormously together with the global population. Unfortunately, the increasing of anthropogenic activities can have a damaging impact on the environment in terms of its degradation and pollution.^[1,2]

Pollution occurs when something is introduced to the environment which is harmful to ecosystems and human health. In other words, pollution is an adulteration of the environment by a chemical, biological or nuclear pollutant that renders it unfit for desired use.^[3]

Activities such as manufacturing and processing industries, transportation and consumption of natural resources, agriculture practices release a large amount of toxic pollutants in air, soil and water and this give consequently adverse health effects in human population. (Figure. 1.1)



Figure 1.1. Environmental pollution from anthropogenic activities. Adapted from references.^[4-9]

The pollutants produced from anthropogenic activities can be released to the environment in different forms. For instance, the atmospheric pollutants can be toxic gases (*i.e.* nitrogen oxides, sulfur oxides, carbon oxides, ozone, etc.), suspended particulate matter (SPM), and volatile organic compounds (VOCs). Soil and water pollutants may be of organic compounds (*i.e.* pesticides, insecticides, herbicides, phenols, hydrocarbons, etc.), heavy metals (*i.e.* lead, chromium, arsenic, zinc, cadmium, copper, mercury and nickel), as well as pathogenic agents.^[10]

Furthermore, the significant increase of pollutants in soil, water and atmosphere has warned the societies' conscience and consequently the concern on the human health. For example, substances that are toxic at low concentrations, carcinogenic, mutagenic and/or teratogenic can be bioaccumulated, particularly if they are persistent in the environment. For this reason, is important that pollutants emission from anthropogenic activities keeps below a level that limit their harmful effects.

The environmental challenges and the natural resources management were first focused in 1972 at the United Nations Human Environment Conference at Stockholm. Since then, a much greater awareness has been marked in the development of international environmental politics.^[11-15]

EPA (United States Environmental Protection Agency), that is an authority to control hazardous waste, established "The Resource Conservation and Recovery Act" (RCRA)-42 U.S.C. §6901 et seq. (1976). This act regularizes the generation, transportation, treatment, storage, and disposal of hazardous waste. Amendments to RCRA at 1986 were done to address environmental problems that could result from underground tanks that storing petroleum and other hazardous substances.^[16]

1.2 Groundwater pollution

Water is considered one of the most important resources for life on Earth, without water any organism could not survive. The total amount of water on Earth is approximately constant as indicated by the hydrologic cycle (Figure 1.2) because water moves from one reservoir to another remaining almost unchanged. Water evaporates from land and oceans into the atmosphere, forming clouds and then precipitates to land as rain or snow, and then goes into rivers and streams and comes back to the oceans and air.

Vaporization and transpiration release about $495 \times 10^{12} \text{ m}^3$ to the atmosphere each year. The $71 \times 10^{12} \text{ m}^3$ derived from land from evaporation of lakes, swamps, and soil water. Precipitation falls over the oceans, with the remaining over the landscape. Water vapor is transported in the atmosphere, with roughly $39 \times 10^{12} \text{ m}^3$ from the oceans each year. The additional $71 \times 10^{12} \text{ m}^3$ from evapotranspiration

over land gives a total atmospheric water volume of $110 \times 10^{12} \text{ m}^3$ that falls as precipitation over the continents each year.^[17-19]

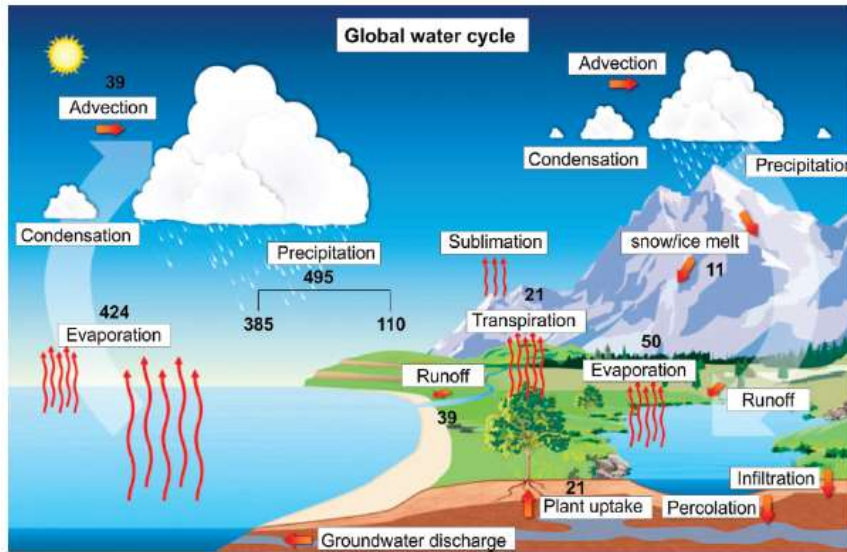


Figure 1.2: The global water cycle, with fluxes in $10^{12} \text{ m}^3 \text{ yr}^{-1}$. Adapted from ref.^[17]

However, about 71% of the Earth's surface is covered with water. The 97% of water on Earth is concentrated in the oceans and only the 3% of the water is fresh water (see Figure 1.3) and can be used by humans as drinking-water. Nevertheless, most of this useable water is inaccessible because this water is frozen in glaciers in places like the Antarctic and Greenland ice sheets. Fresh water can be found in underground (Groundwater) as soils moisture and aquifers. The rest of the water used by humans can be found on the surface (Surface water) which comes from rivers, lakes and swamps.^[20-22]

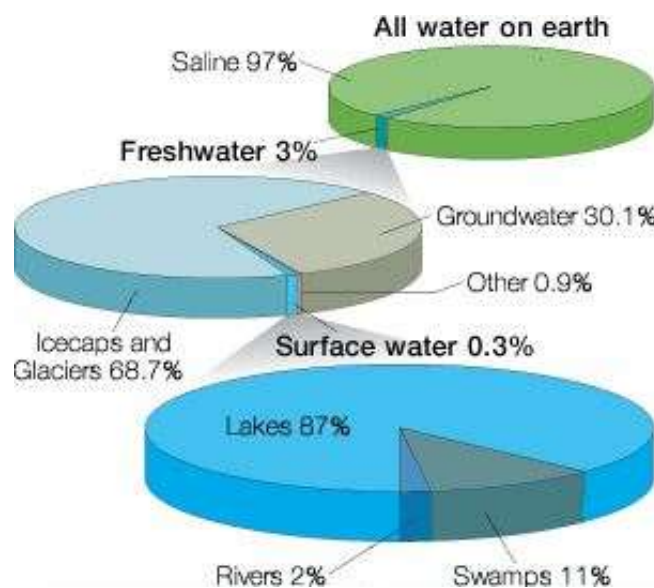


Figure 1.3: Water distribution on earth. Adapted from ref.^[23]

Groundwater which is defined as the water that is found under the surface of the Earth in conditions of 100% saturation. Water in the ground travels through the pores of soil and rocks, and in fractures and weathered areas of bedrock.^[24,21]

Furthermore, an aquifer is sediment of saturated water or rock in underground in which water can move easily. There are two main kinds of aquifers: unconfined and confined (Figure 1.4). Unconfined aquifer is a partially or fully filled aquifer which is exposed to the surface (atmosphere), additionally there is not an impermeable layer to protect it. In fact, anthropogenic activities can impact significantly on conditions of formation of groundwater because unconfined aquifer impacts by meteoric water and any kind of surface contamination.

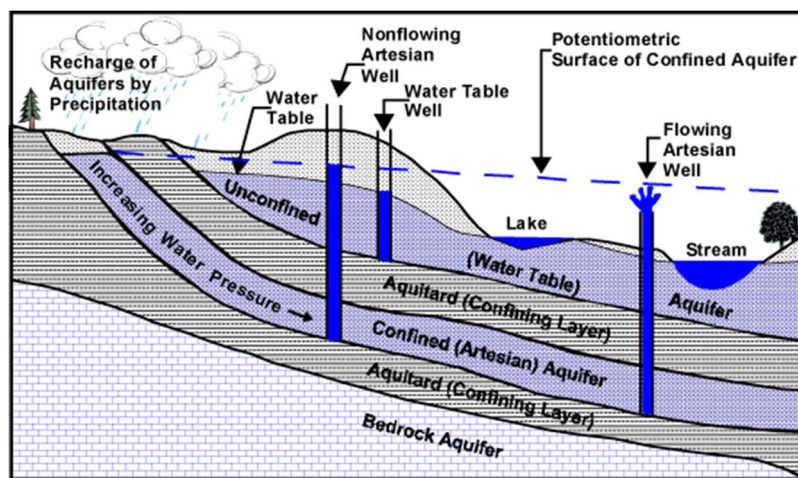


Figure 1.4: Aquifer types and groundwater movement. Adapted from ref.^[25]

Groundwater pollution affects human health. For example, high concentration of heavy metals such as As, Hg, Cd, Pb and Cu in drinking water cause several diseases as cancer of the skin, nervous diseases, kidney dysfunction, genetic changes, attacks bone tissues, attacks organic tissue, blood diseases, etc. On the other hand, changes in the acidity and free carbon dioxide concentration can increase groundwater corrosive activity and consecutively change the ecosystem productivity.

Hydrocarbon product leakage can create gas 'caps' and origin odour problems and fires.^[22] Groundwater can be contaminated from several sources. Thousands of pollutants are released into the groundwater coming principally from industrial manufacturing wastes, municipal landfills, leaking underground storage tanks, agriculture activities, mineral extraction (mining) and petroleum and gas production/storage.^[26]

For this, the effective application of environmental protection policies for groundwater source improves drinking water quality. With the aim of assure water quality, the European Union in 2000 adopted the Water Framework Directive (Directive 2000/60/EC) of the European Parliament and of the Council, establishing a basis for public action in the field of water policy.^[27]

1.2.1 Organic pollution in groundwater

Organic pollutants detected in groundwater are pesticides, herbicides, solvents degreasers and petroleum components.^[26,28-31]

Some classes of organic contaminants are listed in Table 1.1:

Table 1.1: Examples of organic pollutants:

Organic Pollutants
Petroleum hydrocarbons (fuels): Benzene, toluene, xylene, polynuclear aromatic hydrocarbons (PAHs), polychlorinated biphenyl (PCBs) and metals, in particular Pb.
Aliphatic compounds: methane, ethane and propane
Nitrogen compounds- pyrrole and pyridine.
Sulphur compounds- thiols and thioethers.
Chlorinated solvents- Trichloroethene, tetrachloroethene, trichloroethane, carbon tetrachloride
Pesticides and herbicides- DDT (dichloro-diphenyl-trichloro-ethane); 2,4-D (2,4-dichlorophenoxyacetic acid), atrazine, organophosphorus (glyphosate).
Polychlorinated biphenyls (PCBs)- insulating fluids, plasticizers, pigments.
Coal tar/creosote-Polycyclic aromatics
Pharmaceuticals/food additives/cosmetics-Drugs, surfactants, dyes.
Gaseous compounds-Chlorofluorocarbons (CFCs), hydrochlorofluorocarbons (HCFCs)

Hazardous organic pollutants present in groundwater can be defined as organic substances or groups of substances that are toxic and have an average degradation of more than one year and are widely detected or bioaccumulate in animal tissues.^[32] Furthermore, the toxicity of an organic contaminant is defined as its inherent capacity to cause an adverse health effect.^[33] Using information from Regulation 1272/2008 (EC, 2008) and guidance provided by the European Chemicals Agency (ECHA, 2009), substances are defined as being toxic if the substance is classified as being Acutely Toxic (Category 1, 2, 3).

Therefore, when a substance is classified as hazardous, the entry to groundwater should be prevented. The appropriate controls on hazardous and non-hazardous substances should be meditated in conditions of the surround activities of release of pollutants to groundwater.^[32] For example, oils and fuels generally enter to groundwater near to refinery activities as a result of leaking piping or accidental spills during transport and leaks from storage tanks.^[34]

1.2.1.1 Hydrocarbons

Organic pollutants such as hydrocarbons persist as the major class of pollutants of groundwater. Generally, when hydrocarbons released into the aquatic environment tend to float on the water surface and result in the formation of a thin surface film called the light non-aqueous phase liquids (LNAPLs). Others hydrocarbon fractions which have higher molecular weight dense non-aqueous phase liquids (DNAPLs) will accumulate in the sediment at the bottom of the water (see Figure 1.5).

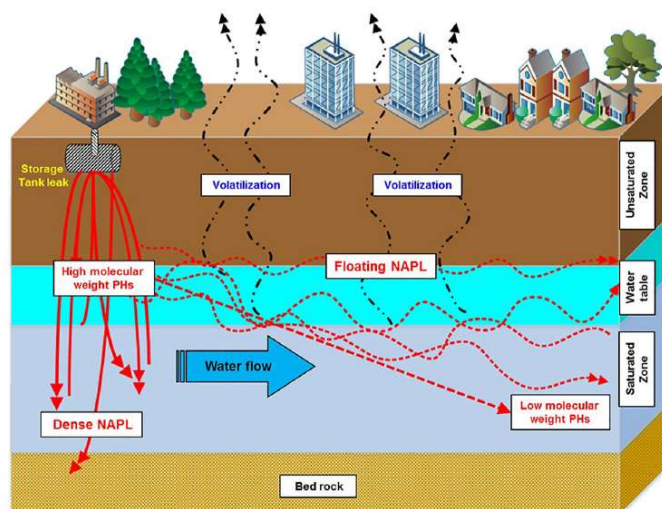


Figure 1.5: Schematic hydrocarbons movement after the storage tank leak into the groundwater. Adapted from ref.^[35]

Hydrocarbons are organic compounds constitute of carbon and hydrogen atoms arranged in varying structural configurations. Hydrocarbons can be divided into two families: aliphatic and aromatic. The aliphatic hydrocarbons could be further subdivided into four groups: alkanes (straight and branched chain), alkenes, alkynes and cyclic alkanes.

The aromatic components of gasoline and other petroleum products are a group of aromatic molecule hydrocarbon (BTEX compounds: benzene, toluene, ethyl benzene and the three xylene isomers o-, m-, and p- xylene) are considered hazardous and are the principal concern about groundwater pollution.^[32] Aromatic hydrocarbons with lower molecular weight tend to be highly soluble in water whereas alkanes are non-polar and hydrophobic and are considered as slightly soluble in water. Nevertheless, BTEX due to their high solubility frequently are found in contaminated groundwater plumes. Normally, solubility of benzene, toluene, ethyl benzene, xylenes and gasoline in water are 18, 25, 3, 20, 50–100 mg L⁻¹, respectively.^[36]

EPA has established a maximum contaminant level (MCL) in drinking water for benzene, toluene, ethylbenzene and isomers of xylenes at 0.005, 1, 10 mg L⁻¹, respectively.^[37,38]

Toluene is an aromatic hydrocarbon which has a sweet and pungent odour. The lowest concentrations reported to be perceptible to humans on inhalation range from 0.64 to 139 mg m⁻³. The odour threshold in water is 0.024–0.17 mg L⁻¹. The reported taste threshold ranges from 0.04 to 0.12 mg L⁻¹.^[38] In groundwater contaminated, toluene levels of 0.2–1.1 µg L⁻¹ were reported and the highest level reported in groundwater in the USA in 1983 was 1.4 µg L⁻¹.^[39]

In approximately 1% of all groundwater-derived public drinking-water systems in the USA, toluene levels are above 0.5 µg L⁻¹.^[38,39]

The health effect to the exposure of toluene by inhalation is impairment of the central nervous system and irritation of mucous membranes. Fatigue and drowsiness were the most sensitive effects, being present at 375 mg L⁻¹ and absent at 150 mg L⁻¹. Furthermore, the toxic effects of toluene after long-term exposure are basically identical.^[38]

n-Hexane is an aliphatic hydrocarbon which is a colourless liquid with a slightly disagreeable odour. Additionally, *n*-hexane is highly flammable and explosive gas. The toxicity of this compound is related primarily to inhalation exposure because its high volatility (vapor pressure of 150 mm Hg at 25 °C) and low solubility in water (9.5 mg/L at 25 °C).^[40]

Significant oral exposure of *n*-hexane through food or drinking water has not been reported. Little information exists for oral or dermal exposure to *n*-hexane in humans or animals.^[41]

Most petroleum hydrocarbon mixtures contain very low concentrations of the polycyclic aromatic hydrocarbons (PAHs) which contain 2-6 aromatic rings and are generally toxic, carcinogenic and mutagenic. PAHs with less aromatic rings (<4 ringed) such as naphthalene are more volatile and thus less toxic than non-volatile, persistent, hydrophobic PAHs. PAHs could potentially affect the nervous system, immune systems, excretory system (kidney) and also cause cancer and mutations.^[35] In particular, benzo(a)pyrene and benz(a)anthracene are classified as probable human carcinogens, and a small concentration have been shown to induce skin tumours in skin painting studies in laboratory mice.^[40,42] Benzo(a)pyrene is normally considered to be the most potent carcinogenic PAH, but the carcinogenic potency of most PAHs is not well characterized. Nevertheless, under situations of spills of petroleum products affecting water, PAHs are not usually a specific concern.^[40,42]

Besides, petroleum derived products will frequently also contain additives such as oxygenated fuel additives as methyl tert-butyl ether (MTBE) in very low concentrations. Nevertheless, MTBE can

make water supplies undrinkable, even at low concentrations. For this reason, the use of MTBE in gasoline is now being replacing out.^[40,42]

1.2.1.2 Herbicides

In recent years, researchers deserved interest for the depollution of groundwater by pollutant coming from agriculture activities.^[43-45]

Chemical substances such us pesticides and herbicides are frequently used in the agriculture field.^[46]

More specifically, herbicides are widely used in field crops to control the presence of weeds. Their broad application range entails a significant use and consequently an increase of their impact on the environment. In particular, it is known that long-term use of herbicides can lead to pollution of groundwater.^[44]

Herbicides are classified as: i) contact herbicides (they affect only the part of the plant that they touch) and ii) translocated herbicides (that are altering the normal biological function of the plant-systemic herbicides). Furthermore, a combination of systemic and contact herbicides (Chlorinated aliphatic acid herbicides) such as trichloroacetic acid (TCA), amide herbicides (e.g., alachlor, metachlor), carbamates (thiocarbamates and dithiocarbamates) and phenoxy herbicides (e.g., 2,4-D) are also used. Examples of contact herbicides are diclofop, dinoseb, diquat, and paraquat whereas translocated herbicides are atrazine, glyphosate, 2,4-dichlorophenoxyacetic acid (2,4-D) and simazine.^[47]

Particular attention was recently given to glyphosate-based herbicides which are enormously common around the world due to their cost-effectiveness. Glyphosate [N-(phosphonomethyl) glycine] is a broad spectrum, non-selective systemic herbicide.^[48] According to literature data glyphosate is less dangerous than other herbicides from the organophosphorus family, toxic effects can only be at high doses.^[49-51]

Glyphosate is a compound of EPA Toxicity Class III.^[52] However, studies suggest that when combined with other ingredients, it may be considerably more toxic than glyphosate alone, for example the Roundup Original mixture (commercial herbicide product) formula contains polyoxyethylene amine (POEA) that is already demonstrated to be more toxic than glyphosate to aquatic organisms.^[43]

The US maximum contaminant level (MCL) of glyphosate in drinking water is $700 \mu\text{gL}^{-1}$, which is higher than for other pesticides.^[53] Nevertheless, this concentration is much higher than the European tolerable level of only $0.1 \mu\text{gL}^{-1}$.^[54]

The large difference between American and European permissible levels is due to different policies. In Europe, $0.1 \mu\text{gL}^{-1}$ is administratively established as the upper tolerable threshold for all pesticides, while the US maximum is based on toxicity tests on glyphosate.^[55]

1.3 Removal of pollutants from groundwater

The increased agricultural, industrial, and domestic activities have resulted in the increased of large amount of organic compounds which are polluting the available groundwater and affect the human and animal health. As a consequence, in the last decades, research efforts were focused to the decontamination of groundwater from organic contaminants (*e.g.* methyl tert-butyl Ether, MTBE). Several treatment technologies have been established to remove pollutants from wastewater (*i.e.* physical techniques, chemical methods and biological processes methods) (Figure 1.6), such as biological or chemical oxidation, coagulation, sedimentation, photo-Fenton treatment, advanced oxidation processes (AOPs), photocatalytic oxidation/degradation, membrane processes, electrochemical oxidation/degradation, adsorption.^[56,57]

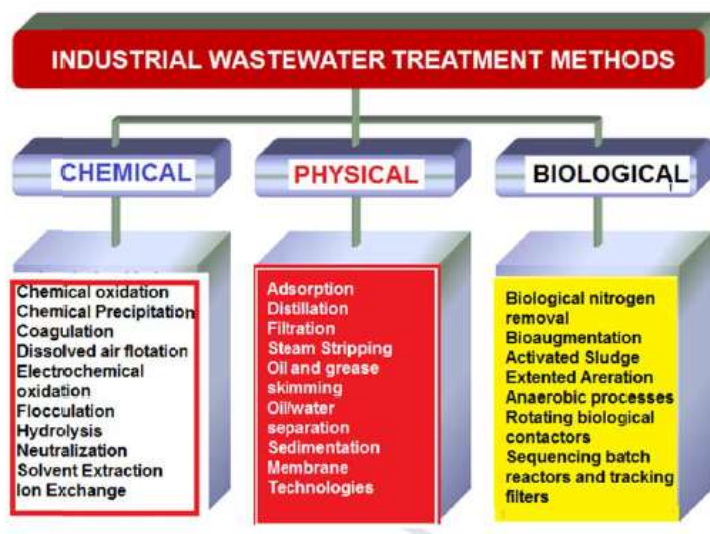


Figure 1.6: Methods for water or wastewaters treatment. Adapted from ref. ^[56]

All above mentioned methods can be applied alone or in combination and can be further divided into *in situ* (*air sparging, flushing, permeable reactive barriers, sand filtration*) and *ex situ* (*pump and treat methods*) remediation technologies.^[36]

Pump and Treat (P&T) is one of the most conventional used *ex situ* groundwater remediation technologies. Conventional “pump and treat” methods involve pumping contaminated water to the surface for treatment.^[58]

In-situ remediation is the in-place remediation of the contaminated groundwater. One example of this technology is represented by permeable reactive barriers (PRBs), which have been used for treatment of petroleum contaminated groundwater.^[36, 59-61]

Permeable reactive barriers PRBs are an emerging alternative to traditional P&T methods for groundwater remediation.^[59,60,62]

In fact, PRBs results advantageous with respect to P&T because: once built PRBs don't require any surface manipulation; polluted groundwater is treated underground without any further work by operators; can be used while operations are in progress and there are no energy costs because PRBs exploit natural flow of groundwater.^[63]

The PRB consists of the emplacement of a reactive media perpendicular to the trajectory of the contaminated groundwater. In fact, the contaminate plume migrates through the reactive barrier interacting with the media under the influence of the natural hydraulic gradient (us shown in Figure 1.7).

The contaminants in the plume react with the media leading to either their transformation to less harmful compounds or fixation to the reactive materials^[64-67]

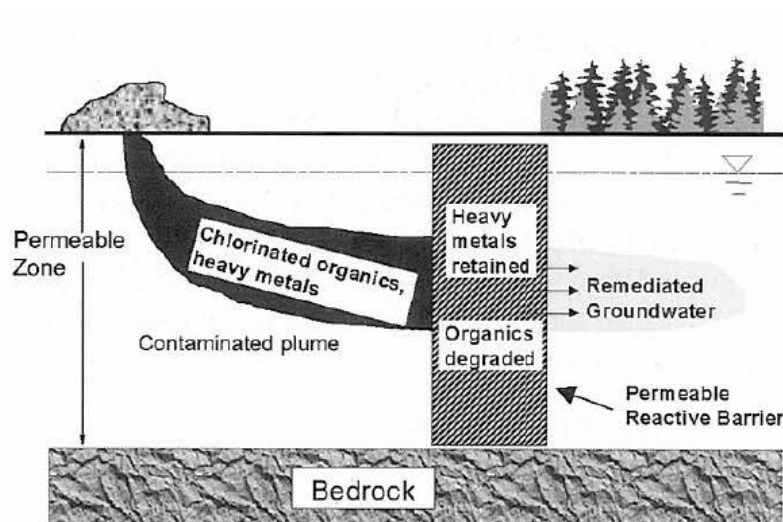


Figure 1.7: PRB intercepting pollutants from a contaminate plume. Adapted from ref.^[68]

Reactive materials within the barrier are selected to promote reactions that result in the destruction or stabilization of the groundwater contaminants.^[69]

For instance, zero-valent iron (ZVI) has been successfully applied for the remediation of groundwater and wastewater contaminated with chlorinated organic compounds (COCs), nitroaromatic compounds (NACs), arsenic, heavy metals, nitrate, dyes and phenol due ZVI is non-toxic, abundant, cheap, easy to produce, and its reduction process requires little maintenance.^[70] Another type of

adsorbent a lot used and studied is granulated activated carbon (GAC). The simplicity of the GAC system operation, commercial availability, no off-gas treatment requirements and well-known equipment and methods make such systems relatively beneficial.^[71]

However, it is known that GAC performance is reduced in the presence of other organic compounds and natural organic matter.^[72]

Other examples of reactive materials for the PRBs are activated carbons, clay minerals, biomaterials microorganisms, natural zeolites, peat, phosphates, limestone and amorphous ferric oxide.^[73,74]

The contaminants are immobilized in the PRB through chemical or physical processes. These interactions could be reduction, sorption, precipitation and biochemical degradation of contaminants. Sorption and precipitation are potentially reversible and may thus require removal of the reactive media and gathered products in order to continue with remediation.^[75] In particular, sorption includes adsorption, absorption and ion exchange by a reactive media.^[76]

Specifically, *adsorption* is a process that occurs when pollutants molecules (adsorbate) come in contact with the surface of the reactive media (adsorbent). The adsorption process is referred to a *chemisorption*, if the interactions between the reactive media and pollutants are due to the formation of chemical bonds. Contrary to chemisorption, *physisorption* process occurs if the attraction forces between the pollutants (adsorptive) and adsorbent surface are due to physical bonding (*i.e.* van der Waals forces) and processes are reversible since attractions are weak.^[77]

Since the adsorption process is a surface process, structural and textural properties (*i.e.* specific surface area (SSA), pores size distributions and pores morphology) of the adsorbent is of relevant importance to guarantee high adsorption performances. The porous solid materials classified are pores according to their size (IUPAC recommendation):(i) pores with widths above about 50 nm are called macropores; (ii) pores of widths between 2 nm and 50 nm are called mesopores; (iii) pores with widths not exceeding about 2 nm are called micropores.^[78]

1.3.1 Materials used as adsorbents for groundwater decontamination

Different adsorbents have been studied for depollution of groundwater purpose and their interactions with contaminants have been discussed in a lot of reviews.^[79] In general, the adsorbent material is selected on the basis of the type and concentration of the pollutant to be removed, the treatment technologies, the hydrogeological and biogeochemical conditions of the aquifer, the environmental/health impacts, mechanical/hydrothermal stability, the availability and cost of the material.^[64,80]

In any case, the effectiveness of the adsorbents materials depends of the physical–chemical properties and the nature of the pollutants to be removal. Particularly importance is related to the decontamination of groundwater from hydrocarbons, chlorinated hydrocarbons and oxygenates (MTBE).

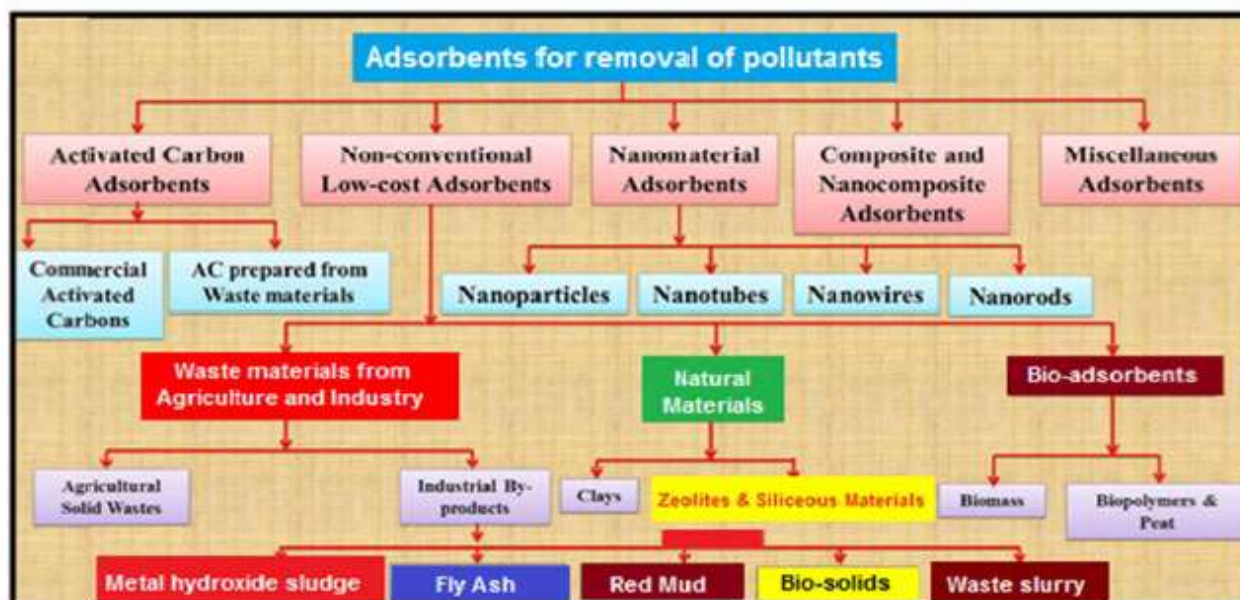


Figure 1.8: The most common adsorbents for pollutants removal from aqueous solution. Adapted from ref.^[56]

Zero-valent iron (ZVI) is the most common adsorbent. Generally, ZVI with specific surface area ranging 0.5 to $1.5 \text{ m}^2 \text{ g}^{-1}$.^[64] Their advantages are being non-toxic, high activity, low price, and global availability.^[81] It's used for groundwater treatment started in early 1990s. For instance, Gillham et. al. obtained positive results by testing ZVI as an enhancing agent for the dehalogenation of chlorinated methanes, ethanes and ethenes in aqueous solutions.^[82,83]

Works in recent years has demonstrated that ZVI can successfully applied for the treatment of groundwater to remove different types of organic pollutants, such as dyes^[84,85], chlorinated organic compounds (COCs)^[86,87] and phenols.^[88,89] Although ZVI has been extensively used to remediate polluted groundwater, its application has been limited due to main problems, such as a narrow

working pH, low reactivity due to its low specific surface area and accumulation of some toxic intermediates (especially the lightly chlorinated hydrocarbons).^[90]

Other examples of reactive media are activated carbons (ACs). ACs are chemically stable materials and are widely considered as suitable adsorbent for treatment of polluted groundwater.^[91] In addition, ACs present a high adsorption capacity for organic contaminants due to its high surface area (about $1000 \text{ m}^2 \text{ g}^{-1}$). ACs are carbonaceous materials possessing chemically heterogeneous surfaces (phenolic and carboxylic groups) with high adsorption capacity. Thus, ACs, mostly in granular form (GAC), were commonly used materials in the early stages of PRB technology for groundwater depollution to removal of contaminants such as phenols, BTEX, tetrachloroethylene (PCE), trichloroethylene (TCE) and polycyclic aromatic hydrocarbons (PAHs).^[92-94] Generally, GAC has a macro and microporous structure with quite high surface areas ($1000\text{--}1500 \text{ m}^2 \text{ g}^{-1}$).^[95] These properties make to GAC an efficient adsorbent for organic molecules with high molecular weight.

Although ACs has been used for groundwater treatment in many cases, the drawback of ACs is that the adsorption of contaminants is influenced by the pH. Peng et al. noticed that high pH causes ionization of the carboxylic and hydroxylic groups on the surface of the AC.^[96] This ionization promotes the interactions between the water molecules with the AC surface consequently decreasing the adsorption of particularly hydrophobic contaminants. Moreover, Liu and Pinto also observed a decrease in phenol adsorption when the pH was reduced from 6.3 to 3.07.^[97] Other limitation of ACs is the low selectivity for organic pollutants, for example Cornelissen et al. founded that the adsorption capacity of ACs to adsorb organic pollutants may also be affected by other constituents such as natural organic matter. Therefore, if ACs are considered as adsorbents, then the aquifer must be adequate characterized.^[64]

To front these drawbacks of ACs, zeolites have been recently distinguished as an alternative despite of the high adsorption capacity of ACs. This due to the selectivity of zeolites is confirmed of their regular pores able to adsorb organic molecules with dimension and polarity similar with those of the contaminants present in groundwater. For example, Rossner et. al. verified the adsorption performances of zeolite, in terms of both selectivity and stability under realistic operating conditions, better than that of traditional adsorbents based on granular active carbons (GACs). Authors found adsorption uptakes of MTBE was higher for the silicalite zeolite than for GAC and the co-adsorbing with natural organic matter had more effect on GAC than the silicalite zeolite.^[98]

1.3.1.1 Zeolites as adsorbents for hydrocarbons removal from groundwater

Zeolites are aluminosilicate minerals with an ordered structure. They are characterized by high internal and external surface areas. A short overview of the structural and physico-chemical features of zeolites is given in Appendix I.

It is acknowledged that the adsorption properties of zeolite minerals are definite by their pore size and superficial chemical properties.^[99]

The pore architecture i.e. pore size, pore size distribution, pore volume, and pore topology of zeolites play a key-role for the adsorption of organic molecules. For instance, zeolites have pore size ranging between 2-10 Å.^[156] In addition, adsorption of organic molecules on zeolites occurs by filling the micropores volume as other microporous adsorbents. This process of adsorption occurs by physisorption and is characterised by an enhancement of the adsorption energy due to the increase of dispersion forces.^[100] This means that the pollutants which have molecular dimensions similar to the dimensions of the channels can enter into and interact with the zeolite through Van der Waals and other electrostatic interactions. Therefore, zeolites can be used for selective adsorption of organic pollutants on the basis of their differences in molecular size and shape.

Natural zeolites generally have larger particle size and specific surface areas up to $145 \text{ m}^2 \text{ g}^{-1}$ which makes them able for use as a reactive media, but their low hydrophobicity limits their sorption for organic compounds.^[101,102]

In addition, researchers have focused on the development of modified zeolites with the aim of increasing their hydrophobic properties to obtain higher hydrocarbon adsorption capacities compared to natural zeolite.^[103] For instance, Scherer et al. reported the effectiveness of surfactant-modified zeolites (SMZs) to remove non-polar organic contaminants such as benzene, toluene, ethylbenzene and p-, m- and o-xylene (BTEX compounds) and chlorinated solvents such as perchloroethene, 1,1,1-trichlorethane, and pentachloroethane) by modifying the surface chemistry of zeolites with surfactants (e.g. hexadecyltrimethylammonium, HDTMA, $(\text{C}_{16}\text{H}_{33})(\text{CH}_3)_3\text{N}^+$) and by adding hydrophobic segments on the zeolite surface. Unfortunately, sorption of non-polar organic compounds is favoured at low concentrations.^[104]

Another example of surfactant modified zeolites (SMZs) was reported as highly effective for the treatment of hydrocarbon-containing wastewater by Altare et al. In particular for the adsorption of benzene, toluene, ethylbenzene, and p-, m- and o-xylene (BTEX compounds). Unfortunately, there

was evident a progressive surfactant release with a negative impact both on economics and environmental issues.^[105,106]

Northcott et. al. studied a modified natural zeolite (clinoptilolite) as an adsorbent in permeable reactive barrier (PRB) for treatment of hydrocarbons in groundwater. The hydrophobic zeolite was obtained by modifying the surface by covalently bonding to octadecyltrichlorosilane (C18). In particular, the authors characterized the hydrophobic zeolite (Z-C18) for the adsorption of hydrocarbons in water solutions of naphthalene and o-xylene of 20 and 30 mg L⁻¹ of concentration, respectively. As showed in Figure 1.9, an effective adsorption capacity was obtained with Z-C18 for xylene and naphthalene removal from water. Besides high adsorption capacity, regeneration is another important issue for the longevity of PRBs, authors also have demonstrated that only MilliQ water and methanol followed by a MilliQ wash can be used to clean the Z-C18 and the regenerated Z-C18 can be reused for hydrocarbon sorption at least 3 times.^[107]

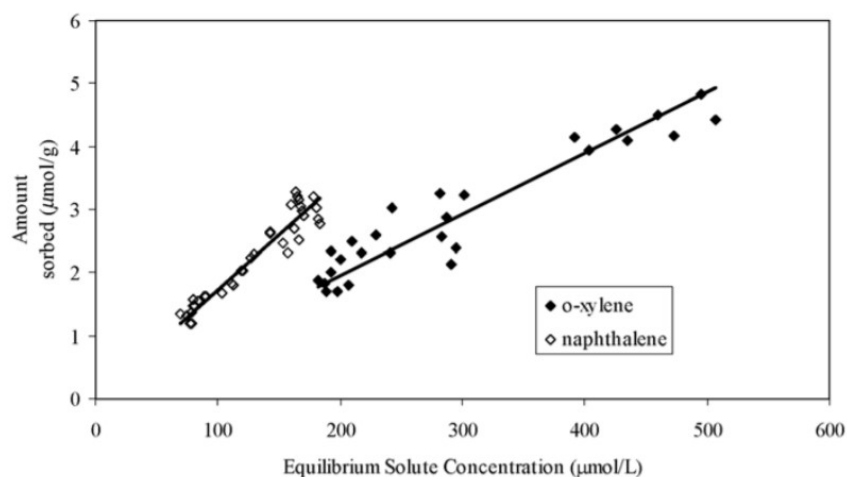


Figure 1.9: Adsorption isotherms of o-xylene (30 mg L⁻¹) and naphthalene (20 mg L⁻¹) on Z-C18.

Experiments at 20 °C with 1.5 g of Z-C18 and 50 mL of the organic component dissolved in water. Adapted from reference.^[107]

Recently, J. Ma et al. studied the effect of temperature on hydrocarbon adsorption by using a natural clinoptilolite zeolite modified with diphenyldichlorosilane (DPDSCI) for its application in PRBs in cold regions. They obtained good performances for batch adsorption test for toluene at cold temperatures (4 °C). Authors demonstrated that the modification of the zeolite surface improves the adsorption capacity of the raw zeolite (at low toluene concentrations, DPDSCI coated zeolite presented 17% of toluene uptake whereas the raw zeolite exhibited less than 1% of toluene uptake), as shown in Figure 1.10 (adapted from reference). The comparison of adsorption isotherms of the modified zeolite at various toluene concentrations at 20 and 4 °C showed that at low concentrations

of toluene, the adsorption capacity of modified zeolites decreased to 8.7% of toluene uptake at low temperatures. The free energy and enthalpy change of toluene adsorption of DPDSCI coated zeolite at 20 and 4 °C, respectively resulted negative ($\Delta G = -19.15$ and -18.04 kJ mol⁻¹) indicating that the sorption process occurs spontaneously, which is the nature of adsorption processes. This process was found to be endothermic as the enthalpy change of this process resulted positive (1.5 kJ mol⁻¹) concluding that interactions during adsorption process between hydrocarbon and DPDSCI coated zeolite were mainly Van der Waals interactions with some hydrophobic bonding between aromatic moieties (π - π electron stacking interactions).^[108]

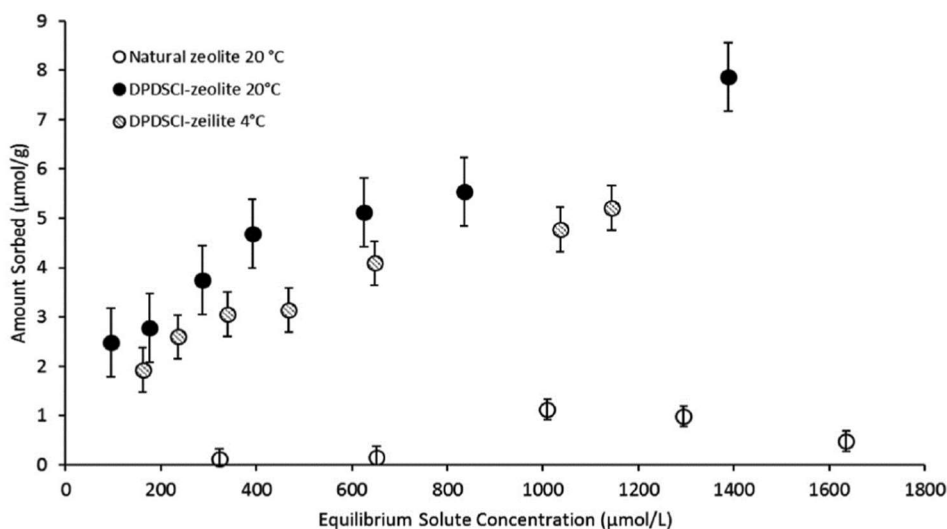


Figure 1.10: Toluene adsorption isotherms on DPDSCI-zeolite at 20 °C and 4 °C. Adapted from reference.^[108]

Several studies of natural and synthetic modified zeolites have been extensively performed. A summary of these studies is reported in Table 1.2.

Table 1.2: Overview of studies of modified and natural zeolites for groundwater remediation from hydrocarbons.^[108]

Adsorbent Material	Surfactant modification	Organic pollutant to be removal	Adsorption Capacity [$\mu\text{mol g}^{-1}$]	Ref.
Clinoptilolite	Diphenyldichlorosilane (DPDSCI)	Toluene Xylene Naphthalene	5.16 8.90 22.32	[109]
	Octadecyltrichlorosilane (C18)	Naphthalene o-Xylene	5.0 3.5	[110]
	Hexadecyltrimethylammonium (HDTMA)	Benzene Phenol Chlorophenol	212.95 120.74 98.86	[111, 112]
	n-Cetylpyridinium bromide (CPB)	Benzene Phenol	295.77 126.38	[111]

	Benzyltetradecyl ammonium chloride (BDTDA)	Phenol Chlorophenol	13.81 49.86	[112]
	Stearyldimethyl benzyl ammonium chloride (SDBAC)	Atrazine Lindane Diazinone	2.00 3.40 4.40	[113]
	Octadecyldimethyl benzyl ammonium (ODMBA)	Ochratoxin A Fumonisin B1	8.45 10.18	[114, 115]
<i>Synthetic zeolites</i>				
NaY zeolites Si/Al=1.8 and 2.0	Octylmethyldichlorosilane	Toluene	2340	[116]
ZSM-5 zeolites Si/Al= 31	Hexadecyltrimethylammonium (HDTMA)	Benzene Toluene Phenol	99.26 101.43 78.96	[111]
ZSM-5 zeolites Si/Al= 31	n-Cetylpyridinium bromide (CPB)	Benzene Toluene Phenol	191.67 178.70 100.27	[111]
Nano-zeolite NaA particles (NaAZNPs)	Hexadecyltrimethylammonium bromide (CTAB)	Total Petroleum Hydrocarbons (TPH)	92.30%	[117]

1.3.1.2 Hydrophobic zeolites as adsorbents for hydrocarbons removal from groundwater

The effective adsorption properties of zeolites for non-polar organic pollutants can be controlled by increasing the SiO₂/Al₂O₃ ratio due that highly siliceous zeolites have a hydrophobic nature and thus strong affinity for hydrocarbons.^[118,119]

Flanigen et. al. in 1978 synthesized the first high-silica zeolite (ZSM-5 silicalite) with hydrophobic, organophilic properties and selective for organic molecules such as methanol, propanol, butanol, phenol, 1,4-dioxane, neopentane and hexane in presence of water.^[100] Silicalite was synthesized by using alkylammonium cations (tetrapropylammonium hydroxide TPAOH) as template in basic medium (sodium hydroxide). Silicalite was characterized by a framework with a system of intersecting channels composed of zig-zag and straight channels with pore sizes about 6 Å and a pore volume of 0.19 cm³ g⁻¹. Authors obtained that the most remarkable adsorption property of Silicalite was surface selectivity due that this zeolite adsorbs molecules with dimensions similar to benzene (kinetic diameter 5.85 Å) but reject molecules with dimension larger than 6 Å such as neopentane (kinetic diameter 6.2 Å). Silicalite showed a very low selectivity for the adsorption of water and a very high preference for the adsorption of organic molecules smaller than its limiting pore size.^[100] In addition, this silicalite resulted electrically neutral, therefore there was not strong interaction with water

molecules and energetically the molecules of water preferred to remain as a liquid outside the silicalite.

Moreover, hydrophobicity of zeolites can be improved by increasing the Si/Al ratio. This can be obtained by modifying the method of synthesis. For instance, by replacing partially or totally the hydroxide media (mineralizer agent) with fluoride media such as sodium fluoride (NaF), potassium fluoride (KF) and ammonium fluoride (NH₄F).^[155]

Anderson et. al. obtained positive results using three different high silica zeolites mordenite (MOR), ZSM-5 and Y with diverse pore size and SiO₂/Al₂O₃ ratio (200, 1000 and 75, respectively) for the batch adsorption of solution concentrations of 100 µg L⁻¹ of MTBE, chloroform, and trichloroethylene (TCE). MOR and ZSM-5 with the highest SiO₂/Al₂O₃ ratio resulted to have higher sorption properties for MTBE and TCE than Y zeolite and two activated carbons used as reference sorbents.^[120]

Other work about the importance of hydrophobic zeolites was reported by Meininghaus et al. They studied the adsorption properties of NaZSM-5, Faujasites and dealuminated Mordenite zeolites for five solvents (methanol, methyl ethyl ketone, toluene, p-xylene, *n*-pentane) as single components and for the mixture of all five organic solvents in the presence and absence of water. Meininghaus et. al. concluded that reducing the amount of aluminium in the zeolites structure gives hydrophobicity properties. The authors also concluded that Faujasites and dealuminated mordenite are more suitable than ZSM-5 for separating mixtures with several components due their larger pore sizes.^[121]

Similarly, Khalid et. al. compared the adsorption properties of three large-pore zeolites (HFAU, HBEA, and HMOR) possessing a high Si/Al ratio (16-100), a medium-pore zeolite (MFI) and a one purely siliceous BEA zeolite (Si/Al=∞) to those of an activated carbon for the phenol removal from aqueous solution (concentration range from 0.1 to 1.6 g L⁻¹).^[122]

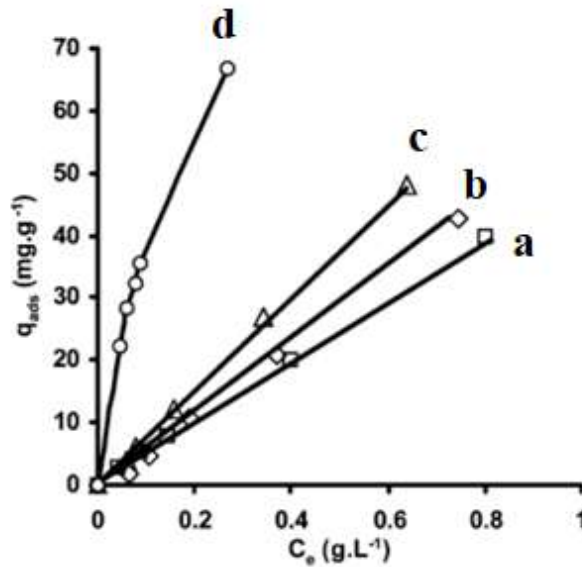


Figure 1.11: Adsorption isotherms of phenol on zeolites where C_e is the residual concentration of phenol in aqueous solution: HMOR (80) curve a; HFAU (100) curve b; MFI (500) curve c and BEA (∞) curve d.

Adapted from reference.^[122]

Khalid concluded the hydrophobic character of the zeolite plays an important role in defining the adsorption properties. BEA and MFI which possess a high Si/Al ratio resulted more efficient to adsorb the phenol concentrations than the other zeolites as shown in Figure 1.11(adapted from reference). At low phenol concentration, no significant differences between MFI, FAU, and MOR zeolites whereas for higher concentrations, the adsorption capacity follows the Si/Al ratio of the adsorbent: BEA (∞) > MFI (500) > FAU (100) > MOR (80). Authors also concluded that BEA (Si/Al= ∞) zeolite appeared to be more efficient than an activated carbon at low phenol concentration ($<1.6 \text{ g L}^{-1}$) due to a pore-size effect whereas the activated carbon resulted to have high capacity at high phenol concentrations due to the higher specific surface area ($1150 \text{ m}^2 \text{ g}^{-1}$ for activated carbon and $500 \text{ m}^2 \text{ g}^{-1}$ for BEA zeolite).^[122]

Koubaissy et. al. studied the importance of the pH and solubility in water of organic aromatic compounds (nitrophenols, nitroaniline, chlorophenols, chloroanilines) on the adsorption properties of a dealuminated faujasite zeolite (HFAU, Si/Al=100). Authors observed a linear correlation between the adsorption capacities and the solubility of the organic aromatic compounds. Indeed, authors demonstrated that although the adsorption capacity increased with decreasing the pH of the solution, increasing the acidity in significant amounts does not always improve the adsorption capacities (optimal pH = 4). With this, authors concluded that the neutral form of the pollutants is more easily adsorbed into zeolite than the dissociated form and the relative affinity of the phenolic compounds

toward the surface of HFAU was related to the electron donor-acceptor complex formed between the basic sites (oxygens) on the zeolite and acidic sites (hydrogens) of the aromatic ring and of the phenols and anilines compounds.^[123]

These previous encouraging results have confirmed that high silica zeolites with hydrophobic properties are able to be used as efficient adsorbent materials for the decontamination of groundwater from organic pollutants. Consequently, attention has been focused on the characterization and the adsorption properties (*i.e.* adsorption capacity, interaction types and selectivity) of different dealuminated zeolites for hydrocarbons removal from groundwater.

For instance, Vignola et. al. developed a technology called En-Z-Lite™ at ENI S.p.A. (Ente Nazionale Idrocarburi, Italy). Vignola considered the performances of ZSM-5 and mordenite zeolites with high SiO₂/Al₂O₃ molar ratio used for one year as adsorbents in a permeable reactive barrier (PRB) located under a coastal refinery in Italy for hydrocarbons removal. The reactive media was selected according to its specificity towards different classes of contaminants present in the aquifer such as aliphatic hydrocarbons (olefins:1-butene and substituted cyclopentanes), aromatic hydrocarbons (benzene, ethylbenzene, cumene, xylenes) and oxygenates (e.g. methyl tert-butyl ether, MTBE and trace amounts of ketones). The removal of contaminants by zeolite materials has been monitored during one year by analysing water samples and the effective adsorption on adsorbed in the in the structural channels of both adsorbents. The results of this year of studies demonstrated that ZSM-5 was more appropriate for the adsorption of light hydrocarbons than mordenite zeolite which structures make it more effective against heavy hydrocarbons and MTBE. As showed in Figure 1.12, mordenite reported significative adsorptions of MTBE and was the responsible to maintain the concentration of MTBE below the target level (350 µg L⁻¹) whereas ZSM-5 adsorbed over 0.1 ppb of MTBE only after the first 100 days.^[124,63]

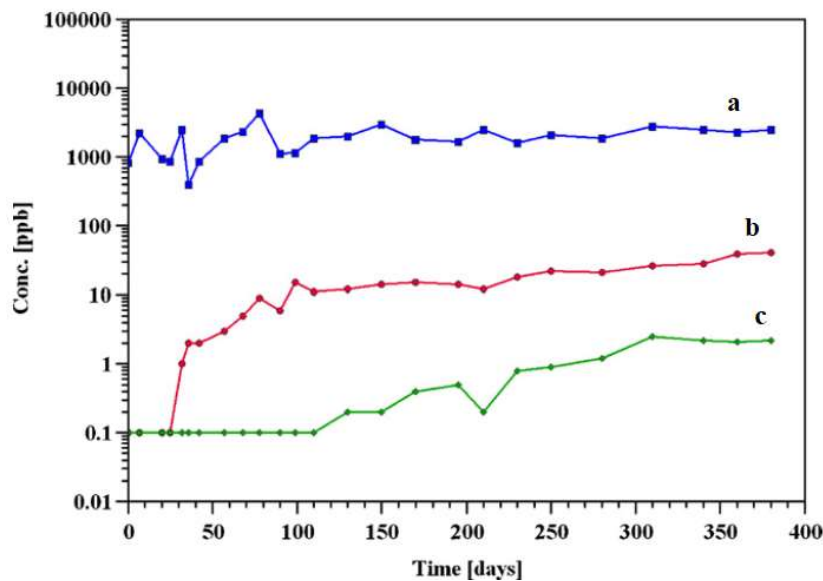


Figure 1.12: Evolution and treatment trend during one year with ZSM-5 and mordenite in the presence of MTBE in groundwater: concentration evolution of groundwater samples (curve a), concentration uptake on ZSM-5 (curve b) and mordenite (curve c). Adapted from reference.^[124]

It is known that zeolites contain both isolated and H-bonded silanols (description of silanols surface species present on the surface of zeolites is given in Appendix I), our research group studied the role of silanols groups in the interactions between MTBE and high silica Faujasite Y ($\text{SiO}_2/\text{Al}_2\text{O}_3 = 200$) by means. The structure of HSZ-Y was characterized by approximately 12 Å diameter cages, which allows quite large molecules to enter and making this zeolite potentially useful in the adsorption of MTBE. Braschi et. al. identified the silanol types present on both external and internal surfaces the surface of HSZ-Y by of FTIR spectroscopy by outgassing the zeolite from RT to 700 °C. As showed in Figure 1.13 (adapted from the reference), the absorption frequencies at 3746 and 3738 cm^{-1} have been assigned to isolated silanols on both external and internal surfaces, respectively and the band at 3530 cm^{-1} to H-bonded silanols. Authors concluded that the adsorption process involves isolated silanol sites and the siloxane network of the zeolite. Silanols interactions was favored respect to the siloxane network through weak H-bonding interactions between external and internal isolated silanol groups of HSZ-Y zeolite and MTBE molecules.^[125]

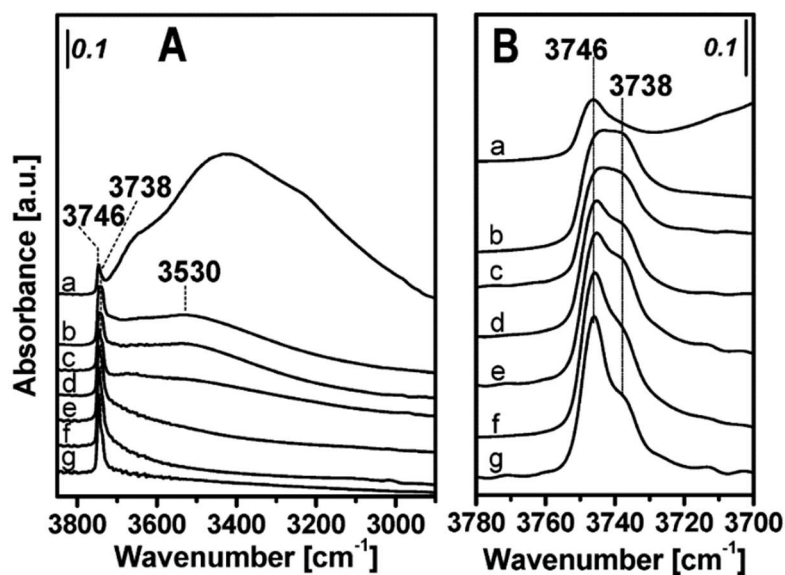


Figure 1.13: Spectra of HSZ-Y treated in vacuum at increasing temperature: A: in air (a), after outgassing at room temperature (b), and at 100 to 700 °C (c–g). (B) Enlargement of spectral region of external and internal isolate silanols at 3746 and 3738 cm^{-1} , respectively. Adapted from reference.^[125]

In another study of our research group was outlined the effect of the surface and of the textural properties of dealuminated high silica zeolites such as mordenite (MOR) and HSZ-Y zeolites (both with a $\text{SiO}_2/\text{Al}_2\text{O}_3 = 200$) and ZSM-5 solid ($\text{SiO}_2/\text{Al}_2\text{O}_3 = 500$) towards MTBE adsorption. HSZ-Y with SSA of $991 \text{ m}^2 \text{ g}^{-1}$ zeolite is characterized by large supercages characterized by approximately 12 \AA of diameter, whereas in ZSM-5 (SSA of $550 \text{ m}^2 \text{ g}^{-1}$) structure is characterized by two types of intersecting straight channels with smaller dimensions. The pore structure of MOR (SSA of $458 \text{ m}^2 \text{ g}^{-1}$) was described by fusing together two adjacent side-pockets. Sacchetto et. al. combined FTIR and SS-NMR (^1H and ^{13}C CPMAS NMR) spectroscopy to follow the MTBE adsorption process on MOR, characterized by a higher concentration of surface silanols species than in HSZ-Y and ZSM-5. From these analyses Sacchetto et. al. concluded that adsorption process on MOR involves isolated silanol sites, weakly H-bonding silanols, and the siloxane network of the zeolite. Sacchetto et. al. used FTIR spectroscopy and gravimetric measurements to determine the interaction strength and sorption capacities of MOR, HSZ-Y and ZSM-5 zeolites. Authors observed that the amount of adsorbed MTBE is much higher in HSZ-Y zeolite than in MOR zeolite, this probably due to the fact that the surface area of HSZ-Y zeolite is twice with respect to the MOR solid. Nevertheless, authors observed higher affinity at low pressure of MTBE for MOR than in HSZ-Y zeolite. In addition, authors concluded that MTBE molecules interact with silanol groups (both on internal and external zeolite surfaces) and van der Waals interactions between zeolites walls and MTBE molecules (host–guest) and between MTBE molecules (guest–guest), whereas ZSM-5 which is characterized by a low

amount of surface silanol species, shows low adsorption capacity for MTBE due mainly to van der Waals interactions with zeolite siloxane network.^[126]

Recently, the interactions of toluene and *n*-hexane molecules on two dealuminated high silica HSZ-Y and ZSM-5 zeolites ($\text{SiO}_2/\text{Al}_2\text{O}_3 = 200$ and 280, respectively) were studied.

Sacchetto et. al. monitored the adsorption properties of toluene and *n*-hexane as single pollutants by different experimental techniques. FTIR analysis of adsorbed toluene allowed monitoring different types of interactions between the zeolites and the pollutant. The admission of small doses (Figure 1.14 A, curves b-e) of toluene on HSZ-Y results in a progressive disappearance of the band related to isolated silanols species at ca. 3745 cm^{-1} and 3738 cm^{-1} and the formation of intense band at 3595 cm^{-1} due to O-H... π interactions between HSZ-Y silanols and toluene molecule. After admission of toluene, several bands are formed in the range $3100\text{-}2850$ and $1650\text{-}1350\text{ cm}^{-1}$: these are relative to the vibration modes of toluene molecule. In particular, the bands at 3090 , 3065 and 3030 cm^{-1} are related to C-H stretching modes of the toluene aromatic ring, whereas the signals at 2925 and 2875 cm^{-1} can be assigned to C-H stretching modes of the toluene methyl groups. The sharp signal at 1605 cm^{-1} is due to the quadrant stretching mode of the mono-substituted ring C=C bond whereas the band at 1495 cm^{-1} is associated to the semicircular stretching vibration of mono-substituted aromatic ring. Finally, the bands at 1460 and 1380 cm^{-1} correspond to the out-of-phase and in-phase deformations of the methyl group, whereas the component at 1460 cm^{-1} is associated to semicircular stretching and bending normal modes of mono-substituted benzene ring.

By increasing toluene pressure, the bands due to toluene increase of intensity, this suggests there are also interaction between the zeolite walls and the toluene molecules (host-guest interactions) and among toluene molecules (guest-guest interactions). Upon toluene adsorption on ZSM-5 zeolite, host-guest and guest-guest interactions were also enlightened for ZSM-5 zeolite.^[127]

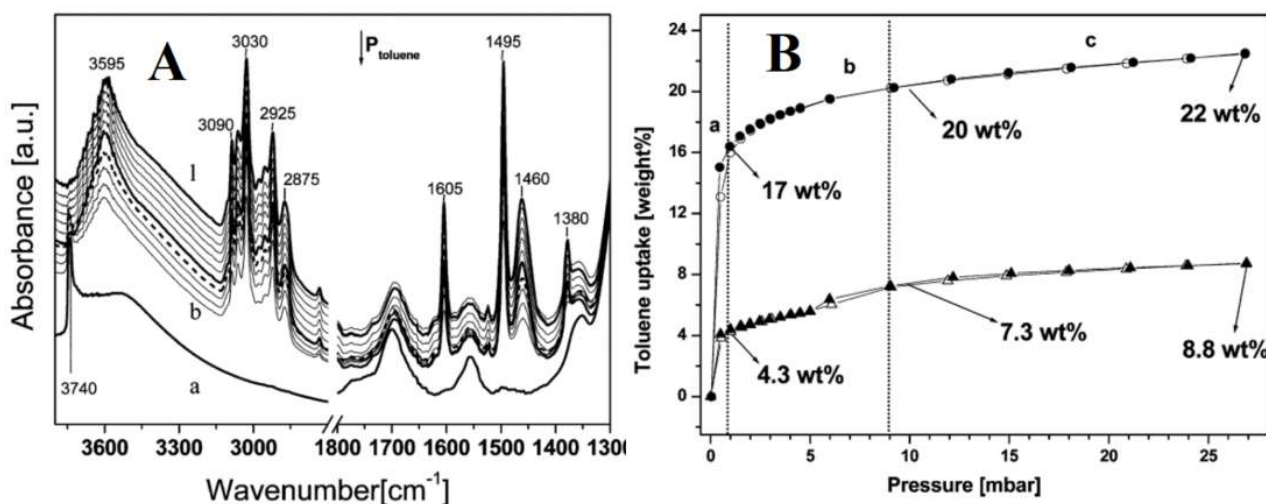


Figure 1.14: A: FTIR spectra at different doses of toluene adsorbed on HSZ-Y zeolite. spectra b to l were collected upon dosage of 0.1–30 mbar toluene. B: Toluene gravimetric adsorption/desorption isotherms of toluene on Y (circles) and ZSM-5 (triangles). Adapted from ref.^[127]

Gravimetric isotherms of toluene adsorbed on both zeolites (Figure 1.14 B) allowed to conclude that at low pressure surface silanols play a key role thus explaining the high affinity of toluene for the HSZ-Y. The toluene uptake at 1 mbar is 17 wt% and the overall toluene adsorption at 27 mbar is ca. 22 wt% on Y. Whereas ZSM-5 zeolite, the overall toluene uptake is considerably lower. Indeed at 1 mbar, ZSM-5 adsorbs ca. 4.3 wt% of toluene whereas the overall adsorption capacity is 8.8 wt%.

¹H MAS and ¹³C CPMAS SS-NMR experiments were carried out to get more insights on the local environment that the pollutants experience inside the pores of zeolites.

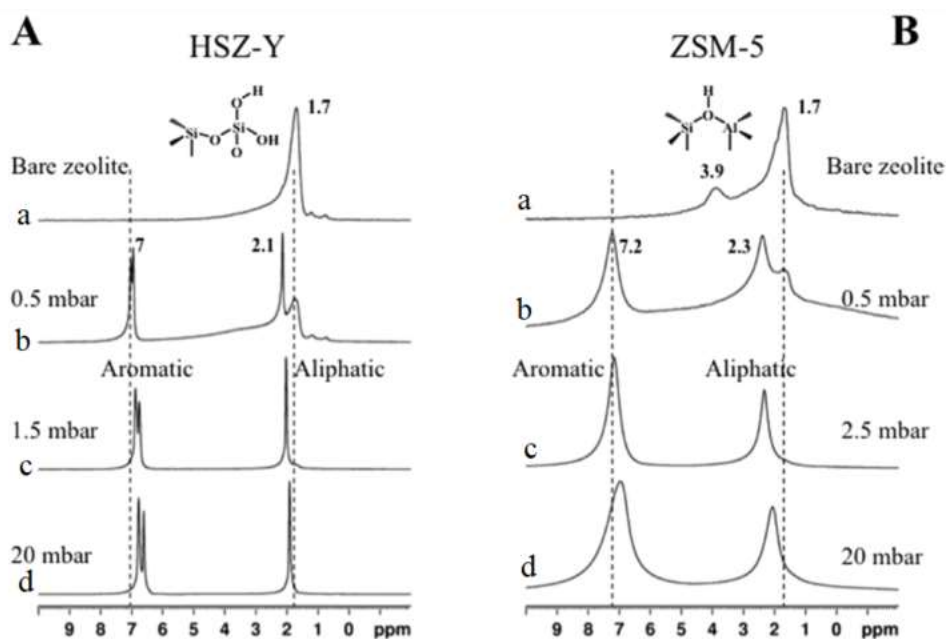


Figure 1.15: A: Toluene ^1H solid state MAS NMR spectra recorded at RT with a MAS rate of 15 kHz of (curves a) bare zeolite HSZ-Y (A) and ZSM-5 (B) and spectra of toluene adsorbed at different pressures (curves b-c) on HSZ-Y (A) and ZSM-5 (B). Adapted from reference.^[127]

In the spectrum of bare zeolite HSZ-Y (Figure 1.15A, curves a) shows a narrow resonance at 1.7 ppm is attributed to isolated silanols whereas the broad feature between 2 and 7 ppm is due to silanol species involved in hydrogen bonds with varying strengths and types. In the spectra of toluene adsorbed on HSZ-Y (Figure 1.15A, curves b-d) sample show peaks at *ca.* 2 and 7 ppm due to methyl and aromatic protons. These two resonances move upfield to lower chemical shift values as the toluene loading increases. Besides, the intensity due to isolated silanol protons reduces as the toluene loading increases.

Similarly, in the spectrum of bare zeolite ZSM-5 (Figure 1.15B, curves a) shows a narrow resonance due to isolated silanols, whereas the broad feature is due to hydrogen bonding silanol species. In addition, the proton signal at 3.9 ppm is due to Brønsted acid sites (bridging OH group, SiOHAl). Similarly, spectra of toluene adsorbed on the ZSM-5 show peaks due to methyl and aromatic protons and the intensity due to isolated silanols diminishes as the toluene loading increases. The main difference between toluene and *n*-hexane adsorbed singularly on both different zeolites is in the environment of adsorbed molecules. Toluene and *n*-hexane adsorbed as single pollutants on HSZ-Y showed sharp resonances with narrow line widths, whereas in the case of ZSM-5 relatively broad resonances are observed.

These results allowed to conclude that the adsorption and diffusion of toluene and *n*-hexane adsorbed as single pollutants are significantly influenced by the pore/channel architecture and volume availabilities in zeolites. The large space available in supercages of HSZ-Y helps in the enhancement of diffusion of pollutants whereas restricted space in ZSM-5 limits mass transfer through channels. Computational approaches were used to estimate the energies of interaction between the pollutant and zeolite surfaces. For both zeolites the interaction of toluene with isolated silanols is fairly weak and the adsorption process is mainly driven by dispersion forces (even more evident for ZSM-5 zeolite). The same kind of analysis to monitored adsorbed *n*-hexane singularly on both zeolites was also performed. Interactions between this molecule and zeolites were in general weaker than those observed for toluene.^[127]

Although, zeolites have better performance compared to GACs, in terms of selectivity for organic pollutants instead of natural organic matters, one disadvantage of the zeolites is their low adsorption capacity.^[128] Moreover, high silica zeolites are considered expensive adsorbents because are quoted at more than 10 USD/kg compared to less than 3 USD/kg for GACs. ^[63, 129]

Therefore, methods of synthesis of mesoporous adsorbents have been also developed for the groundwater depollution, such as mesostructured silicas with pores of larger size with respect to zeolites in order to adsorb larger molecules and increases the adsorption capacity.^[130]

1.3.1.3 Ordered mesoporous silica as adsorbents for hydrocarbons removal from groundwater

Ordered mesoporous silica have interest in water treatment chemistry due to its various remarkable properties such us high specific surface area, large pore-size, high amount of surface functional groups that can be useful for excellent selectivity towards specific pollutants and low cost of manufacture.^[131, 132]

An introduction to mesoporous solids in given in Appendix I.

Ordered mesoporous silicas such as MCM-41 and SBA-15 have been investigated as possible sorbents for hydrocarbons removal.^[133] Ordered mesoporous materials have drawn attention for the sorption of huge amounts of organic contaminants with huge dimensions and are not able to diffuse through zeolite micro-pores. This due to the fact that these materials have wide pore openings, high specific surface area and large specific pore volume.^[63]

Zhao et. al. evaluated the organophilic properties of MCM-41 by analysing the thermogravimetric desorption of some representative non-polar molecules (hexane, cyclohexane, benzene) and polar molecules (acetone, methanol). The adsorption capacity of MCM-41 was compared with the hydrophobic silicalite-1 (ZSM-5). The authors demonstrated that the different affinity for the non-polar and polar molecules between MCM-41 and silicalite-1 is due to the difference between their surface hydrophilicity and the difference between their pore structures.^[134]

Zhao et. al. also tested MCM-41 as adsorbent for some organic pollutants (benzene, carbon tetrachloride, and *n*-hexane) removal. The adsorption/desorption properties were evaluated and compared with other hydrophobic zeolites (silicalite-1 and zeolite Y) and a commercial activated carbon (BPL). In this study was able showed the potential of the hydrophobic MCM-41 for the removal of organic pollutants present in high concentrations and high humidity streams. The hydrophobic zeolite Y (Si/Al= 300) has a SSA of 692 m² g⁻¹ whereas the pure silicas (Si/Al= ∞) MCM-41 and the Silicalite-1 (ZSM-5) have 1060 and 371 m² g⁻¹, respectively. Finally, the commercial activated carbon, BPL has a SSA of 923 m² g⁻¹. Authors concluded that hydrophobic MCM-41 is a potential adsorbent for the removal of VOCs present in high concentrations, as can be observed in Figure 1.16 (adapted from reference).

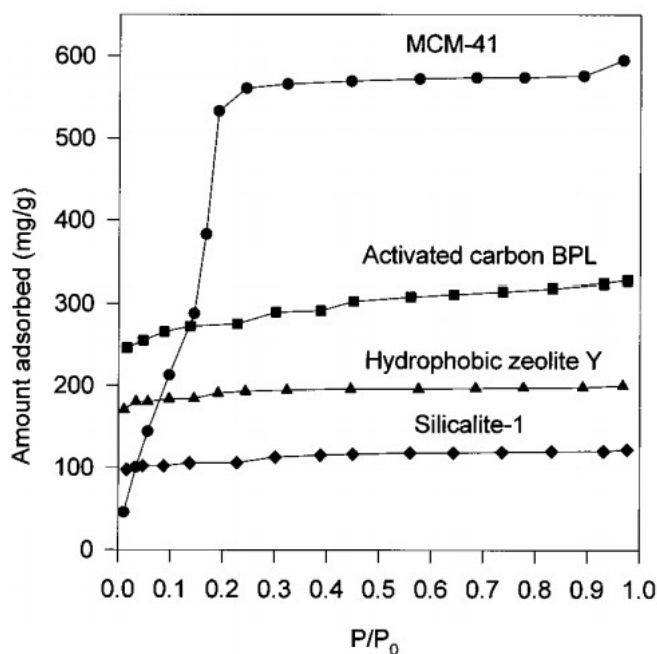


Figure 1.16: Adsorption isotherms of *n*-hexane over the various adsorbents. Adapted from ref.^[135]

For example, as observed on the adsorption isotherms of *n*-hexane over the adsorbents at 22 °C (Figure 1.16). Zhao demonstrated that at low concentration levels of *n*-hexane, the adsorption

capacity followed the sequence of BPL > Y > ZSM-5 > MCM-41, while at higher concentration levels, the sequence changed to MCM-41 > BPL > Y > ZSM-5. Authors indicated that the higher amount of adsorption of MCM-41 compared to the microporous adsorbents is due to the large accessible internal pore volumes which are filled at higher relative pressures.^[135]

Another comparison study of the adsorption capacities of toluene and chlorobenzene on mesoporous and microporous materials was performed by Batonneau-Gener and coworkers.^[136] The authors modified MCM-41 by grafting procedures and by using hexamethyl-disilazane (HMDS) with two different HMDS/SiO₂ molar ratios. The hydrophobic and hydrophilic properties of grafted MCM-41 were studied and compared to an all-silica BEA zeolite as reported in the Figure 1.17. A linear correlation between the silylation degree and the hydrophobicity measurements has been found for MCM-41 materials. The highly silylated MCM-41 sample exhibited a storage capacity for toluene and chlorobenzene (3 times higher than BEA zeolite).

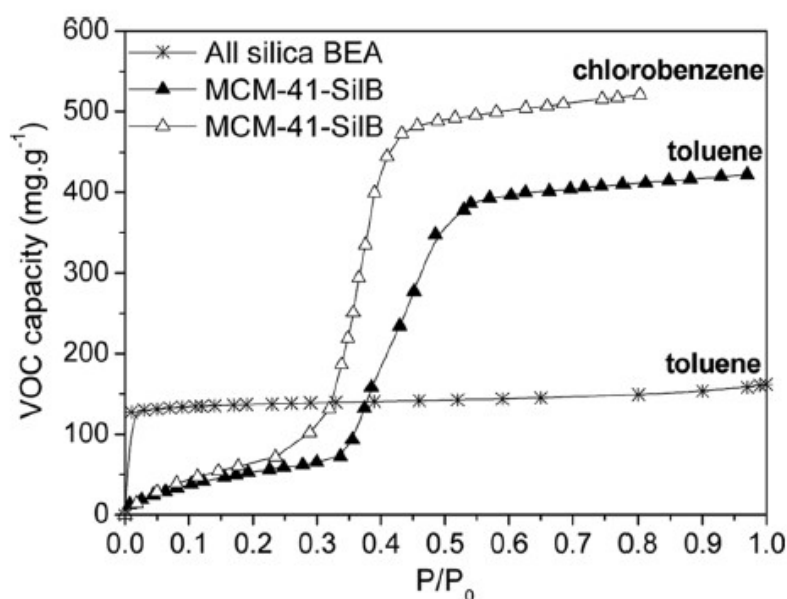


Figure 1.17. Toluene and chlorobenzene adsorption isotherms at 294K for MCM-41-SilB and all silica BEA zeolite. Adapted from ref. ^[136]

Serrano et. al. studied the adsorption/desorption properties of different ordered mesoporous materials (MCM-41 and SBA-15 synthesized through different methods) for toluene, isopentane, and water by means of a thermal programmed desorption technique (TPD). Four pure silicas (Si/Al= ∞), SBA-15, MCM-41(H-sg) prepared by a sol-gel route, MCM-41(D-sg) synthesized with a similar procedure for MCM-41(H-sg) but using a different surfactant (with a shorter chain length to obtain a material with a smaller pore size and MCM-41(H-ht) material synthesized by a hydrothermal treatment. A sample Al-MCM-41(H-sg) with Si/Al=48 was prepared by a sol-gel synthesis using an aluminium source.

Authors observed as predictable that Al-MCM-41 resulted a hydrophilic material which adsorbed high amounts of water due to the presence of acid sites. The best performance of adsorption (amount adsorbed, adsorption strength, and hydrophobicity) for both toluene and isopentane was observed for the MCM-41(H-sg). In contrast, pure silica MCM-41(H-ht) presented a very weak interaction (low adsorption amounts) with toluene and isopentane and high hydrophobic character. Authors also concluded that SBA-15 shows high strength of adsorbate/adsorbent interactions as denoted by the high values of the desorption peak temperature obtained in the TPD curves due to the presence of microporous in SBA-15 connecting the mesoporous channel structure where the adsorption is limited by the small available micropore surface area.

Although MCM-41(H-sg) and MCM-41(H-ht) were synthesized with the same surfactant and having close textural properties, MCM-41(H-sg) presented better adsorption performance than MCM-41(H-ht) for the three molecules. Authors assigned this due to significant differences between the pore networks and pore ordering of these two mesoporous materials such as a three-dimensional pore system, a wider pore size distribution, high concentration of defective silanol and siloxane groups.

It is known that pure silica MCM-41 materials exhibit poor hydrothermal stability in water at high temperatures^[137] due to the collapse of the porous structure.^[138]

For this reason, although ordered mesoporous silica have higher adsorption capacity compared to hydrophobic zeolites, one parameter to be pointed of these materials is the hydrothermal stability under severe hydrothermal conditions as an important feature of these adsorbents to obtain invariant performance over several regeneration cycles, considering that they are soaked in water during its application and in most cases thermal regeneration is applied.^[63]

1.3.1.3 Materials for herbicides removal from groundwater

As stated above, other important concern for environment and researchers is the depollution of herbicides from groundwater, specifically glyphosate which is a broad-spectrum, non-selective and efficient herbicide. Several methods are already used to reduce the glyphosate content in the effluents. In particular adsorption method from aqueous solution has been performed to solve glyphosate contamination.^[139-141]

Great efforts for development of novel adsorbents with high adsorption capacities for the removal of glyphosate are proposed including iron oxide/SBA-15,^[142] Zr-MOF,^[143] ferric supported active carbon,^[144] magnetic MnFe₂O₄-grafene hybrid composite,^[145] polyaniline polymers,^[146] clays,^[45] and resins.^[147]

For example, Milojevic'-Rakic' et. al. evaluated nanostructured and granular polyanilines (PANIs) and their composites with ZSM-5 zeolite as adsorbents of the organic herbicide glyphosate in aqueous solution.^[146] Milojevic'-Rakic' et. al. obtained that among the studied adsorbents, the most efficient adsorption for glyphosate (98.5 mg/g) was achieved by the deprotonated granular PANI. High adsorption capacity was also measured for the deprotonated PANI/ZSM-5 composite with the lowest content of zeolite. Authors concluded that high adsorption capacity of the pure PANIs and their composites with lowest content of zeolite were due predominately by the molecular structure of polymer chains (level of protonation, oxidation state, chain branching, the amount of structure defects, and interactions between PANI and glyphosate such as hydrogen bonding or acid–base interactions).^[146]

Further studies about the adsorption mechanism was performed by Guo et. al.^[148] With the aim of investigate adsorption kinetics, isotherm and thermodynamics of glyphosate from aqueous solution. For this, Guo et. al. evaluated the effect of adsorption time, glyphosate concentration, temperature, pH and ionic strength on the adsorption of glyphosate by cross-linked amino-starch (CAS). To examine the controlling mechanism and comprehend the adsorption rate-limiting step of the transport of solute between liquid and solid and design of the process, the pseudo first order and second-order kinetic models were used in this study. Whereas, to describe the interactions between the adsorbent and the solute (glyphosate) at different concentrations, Langmuir, Freundlich and Sips models were applied to describe the adsorption equilibrium between the liquid and solid phases. According to the kinetic data, Guo et. al. observed that adsorption equilibrium was attained in ca. 60 min and the pseudo second-order kinetics model was well fitted for the adsorption process. Guo et. al. observed that Sips isotherm was more suitable than Langmuir and Freundlich isotherms for the adsorption of glyphosate on CAS, and the maximum adsorption capacity was 3.61 mmol g^{-1} . From this studied, Guo et. al. could conclude that the adsorption of glyphosate on CAS was a spontaneous and exothermic process, the adsorption mechanism is a chemical adsorption process combined with physical adsorption. The results also demonstrated that pH and the ion strength have a significant influence on the adsorption capacity, the adsorption capacity reaches a maximum value at pH 6.0 and the adsorption capacity decreases with the rising of the ion strength.^[148]

Another aspect to be considered to select a possible adsorbent for glyphosate when it is found in groundwater is the ionic form of this molecule. It's already known that glyphosate is a polyprotic acid with $\text{pK}_{\text{a}1}=0.78$, $\text{pK}_{\text{a}2}=2.29$, $\text{pK}_{\text{a}3}=5.96$, and $\text{pK}_{\text{a}4}=10.9$, which forms zwitterion (neutral form with positive and negative electrical charge) and mono/divalent anions in the pH range 2–12 (see Figure

1.18, adapted from reference).^[149] Moreover, some literatures have reported that glyphosate can only be adsorbed onto variable-charge surfaces and not onto sites with negative permanent-charge, this is due glyphosate is present as an anion in the pH range of soils (see Figure 1.18). For example, minerals such aluminium and iron oxides, poorly ordered aluminium silicates (*i.e.* allophane/imogolite) and edges of layer silicates especially by goethite (α -FeOOH) which present variable-charge have been demonstrated to be effective glyphosate sorbents.^[150-153]

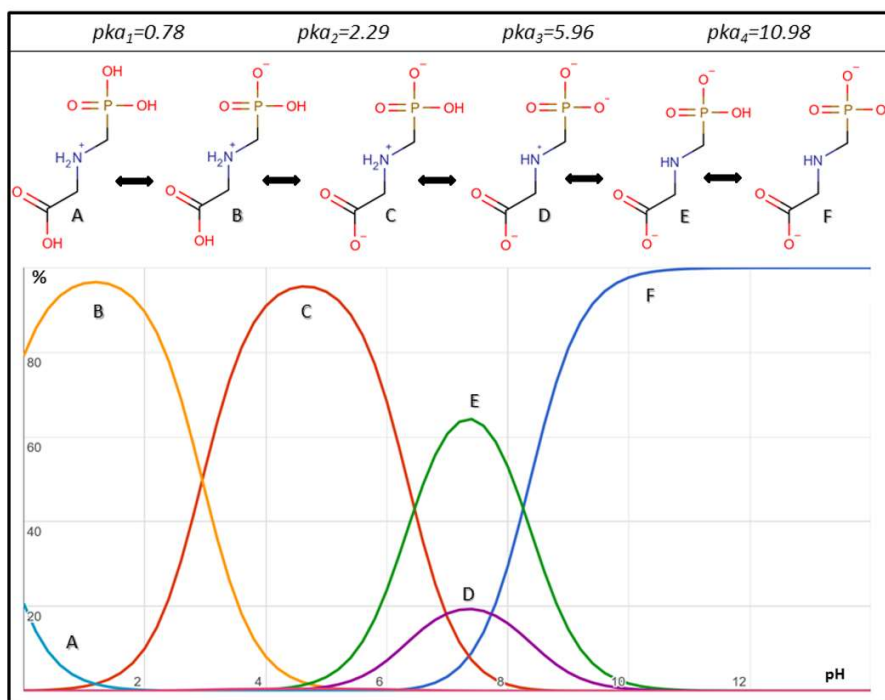


Figure 1.18: Deprotonation reactions and their relative pKa values of glyphosate molecule, and their percentage distribution according to pH. The zwitterionic structure of carboxyl and amino groups is shown in the entire pH range.^[149]

For this reason, recently S. Fiorilli et. prepared silica-based materials modified with functional groups which can provide cationic sites (*i.e.* aminopropyl groups), in order to promote specific interactions between the mesoporous silica and glyphosate. Iron oxide nanoparticles were encapsulated together a surface functionalization with (3-aminopropyl) triethoxysilane (APTES) on SBA-15 surface. SBA-15 was impregnated with an aqueous solution of $\text{Fe}(\text{NO}_3)_3 \cdot 9\text{H}_2\text{O}$ and successively functionalized with APTES. From the characterization, authors concluded that iron oxide nanoparticles were regularly dispersed into the pores of SBA-15 and that the final Fe- NH_2 -SBA-15 exhibited accessible porosity and high SSA ($177 \text{ m}^2 \text{ g}^{-1}$).^[149]

The adsorption of glyphosate on Fe- NH_2 -SBA-15 sample was performed as a function of pH, ionic strength, and adsorbate to adsorbent ratio by the means of a chromatographic method based on anion-

exchange mechanism optimized. The batch adsorption experiments were performed with initial concentration of 2 mg L^{-1} in a volume of 17.5 mL with 0.1 g of sorbent. Authors observed a good performance of Fe-NH₂-SBA-15 at pH 2.1 for the removal of glyphosate in water solutions (after 24 h of contact of equilibrium conditions), due to the ionic interactions between the positive charge of the protonated amino groups present on the sorbent surface (pK_a 7.6 for surface NH₃⁺ species) and the negative charge of the functional groups of glyphosate molecules. Authors suggested that although the pH 2.1 is far from pH conditions usually adopted in drinking and wastewater treatment processes, the ideal acidic pH of Fe-NH₂-SBA-15 is well-matched with some industrial activities.^[142]

Recently, Wang et. al. developed a smart adsorbent for glyphosate removal from water.^[154] For this Wang et. al. synthesized a novel MOF-based smart adsorbent (Fe₃O₄@SiO₂@UiO-67) which contains Zr-OH groups with high affinity for the phosphonate group of the glyphosate molecule. Furthermore, using Fe₃O₄ as the magnetic core facilitates adsorption via an external magnetic field. Wang et. al. observed that the obtained smart adsorbent exhibits excellent detection and adsorption performance with a high adsorption capacity (256.54 mg g^{-1}) for glyphosate.^[154]

References

- [1] B. Dubey, R.K. Upadhyay, J. Hussain, *Ecological Modelling*, 2003, 167, 83–95.
- [2] G. S. Senesil, G. Baldassarre, N. Senesi, B. Radina, *Chemosphere*, 1999 (39), 343-377.
- [3] Z.A. Ansari and S.G.P. Matondkar, *J. Ecophysiol. Occup. Hlth.*, 2014, 14(1 - 2), 71–78.
- [4] Barbara Fraser-Mongabay, 9 months after Amazonian oil pipeline spill, effects and fears linger, 30 March 2015, Available: <https://news.mongabay.com/2015/03/9-months-after-amazonian-oil-pipeline-spill-effects-and-fears-linger/>
- [5] Hardison & Cochran, Latest Developments in Non-Hodgkin Lymphoma Lawsuits Against Roundup® Manufacturer Monsanto, last update 2019, Available: <https://www.lawyernc.com/blog/2017/03/latest-developments-in-non-hodgkin-lymphoma-lawsuits-against-roundup-manufacturer-monsanto/>
- [6] Egypt Business Directory, Focus On Industrial Emission Control Systems Market and Industry Development Research Report 2014 to 2021, 2016, Available: <https://www.egypt-business.com/Ticker/details/1621-Focus-On-Industrialemission-Control-systemsMarket-and-Industry-Development-Research-Report-2014-to-2021/38128>
- [7] News 20minutos, Controlada la fuga de un producto tóxico e inflamable en el Port de Barcelona, 23/05/2008, Available: [https://www.20minutos.es/noticia/381837/0/escape/ronda/litoral/](https://www.20minutos.es/noticia/381837/0/escape/ronda/litoral/#xtor=AD-15&xts=467263https://www.20minutos.es/noticia/381837/0/escape/ronda/litoral/)
- [8] Envione Global Environmental, Health & Safety Magaine, Top 10 Causes of Air Pollution, Posted on April 17, 2017 in Air Pollution, Available: <http://www.envione.com/top-10-causes-of-air-pollution/>
- [9] Asia Pacific Report, Greenpeace blasts palm oil industry deforestation in West Papua, Posted on May 1, 2018, Available: <https://asiapacificreport.nz/2018/05/01/greenpeace-blasts-palm-oil-industry-deforestation-in-west-papua/>
- [10] R. K. Ibrahim, M. Hayyan, M. A. AlSaadi, A. Hayyan, S. Ibrahim, *Environ Sci Pollut Res Int.*, 2016, 23(14), 13754-13788.
- [11] Anna Burzykowska, Torsten Bondo and Stephen Coulson, Green Growth, Earth observation for international development projects, , European Space Agency, Bulletin, 2013, 155.
- [12] European Commission, Environment Impact Assessment (EIA), Last updated: 02/05/2017, Available: <http://ec.europa.eu/environment/eia/eia-legalcontext.htm>
- [13] The Economics of Ecosystems & Biodiversity (TEEB), EEB and the Sustainable Development Goals (SDGs), <http://www.teebweb.org/sdgs/>
- [14] System of Environmental Economic Accounting, Available: <https://unstats.un.org/unsd/envaccounting/seea.asp>

- [15] Wealth Accounting and the Valuation of Ecosystem Services, Available: <http://www.wavespartnership.org/en>
- [16] EPA United Environmental Protection Agency, Summary of the Resource Conservation and Recovery Act, Last Updated on January 19, 2017, Available: <https://www.epa.gov/laws-regulations/summary-resource-conservation-and-recovery-act>
- [17] National Oceanic and Atmospheric Administration (NOAA)- Earth Science Research Lab and National Centers for Environmental Prediction., Water cycle, National Weather Service, Last updated: 10/5/2015, Available: <https://www.noaa.gov/resource-collections/water-cycle>
- [18] National Weather service- National Oceanic and Atmospheric administration, The hydrologic Cycle, Available: <https://www.weather.gov/jetstream/hydro>
- [19] L. Bengtsson, *Environ. Res. Lett.*, 2010, 5, 025202
- [20] K. Katsanou and H. K. Karapanagioti, *The Handbook of Environmental Chemistry*, Springer, Barceló, Damià, Kostianoy, Andrey G. Berlin, Heidelberg, 2017.
- [21] Kimberly Mullen, CPG, National Ground Water Association, Information on Earth's water, 2018, Available: <http://www.ngwa.org/Fundamentals/teachers/Pages/information-on-earth-water.aspx>
- [22] I. S. Zektser, L. G. Everett, *Groundwater Resources of the World and Their Use*, UNESCO IHP-VI Series on Groundwater, N° 6, UNESCO (United Nations Educational, Scientific and Cultural Organization), Paris, 2004.
- [23] S. H. Schneider, *Encyclopedia of Climate and Weather*, Oxford University Press, 1996, New York, (2), 817-823.
- [24] F. R. Spellman, *The Science of Water: Concepts and Applications*, 3rd Edition, CRC Press, 2014.
- [25] DNR Indiana Department of Natural Resources, Potentiometric Surface Mapping (1:48,000) Overview, 2019, Available: <https://www.in.gov/dnr/water/7258.htm>
- [26] I. L. Pepper, C. P. Gerba, M. L. Brusseau, *Physical-Chemical Characteristics of Waters*, Environmental and Pollution Science, Elsevier Science/Academic Press 2nd Edition, University of Arizona at Tucson, U.S.A., 2006.
- [27] S. Cerar and N. Mali, *Journal of Geochemical Exploration*, 2016, 170, 78–93.
- [28] C. Mason, *Organic Pollution*, Pearson Education Limited, *Biology of Freshwater Pollution*, Edinburgh Gate, 4th Edition, 2001, pp 81
- [29] A. Mudhoo, *Microwave-Assisted Organic Pollutants Degradation in Advances in Water Treatment and Pollution Prevention*, Sanjay K. Sharma, Rashmi Sanghi, Springer Edition, 2012.
- [30] R. M. Harrison, *Pollution: Drinking Water Quality and Health, Causes, Effects and Control*, RCS 4th Edition, 2001, pp 59

- [31] W. Dong, W. Xie, X. Su, C. Wen, Z. Cao and Y. Wan, *Hydrogeology Journal*, 2018, 26, 1351–1369.
- [32] C. Matthew; Classification of Hazardous and non-hazardous substances in groundwater, Environmental Protection Agency, Ireland, 2010 Available: <https://www.epa.ie/pubs/reports/water/ground/Classification%20of%20Hazardous%20and%20Non-Hazardous%20Substances%20in%20Groundwater.pdf>
- [33] M. P. Rao and P. S. C. Rao; Organic Pollutants in Groundwater: Health and Effects; Soil and Water Science Department; Cooperative Extension Service-Institute of Food and Agricultural Sciences, University of Florida, 1997 pp 1-3
- [34] Alloway B.J., Ayres D.C, Organic Pollutants, Chemical Principles of Environmental Pollution, Springer 2nd Edition, 1997, pp 247
- [35] P. Logeshwaran, M. Megharaj, S. Chadalavada, M. Bowmanc, R. Naidu, *Environmental Technology & Innovation*, 2018, 10, 175–193.
- [36] M. Farhadian, C. Vachelard, D. Duchez, C. Larroche, *Bioresource Technology*, 2008, 99, 5296–5308.
- [37] EPA United Environmental Protection Agency, Contaminants and Standards Fact Sheets, Last Updated on January 19, 2017, Available: <https://safewater.zendesk.com/hc/en-us/categories/201454937-Fact-Sheets>.
- [38] Toluene in Drinking-water; Background document for development of WHO Guidelines for Drinking-water Quality; World Health Organization 2004.
- [39] The U.S. Environmental Protection Agency's 1988 Risk Assessment for Arsenic, Subcommittee on Arsenic in Drinking Water, National Research Council, This PDF is available from the National Academies Press at: <http://www.nap.edu/catalog/6444.html>
- [40] Background document for development of WHO Guidelines for Drinking-water Quality; Background document for development of WHO Guidelines for Drinking-water Quality; World Health Organization 2008. World Health Organization 2008, Available: https://www.who.int/water_sanitation_health/dwq/fulltext.pdf
- [41] U.S Department of Health and Human Services, Public Health Service Agency for Toxic Substances and Disease Registry, Toxicological profile of n-hexane, Atlanta, Georgia, 1999, Available: <https://www.atsdr.cdc.gov/toxprofiles/tp113.pdf>
- [42] J.F. Artiola, I. L. Pepper, M.L. Brusseau, Chemical Contaminants, Environmental Monitoring and Characterization, Academic Press/Elsevier, University of Arizona at Tucson, U.S.A., 1st Edition, 2004, pp 299
- [43] F. R. de Mouraa, R. R. da Silva Lima, A. P. S. da Cunha, P. da Costa Marisco, D. H. Aguiar, M. M. Sugui, A. P. Sinhorin, V. D. G. Sinhorin, *Environmental Toxicology and Pharmacology*, 2017, 56, 241–248.
- [44] B.S. Ismail, M. Sameni and M. Halimah, *World Applied Sciences Journal*, 2011, 15 (1), 05-13.
- [45] H. de Santana, L. R.M. Toni, L. O. de B. Benetoli, C. T.B.V. Zaia, R. Jr. Maurilio, Dimas A.M. Zaia, *Geoderma*, 2006, 136, 738–750.

- [46] A. Grube, D. Donaldson, T. Kiely, and L. Wu, Pesticides Industry Sales and Usage, U.S. Environmental Protection Agency, Washington February 2011, pp 1-30.
- [47] A. M. Au, Types Uses and Determination of Herbicides, Encyclopedia of Food Sciences and Nutrition 2nd Edition Department of Health Services, State of California – Health and Welfare Agency, , USA 2003, 4483–4487.
- [48] S. Munira, A. Farenhorst, W. Akinremi, *Geoderma*, 2018, 313, 146–153.
- [49] J.P Giesy, S. Dobson and K.R Solomon, *Rev Environ Contam Toxicol*, 2000, 167, 35–120.
- [50] S. Monheit, Glyphosate-based Aquatic herbicides. An overview of risk, *Noxious Times*, 2002, 5-9.
- [51] National Toxicology Program, Testing Status of Glyphosate, Glyphosate, last updated on January 15, 2019, Available: <https://ntp.niehs.nih.gov/testing/status/agents/ts-m88067.html>
- [52] John Bergendahl, Pesticide Removal from Water; Worcester Polytechnic Institute, Massachusetts April 25, 2012.
- [53] Chemical Contaminants. Health Effects Technical Support Document, Six-Year Review. United States Environmental Protection Agency, Washington, DC, 2003, pp 32.
- [54] European Community Council Directive concerning the quality of water intended for human consumption. *Off. J. Eur. Commun. L.* 1998, 330, 32–54.
- [55] O.K Borggaard and A. L. Gimsing, *Pest Manag Sci*, 2008, 64, 441–456.
- [56] N. B. Singh, G. Nagpal, S. Agrawal & Rachna, *Environmental Technology & Innovation*, 2018, 11, 187–240.
- [57] Krupińska, *Chem. Biochem. Eng. Q.*, 2016, 30, (4) 465–475.
- [58] Eastern Research Group, Inc., Pump and Treat Groundwater remediation: A guide for decision makers and Practitioners. EPA/625/R-95/005 (NTIS PB97-154009), 1997, Available: https://cfpub.epa.gov/si/si_public_record_Report.cfm?Lab=NRML&dirEntryID=115422
- [59] T.F. Guerin, *J. Hazard. Mater.*, 2002, 89, 241–252.
- [60] F.I Khan, T. Husain, R. Hejazi, *J. Environ. Manage.*, 2004, 71, 95–122.
- [61] E. Arvin, P. Engelsens, U. Sebber, *Water Supply.*, 2005 4, 29–33.
- [62] T. Meggyes and F.-G. Simon, *Land Contamination & Reclamation*, 2000, 8 (3), 175-187.
- [63] C. Perego, R. Bagatin, M.Tagliabue, R. Vignola, *Microporous and Mesoporous Materials*, 2013, 166, 37–49.
- [64] F. O.-Nyarko, S. J. Grajales-Mesa, G. Malina, *Chemosphere*, 2014, 111, 243–259.

- [65] R. M. Powell, D.W. Blowes, R. W. Gillham, D. Schultz, T. Sivavec, R. W. Puls, J. L. Vogan, P.D. Powell, R. Landis, *Permeable Reactive Barrier Technologies for Contaminant Remediation*. Report EPA/600/R-98/125, U. S. Environmental Protection Agency, Washington, DC, 1998, pp.51.
- [66] M. A. Carey, B.A Fretwell, N. G. Mosley, J. W. N. Smith, National Groundwater and Contaminated Land Centre Report NC/01/51, UK Environment Agency, Bristol. 2002, pp 140.
- [67] S. J. Skinner, C. F. Schutte, *Water SA*. 2006, 32 (2), 129–136.
- [68] F.-G. Simon and T. Meggyes, Permeable reactive barrier for pollutant removal from groundwater, Bundesanstalt für Materialforschung und-prüfung (BAM), Berlin, 2001, pp 7.
- [69] D. W. Blowes, C. J. Ptacek, S. G. Benner, C. W.T. McRae, T. A. Bennett, R.W. Puls, *Journal of Contaminant Hydrology*, 2000, 45, 123–137.
- [70] F. Fu, D. D. Dionysiou and H. Liu, *Journal of Hazardous Materials*, 2014, 267, 194– 205.
- [71] G. Melin, Treatment technologies for removal of methyl tert-butyl ether from drinking water, Center for Groundwater Restoration and Protection National Water Research Institute, California 2000, pp 209.
- [72] I. Levchuk, A. Bhatnagar and M. Sillanpää, *Science of the Total Environment*, 2014, 476–477, 415–433.
- [73] S. Wang and Y. Peng, *Chemical Engineering Journal*, 2010, 156, 11–24.
- [74] R.Vignola, R. Bagatin, A. De F. D’Auris, C. Flego, M. Nalli, D. Ghisletti, R. Millini; R. Sisto, *Chemical Engineering Journal*, 2011, 178, 204– 209.
- [75] M. Javed, *International Journal of Engineering Research & Technology (IJERT)*, 2014, 3 (5), 2304-2307.
- [76] I. Ali, *Chem. Rev.* 2012, 112, 5073–509.
- [77] G. Crini and E. Lichtfouse, *Green Adsorbents for Pollutant Removal: Innovative materials*, Springer, France, 2018, p. 399.
- [78] M. Thommes, K. Kaneko, A. V. Neimark, J. P. Olivier, F. Rodriguez-Reinoso, J. Rouquerol and K. S.W. Sing, *Pure Appl. Chem.*, 2015, 87(9-10), 1051–1069.
- [79] A. Bhatnagar and A. K. Minocha, *Indian Journal of Chemical Technology*, 2006, 13, 203-217.
- [80] D. Mohana and C.U. Pittman Jr., *Journal of Hazardous Materials*, 2007, 142, 1–53.
- [81] N. Ezzatahmedi, G. A. Ayoko, G. J. Millar, R. Speight, C. Yan, J. Li, S. Li, J. Zhu, Y. Xi, *Chemical Engineering Journal*, 2017, 312, 336–350.
- [82] R.W. Gillham, S.F. O’Hannesin, *Ground Water*, 1994, 32, 958–967.
- [83] B. Gu, T.J. Phelps, L. Liang, M.J. Dickey, Y. Roh, B.L. Kinsall, A.V. Palumbo, G.K. Jacobs, *Environ. Sci. Technol.*, 1999, 33, 2170–2177.

- [84] S. Luo, P. Qin, J. Shao, L. Peng, Q. Zeng, J.D. Gu, *Chem. Eng. J.*, 2013, 223, 1–7.
- [85] S. Shirin, V.K. Balakrishnan, *Environ. Sci. Technol.*, 2011, 45, 10369–10377.
- [86] R.T. Wilkin, S.D. Acree, R.R. Ross, R.W. Puls, T.R. Lee, L.L. Woods, *Sci. Total Environ.*, 2014, 468–469, 186–194.
- [87] M. Baric, M. Majone, M. Beccari, M.P. Papini, *Chem. Eng. J.*, 2012, 195–196, 22–30.
- [88] A. Shimizu, M. Tokumura, K. Nakajima, Y. Kawase, *J. Hazard.Mater.*, 2012, 201–202, 60–67.
- [89] Y. Segura, F. Martínez, J.A. Melero, R. Molina, R. Chand, D.H. Bremner, *Appl. Catal. B: Environ.*, 2012, 113–114, 100–106.
- [90] X. Guan, Y. Sun, H. Qin, J. Li, I. M.C. Lo, D. He and H. Dong, *Water Research*, 2015, 75, 224–228.
- [91] R. Thiruvenkatachari, S. Vigneswaran and R. Naidu, *Journal of Industrial and Engineering Chemistry*, 2008, 14, 145–156.
- [92] Di-Nardo, A., Di Natale, M., Erto, A., Musmarra, D., Bortone, I., In: Pierucci, S., Ferraris, G.B. (Eds.), *Proceedings of the 20th European Symposium on Computer Aided Process Engineering—ESCAPE20*. Elsevier B.V., 2010, Naples, Italy.
- [93] B. D. Bone, 2012. Review of UK guidance on permeable reactive barriers. 2012 Taipei International Conference on Remediation and Management of Soil and Groundwater Contaminated Sites, Taipei, Taiwan, 611–768.
- [94] Valderrama, X. Gamisans, X. de las Heras, A. Farran and J.L. Cortina, *Journal of Hazardous Materials*, 2008, 157, 386–396.
- [95] E. Mohammad-pajooha, A. E. Turcios, G. Cuff, D. Weichgrebe, K.-H. Rosenwinkel, M.D. Vedenyapina, L.R. Sharifullin; *Journal of Environmental Management*, 2018, 228, 189–196.
- [96] X. Peng, Y. Li, Z. Luan, Z. Di, H. Wang, B. Tian, Z. Jia, *Chem. Phys. Lett.*, 2003, 376 (1–2), 154–158.
- [97] X. Liu, , N. G. Pinto, *Carbon*, 1997, 35 (9), 1387–1397.
- [98] A.Rossner and D. R.U. Knappe, *Water Research*, 2008, 42, 2287– 2299.
- [99] J. M. Newsam, *Science*, 1986, 231, 1093–1099.
- [100] E. M. Flanigen, J. M. Bennett, R. W. Grose, J. P. Cohen, R. L. Patton, R. M. Kirchner & J. V. Smith, *Nature*, 1978, 271, 512–516.
- [101] D. Zhou, Y. Li, Y. Zhang, C. Zhang, X. Li, Z.Chen, J. Huang, X. Li f, G. Flores, M. Kamon, *Journal of Contaminant Hydrology*, 2014, 168, 1–16.
- [102] P. Misaelides, *Microporous and Mesoporous Materials*, 2011, 144, 15–18.

- [103] S. Wang and Y. Peng, *Chemical Engineering Journal*, 2010, 156, 11–24.
- [104] M. M. Scherer, S. Richter, R. L. Valentine, and P. J. J. Alvarez, *Critical Reviews in Microbiology*, 2000, 26(4), 221–264.
- [105] C. R. Altare, R. S. Bowman, L. E. Katz, K. A. Kinney, E. J. Sullivan, *Micropor. Mesopor. Mater.*, 2007 105, 305–316.
- [106] J. Schick, P. Caullet, J. L. Paillaud, J. Patarin, C. Mangold Callarec, *Micropor. Mesopor. Mater.* 2011, 142, 549–556.
- [107] K. A. Northcott, J. Bacus, N. Taya, Y. Komatsu, J. M. Perera, G. W. Stevens, *Journal of Hazardous Materials*, 2010, 183, 434–440.
- [108] J. Ma, G. W. Stevens, K. A. Mumford, *Cold Regions Science and Technology*, 2018, 145, 169–176.
- [109] P. Huttenloch, K. E. Roehl, K. Czurda, *Environ. Sci. Technol.*, 2001, 35, 4260–4264.
- [110] K. A. Northcott, J. Bacus, N. Taya, Y. Komatsu, J.M. Perera, G.W. Stevens, *J. Hazard. Mater.*, 2010, 183 (1–3), 434–440.
- [111] M. Ghiaci, A. Abbaspur, R. Kia, F. Seyedeyn-Azad, *Sep. Purif. Technol.*, 2004, 40 (3), 217–229.
- [112] A. Kuleyin, *J. Hazard. Mater.*, 2007, 144 (1–2), 307–315.
- [113] J. Lemic, D. Kovacevic, M. Tomasevic-Canovic, D. Kovacevic, T. Stanic, R. Pfend, R., *Water Res.*, 2006, 40 (5), 1079–1085.
- [114] A. Daković, M. Tomašević-Čanović, G. Rottinghaus, V. Dondur, Z. Mašić, *Colloids Surf. B: Biointerfaces*, 2003, 30 (1–2), 157–165.
- [115] A. Daković, M. Tomašević-Čanović, G. E. Rottinghaus, S. Matijašević, Ž. Sekulić, *Microporous Mesoporous Mater.*, 2007, 105 (3), 285–290.
- [116] W. Song, G. Li, V. H. Grassian, S. C. Larsen, *Environ. Sci. Technol.*, 2005, 39 (5), 1214–1220.
- [117] B. Saremmia, A. Esmacili, M.-R Sohrabi, *Can. J. Chem.*, 2016, 94 (2), 163–169.
- [118] H. Nakamoto and H. Takahashi, *ZEOLITES*, 1982, 12, 67-68.
- [119] S. E. Sen, S. M. Smith, K. A. Sullivan, *Tetrahedron*, 1999, 55, 12657-12698.
- [120] M.A. Anderson, *Environ. Sci. Technol.*, 2000, 34, 725–777.
- [121] C. K. W. Meininghaus and R. Prins, *Microporous and Mesoporous Materials*, 35–36, 2000, 349–365.
- [122] M. Khalid, G. Joly, A. Renaud, and P. Magnoux, *Ind. Eng. Chem. Res.*, 2004, 43, 5275-5280.
- [123] B. Koubaissy, G. Joly, I. Batonneau-Gener and P. Magnoux, *Ind. Eng. Chem. Res.* 2011, 50, 5705–5713

- [124] R. Vignola, R. Bagatin, D'Auris A. De Folly, D. Flego, M. Nalli, D. Ghisletti, R. Millini, R. Sisto, *Chemical Engineering Journal*, 2011, 178, 204–209.
- [125] I. Braschi, G. Gatti, C. Bisio, G. Berlier, V. Sacchetto, M. Cossi and L. Marchese, *J. Phys. Chem. C*, 2012, 116, 6943–6952.
- [126] V. Sacchetto, G. Gatti, G. Paul, I. Braschi, G. Berlier, M. Cossi, L. Marchese, R. Bagatin and C. Bisio, *Phys. Chem. Chem. Phys.*, 2013, 15, 13275-13287.
- [127] V. Sacchetto, C. Bisio, D. F. Olivas Olivera, G. Paul, G. Gatti, I. Braschi, G. Berlier, M. Cossi, and L. Marchese, *J. Phys. Chem. C*. 2015, 119, 24875–24886.
- [128] J. Kuntzel, R. Ham and T. Melin, *Chem. Eng. Technol.*, 1999, 22 (12), pp. 991.
- [129] M. Maretto, F. Bianchi, R. Vignola, S. Canepari, M. Baric, R. Iazzoni, M. Tagliabue, M. Petrangeli Papini, *Journal of Cleaner Production*, 2014, 77, 22-34.
- [130] P. N.E. Diagboya and E. D. Dikio, *Microporous and Mesoporous Materials*, 2018, 266, 252–267.
- [131] Q. Qin and Y. Xu, *Microporous and Mesoporous Materials*, 2016, 232, 143-150.
- [132] S. O. Ganiyu, C. Bispo, N. Bion, P. Ferreira and I. Batonneau-Gener, *Microporous and Mesoporous Materials*, 2014, 200, 17–123.
- [133] D. P. Serrano, G. Calleja, J. A. Botas, and F. J. Gutierrez, *Ind. Eng. Chem. Res.*, 2004, 43, 7010-7018.
- [134] X.S. Zhao, G.Q. Lu, X. Hu, *Colloids and Surfaces A: Physicochemical and Engineering Aspects*, 2001, 179, 261–269.
- [135] X.S. Zhao, Q. Ma, G.Q. Lu, *Energy & Fuels*, 1998, 12, 1051-1054.
- [136] I. Batonneau-Gener, A. Yonli, A. Trouve', S. Mignard, M. Guidotti, and M. Sgobba, *Science and Technology*, 2010, 45, 768–775.
- [137] S. Jun, J. M. Kim, R. Ryoo, Y.-S. Ahn and M.-H. Han, *Microporous and Mesoporous Materials*, 2001, 41, 119-127.
- [138] M. W. Hahn, J. R. Copeland, A. H. van Pelt, and C. Sievers, *ChemSusChem.*, 2013, 6, 2304 – 2315.
- [139] C. Zhou, D. Jia, M. Liu, X. Liu, C. Li, *J. Chem. Eng.* 2017, 62, 3585–3592.
- [140] J. Sheals, S. Sjöberg, P. Persson, *Environ. Sci. Technol.*, 2002, 36, 3090–3095.
- [141] A. Piccolo, G. Celano, P. Conte, *J. Agric. Food Chem.*, 1996, 44, 2442–2446.
- [142] L. Rivoira, M. Appendini, S. Fiorilli, B. Onida, M. Del Bubba and M. C. Bruzzoniti, *Environ Sci Pollut Res*, 2016, 23, 21682–21691.

- [143] Q. Yang, J. Wang, X. Chen, W. Yang, H. Pei, N. Hu, Z. Li, Y. Suo, T. Li and J. Wang, *J. Mater. Chem. A*, 2018, 6, 2184–2192.
- [144] M. Xie and Y. H. Xu, *J. Environ. Sci-China*, 2011, 31, 239–244.
- [145] N. U. Yamaguchi, R. Bergamasco, S. Hamoudi, *Chem. Eng. J.*, 2016, 295, 391–402.
- [146] M. Milojević-Rakić, A. Janošević, J. Krstić, B. Nedić Vasiljević, V. Dondur, G. Ćirić-Marjanović, *Microporous and Mesoporous Materials*, 2013, 180, 141–155.
- [147] G. Xiao and R. Wen, *Fluid Phase Equilib.*, 2016, 411, 1–6.
- [148] L. Guo, Y. Cao, K. Jin, L. Han, G. Li, J. Liu, and S. Ma, *J. Chem. Eng. Data* 2018, 63, 422–428.
- [149] S. Fiorilli, L. Rivoira, G. Cali, M. Appendini, M. Concetta Bruzzoniti, M. Coissonc and B. Onida, *Applied Surface Science*, 2017, 411, 457–465.
- [150] O. K Borggaard and A. L. Gimsing, *Pest Manag Sci*, 2008, 64, 441–456.
- [151] G. AL and B. OK, *Clay Miner*, 2002, 37, 509–515.
- [152] G. AL and B. OK, *Clays Clay Miner*, 1 2007, 55, 110–116.
- [153] B.C. Barja and A. M. Dos Santos, *Environ Sci Technol*, 2005, 3, 585–592.
- [154] Q. Yang, J. Wang, X. Chen, W. Yang, H. Pei, N. Hu, Z. Li, Y. Suo, T. Li and J. Wang, *J. Mater. Chem. A*, 2018, 6, 2184–2192.
- [155] M. A. Sanhoob and O. Muraza, *Microporous and Mesoporous Materials*, 2016, 233, 140–147.
- [156] C. D. Chudasama, J. Sebastian and R. V. Jasra, *Industrial & Engineering Chemistry Research*, 2005, 44(6), 1780–1786.

Chapter II

Outline of The Thesis

As it was pointed out in Chapter I, groundwater depollution is of great interest in these last years, because of the need to remove organic compounds coming from industrial waste of oil refineries and gas stations.

In the frame of my Ph.D. thesis, special attention was devoted to the preparation and physico-chemical characterization of silica-based solids with variable porosity (from completely amorphous to long-range ordered materials) for potential application in groundwater depollution. In this respect, materials with different pore dimensions and architecture, particle size and textural properties have been selected and tested as sorbents for hydrocarbons, with particular attention to toluene and *n*-hexane molecules chosen as model of aromatic and aliphatic molecules, respectively. Moreover, some of the porous materials considered during my Ph.D. were tested also as adsorbents for the removal of more complex molecules such as N-(phosphonomethyl)glycine (glyphosate, an herbicide largely used in the last years) from aqueous media. This was possible thanks to a collaboration with a research group of Perú interest are also related to the study of materials with environmental applications.

The different aspects considered in the frame of the thesis are described in Figure 2.1

Silica-based materials...

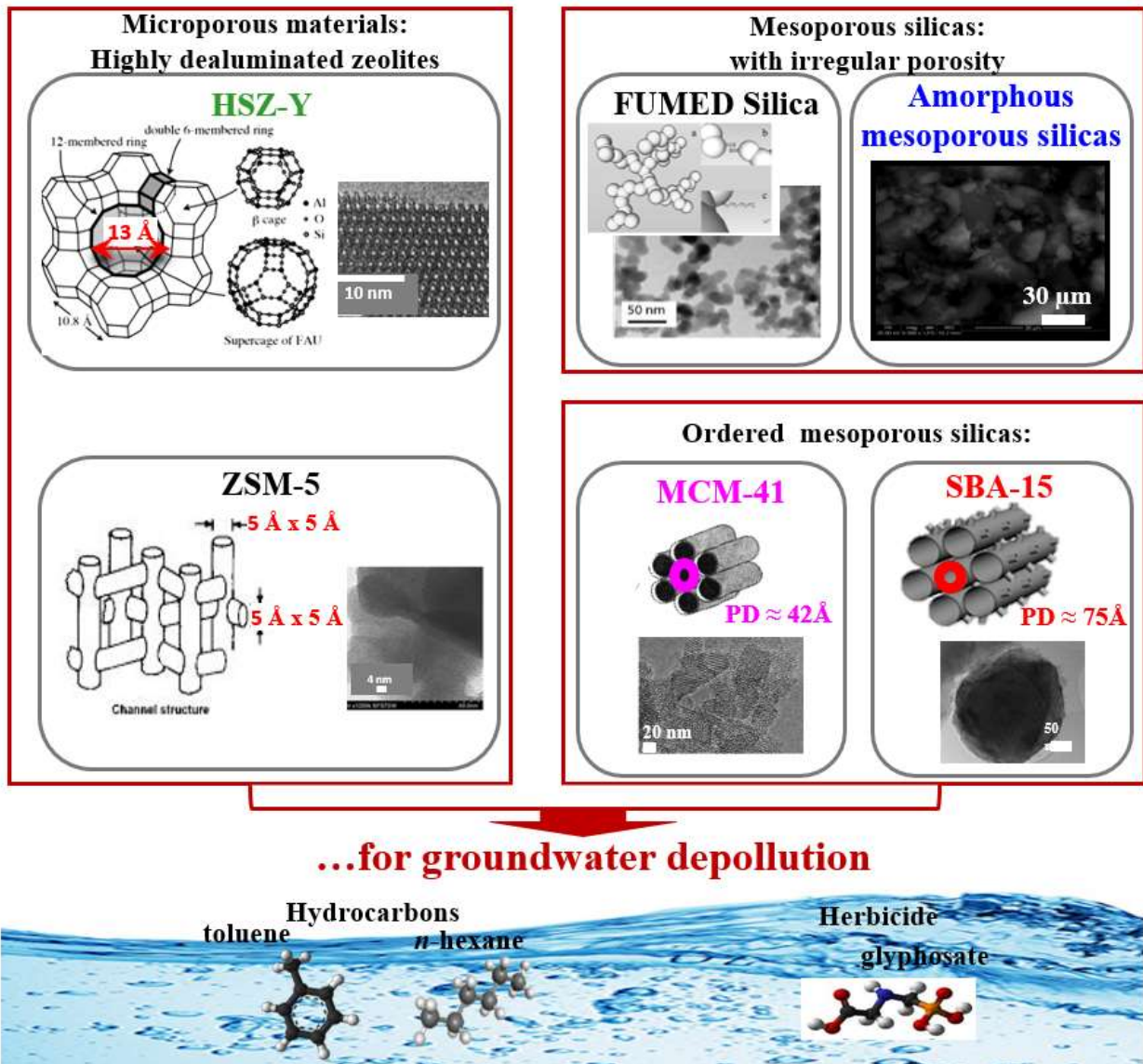


Figure 2.1: Schematic representation of the aspects related application silica-based solids for groundwater depollution investigated in this Ph.D. thesis.

The first part of the thesis work related to the study of the interactions that are driving the on the co-adsorption of hydrocarbons (mainly toluene and *n*-hexane) on dealuminated microporous systems of commercial origin (HSZ-Y and ZSM-5 zeolites). This issue is relevant from the environmental point of view in that, under real conditions, hydrocarbons are often present in groundwater as a mixture. For this, the contribution of surface groups on the adsorption properties of HSZ-Y and ZSM-5 zeolites were investigated by means of different experimental techniques. FT-IR spectroscopy of adsorbed toluene and *n*-hexane equimolar mixture from the gas phase and SS-NMR spectroscopy were used to

gain deeper insight into the interactions and selectivity of the pollutant molecules inside the zeolite cavities.

This research activity is developed in the frame of a collaboration with the Research Center for Non-Conventional Energy, Istituto ENI Donegani–Environmental Technologies and inserted in a project called: "*Treatment of water contaminated by mixtures of hydrocarbons: selective adsorption of micro and mesoporous materials from model systems representative of groundwater and production*".

The estimation of concentration of toluene and *n*-hexane co-adsorbed on the zeolites was possible by using of the molar absorption coefficient of *n*-hexane and toluene adsorbed on microporous systems (HSZ-Y and ZSM-5).

The collection of data coming from FTIR and microgravimetric analysis was used for the determination of the molar absorption coefficients of toluene and *n*-hexane adsorbed on high silicas zeolites by adapting the Beer–Lambert law to specific adsorbent/substrate systems. The relevance of this study applied for the first time is based on knowledge of molar absorption coefficients of adsorbed molecule providing the basis for the quantitative determination of the gas mixtures dosed on porous solids.

Moreover, to overcome the limitations related to the use of microporous materials, the interest was also given to the use of mesoporous materials.

In this respect, mesoporous silicas samples with irregular porosity (commercial FUMED and AMS silicas) were selected and characterized to be tested as adsorbents towards toluene. Then, the interest was devoted to mesoporous SBA-15 and MCM-41 silicas with ordered porosities.

Volumetric analyses were performed to study the toluene adsorption capacity of these solids. These experiments were performed during a period of internship at the laboratories of the Department of Environmental and Chemical Engineering at the University of Calabria in Italy under the supervision of the Prof. Giovanni Golemme.

Hydrothermal stability of studied solids was considered also an important task in my Ph.D., considering that in real conditions solids are soaked in water during their adsorption use. For this reason, the hydrothermal stability of some mesoporous samples was studied by means of different experimental techniques. FT-IR spectroscopy and gravimetric analysis of toluene adsorption were performed to evaluate the sorption capacity after the hydrothermal treatment.

The determination of molar absorption coefficients of toluene adsorbed on mesoporous silicas (*i.e.* mesoporous silica samples with irregular porosity (FUMED) and ordered mesoporous MCM-41 and

SBA-15 silicas) were also carried out by combining the results of the volumetric and FT-IR analyses of adsorbed toluene on these materials.

Finally, the last part of my Ph.D. work was devoted to the study of the adsorption properties of ordered mesoporous silicas (mainly SBA-15, also functionalized with organic species) for glyphosate removal from aqueous solution.

Kinetics and equilibrium adsorption isotherms of glyphosate on these solids were obtained from the adsorption measurements of glyphosate in contact with the selected solids in aqueous media. UV–vis spectroscopy was used to determinate the glyphosate concentrations present in the aqueous solutions after the batch adsorptions. In order to understand the adsorption mechanisms and the kinetic process, different models were applied to the glyphosate uptake isotherms on the select solids.

These measurements of glyphosate adsorption were performed during a period of internship at Department of Sciences, Section Chemistry, Pontifical Catholic University of Peru under the supervision of the Prof. Maria del Rosario Sun Kou.

Chapter III

Microporous Systems for Groundwater Depollution

3.1 Introduction

As reported in Chapter I, organic pollutants can end up in groundwater where industrial areas, especially oil refineries or petrochemicals plants, are located. For this reason, great research efforts and several literatures are devoted to the optimization of adsorption processes and to the development of novel adsorbents for remediation and separation of organic pollutants from groundwater.^[1]

In this respect, the understanding of the competition of organic contaminants for a specific adsorbent is relevant from an environmental point of view in that, under real conditions, pollutants are generally present in groundwater as complex mixtures.^[2,3]

This is why the research activities carried out during my Ph.D. thesis were focused on the co-adsorption of different pollutants (specifically *n*-hexane and toluene binary mixtures, chosen as model molecules of aliphatic and aromatic fuel-based pollutants, respectively) on HSZ-Y and ZSM-5 zeolites (with a SiO₂/Al₂O₃ ratio of 200 and 280, respectively) with environmental interest.^[4,5]

Highly dealuminated Y (HSZ-Y) and ZSM-5 zeolite with commercial origin were selected as microporous adsorbents on the basis of their pore dimensions, high hydrophobicity and capacity to adsorb organic pollutants. It is well-known in the literature that zeolites, particularly those with hydrophobic character (*i.e.*, having high SiO₂/Al₂O₃ ratio), are capable of interacting with hydrocarbons in presence of water.^[6-8]

As reported in Chapter I, the adsorption properties of toluene and *n*-hexane on HSZ-Y and ZSM-5 zeolites as single pollutants was monitored and reported by our research group by different experimental techniques (see Chapter I, paragraph 1.3.1.2).

Taking into account these previous results, in this chapter the results related to the co-adsorption process of toluene and *n*-hexane equimolar mixture on hydrophobic HSZ-Y and ZSM-5 from gas phase and in dry conditions are discussed.

3.2 Structural, textural and surface properties of HSZ-Y and ZSM-5 zeolites

In table 3.1 are reported the codes of the zeolites used in the frame of this Ph.D. thesis work together with their SiO₂/Al₂O₃ ratio.

Table 3.1: Commercial specifications of HSZ-Y and ZSM-5 zeolites.

Zeolite	Framework Type Code	Purchased from	Commercial Code	SiO ₂ /Al ₂ O ₃	Cationic form ^a
HSZ-Y	FAU	Tosoh Corp (Japan)	HSZ-390HUA	200	H ⁺
ZSM-5	MFI	Zeolyst	CBV28014	280	NH ₄ ⁺

^aBefore use, zeolites in ammonium form have been transformed into protonic form by calcination at 600°C for 4h at a heating rate of 3 °C/min under oxygen flow (100 mL/min).

The HSZ-Y zeolite belongs to the Faujasite family (FAU) and its framework is characterized of the presence of unit cells formed by eight cuboctahedrons or *sodalite cages* (cage β) which are linked together through double T6-rings into a hexagonal layer (D6R, hexagonal prism), forming the three-dimensional structure called supercage composed of rings of 12 linked tetrahedra (12MR) of diameter ca. 7.4 Å x 7.4 Å (see Figure 3.1 A and B).

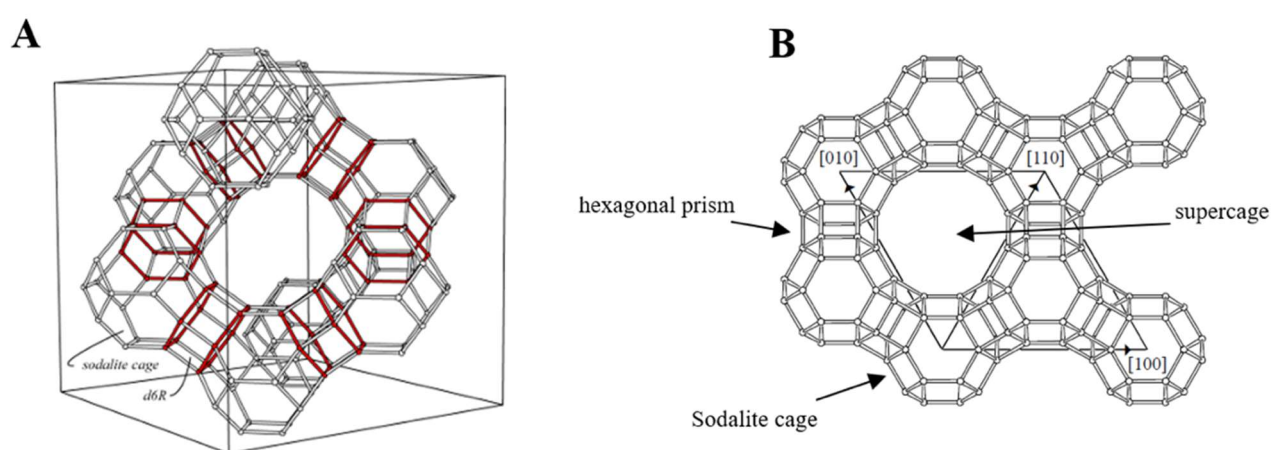


Figure 3.1: Schematic representation of the FAU zeolite supercage along the direction [111] (A) and [001] (B). Adapted from ref. [9-11]

The Faujasite family (FAU) zeolites are characterized by a cell with cubic symmetry $Fd3m$, by a chemical composition of the framework: $| (Ca^{2+}, Mg^{2+}, Na^+)_{29} (H_2O)_{240} | [Al_{58} Si_{134} O_{384}]$ -FAU and by an accessible volume of 3956.18 \AA^3 .^[9]

Since HSZ-Y zeolite was dealuminated it presents some structural defectivity and it was calculated that the structure contains an average of three silanols groups given by the composition of the unit cell of $Si_{186} O_{360} (OH)_{24}$ formed by eight sodalite cages.^[8]

Zeolite ZSM-5 (Zeolite Socony Mobil-five) has the framework type with MFI code in the IZA (International Zeolite Association) classification and is characterized by the presence of *pentasil units*, whose structure is defined by 8 rings 5-T $[5^8]$ (Figure 3.2A). The pentasil units are linked to each other forming chains three-dimensional (Figure 3.2B), in turn connected one above the other to form a sort of layer (Figure 3.2C).^[12]

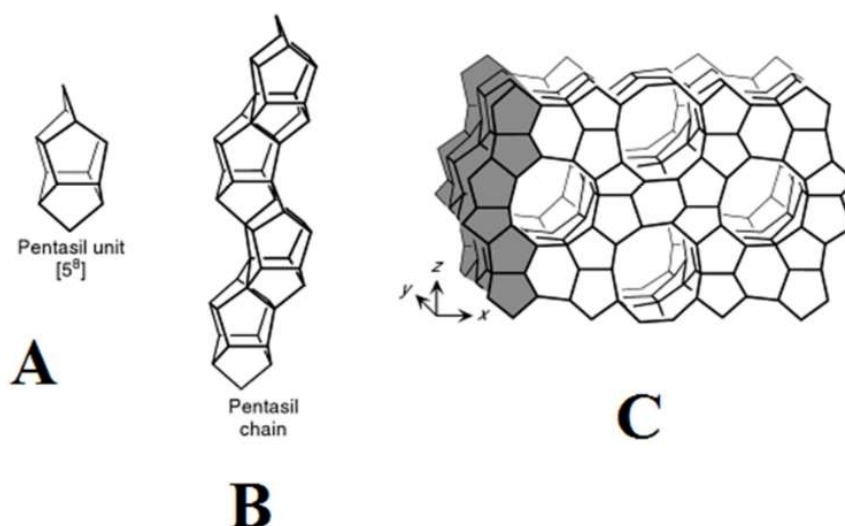


Figure 3.2: Schematic representation of the Pentasil Unit (A), Pentasil chain (B) and MFI framework type formed by pentasil chains. Adapted from ref.^[12]

The particular structure of the ZSM-5 zeolite is characterized by a three-dimensional pore system (Figure 3.3C) consisting of sinusoidal circular pores 10 MR channels with dimension of $5.5 \times 5.1 \text{ \AA}$ (Figure 3.3A) along the direction $[100]$ and intersecting straight 10MR channels with dimension $5.6 \times 5.3 \text{ \AA}$ (Figure 3.3B) that extend along the direction $[010]$.

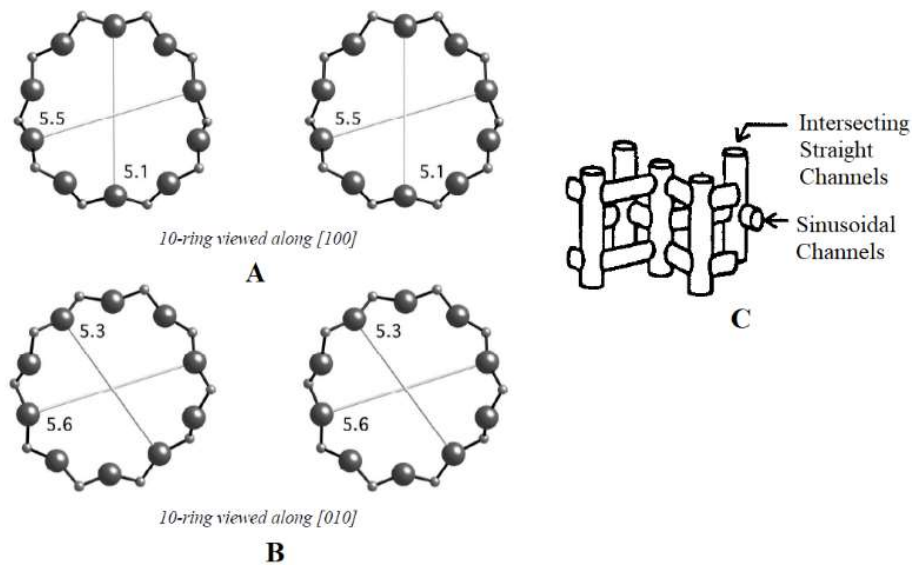


Figure 3.3: Schematic representation of the pores of ZSM-5 zeolite along the direction [100] (A) and along the direction [010] (B). Three-dimensional representation of the structure of the ZSM-5.^[10,13]

The MFI family is characterized by a cell with orthorhombic symmetry, $Pnma$, by a chemical composition of the framework: $[Na^+_n (H_2O)_{16}] [Al_n Si_{96-n} O_{192}]$ -MFI, $n < 27$ and by an accessible volume of 511.01 \AA^3 .^[9]

The ZSM-5 used in the frame of the thesis has a composition of the unit cell of $Al_{0.17}Si_{95.83}O_{192}H_{0.17}$.^[8]

The morphology of the two zeolites was investigated by using scanning electron microscopy (SEM) and the images are reported in Figure 3.4.

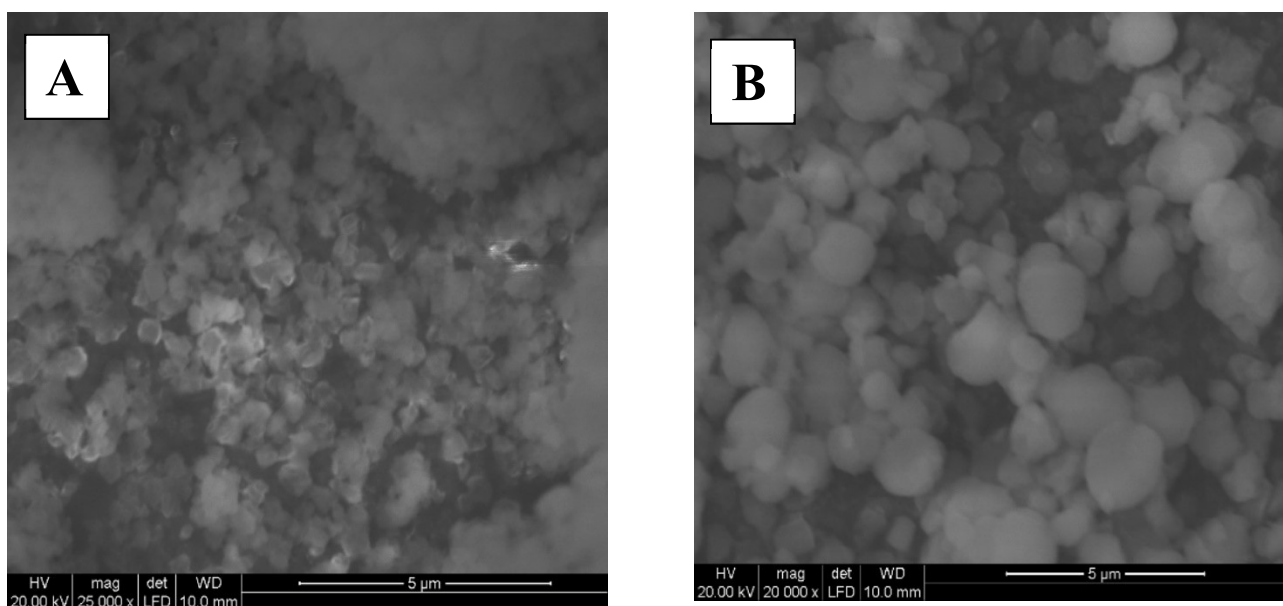


Figure 3.4: SEM micrographs of HSZ-Y(A) and ZSM-5 samples

The SEM images of HSZ-Y (Fig. 3.4A) and ZSM-5 (Fig. 3.4B) showed a polygonal like morphology and particle sizes between 0.4 - 0.6 and 0.5 - 2.2 μm , respectively.

Specific surface area and pore size distribution of the two zeolites used in the frame of the Ph.D. thesis work has been determined by N_2 adsorption isotherms (Table 3.2).

Table 3.2: Main Textural features of HSZ-Y and ZSM-5 zeolites

Sample	$\text{SSA}_{\text{BET}}^{\text{a}}$ [m^2g^{-1}]	$\text{SSA}_{\text{microp}}^{\text{b}}$ [m^2g^{-1}]	V_{T}^{c} [cm^3g^{-1}]	$V_{\text{microp}}^{\text{d}} (\leq 20 \text{ \AA})$ [cm^3g^{-1}]	$V_{\text{mesop}}^{\text{d}} (20-160 \text{ \AA})$ [cm^3g^{-1}]
HSZ-Y	991	710	0.68	0.28	0.17
ZSM-5	550	355	0.52	0.02	0.43

^a Braunauer-Emmett-Teller (BET) specific surface area (SSA); ^bMicropore surface area a by t-plot method; ^cTotal pore Volume by NLDFT method. ^dVolume calculated by NLDFT method^[5]

The SSA for the zeolite HSZ-Y is of $991 \text{ m}^2 \text{ g}^{-1}$, more than half of which is due to the presence of micropores ($710 \text{ m}^2 \text{ g}^{-1}$) with a related microporous volume of $0.28 \text{ cm}^3 \text{ g}^{-1}$; whereas ZSM-5 zeolite has a SSA of $550 \text{ m}^2 \text{ g}^{-1}$, and the presence of micropores is related by a $\text{SSA}_{\text{micro}}$ of $355 \text{ m}^2 \text{ g}^{-1}$ with a volume of $0.02 \text{ cm}^3 \text{ g}^{-1}$. Two families of pores at ca. 13 and 22 \AA are found on HSZ-Y whereas micropores of ca. 8 \AA are present in ZSM-5 sample, along with mesopores whose diameter is in the 30–100 \AA range. The presence of micropores, along with mesopores in the case of the ZSM-5 sample is due to the dealumination process. It is known, in fact, that the dealumination process modifies the zeolite pore architecture, enlarging the windows between interconnected cages with the formation of mesopores or large micropores.^[14]

The large dimension of the porous of both zeolites allows to enter large molecules, making these microporous materials useful in the adsorption of the pollutants.^[5]

Surface properties of both zeolites were studied by IR spectroscopy (Figure 3.5). The IR spectrum of zeolite HSZ-Y (Figure 3.5 curve a) shows two bands at ca. 3745 and 3738 cm^{-1} , which were assigned to surface Si–OH groups located on the external and internal surface of the material (inside the zeolite cage). In addition, a broad absorption extending $3700-3200 \text{ cm}^{-1}$, which is due to H-bonded silanols had been also found.^[14,5] The IR spectrum of ZSM-5 zeolite (Figure 3.5 curve b) showed bands of silanols much less intense than the HSZ-Y sample, thus indicates that ZSM-5 has smaller concentrations of isolated silanols respect to HSZ-Y zeolite.

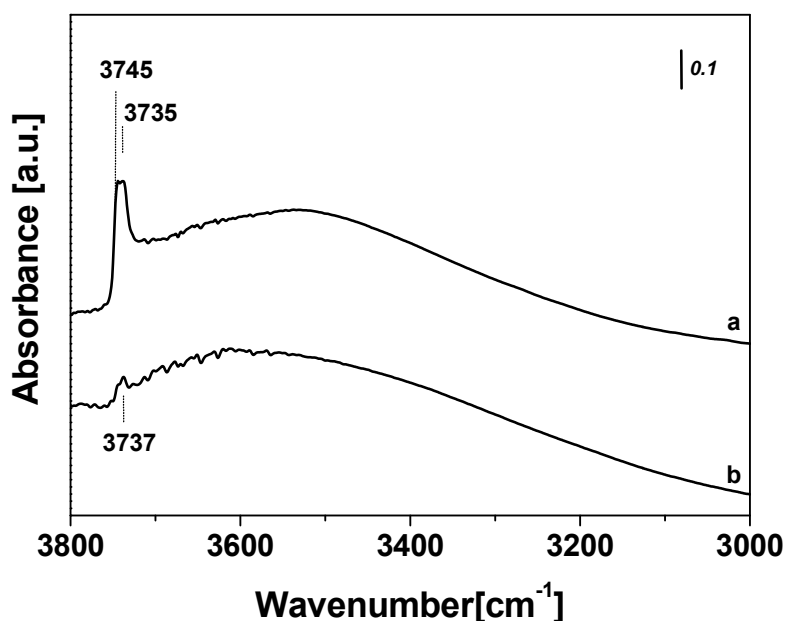


Figure 3.5: FTIR spectra of HSZ-Y and ZSM5 samples after outgassing at room temperature (spectra a and b, respectively). Adapted from Ref.^[5]

The amount of silanol groups of HSZ-Y and ZSM-5 zeolites was determined by thermogravimetric analysis by considering the weight loss within the range 150–1100 °C and by following the equation given in Appendix II. The weight loss within the range 150–1100 °C was approximately 2.3 and 0.8 wt % corresponding to 1.30 and 0.92 OH/nm² for HSZ-Y and ZSM-5 zeolites, respectively.^[5]

3.3 Adsorption of gaseous mixture of toluene and *n*-hexane on HSZ-Y and ZMS-5 zeolites

Toluene and *n*-hexane were adsorbed as an equimolar mixture on both zeolites to gain insight on the adsorption selectivity of the different solids. The contribution of surface groups (*i.e.*, the type and distribution of silanol groups) on the adsorption properties of dehydrated HSZ-Y and ZSM-5 zeolites were investigated by FT-IR spectroscopy of adsorbed toluene and *n*-hexane mixture. Moreover, SS-NMR spectra are also collected to gain deeper insight into the interactions and selectivity of the pollutant molecules inside the zeolite cavities.

3.3.1 FTIR spectroscopy analysis

The IR spectra of adsorbed toluene and *n*-hexane mixture on HSZ-Y are reported in Fig. 3.6.

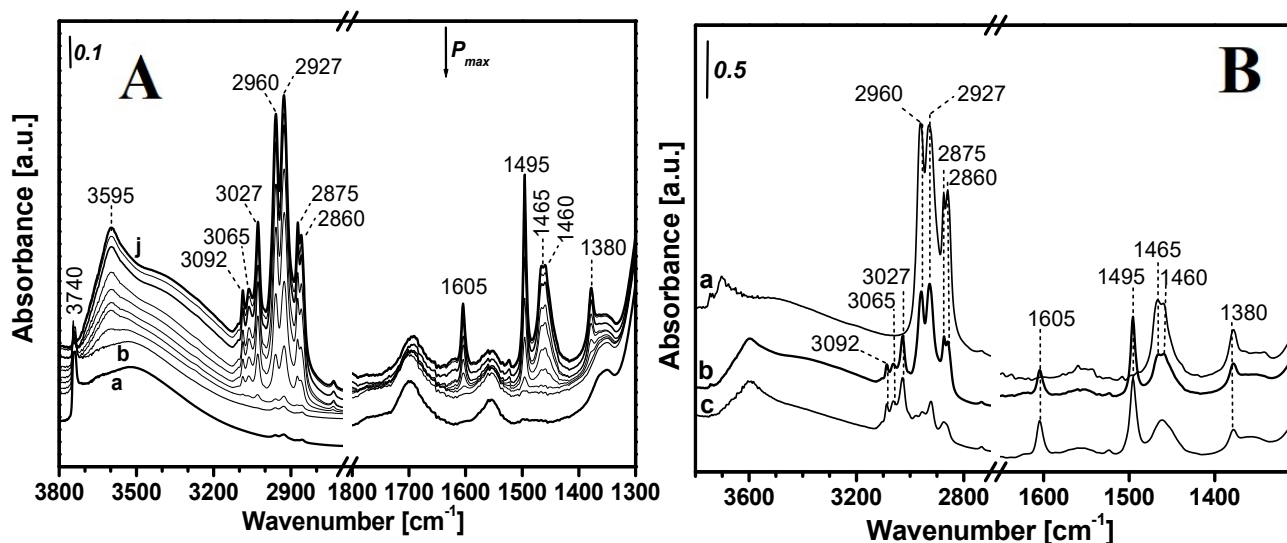


Figure 3.6: A: Infrared spectra of increasing doses of toluene and *n*-hexane equimolar mixture on HSZ-Y zeolite outgassed at r.t. Spectrum a was recorded after outgassing the sample for 60 min at beam temperature before mixture adsorption. Spectra collected upon adsorption of 0.1, 0.4, 0.6, 1, 2, 4, 8, and 30 mbar (spectra b-j) of pollutant mixture. B: Infrared spectra of 15 mbar of pure *n*-hexane (spectrum a) and toluene (spectrum c) on HSZ-Y zeolite outgassed at r.t. compared with the spectrum collected upon adsorption of 30 mbar of their equimolar mixture (spectrum b).

As reported above, the IR spectrum of HSZ-Y zeolite (Figure 3.6A, curve a) presents absorptions at 3740 and 3735 cm^{-1} , corresponding to the vibration of OH groups located on the external and internal (*i.e.*, inside the zeolite cage) surface of the HSZ-Y, respectively. A broad absorption extending in the region between 3700 and 3200 cm^{-1} , due to the stretching modes of H-bond donor silanols that are present on the zeolite (internal) surface, is also visible.

In order to investigate the interactions occurring between the equimolar mixture of pollutants and zeolite surface, 30 mbar of vapor mixture was admitted and then gradually decreased. However, for the sake of clarity, the spectra will be described starting from the low to high pressure.

The adsorption of small doses of the *n*-hexane/toluene mixture (from 0.1 to 1 mbar) led to the partial disappearance of the band related to isolated SiOH species at 3745 cm^{-1} with a consequent formation of a broad band with a maximum at about 3595 cm^{-1} (Figure 3.6A, curves b–f).

This behavior has been already observed in the case of toluene adsorption (see Chapter I, paragraph 1.3.1.2): the band at 3595 cm^{-1} is due to the interaction of isolated silanols with the aromatic ring of the toluene molecules (*i.e.*, O–H $\cdots\pi$ interactions).^[5] The spectra of increasing doses of mixture, up to

ca. 4 mbar of pollutants mixture (Figure 3.6, curves b–h) show a progressive decrease of the bands related to isolated silanols. Nevertheless, the opposite occurs when toluene is adsorbed as a single pollutant on HSZ-Y, and the bands related to isolated SiOH species do not completely disappear, thus indicating that a fraction of OH species is not accessible to the pollutants because of the copresence of *n*-hexane. This fact suggests that the presence of *n*-hexane (that following SS-NMR studies is more mobile than toluene in HSZ-Y cages) generates steric hindrances that partially limit the interactions between toluene and SiOH species.

It is also observed a broad band with a maximum at *ca.* 3400 cm⁻¹, becoming especially evident at pressure higher than 2 mbar.

To understand better the interactions occurring between the mixture and the surface sites on HSZ-Y zeolite, the HSZ-Y zeolite was outgassed at 700 °C to reduce the heterogeneity of surface (H-bonded Si–OH species). With this purpose, the comparison of selected IR spectra related to the adsorption of 30 mbar of the equimolar mixture, pure toluene and pure *n*-hexane adsorbed on the HSZ-Y outgassed at rt and 700 °C is reported in Figure 3.7.

In the Figure 3.7 it is possible to distinguish that after the adsorption of the mixture, or toluene and *n*-hexane singularly adsorbed on HSZ-Y zeolite outgassed at 700 °C, which does not show H-bonded silanols, the broad band with a maximum at *ca.* 3400 cm⁻¹ is not evident.

This suggest that the band at 3400 cm⁻¹ is due to the interactions of pollutants (mostly toluene, as it can be derived from Figure 3.7) with H-bonded Si–OH species.

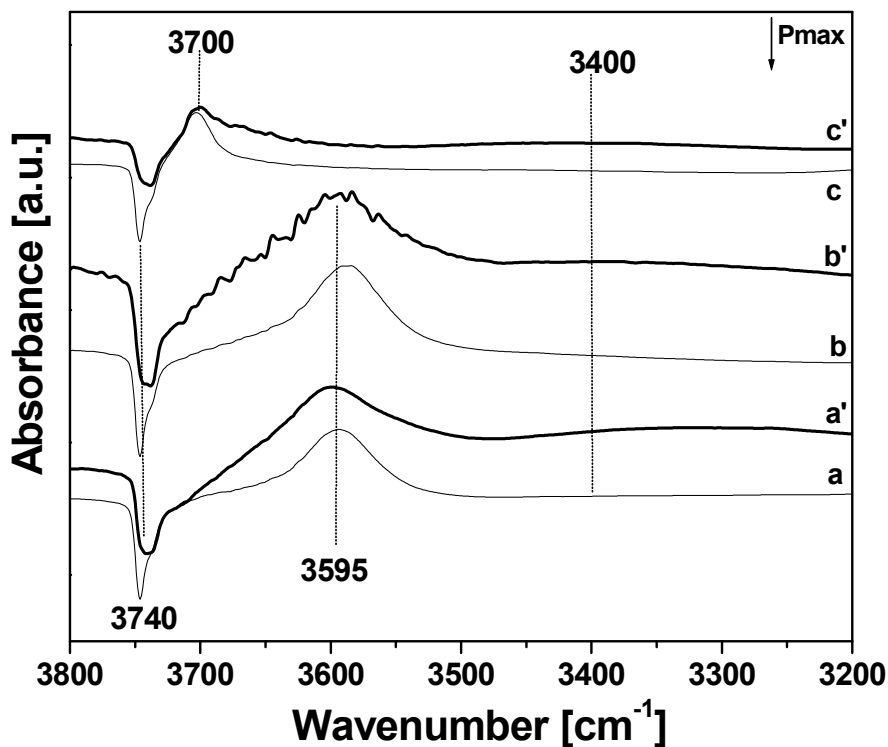


Figure 3.7: Infrared Differential spectra of the mixture (curves a and a'), of pure toluene (curves b and b') and of pure *n*-hexane (curves c and c') adsorbed on HSZ-Y outgassed at 700 °C (curves a, b and c) and adsorbed on HSZ-Y outgassed r.t. for 60 minutes (curves a', b' and c'). The spectrum of the bare samples was used as references and subtracted from the spectra obtained after exposure of 30 mbar of each pollutants vapor.

Upon adsorption of toluene and *n*-hexane mixture (total pressure of 30 mbar) on HSZ-Y zeolite, IR bands at 3100–2800 and 1650–1300 cm^{-1} are found: for a better description of these absorptions, spectra obtained after a dose of 15 mbar (partial pressure) of both toluene and *n*-hexane, as single pollutants, are directly compared in Figure 3.6B.

As can be derived from the comparison with the IR spectra of singly adsorbed molecules (Figure 3.6B, curves a and c), bands of pollutants mixture (Figure 3.6B, curve b) at 3092, 3065 and to 3027 cm^{-1} can be attributed to the C–H stretching modes of the toluene ring. Instead, the intense bands at 2960 and 2927 cm^{-1} are associated with the asymmetric stretching modes of CH_3 and CH_2 moieties of *n*-hexane, the associated symmetric modes falling at 2875 and 2860 cm^{-1} , respectively.^[15] These bands are intense and overlapped to the C–H stretching modes of the toluene methyl group. In the low frequency range, the absorptions can be assigned as follows: (i) the sharp signals at 1605 and 1495 cm^{-1} are due to the quadrant stretching mode of C=C groups in monosubstituted aromatic molecules and to the semicircular stretching vibration of the toluene aromatic ring, respectively; (ii) the bands at ca. 1465 and 1460 cm^{-1} are mainly associated with the asymmetric bending modes of

the CH₃ and CH₂ moieties of *n*-hexane. Nevertheless, out-of-phase bending modes of toluene methyl groups also contribute to the 1460 cm⁻¹ band; (iii) the band at 1380 cm⁻¹ is due to the in-phase deformation of CH₃ groups of both *n*-hexane and toluene molecules.^[5]

The adsorption of toluene and *n*-hexane mixture were carried out also for ZSM-5 zeolite. The comparison of selected IR spectra related to the adsorption of equimolar mixture of toluene and *n*-hexane on HSZ-Y and ZSM-5 zeolites is reported in Figure 3.8A,B.

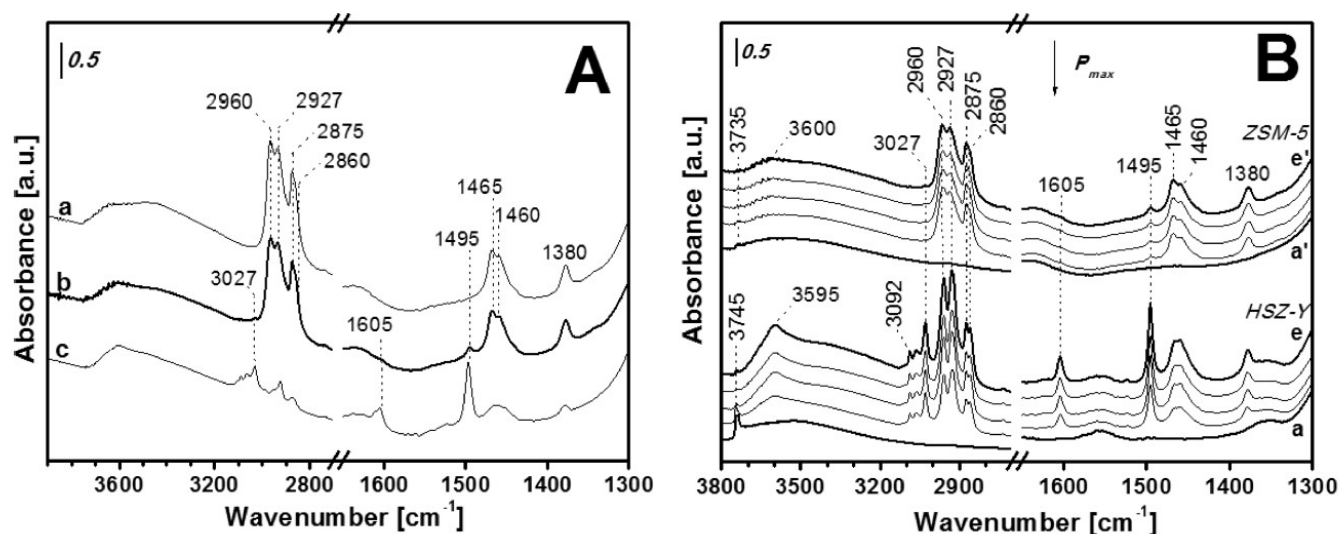


Figure 3.8: A: Infrared spectra of 15 mbar of pure *n*-hexane (spectrum a) and toluene (spectrum c) on ZSM-5 zeolite outgassed at r.t., compared with the spectrum collected after contacting 30 mbar of their equimolar mixture (spectrum b). B: IR spectra of equimolar toluene/*n*-hexane mixture on the two zeolites. Spectra related to HSZ-Y and ZSM-5 zeolites outgassed at r.t. for 1 h (curves a and a', respectively), spectra collected after adsorption of the mixture on the same supports at a pressure of 1 mbar (curves b and b', respectively), 5 mbar (curves c and c', respectively), 15 mbar (curves d and d', respectively), and 30 mbar (curves e and e', respectively).

Upon adsorption of the pollutant mixture on the ZSM-5, IR bands in the 3100–2800 and 1650–1300 cm⁻¹ range are observed: for a better comprehension of these absorptions, spectra obtained after a dose of 15 mbar (partial pressure) of both toluene and *n*-hexane, as single pollutants are reported (Figure 3.8A, curves a and c). It is evident from the comparison reported in Figure 3.8A that the adsorption of 30 mbar (total pressure) of the mixture pollutants on ZSM-5 (curve b) led to the appearance of intense bands typical of adsorbed *n*-hexane molecule, thus suggesting that this species is preferentially retained on the ZSM-5 zeolite. The presence of a small amount of toluene molecule is nevertheless attested by the formation of bands at 3027 and 1495 cm⁻¹ (see also Figure 3.8A curve b).

As already pointed out, the spectrum of ZSM-5 (Figure 3.8B, curve a') is characterized by a band at *ca.* 3737 cm^{-1} and a broad and weak band visible in the $3700\text{--}3200\text{ cm}^{-1}$ range related to the presence of Si–OH species mainly interacting with each other through H-bonding.^[5]

The adsorption of increasing amounts of the toluene/*n*-hexane mixture on ZSM-5 zeolite (Figure 3.8B, curves b'–e') shows that the peak of isolated silanols at 3735 cm^{-1} decreases in intensity and that a broad and weak band at *ca.* 3600 cm^{-1} appears. This behavior is due to the interactions of surface OH groups with adsorbed *n*-hexane molecules, as already reported in the case of singularly adsorbed pollutant.^[5]

After adsorbing the pollutant's mixture, intense IR stretching bands of the aliphatic chain of *n*-hexane ($2960, 2927, 2875$ and $2860, 1465, 1460, \text{ and } 1380\text{ cm}^{-1}$) dominate the spectra.^[15] Very weak bands at $3027, 1605, \text{ and } 1495\text{ cm}^{-1}$ testify that a limited amount of toluene is adsorbed, thus suggesting that *n*-hexane is preferentially retained on ZSM-5.^[16]

The collected IR spectra suggested that the two zeolites behave differently in the presence of the toluene/*n*-hexane mixture: indeed, the HSZ-Y zeolite preferentially retains toluene, whereas *n*-hexane results are more similar to those of ZSM-5 (Figure 3.8B b'–e'). The high affinity of toluene for HSZ-Y can be partially associated with the presence of silanol species in this specific zeolite that, already at low pressure, have an important role in stabilizing the aromatic molecule through H-bond interactions.^[16]

3.3.2 ^1H MAS and ^{13}C CPMAS SS-NMR analysis

Solid-state NMR spectroscopy is often been used to characterize inorganic–organic hybrid materials in which proton and carbon atoms are present in several environments labeled by very different isotropic chemical shifts due to their molecular interactions with inorganic interfaces. Isotropic chemical shifts of NMR-active nuclei are very sensitive to their local bonding environments and therefore can give valuable information on the nature of pollutant interactions with zeolites. The “local probe” nature of solid-state NMR spectroscopy offers insights into the guest–host interactions between gas molecules and zeolites. The versatility of the NMR approach has been used in the past to conduct investigations of gas adsorption in zeolites.^[5,16]

Complementary solid-state ^1H and ^{13}C NMR methods along with variable temperature measurements have been used in the frame of the Ph.D. to establish the adsorption and investigate the nature of the interactions of pollutant molecules at the zeolite interfaces. The results are then correlated with other

physicochemical characterization techniques, such as textural properties determined by N_2 physisorption.

As already reported (see Chapter I, paragraph 1.3.1.2), the adsorption and diffusion of toluene and *n*-hexane adsorbed as single pollutants are significantly influenced by the pore/channel architecture and volume availabilities of both HSZ-Y and ZSM-5 zeolites. The large space of supercages of HSZ-Y helps in the improvement of diffusion of pollutants whereas restricted space of ZSM-5 limits mass transfer through channels.^[5]

1H MAS and ^{13}C CP-MAS experiments were carried out to gain deeper insight into the competitive adsorption selectivity of pollutant mixtures inside the zeolite cages/channels.

Figure 3.9 (A, curve c) shows the 1H MAS NMR spectrum recorded after the adsorption of the equimolar mixture of pollutants at a total pressure of 3 mbar has been in contact with zeolite HSZ-Y for 30 min. For comparison purposes, spectra of single pollutants adsorbed on the same zeolite under the same conditions are shown (Figure 3.9A, curve a and b). The spectra have been normalized to the highest peak intensity.

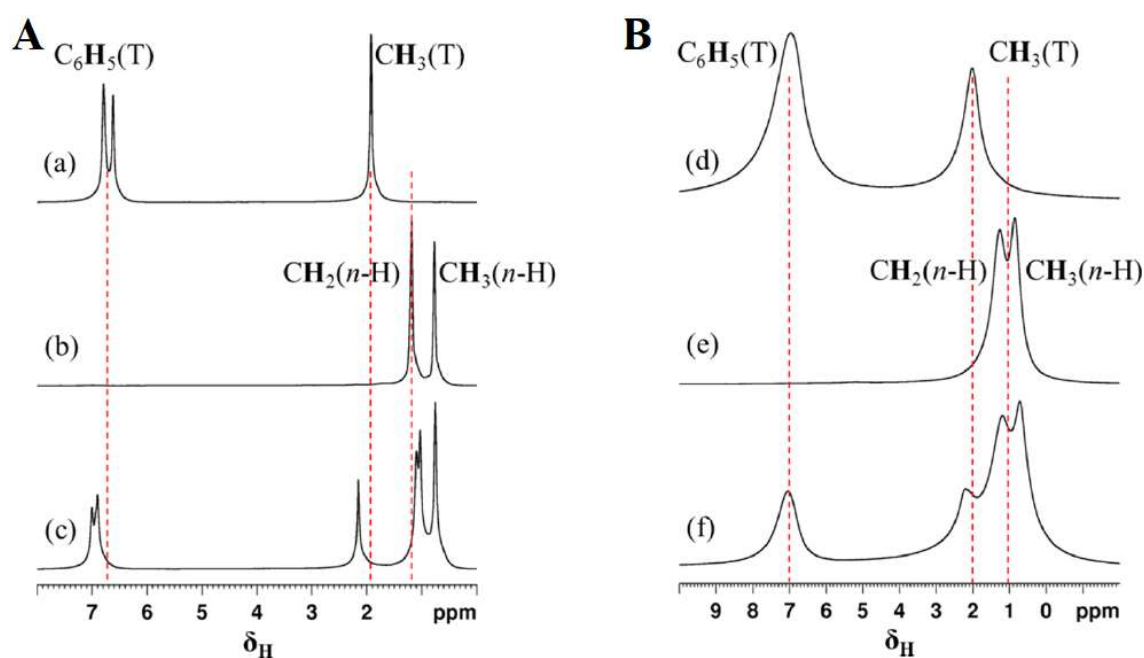


Figure 3.9: 1H solid state MAS NMR spectra of toluene (a,d), *n*-hexane (b,e), and their mixture (c,f) adsorbed at a partial pressure of 3 mbar (equimolar quantity of pollutants in the gas phase) on zeolite HSZ-Y (A) and ZSM-5 (B). The spectra were recorded at r.t. and a MAS rate of 15 kHz.

As reported in Chapter I, the description of SS-NMR spectra related to pollutants singularly adsorbed on the HSZ-Y zeolite has been already reported (see Chapter I, paragraph 1.3.1.2).^[5] The spectrum of toluene adsorbed singularly on HSZ-Y zeolite (Figure 3.9A, curves a) shows peaks at *ca.* 2 and 7 ppm due to methyl and aromatic protons, respectively. Whereas the spectrum of *n*-hexane adsorbed singularly on HSZ-Y (Figure 3.9A, curves b) shows resonances due to methyl and methylene protons at around 0.8 and 1.2 ppm, respectively.

In the spectrum of the mixture adsorbed on the HSZ-Y zeolite (Figure 3.9A, curve c), narrow peaks due to methyl protons from *n*-hexane at 0.76 ppm and from toluene at 2.16 ppm are visible.

In addition, two peaks due to methylene protons from *n*-hexane are also observed at 1.03 and 1.1 ppm. In the aromatic region, peaks due to toluene protons are also seen at around 7 ppm.

If we compare the spectra of a single pollutant adsorbed on zeolites with those of the adsorbed mixture, it is evident that the peaks are shifted in the latter case. In particular, a downfield shift was observed for toluene protons, while an upfield shift was observed for *n*-hexane protons in mixture. This can be expected due to the fact that the co-presence of another kind of pollutant leads to a mutual change in the environment of adsorption when compared to the single pollutant adsorption scenario. An explanation of this behaviour is that nuclei are extremely sensitive to the surrounding chemical environment and multicomponent adsorption leads to a competition for adsorption sites, and the nature of interactions between different adsorbed components (guest–guest and guest–host) influences their NMR behavior within the interfaces of cages. This proved indirectly that the non-covalent guest–host as well as guest–guest interactions are different when the pollutants are adsorbed in single or mixed state.^[16] Upon increase in the total pressure to 25 mbar (Figure 3.10A, curve c) of the mixture adsorbed on HSZ-Y zeolite, no dramatic change in the spectrum has been observed. Nevertheless, despite similar chemical shifts of ¹H MAS NMR signals, these peaks are characterized by different intensities. The higher pressure used in the adsorption of the mixture of pollutants leads to intense peaks.

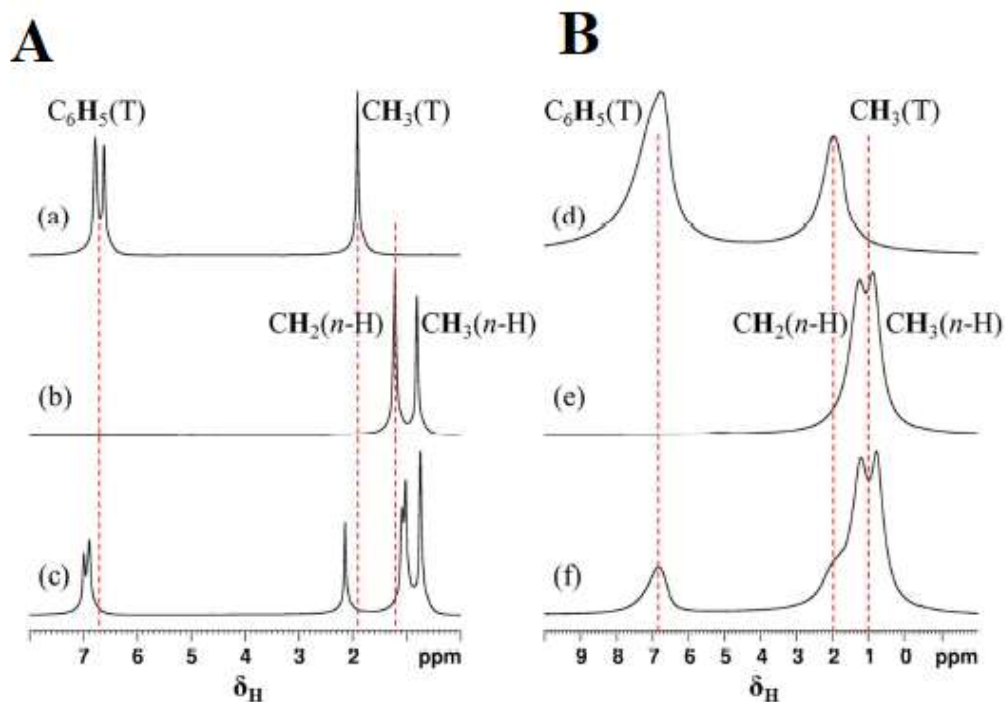


Figure 3.10: ^1H solid state MAS NMR spectra of toluene (a, d), *n*-hexane (b, e) and mixture (c, f) adsorbed at a pressure of 25 mbar on zeolite HSZ-Y (A) and on zeolite ZSM5 (B). The spectra were recorded at r.t. and a MAS rate of 15 kHz was used in all the experiments.

Figure 3.9B curve c shows the ^1H MAS NMR spectrum of a mixture of pollutants (3 mbar) adsorbed on zeolite ZSM-5. Again, for comparison purposes, spectra of single pollutants adsorbed on ZSM-5 under the same conditions are also shown (Figure 3.9B, curve d and e). As reported in (see Chapter I, paragraph 1.3.1.2), the description of SS-NMR spectra related to pollutants singularly adsorbed on the ZSM-5 zeolite has been already reported.^[5] Likewise of HSZ-Y, spectrum of toluene adsorbed singularly on the ZSM-5 (Figure 3.9B, curves d) shows peaks at *ca.* 2 and 7 ppm due to methyl and aromatic protons, respectively. Whereas in the spectrum of *n*-hexane adsorbed singularly on the same zeolite (Figure 3.9B, curves e) shows resonances due to methyl and methylene protons at around 0.8 and 1.2 ppm, respectively. All spectra (Figure 3.9B, curves d-f) are generally characterized by broad resonance lines. The cubic symmetry of the zeolite HSZ-Y offers higher symmetry than ZSM-5. Residual dipolar broadening is almost completely averaged out due to the isotropic motion of molecules inside the cubic symmetry zeolite HSZ-Y. However, ZSM-5 possesses a non-cubic symmetry, and generally, the anisotropy of mobility is expected here, which indeed retains residual dipolar broadening. Similar chemical shifts are observed here for *n*-hexane and toluene as in zeolite HSZ-Y. Resonances due to methyl protons are at 0.71 and 2.2 ppm for *n*-hexane and toluene,

respectively, and are also observed (Figure 3.9B curve f). While methylene protons from *n*-hexane appeared at 1.2 ppm, aromatic protons from toluene are seen at 7.06 ppm.

Increasing the pressure to 25 mbar (Figure 3.10B) of the mixture on ZSM-5 zeolite, the broader resonances further broaden, and no distinguishable peaks for different methylene protons from *n*-hexane were observed.

The change in the chemical shift of the proton sites (when compared with the individual pollutant adsorbed system) is almost absent conversely to what is found for the zeolite HSZ-Y system. Zeolite ZSM-5 is characterized by a network of straight and zigzag intersecting channels. Since toluene and *n*-hexane can be considered non-branched molecules, they can locate either in the channels or at the intersections. Therefore, no change in environment is expected by the pollutant molecules either being in single or mixed state.^[16]

Besides ¹H NMR spectra, also ¹³C CP-MAS spectra were collected. Short CP contact time (1 ms) experiments gave maximum signal intensity for ZSM-5 system, while long values (40 ms) were used for the zeolite HSZ-Y system. In general, short cross-polarization contact time reveals rigid components, while mobile units are exposed with longer CT experiments. The peak assignments are straightforward as shown in Figure 3.11.

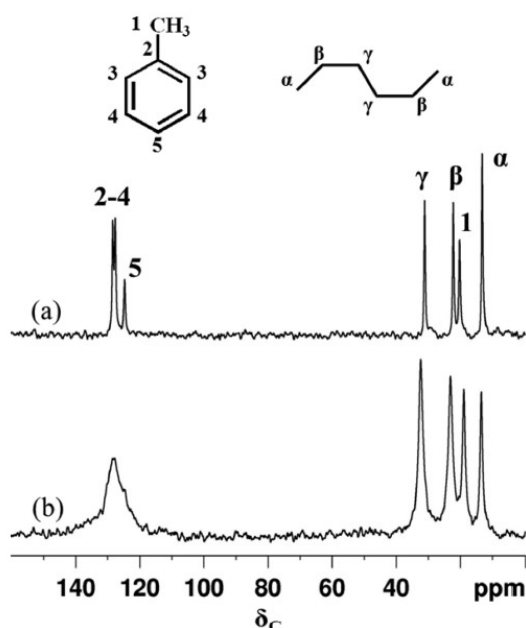


Figure 3.11: ¹³C solid state CPMAS-NMR spectra of mixture of pollutants (at a total pressure of 3 mbar) adsorbed on zeolite HSZ-Y (a) and ZSM-5 (b). A cross-polarization contact time of 40 and 1 ms was used in experiments a and b, respectively.

The main difference between the two spectra is highlighted by the distinction in the line-width of resonance lines. While pollutants adsorbed on ZSM-5 show relatively broad resonances, sharper resonances with narrow line widths are observed in the case of HSZ-Y. It is important to note here that the flipping motion of the aromatic ring is restricted in zeolite ZSM-5 which gives away the preferred adsorption site of toluene. The narrow lines in HSZ-Y indicate an isotropic motion of the pollutant molecules inside the zeolite cages.

These findings are in full agreement with ^1H MAS NMR (Figure 3.9) results, thus confirming that the pore/channel architecture and volume accessibilities play a decisive role in the adsorption and diffusion of pollutant molecules. The presence of large cages in HSZ-Y supports the pollutant adsorption and storage, and restricted channel space in ZSM-5 leads to the surface interaction with pollutants.

SS-NMR measurements of the mixture adsorbed on the HSZ-Y zeolite were also carried out at low temperature (163 K). The major motivation of studying a mixture of pollutant adsorbed systems at low temperature was to slow down the motion of toluene and *n*-hexane to an extent sufficient to enable their investigation by solid state NMR. All of the NMR interactions measured in the solid state are susceptible to modifications by thermal molecular motions and therefore expected to show diverse spectral patterns at different temperatures. In Figure 3.12 is reported the ^1H MAS NMR spectra of pollutant mixtures (at 6 mbar) adsorbed on zeolite HSZ-Y at low temperature (curve b) and r.t. (curve a).

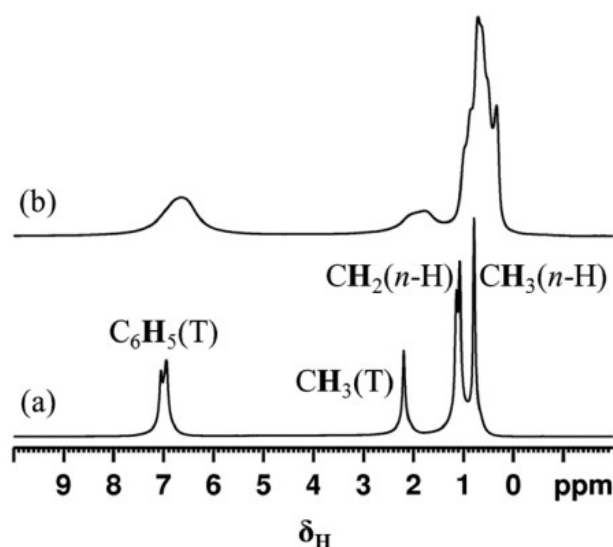


Figure 3.12: ^1H solid state MAS NMR spectra of pollutant mixture (at 6 mbar) adsorbed on zeolite HSZ-Y at r.t. (a) and 163 K (b). The spectra were recorded with a MAS rate of 15 kHz.

The peaks are very broad in the spectrum recorded at 163 K (curve b), and they show multiple lines for CH₃ groups from toluene and *n*-hexane. Broad lines generally result from the superposition of multiple resonances, in addition to the strong homonuclear dipolar interactions. A considerable change in the isotropic chemical shift values at low temperatures was observed as well. The multiple resonances observed for the single CH₃ group in toluene and *n*-hexane at low temperature are attributed to the presence of non-equivalent environment for the methyl moieties. The methyl group conformations are locked in space, revealing specific chemical environments with diverse chemical shifts. At r.t. (curve a), molecules tumble rapidly as well as isotropically leading to an averaged equivalent environment and show narrow sharp lines. At low temperature, a majority of toluene molecules are adsorbed on the surface of zeolite cages leading to various intermolecular interactions which result in broad resonances. It is important to note here that these spectra were recorded well below the toluene freezing point (approximately 178 K).

However, molecules confined in small pores behave differently from the bulk. Therefore, it can be concluded that toluene molecules are in a weakly adsorbed state with a mobility resembling that in the gas phase at r.t. inside the zeolite cages (at 6 mbar), while an adsorbed frozen state can be envisaged at 163 K. However, *n*-hexane behaves as a gas at r.t. inside the zeolite cages, and a partially frozen state but still with mobile methyl units was detected at 163 K. The diverse behavior at 163 K for pollutants with similar freezing point can be supported by the fact that a higher amount of toluene adsorbed will lead to liquefaction and further to freezing, while the low amount of *n*-hexane will probably restrict the eventual freezing inside large cages. On the other hand, the coexistence of multiple components below the freezing point is characteristic of the formation of plastic crystals, a highly disordered solid phase.

The ¹³C CPMAS NMR spectra of pollutant mixtures (at 6 mbar) adsorbed on zeolite HSZ-Y at low and r.t. are shown in Figure 3.13.

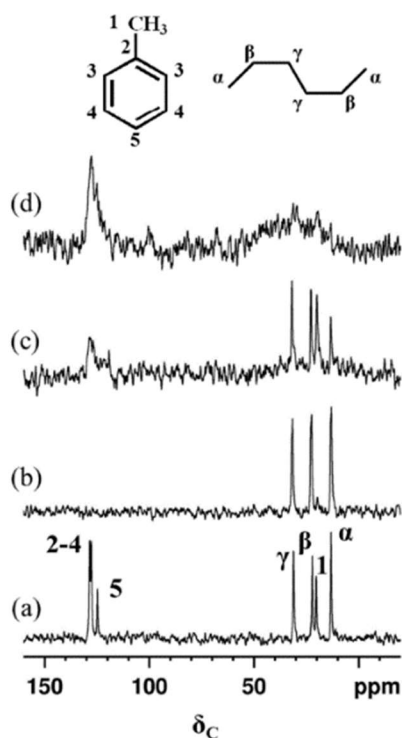


Figure 3.13: ^{13}C solid state CPMAS-NMR spectra of mixture of pollutants (at 6 mbar) adsorbed on zeolite HSZ-Y recorded at r.t. with a contact time of 20ms (a), at 163 K with a contact time of 20 ms (b), 5 ms (c) and 0.2 ms (d).

The spectra recorded with a long cross-polarization contact time of 20 ms show different patterns at r.t. and 163 K. While resonance peaks due to toluene and *n*-hexane are visible in the spectrum recorded at r.t. (Figure 3.13, curve a), only peaks due to *n*-hexane are observed at 163 K (Figure 3.13, curve b). However, peaks due to toluene start to emerge when the crosspolarization contact time was lowered to 5 ms. In this spectrum (Figure 3.13, curve c), resonances due to both molecules are visible albeit broader ones for toluene. Furthermore, the spectrum recorded with very short contact time of 0.2 ms shows only broad aromatic peak (Figure 3.13, curve d). Ring-flipping motions of the aromatic carbons are probably frozen at this temperature. Nevertheless, a very broad peak in the range 10–40 ppm was detected and is due to aliphatic carbons in a very rigid environment. Since the spectra were recorded well below pollutant freezing points, toluene molecules may find themselves in a “frozen” state leading to line broadening.

This is characteristic of the formation of plastic crystals and is attributed to the formation of a highly disordered phase. It is important to note here that the sharper lines due to *n*-hexane carbons are missing in this spectrum. From the ^{13}C CPMAS data recorded at 163 K, it is established that toluene

molecules are rigid due to freezing, while *n*-hexane molecules are partially moving inside the zeolite HSZ-Y cages. This conclusion is in line with the fact that HSZ-Y retains more toluene than *n*-hexane. Unlike FTIR spectroscopy, solid state NMR measurements characterize the entire sample without spatial resolution between various states of matter at equilibrium. At least three distinct environments can be expected in presented samples at room temperature. The first is adsorbed molecules (but still mobile) in the cages or channels surfaces, the second one is gaseous molecules inside the cages or channels, and the third is gaseous molecules outside the cages or channels (bulk). In equilibrium at r.t., there is a fast exchange (compared to NMR time scale) between these 3 states. As the time scale in NMR is long as well as being a slow technique, any processes occurring at frequencies of the multiple order of chemical shift will tend to average. However, resonance peaks are dominated by contributions from major components which in the current case are gaseous toluene and *n*-hexane, present both inside and outside the cages or channels. Since equimolar gaseous mixtures were used for adsorption, the SS NMR spectra shown in this work represent an equimolar ratio between *n*-hexane and toluene.^[16]

It is clear from this work that solid state NMR spectroscopy is a valuable tool in the study of local effects on the adsorption of pollutant molecules in zeolite cages. The main difference between the behaviour of two different zeolite systems can be explained in terms of their pore architecture (topology and dimension) itself and their interaction with and between the adsorbed molecules. While pollutants adsorbed on HSZ-Y show sharper resonances with narrow line widths, relatively broad resonances are observed in the case of ZSM-5. It is presumed that the isotropic reorientation of the molecules in HSZ-Y is much faster, while slow anisotropic motion of the molecules in ZSM-5 leads to a harmony of molecular mobility and MAS which moderates the MAS line narrowing. We demonstrate that the adsorption and storage characteristics of these two zeolites are markedly different. An interesting feature of solid-state NMR is its ability to visualize directly the co-diffusion, adsorption, and storage of several gases in a mixture.^[16]

3.3.3 Determination of the amount of toluene and *n*-hexane adsorbed on HSZ-Y and ZSM-5 zeolites

An estimation of the relative amount of toluene and *n*-hexane adsorbed on both zeolites was obtained by using the molar absorption coefficients (ϵ) of the specific bands of toluene and *n*-hexane singularly adsorbed on both HSZ-Y and ZSM-5 zeolites.

The molar absorption coefficients (ϵ) of toluene (1605 and 1380 cm^{-1}) and *n*-hexane (1380 cm^{-1}) were determined by combining microgravimetric and IR adsorption data on HSZ-Y and ZSM-5 (see

Chapter IV). In particular, these molar absorption coefficients were obtained adapting the Beer-Lambert Law to adsorbent/substrate systems, described in the Chapter IV.

These coefficients were then used for the determination of the molecules uptake when the two zeolites were put in contact with toluene/*n*-hexane mixtures by the following method.

The spectroscopic data related to the adsorption of pollutants on zeolites HSZ-Y and ZSM-5 at controlled pressures of the gas mixture have been used to quantify the toluene and *n*-hexane uptakes. The estimation of concentration of toluene on HSZ-Y zeolite was calculated using the molar extinction coefficient (ϵ) of the 1605 cm^{-1} band related to the C=C stretching mode of toluene ring (see Chapter IV). For *n*-hexane molecule, the uptake was derived using the band related to the bending mode of CH_3 groups at 1380 cm^{-1} : at this frequency the methyl deformation modes of the toluene and *n*-hexane are strongly overlapped, and thus the fraction of *n*-hexane was obtained taking into account the concentration of the toluene determined by using the extinction coefficient of the band at 1605 cm^{-1} (vide infra).

In both zeolites, the concentration of adsorbed toluene (C_{toluene}) defined as [$\mu\text{mol g}^{-1}$] was obtained by using the formula 3.1:

$$C_{\text{toluene}} = \frac{A_{\text{MIX}(1605)}}{\epsilon_{\text{Y_toluene}} \rho} \quad (3.1)$$

where $A_{\text{MIX}(1605)}$ is the integrated area [cm^{-1}] of the band at 1605 cm^{-1} , $\epsilon_{\text{Y_toluene}}$ is the molar absorption coefficient [$\text{cm } \mu\text{mol}^{-1}$] of toluene adsorbed on FAU zeolite and ρ [g cm^{-2}] is the density of the pellet that represents the path length.

For *n*-hexane adsorption, the concentration was derived from the integrated area of the bending mode of CH_3 groups at 1380 cm^{-1} . Nevertheless, it has to be taken into account that the frequency of this bending mode is very close to that of the toluene methyl group and that when a mixture is adsorbed the components related to both molecules are strongly overlapped (i.e. not distinguishable).

Therefore, the *n*-hexane uptake for each zeolite is obtained taking in account also of the contribution of the aromatic molecules present in the mixture. The integrated area of the band at 1380 cm^{-1} ($A_{\text{MIX}(1380)}$) be derived by the following equation 3.2:

$$\begin{aligned}
A_{MIX(1380)} &= A_{TOL(1380)} + A_{n-HEX(1380)} \\
&= \varepsilon_{toluene(1380)} C_{toluene} \rho + \varepsilon_{n-hexane(1380)} C_{n-hexane} \rho \\
&= [\varepsilon_{toluene(1380)} C_{toluene} + \varepsilon_{n-hexane(1380)} C_{n-hexane}] \rho \quad (3.2)
\end{aligned}$$

Where ρ is the density of the pellet, the molar extinction coefficients of both toluene and n -hexane at 1380 cm^{-1} are determined by the adsorption of the single molecules, and $C_{toluene}$ is determined by using the extinction coefficient of the band at 1605 cm^{-1} . Thus, the n -hexane uptake was estimated as indicated below by the equation 3.3:

$$C_{n-hexane} = \frac{\left[\frac{A_{MIX(1380)}}{\rho} \right] - [\varepsilon_{toluene(1380)} C_{toluene}]}{\varepsilon_{n-hexane(1380)}} \quad (3.3)$$

Therefore, the determination of the uptake of each pollutant (toluene and n -hexane) for each value of vapor pressure was calculated by using Equation 3.4:

$$Uptake\% = C_{toluene/n-hexane} \times M_r \times 100 \quad (3.4)$$

Where $C_{toluene/n-hexane}$ is concentration of adsorbed pollutant [mol g^{-1}] calculated from the equations 3.1 and 3.3, and M_r [g mol^{-1}] is the molecular mass of pollutants (92.14 and 86.18 g mol^{-1} for toluene and n -hexane, respectively).

The optical isotherms of toluene and n -hexane uptake vs pressure obtained on both zeolites are reported in Figure 3.14.

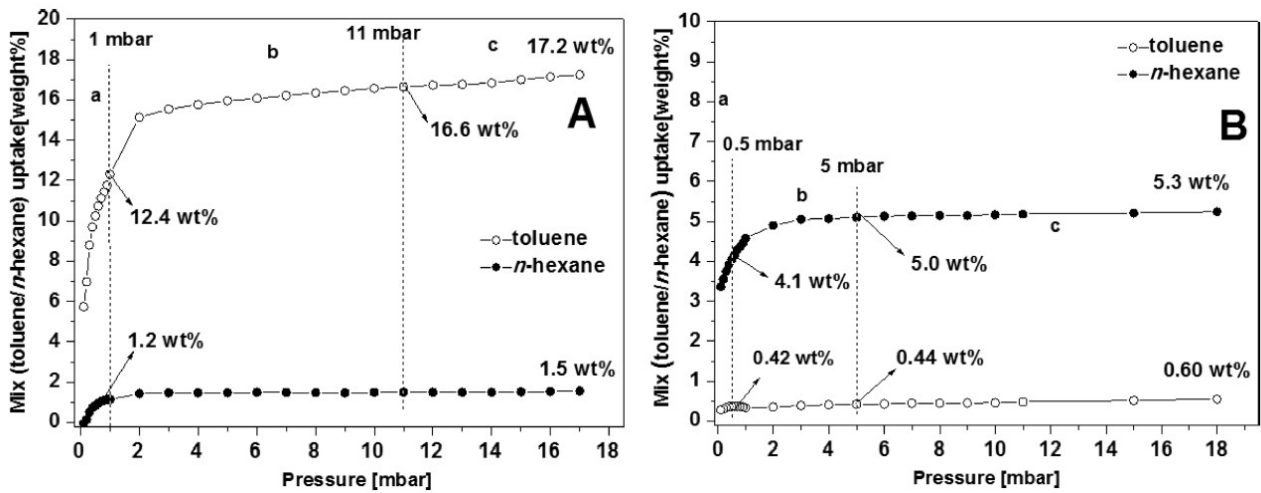


Figure 3.14: Optical isotherms (uptake vs pressure) for toluene and n -hexane derived from IR bands (1605 and 1380 cm^{-1} , respectively) formed upon adsorption as gaseous equimolar mixtures on HSZ-Y (A) and ZSM-5 (B) zeolites.

On HSZ-Y (Figure 3.14A), the uptake of both molecules rapidly increases until *ca.* 1 mbar, and then the slope decreases up to *ca.* 2 mbar when gradually both curves tend to a plateau. At low pressure, the amount of toluene adsorbed on the zeolite HSZ-Y is higher than that of *n*-hexane (15.2 and 1.3 wt %, respectively, at a pressure of 2 mbar). The maximum uptake is 17.2 wt % for toluene and 1.5 wt % for *n*-hexane.

As expected, the maximum uptake of each pollutant when adsorbed from the mixture is lower if compared to the amount of the single contaminant retained on the same support (see Chapter I, paragraph 1.3.1.2)^[5] because of the competition of different molecules for the same adsorption site. In this sense, when the molecules are mixed, toluene is adsorbed preferentially on the HSZ-Y zeolite with respect to *n*-hexane. It has been already observed that the pore diameter of the FAU-type zeolite is sufficiently large, compared with the molecular size of the selected hydrocarbons, and a limited resistance to mass transfer at the pore mouth occurs.^[18, 19] The reasons why HSZ-Y preferentially adsorbs toluene is probably related both to the silanols present at the surface (in large number with respect to ZSM-5 zeolite) which are able to interact through π H-bonding interactions with toluene molecules and to the fact that the architecture of FAU zeolite presents large supercages in which toluene molecules can be easily accommodated. Thus, the molecules of toluene fill the available pore volume of FAU sorbent leaving a reduced space to the *n*-hexane molecules.^[20] This could explain why the *n*-hexane uptake when pollutants are adsorbed in a mixture is extremely reduced compared to the amount of the single pollutant on HSZ-Y support (from 15 to 1.5 wt %).

The ZSM-5 sorbent shows an opposite behavior concerning the molecule uptake after mixture adsorption (Figure 3.14B). In this case, the uptake increases until *ca.* 0.5 mbar for both toluene and *n*-hexane. Then, the slope decreases up to *ca.* 2 mbar when gradually both curves tend to a plateau. The amount of *n*-hexane adsorbed on the zeolite ZSM-5 (Figure 3.14B) is higher than that of toluene (5.0 and 0.44 wt %, respectively, at a pressure of 5 mbar). The maximum uptake is 0.60 wt % of toluene and 5.3 wt % of *n*-hexane. Also, in this case, the co-adsorption of toluene and *n*-hexane as equimolar mixture on the ZSM-5 zeolite is different if compared to the adsorption of the single pollutants: the overall uptake of *n*-hexane from the mixture is reduced passing from 7.3 to 5.3 wt % in comparison to the uptake as a single component (see Chapter I, paragraph 1.3.1.2), and the toluene uptake when adsorbed from a mixture is dramatically reduced to 0.6 wt %, instead of 8.8 wt % when singly adsorbed (see Chapter I, paragraph 1.3.1.2)

However, even if the amount of mixed pollutants adsorbed is considerably lower than the uptake of the contaminants singly retained, ZSM-5 has a higher capacity of adsorption for *n*-hexane than for

toluene. Probably, the diffusion of *n*-hexane is driven by the channel architecture of the zeolite: on MFI zeolites, the *n*-alkanes with short chain length molecules likely have access to both straight and zigzag channel types^[21] and do not allow toluene to arrange at the intersection channel where it is generally favourably adsorbed. In fact, in ZSM-5, only one *n*-hexane molecule fits in the intersection of a channel: in the small pores of MFI, *n*-hexane molecules are stretched along the pore axis and have a better interaction with the zeolite walls than with the faujasite.^[7] It is likely that toluene molecules, when co-adsorbed with *n*-hexane, are not able to get into the straight and zigzag channels of the zeolite where the *n*-hexane molecules accommodate more easily.^[16]

3.4 Conclusions

The co-adsorption of organic molecules from gaseous and/or aqueous mixtures into sorbents is of great relevance from an industrial point of view because this allows one to understand the competition among contaminants for a specific adsorbent. With this aim, this chapter was focused on the adsorption selectivity of HSZ-Y and ZSM-5 zeolites with a specific industrial interest.

For this purpose, the co-adsorption of toluene and *n*-hexane as an equimolar mixture on HSZ-Y and ZSM-5 were performed by FTIR and SSNMR spectroscopies. FTIR spectroscopy allowed to obtain both qualitative and semi-quantitative estimations of the adsorbed pollutants in the case of possible competition among different molecules for the same support and also to have some indications about the affinity of the two zeolites for the specific pollutants, even if present simultaneously. These measurements indicated that *n*-hexane is preferentially adsorbed on ZSM-5 with respect to toluene. The opposite behaviour was found when the mixture was adsorbed on the HSZ-Y sample: in the open pore structure of the zeolite, the retained *n*-alkane shows less steady absorptions, whereas toluene molecules are more interactive with the support. This is probably facilitated by the presence of isolated silanol species able to interact with toluene through O–H··· π interactions.

The determination of optical adsorption isotherms of both molecules co-adsorbed on the zeolites allowed to get the uptakes of each pollutant on supports. The amount of adsorbed toluene and *n*-hexane within each zeolite varies, *n*-hexane is preferentially adsorbed on ZSM-5 with respect to toluene (5.3 wt % of *n*-hexane and 0.60 wt % of toluene) and the opposite behaviour was found when the mixture was adsorbed on the HSZ-Y (17.2 wt% for toluene and 1.5 wt % for *n*-hexane). The topology of MFI zeolite influences the diffusion of *n*-hexane: the aliphatic molecules are able to occupy both linear and zig-zag channel types so that they do not allow toluene to arrange at the intersection channel where molecules are generally favorably adsorbed. In other words, it is likely that toluene diffusion, during co-adsorption, is limited and that the molecules are not able to fill both

the straight and zig-zag channels of the ZSM-5 zeolite where the *n*-hexane molecules are primarily located.

Moreover, SS-NMR spectra are also collected to gain deeper insight on the local environment that the pollutants experience inside the zeolites pores. The main differences between the two different zeolites are in the environment of adsorbed molecules. SS-NMR studies reveal, under the chosen experimental conditions, the hindrance or assistance of toluene and *n*-hexane upon diffusion in zeolite channels and pores. Moreover, it was noticed that, in full agreement with FTIR results, the amount of adsorbed toluene and *n*-hexane within each zeolite varies, thus showing the molecular affinity relative to the two porous systems.

References

- [1] V. B. Cashin, D. S. Eldridge, A. Yu and D. Zhao, *Environ. Sci.: Water Res. Technol.*, 2018, 4, 110-128.
- [2] P. C. Pinheiro, A. L. D.-da-Silva, H. I. S. Nogueira, and T. Trindade, *Eur. J. Inorg. Chem.*, 2018, 3443–3461.
- [3] M. Zeng, I. Echols, P. Wang, S. Lei, J. Luo, B. Peng, L. He, L. Zhang, D. Huang, C. Mejia, L. Wang, M. Sam Mannan, and Z. Chen, *ACS Sustainable Chem. Eng.*, 2018, 6, 3879–3887.
- [4] V. Sacchetto, *Silica Based Materials for Environmental and Energy Applications*, Doctoral thesis, University of Eastern Piedmont, Alessandria, 2017.
- [5] V. Sacchetto, C. Bisio, D. F. Olivas Olivera, G. Paul, G. Gatti, I. Braschi, G. Berlier, M. Cossi, and L. Marchese, *J. Phys. Chem. C*, 2015, 119, 24875–24886.
- [6] Li, S.; Tuan, V. A.; Noble, R. D.; Falconer, J. L, *Environ. Sci. Technol.*, 2003, 37 (10), 4007–4010.
- [7] M. A Anderson, *Environ. Sci. Technol.*, 2000, 34, 4, 725–727.
- [8] V. Sacchetto, G. Gatti, G. Paul, I. Braschi, G. Berlier, M. Cossi, L. Marchese, R. Bagatin, C. Bisio, *Phys. Chem. Chem. Phys.*, 2013, 15, 13275– 13287.
- [9] The International Zeolite Association (IZA), Data Base Zeolites, Data last updated Jul 1, 2007, Available: http://europe.iza-structure.org/IZA-SC/ftc_table.php
- [10] C. Baerlocher, L. B. McCusker and D. H. Olson, *Atlas of zeolite framework types*, Published on behalf of the Structure Commission of the International Zeolite Association by ELSEIVIER Amsterdam - London - New York - Oxford - Paris - Shannon – Tokyo, 2007.
- [11] Meier, W. M. & Olson, D. H. *Atlas of Zeolite Structure Types*, Structure Commission of the International Zeolite Association, Zürich, 1978.
- [12] J. Cejka, H. van Bekkum, A. Corma, F. Schuth, *Zeolite structures, Introduction to the zeolite science and practice*, 3RD Revised Edition/Elsevier Science, Netherlands, 2007.
- [13] J. Weitkamp, *Zeolites and Catalysis, Solid State Ion*, 2000, 131, 175-188.
- [14] I. Braschi, G. Gatti, C. Bisio, G. Berlier, V. Sacchetto, M. Cossi, L. Marchese, *J. Phys. Chem. C*, 2012, 116, 6943–6952.
- [15] N. B. Colthup, L. H. Daly, S. E. Wiberley, *Introduction to Infrared and Raman Spectroscopy*; Academic Press, San Diego CA, 1990.
- [16] V. Sacchetto, D. F. Olivas Olivera, G. Paul, G. Gatti, I. Braschi, L. Marchese, and C. Bisio, *J. Phys. Chem. C*, 2017, 121, 6081–6089.

- [17] M. Fernandez, J. Kärger, D. Freude, A. Pampel, J.M. van Baten, R. Krishna, *Microporous Mesoporous Mater.*, 2007, 105, 124–131.
- [18] M. Fathizadeh, M. Nikazar, *J. Chem. Eng. Jpn.*, 2009, 42 (4), 241–247.
- [19] Y. Fujikata, T. Masuda, H. Ikeda, K. Hashimoto, *Microporous Mesoporous Mater.*, 1998, 21 (4–6), 679–686.
- [20] J. F. Denayer, A. Bouyermaouen, G. V. Baron, *Ind. Eng. Chem. Res.*, 1998, 37 (9), 3691–3698.
- [21] E. E. Romanova, C. B. Krause, A. G. Stepanov, U. Wilczok, W. Schmidt, J. M. van Baten, R. Krishna, A. Pampel, J. Kärger, D. Freude, *Solid State Nucl. Magn. Reson.*, 2008, 33, 65–71.

Chapter IV

*Experimental Determination of the Molar Absorption Coefficient of Toluene and *n*-hexane Adsorbed on Zeolites*

4.1 Introduction

It is already known that FTIR spectroscopy is often used to monitor the adsorption of probe molecules (*i.e.*, carbon monoxide, pyridine, or ammonia) on the surface of materials giving insights into the physico-chemical properties of solids, with special emphasis on surface sites and their role in adsorption/desorption processes.^[1-3] Besides, the intensity of vibrational IR bands expressed as integrated bands of adsorbed molecules can also be determined for a deeper understanding of absorption: the IR band intensity depends on the change of the dipole moment, and therefore, reflects the polarization of the chemical bond, resulting from the vibration.^[4] Thus, the determination of the molar absorption coefficient (ϵ) provides quantitative information about the adsorbed molecules (and indirectly of the adsorbing sites); thereby extending the applications of IR spectroscopy.^[5]

In the literature, there are few examples related to the determination of molar absorption coefficients of molecules (*i.e.*, pyridine, propene, ammonium, water, methanol, alkanes, 1-butanol, 1-pentanol, 1-hexanol, 1-octanol, butanal, and decanal) on different solids.^{[4][6-12]}

As already reported in Chapter I (paragraph 1.3.1.2), the study of toluene and *n*-hexane singularly adsorbed on HSZ-Y and ZSM-5 zeolites have been already reported by our research group.^[13,14] As it was pointed out, in such studies FTIR and microgravimetric analysis have been exploited to monitor the interactions of the model molecule on selected solids.

In the frame of the Ph.D. work, FTIR and microgravimetric data were combined and used for the experimental determination of the molar absorption coefficients of molecules toluene and *n*-hexane adsorbed on microporous solids: the values were obtained by adapting the Beer–Lambert law to adsorbent/substrate systems.^[5,14] To our knowledge, this procedure was applied for the first time to toluene and *n*-hexane adsorbed on microporous systems.

Therefore, FTIR experiments of toluene and *n*-hexane singularly adsorbed on HSZ-Y and ZSM-5 zeolites were thus repeated five times (every time on different pellets of material) and the pellet

surface was calculated by using an accurate image processing software. This with the aim of reducing experimental errors associated with spectroscopic measurements and especially with measurements of the pellet density. And from the microgravimetric experiments of toluene and *n*-hexane singularly adsorbed on HSZ-Y and ZSM-5 was possible to determinate of the uptake of each molecule at specific adsorption vapor pressure and from this the number of adsorbed molecules.

Moreover, experimental determination of the molar absorption coefficients of *n*-hexane adsorbed on HSZ-Y and ZSM-5 were supplemented by theoretical modelling of *n*-hexane molecules embedded in two cluster models of HSZ-Y and ZSM-5 pores: the adduct geometries were optimized at the DFT level with inclusion of long-range nonelectrostatic contributions, and the corresponding harmonic vibrational spectra were simulated.

4.2 Determination of molar absorption coefficient of *n*-hexane adsorbed on HSZ-Y and ZSM-5 zeolites

Figure 4.1A shows the difference IR spectra of *n*-hexane adsorbed on both HSZ-Y and ZSM-5 zeolites at selected pressures (2, 15, and 27 mbar) in the low frequency range between 1550 to 1300 cm^{-1} . This frequency range was preferred due to the fact that the bands are less overlapped compared to those at higher frequency range.

The difference IR spectra reported in Figure 4.1A are obtained by subtracting the spectrum of the bare zeolites outgassed at room temperature (RT), used as a reference, from the spectra of adsorbed *n*-hexane; this allowed the contribution of the solid to be removed from the IR spectra, and therefore, the calculation of integrated absorbances of IR selected bands was simplified.

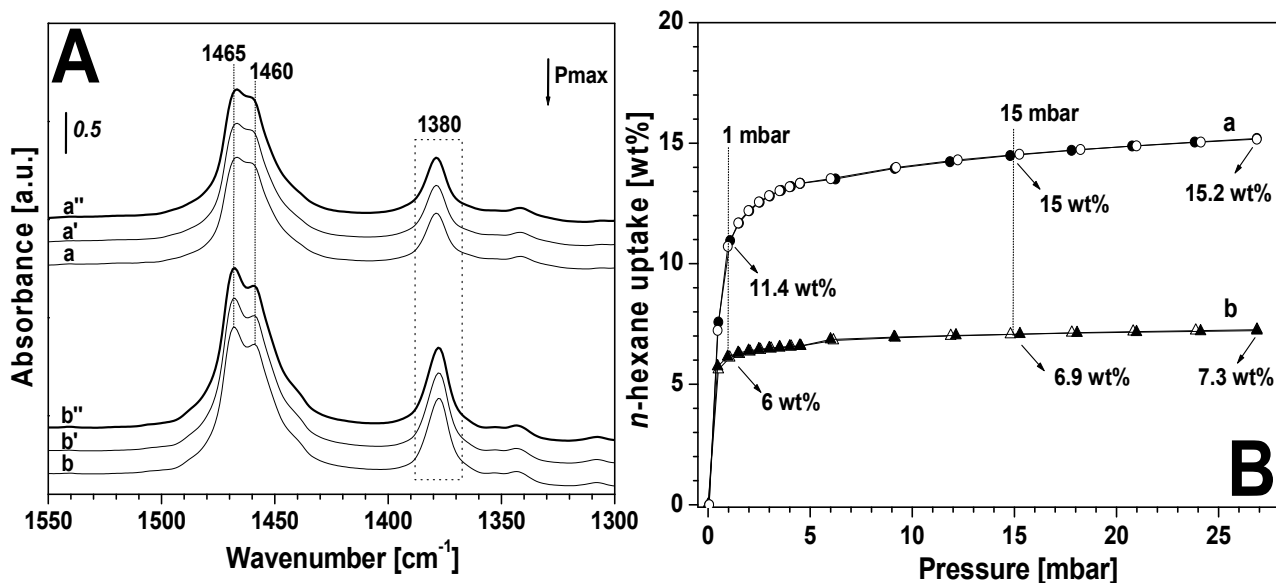


Figure 4.1: A: IR spectra in difference mode (after subtracting the bare solid) of *n*-hexane adsorbed on HSZ-Y (curves a–a'') and ZSM-5 (curves b–b'') materials at pressures of 2 (curves a and b), 15 (curves a' and b'), and 27 mbar (curves a'' and b'') of *n*-hexane. B: *n*-hexane gravimetric adsorption (empty symbols) and desorption (full symbols) isotherms on HSZ-Y (curve a) and ZSM-5 (curve b).

As also detailed in our previous work,^[14] the bands at 1465 and 1460 cm⁻¹ formed upon adsorption of *n*-hexane on HSZ-Y and ZSM-5 zeolites are due to the asymmetric bending modes of CH₃ and CH₂ species, respectively, whereas the band at 1380 cm⁻¹ is related to the symmetric bending mode of CH₃ groups.^[16]

The band at 1380 cm⁻¹ was preferred for determination of the molar absorption coefficient of *n*-hexane adsorbed on both HSZ-Y and ZSM-5 due to the fact that the bands at 1460 and 1465 cm⁻¹ are heavily overlapped.

The uptake of adsorbed species at a specific pressure was determined independently by means of a microgravimetric technique (Figure 4.1B),^[14] see Chapter I (paragraph 1.3.1.2).

The adsorption isotherm of *n*-hexane on HSZ-Y zeolite shows three different adsorption regimes. At pressures lower than 1 mbar, *n*-hexane uptake as a function of the equilibrium pressure is quite steep; thus, suggesting a high affinity of the molecule for the zeolite surface. At 1 mbar, the HSZ-Y retains about 11.4 wt% of *n*-hexane.

Then, the isotherm slope decreases up to 10 mbar, when it gradually comes to a plateau, at which it reaches an uptake of about 15 wt%. The overall uptake of *n*-hexane for ZSM-5 zeolite is lower than that of HSZ-Y zeolite because of the lower SSA and micropore volume. The ZSM-5 isotherm shows

a slope change at 0.45 mbar and then it rapidly becomes a plateau. At pressures lower than 0.45 mbar, the *n*-hexane uptake is 5.5 wt% and the overall adsorption is 7.3 wt%.

The values of molar absorption coefficient for *n*-hexane adsorbed on both zeolites were obtained by combining quantitative gravimetric measurements and IR spectroscopic data. The methodology used for this calculation was already used for other types of molecules on silica systems.^{[17,11][18-21]}

More specifically, to obtain the value of the molar absorption coefficients of specific IR bands of molecules adsorbed on a solid material, the Beer–Lambert law can be rewritten as Equation 4.1:

$$\varepsilon = \frac{A}{N \rho} \quad (4.1)$$

in which ε [cm mmol⁻¹] is the molar absorption coefficient of the adsorbed species; A [cm⁻¹] is the integral absorption of the IR band specifically chosen for the adsorbed molecule, which is calculated by using the OPUS 5.5.4 software; N [mmol g⁻¹] is the concentration of the adsorbed molecules [see below, Eq. 4.3]; and ρ [g cm⁻²] is the density of the pellet of the adsorbent. Indeed, for each experiment, the pellet was weighed, so that the density could be calculated by using Equation 4.2:

$$\rho = \frac{\omega}{S} \quad (4.2)$$

in which ω [g] is the weight and S [cm²] is the pellet surface. The value of S was calculated by using image processing software (ImageJ), which calculated the area of each pellet by correlating the number of pixels of photographs of the pellets to another photograph with pixels of known dimensions. This similar method to determine the area of pellets was used already by Anderson and co-workers.^[7]

As stated above, the integral absorption of the IR band centered at 1380 cm⁻¹ was determined for *n*-hexane adsorbed on both ZSM-5 and HSZ-Y zeolites. The analysis was repeated five times on each zeolite, each time on a different pellet, to reduce experimental errors associated with spectroscopic measurements and especially with measurements of the pellet density.

Microgravimetric experiments allowed the determination of the uptake of *n*-hexane for each value of vapor pressure and from this the number of adsorbed molecules, N [mmol g⁻¹], was calculated by using Equation 4.3:

$$N = \frac{Uptake\%}{M_r} \times 1000 \quad (4.3)$$

in which Uptake% is the weight percentage obtained from each microgravimetric adsorption isotherm and M_r [g mol^{-1}] is the molecular mass of *n*-hexane (86.18 g mol^{-1}).

The average value of the five repeated IR measurements of the integrated area (\bar{A}) at 1380 cm^{-1} and the *n*-hexane uptakes at a determined absolute pressure are reported in Table 4.1.

Table 4.1: *n*-Hexane adsorbed on HSZ-Y and ZSM-5 zeolite. Pressures, integrated areas of the 1380 cm^{-1} band (determined as average of 5 repeated measurements) and uptake of *n*-hexane at increasing pressures (evaluated by microgravimetric measurements).

<i>n</i>-hexane adsorbed on HSZ-Y				<i>n</i>-hexane adsorbed on ZSM-5			
Pressure [mbar]	\bar{A}_{1380} [cm^{-1}]	Uptake		Pressure [mbar]	\bar{A}_{1380} [cm^{-1}]	Uptake	
		[mmol g^{-1}]	[%]			[mmol g^{-1}]	[%]
0.50	0.67	0.84	7.24	0.50	1.74	0.67	5.74
1.00	0.96	1.24	10.72	1.00	1.85	0.71	6.14
2.00	1.12	1.42	12.20	2.00	1.95	0.74	6.39
3.00	1.14	1.49	12.82	3.00	1.96	0.75	6.50
4.00	1.15	1.53	13.19	4.00	1.97	0.76	6.57
4.50	1.16	1.55	13.33	4.50	1.97	0.76	6.59
6.00	1.17	1.57	13.53	6.00	1.98	0.80	6.85
9.20	1.19	1.62	13.99	9.10	2.00	0.81	6.96
12.2	1.21	1.66	14.30	12.1	2.01	0.82	7.02
15.2	1.22	1.69	14.54	15.3	2.02	0.82	7.08
18.2	1.24	1.71	14.74	18.1	2.04	0.83	7.12
24.1	1.28	1.75	15.05	21.0	2.06	0.83	7.16
26.9	1.30	1.76	15.17	26.9	2.09	0.84	7.22

To distinguish the different contributions, the molar absorption coefficients (ϵ) were first estimated over a specific range of pressures, for which the correlation between the Integrated Absorbance of 1380 cm^{-1} band (IA) and the amount of adsorbed molecules [mmol g^{-1}] was linear. These pressure ranges were determined experimentally by comparing the IA values with the concentration of adsorbed *n*-hexane (Figure 4.2 A, B).

Figure 4.2A shows that, in the case of zeolite HSZ-Y, there is a linear trend between IA and *n*-hexane uptake in the range between 2 and 15 mbar *n*-hexane, whereas for ZSM-5 the linear correlation of the abovementioned parameters is from 2 to 12 mbar (Figure 4.2B).

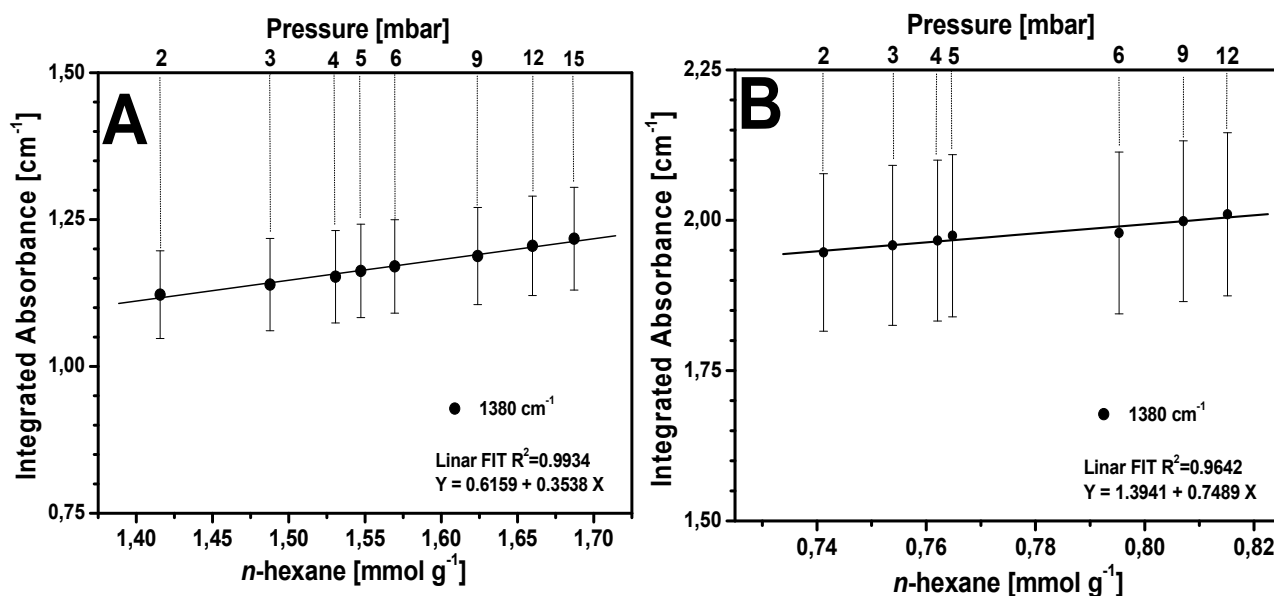


Figure 4.2: Dependence of the integrated absorbance [cm^{-1}] of the band at 1380 cm^{-1} (*i.e.* the IR bending mode of the $-\text{CH}_3$ species of *n*-hexane) versus the amount of *n*-hexane adsorbed on HSZ-Y (A) and ZSM-5 (B).

Linear fitting for both experimental data sets shows high coefficients of correlation (R^2), as reported in Figure 4.2. Error bars have been determined on the basis of repeated experiments (5 repeated IR adsorption experiments for each zeolite). These pressure ranges correspond to the formation of a statistical monolayer on both supports.

Indeed, by applying the linearized BET equation^[22] to the gravimetric isotherms (Figure 4.3), it is possible to derive the range of pressure at which the statistical monolayer of adsorbed molecule is formed; thus defining the range over which adsorption is mainly driven by zeolite/*n*-hexane host-guest interactions. This allows the use of data of the pressure range at which the guest-guest interactions contribute to the overall uptake to be avoided.

The linearized BET equation can be expressed as the following equation 4.4:

$$\frac{1}{V_m \left[\left(\frac{P_0}{P} \right) - 1 \right]} = \frac{1}{V_{Ads1} C} + \frac{C - 1}{V_{Ads1} C} \left(\frac{P}{P_0} \right) \quad (4.4)$$

where V_m is molar volume of *n*-hexane adsorbed on 1 g of material [mL g^{-1}], V_{Ads1} is monolayer volume of *n*-hexane adsorbed on 1 g of material [mL g^{-1}] and C is a constant related to the affinity of *n*-hexane for the surface material. The V_{Ads1} and C constant can be calculated from the slopes and the intercepts of the equation 4.4. V_m obtained from the equation 4.5:

$$V_m = 22.4 \frac{mL}{mmol} \times N \quad (4.5)$$

where the values of N [mmol g⁻¹] are reported in table 4.1.

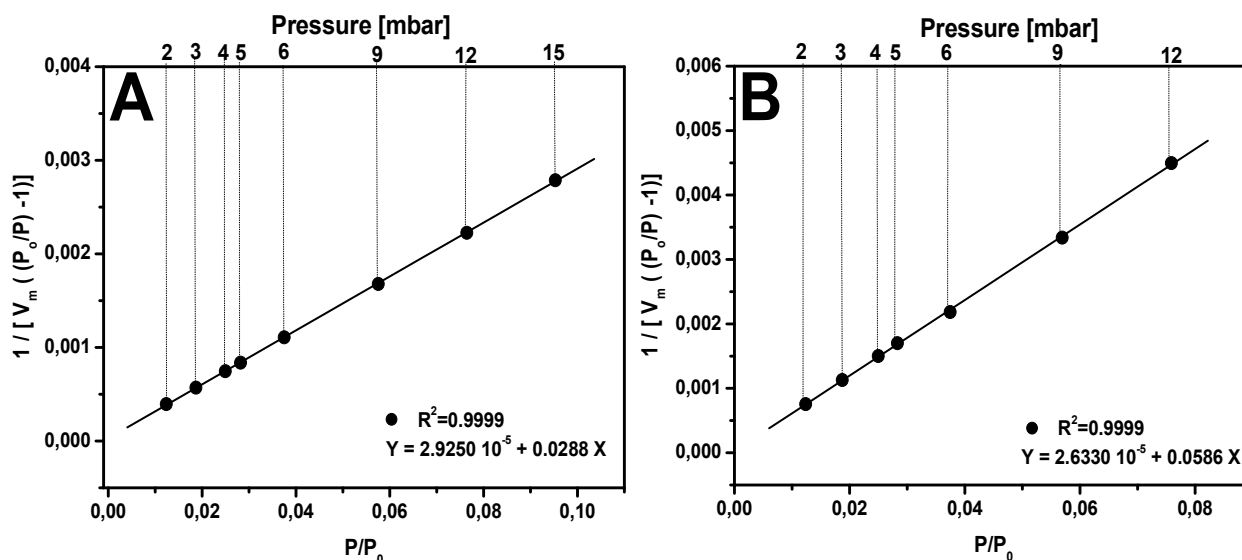


Figure 4.3: Linearized BET plot relative to the gravimetric isotherm of *n*-hexane adsorption on HSZ-Y (A) and ZSM-5 zeolite (B).

The linearized BET equation shows that the monolayer is formed between 2 and 15 mbar for HSZ-Y (Figure 4.3A) and between 2 and 12 mbar for ZSM-5 (Figure 4.3B): very high correlations are derived for both linear curve-fitting procedures.

These ranges are in good agreement with those found by the linear correlation between the experimental absorbance values of the 1380 cm⁻¹ band and the *n*-hexane uptakes (Figure 4.2); thus, indicating that the interactions among *n*-hexane molecules are negligible over the pressure range considered in Figure 4.2, for which monolayers of adsorbed *n*-hexane are essentially formed.

From the BET algorithm, the value of the C constant, which is a measure of the affinity of *n*-hexane for the surface, was also derived and reported in table 4.2.

Table 4.2: Values of C constants of *n*-hexane for the surface of both HSZ-Y and ZSM-5 zeolites and their values of $\Delta H_{(Ads1-Cond)}$ (difference in the heat of adsorption of the first layer and the heat of condensation)

Samples	C	$\Delta H_{(Ads1-Cond)}$ [kJ mol ⁻¹]
HSZ-Y	986	17.66
ZSM-5	2227	19.75

The high value of C of *n*-hexane adsorbed on ZSM-5 indicates that *n*-hexane molecules have greater affinity to MFI framework than that to the FAU structure. These values of C are in full agreement with the results of the co-adsorption of equimolar mixture toluene/*n*-hexane (see Chapter III), where ZSM-5 has a higher affinity of adsorption for *n*-hexane than for toluene and HSZ-Y has the opposite behaviour.

Moreover, the C constant derived from the BET model is related to the difference in heat produced from the formation of the first layer (H_{Ads1}) and of subsequent layers of adsorbed molecules (H_{Cond}).^[23] This relationship can be expressed as the following equation 4.6:

$$C = e^{\left(\frac{H_{Ads1} - H_{Cond}}{RT}\right)} = e^{\left(\frac{\Delta H_{(Ads1-Cond)}}{RT}\right)} \quad (4.6)$$

Where $\Delta H_{(Ads1-Cond)}$ is the difference between the heat of adsorption of the first layer and the heat of condensation [kJ mol⁻¹], R is the universal gas constant [8.314 J mol⁻¹ K⁻¹] and T is the adsorption temperature [K]. La equation 4.7 can be also expressed as:

$$\Delta H_{(Ads1-Cond)} = RT \ln(C) \quad (4.7)$$

Therefore, the large values found for the C constants of both zeolites reflect high adsorption energies, and thus, a large difference between the heat of adsorption of the first layer and the heat of condensation. On this basis, considering the values of C when *n*-hexane is adsorbed on both HSZY and ZSM-5, $\Delta H_{(Ads1-Cond)}$ [kJ mol⁻¹] values were calculated using the equation 4.7 and reported also on Table 4.2.

The calculated value is higher for ZSM-5 with respect to that of HSZ-Y, and this confirms that *n*-hexane interacts more effectively on ZSM-5 than that on Y zeolite, as also derived by the previous results of the co-adsorption of equimolar mixture toluene/*n*-hexane (see Chapter III).^[24]

For *n*-hexane adsorption, a limited P/P_0 range is used because of the interactions that *n*-hexane forms with the two zeolites (host–guest interactions). As also derived from gravimetric isotherms (see Figure 4.1B), the plateau for both supports is reached at low P/P_0 range (*ca.* 0.10 for Y and 0.08 for ZSM-5 zeolite, respectively, corresponding to *ca.* 15 and 12 mbar of *n*-hexane). These data are also in agreement with intervals calculated by the BET method related to the formation of a pseudo-monolayer.

The average values of ϵ of the band at 1380 cm^{-1} , calculated by applying Equation 4.1 over the selected range of pressure for adsorbed *n*-hexane, are as follows on table 4.3

Table 4.3: The average values of ϵ of the band at $\tilde{\nu} = 1380\text{ cm}^{-1}$ of adsorbed *n*-hexane on both HSZ-Y and ZSM-5 zeolites with their standard deviations.

Samples	$\epsilon_{1380} [\text{cm } \mu\text{mol}^{-1}]$
HSZ-Y	0.278 ± 0.018
ZSM-5	0.491 ± 0.032

The experimental error is 6.5% for both zeolites. Interestingly, the calculated molar absorption coefficients are different for the two microporous zeolites and this means that the physico-chemical properties of the different zeolites (in particular, their pore architecture) influence the dipole moment of the adsorbed molecules. The relevance of this result has to be underlined, in that the use of probe molecules for quantitative measurements of surface site has to be judiciously adopted, and the extinction coefficient cannot be used indiscriminately for all systems without an accurate preliminary test study.^[25] This applies especially when adsorption occurs in restricted spaces of microporous solids.

For comparison, the molar absorption coefficient of gaseous *n*-hexane was also determined. Vapours of *n*-hexane were admitted into the IR cell with an optical path length of 10 cm and spectra were recorded at RT over the same range of pressures as those adopted for the adsorption experiments. The integrated absorbance of the band at 1380 cm^{-1} was plotted versus the gas phase concentration, as determined from each pressure measurement and by applying the ideal gas law (see Figure 4.4).^[10]

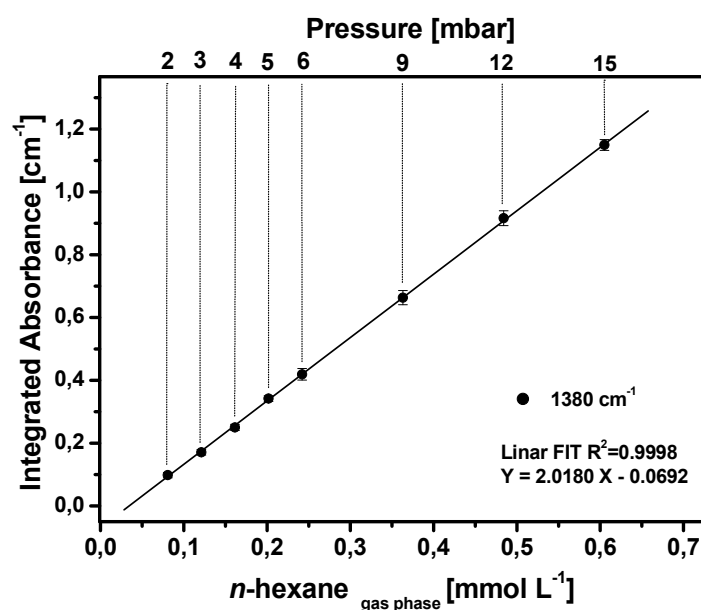


Figure 4.4: Dependence of the integrated absorbance [cm⁻¹] of the band at $\tilde{\nu} = 1380$ cm⁻¹ (i.e. the IR bending mode of the -CH₃ species of *n*-hexane in gas phase) versus the gas phase concentration [mmol L⁻¹].

The average value of the molar absorption coefficient of *n*-hexane in the gas phase was calculated over the range of pressures at which there is a linear trend between IA and gas-phase concentration of *n*-hexane.

The average value of the molar absorption coefficient at 1380 cm⁻¹ of gaseous *n*-hexane (considering six IR experiments) over the range of pressure between 2 and 15 mbar is 0.165 ± 0.005 cm μmol^{-1} . The value is lower with respect to the calculated coefficients of *n*-hexane adsorbed on both zeolites (see table 4.3), especially ZSM-5. This behaviour could also indicate that the interactions of *n*-hexane on ZSM-5 are greater than those on HSZ-Y zeolite, in agreement with our previous work.^[14]

The same approach as that applied above for the determination of the molar absorption coefficient was extended to the entire available pressure range (i.e. from 2 to 27 mbar). As reported by the results in Table 4.4.

Table 4.4: The average values of molar adsorption coefficients (ϵ) at $\tilde{\nu} = 1380$ cm⁻¹ of *n*-hexane on HSZ-Y and ZSM-5 zeolites with their standard deviations.

Sample	ϵ_{1380} [cm μmol^{-1}] <i>n</i> -hexane			
	2 mbar	9 mbar	15 mbar	27 mbar
HSZ-Y	0.298 ± 0.020	0.275 ± 0.019	0.271 ± 0.019	0.279 ± 0.020
ZSM-5	0.504 ± 0.034	0.475 ± 0.032	0.471 ± 0.031	0.479 ± 0.032

Upon adsorption on the HSZ-Y support at 2 mbar, *n*-hexane has a molar absorption coefficient of $0.298 \pm 0.020 \text{ cm } \mu\text{mol}^{-1}$, whereas upon increasing the pressure to 27 mbar the value decreases to $0.279 \pm 0.020 \text{ cm } \mu\text{mol}^{-1}$. Regarding ZSM-5 sorbent, the molar absorption coefficient changes from $0.504 \pm 0.034 \text{ cm } \mu\text{mol}^{-1}$ at 2 mbar to $0.479 \pm 0.032 \text{ cm } \mu\text{mol}^{-1}$ at 27 mbar. The reported data indicate that, due to differences in the textural and structural properties, the overall uptake of *n*-hexane for ZSM-5 zeolite is different from that of the HSZ-Y sample in agreement with our previous work.^[14] This effect is even more evident at low pressures because the molecules interact predominantly with the surface of the zeolites through host–guest interactions and the contribution of guest–guest interactions is reduced. Whereas increasing the pressure from 9 to 27 mbar, the molecules are forced to enter the pores: as a consequence, the system becomes stabilized and the values of molar absorption coefficients do not vary considerably.

4.2.1 Computational DFT study

As anticipated above, some theoretical calculations were performed to support the experimental findings. Two molecule/zeolite adducts were modeled by inserting one *n*-hexane molecule into the HSZ-Y and ZSM-5 cluster models described below and optimizing their geometries at the DFT level with inclusion of the dispersion contributions.

Theoretical calculations were performed with the Gaussian 09 program at the DFT level, with hybrid functional B3LYP,^[26-28] by using the Poples 6-31G(d,p) basis set, including polarization functions on all centers, for light atoms,^[29] and LANL2DZ effective core potentials and basis set for silicon.^[30] The atom–atom pairwise algorithm proposed by Grimme and Schwabe,^[31] and implemented in Gaussian 09 was used to estimate the contribution from dispersion (van der Waals) forces to energies, geometrical structures, and harmonic frequencies and intensities.

The zeolite matrices were simulated by extracting suitable clusters from the database periodic structures. As shown in Figure 4.5, the cluster model of HSZ-Y zeolite was modeled with a single tetragonal cage, whereas the ZSM-5 model reproduced the crossing of straight and sinusoidal channels, which were characteristic of this system. No aluminum atoms were included and all dangling silicon valences were saturated with hydrogen atoms.

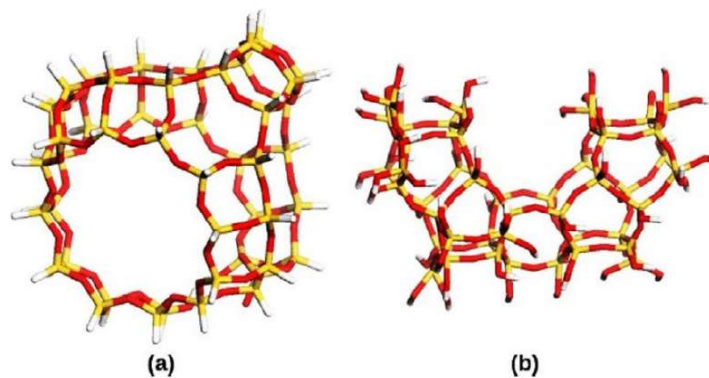


Figure 4.5: Cluster models of HSZ-Y (a) and ZSM-5 (b); hydrogen atoms used to saturate the external valences are not shown.

The optimized structures (molecule/zeolite adducts) are shown in Figure 4.6. As recently revealed by our research work,^[14] the dominant contribution in the *n*-hexane/zeolite interaction comes from dispersion energies, which induce the molecule to stick close to the surface, also undergoing some geometry distortions, especially in ZSM-5.

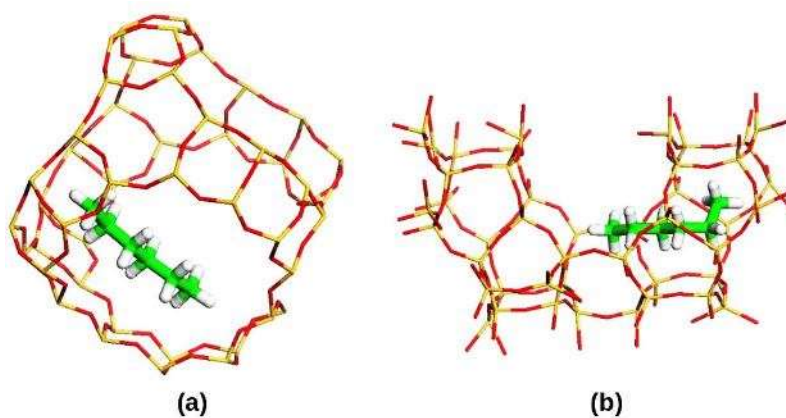


Figure 4.6: Optimized adducts of *n*-hexane in the cluster models of HSZ-Y (a) and ZSM-5 (b); hydrogen atoms used to saturate the external valences are not shown.

The vibrational spectra of *n*-hexane adsorbed on both HSZ-Y and ZSM-5 zeolites were simulated by computing the energy second derivatives by numerical differentiation of gradients in the two adducts: only the *n*-hexane atoms were allowed to move; the zeolite structures were fixed to make the calculations affordable. Because the normal modes of the organic molecule are likely to be well separated from the inorganic matrix, freezing the zeolite atoms is not expected to introduce a significant error into the computed spectra. The computed harmonic spectra are reported in Figure

4.7 (limited to the region of C-C and C-H deformations, $\tilde{\nu} = 1300\text{-}1600\text{ cm}^{-1}$): the vibrational frequencies match well for the two systems, although the intensities are clearly higher for *n*-hexane in ZSM-5 than that in HSZ-Y, in agreement with the experiments described above. The simulated band at 1430 cm^{-1} corresponds to the experimental band at 1380 cm^{-1} , with the expected overestimation in the harmonic spectrum, and it is due mainly to $-\text{CH}_3$ deformations.

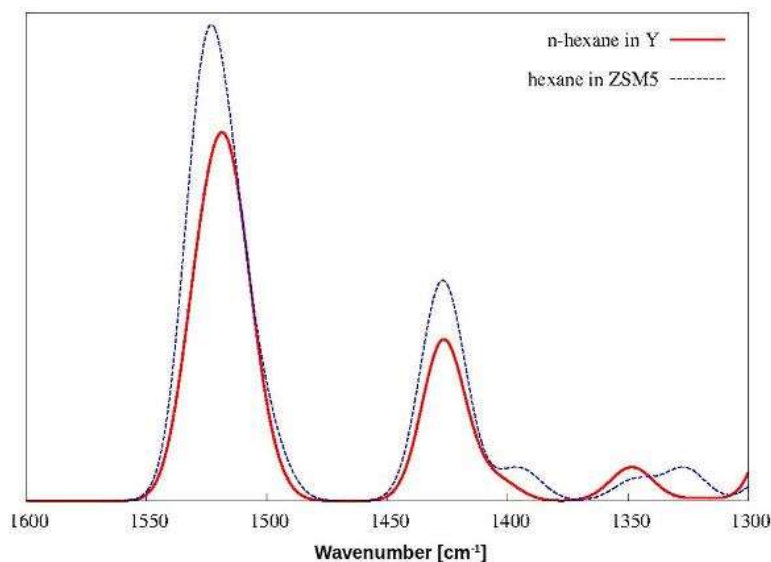


Figure 4.7: Computed harmonic vibrational spectra of *n*-hexane in HSZ-Y and ZSM-5 cluster models in the region of C-C and C-H deformations.

The ratio of the computed band maxima at $\tilde{\nu} = 1430\text{ cm}^{-1}$ in ZSM-5 and in HSZ-Y is 1.37, which should be compared with the experimental value of 1.77 at very low concentration, as derived from the expressions for the average extinction coefficients reported in table 4.4. Clearly, the models optimized herein are just one of many possible structures for the *n*-hexane/zeolite adducts; however, these calculations confirm that the interactions with the zeolite walls can actually modify the IR intensities to an extent comparable to that of the experimental findings, and that *n*-hexane interacts more tightly with the narrower pores of ZSM-5, as already noted in our previous work.^[14]

4.3 Experimental determination of the molar absorption coefficients of adsorbed toluene on HSZ-Y and ZSM-5 zeolites

The adsorption properties of HSZ-Y and ZSM-5 zeolites towards toluene have been already reported by means of both experimental and computational techniques by our research group.^[14] Following these preliminary studies and using the same methodology carried out in the case of *n*-hexane (see paragraph 4.2.1) the molar absorption coefficients of toluene adsorbed on both zeolites were also determined.

The difference IR spectra of toluene adsorbed on dehydrated HSZ-Y and ZSM-5 zeolites at selected pressures (2, 15 and 27 mbar) are reported in Figure 4.8A. As in the case of the molar absorption coefficient of *n*-hexane, to avoid the contribution of absorbances of the materials on the integrated absorbances of the IR selected bands (1605 and 1380 cm^{-1}), the reported difference IR spectra were obtained by subtracting the spectrum of the bare materials outgassed from the spectra of adsorbed toluene.

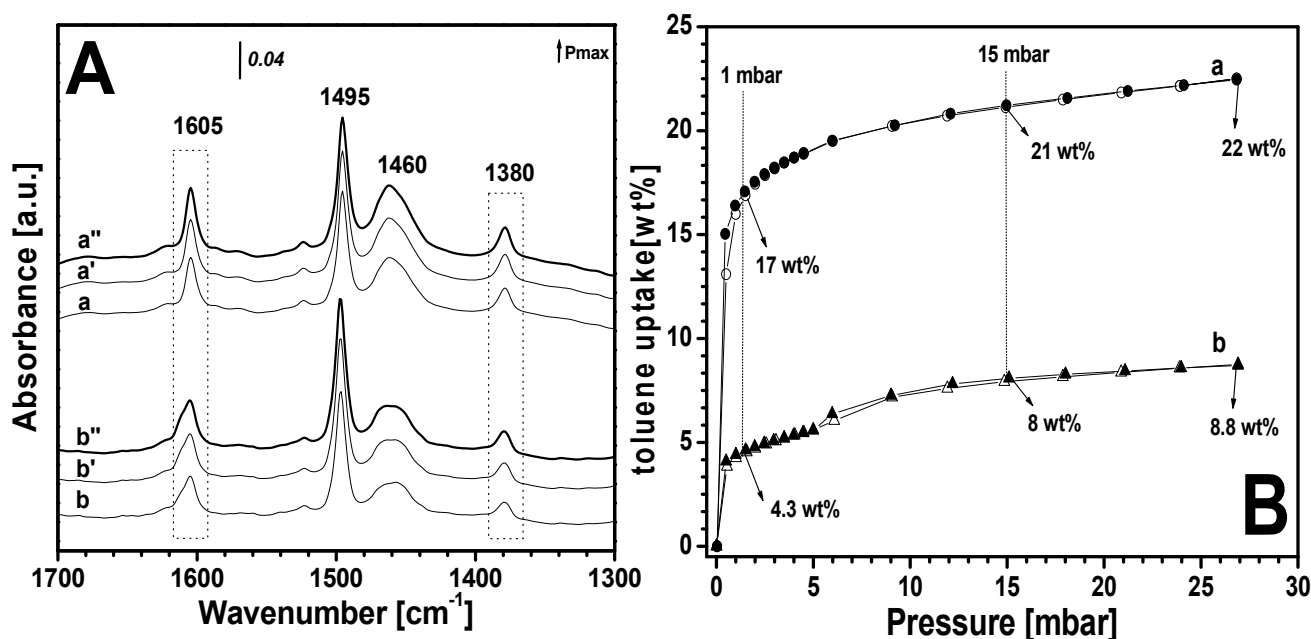


Figure 4.8: A: IR spectra in difference mode (after subtracting the bare solid) of toluene adsorbed on HSZ-Y (curves a–a'') and ZSM-5 (curves b–b'') zeolites at pressures of 2 (curves a and b), 15 (curves a' and b'), and 27 mbar (curves a'' and b'') of toluene. B: toluene adsorption (empty symbols) and desorption (full symbols) isotherms on HSZ-Y (curve a) and ZSM-5 (curve b)

As previously reported, the band at 1605 cm^{-1} is due to the quadrant stretching mode of the monosubstituted ring C=C bond whereas the band at 1495 cm^{-1} is associated with the semicircular

stretching vibration of monosubstituted aromatic ring. The bands at 1460 and 1380 cm^{-1} correspond to the out-of-phase and in-phase deformations of the toluene methyl group.^[14] The single vibrational bands at 1605 and 1380 cm^{-1} were preferred for determination of the molar absorption coefficient of toluene adsorbed on both HSZ-Y and ZSM-5 due to that the bands at 1495 and 1460 cm^{-1} are heavily overlapped.

The concentrations (uptake) of the adsorbed toluene at definite pressure were obtained by means of microgravimetric analysis (Figure 4.8B). The adsorption and desorption isotherms of toluene on both HSZ-Y and ZSM-5 zeolites (Figure 4.8B, curves a and b, respectively) show three regimes of adsorption/desorption. At pressures lower than 1 mbar, the curves are steep thus suggesting the high affinity of the toluene molecules for the zeolites surface. At 1 mbar, the HSZ-Y (Figure 4.8B, curve a) retains ca. 17 wt% of toluene, then the isotherm slope decreases up to 9 mbar when gradually the curve tends to a plateau, at which it reaches an uptake of ca. 22 wt% at 27 mbar. Although the shape of the gravimetric isotherm collected on ZSM-5 is similar to that observed on HSZ-Y, the overall uptake at 27 mbar of toluene for ZSM-5 zeolite is lower than that of HSZ-Y zeolite because of the lower SSA and micropore volume. Indeed, at 1 mbar the zeolite absorbs ca. 4.3 wt % of toluene whereas at 27 mbar the capacity is of 8.8 wt%.^[14]

Moreover, volumetric analyses of toluene adsorbed on has been also performed.

The toluene volumetric adsorption/desorption isotherms (Figure 4.9, curve b) were obtained at 35 °C and at standard temperature pressure (STP) on HSZ-Y silica samples. Prior the adsorption, the samples were outgassed for 30 min at 50 °C, 30 min at 80 °C, 2h at 120°C, 2 h at 220 °C and finally at 12 h at 300 °C under high vacuum conditions (final pressure 7×10^{-4} mbar).

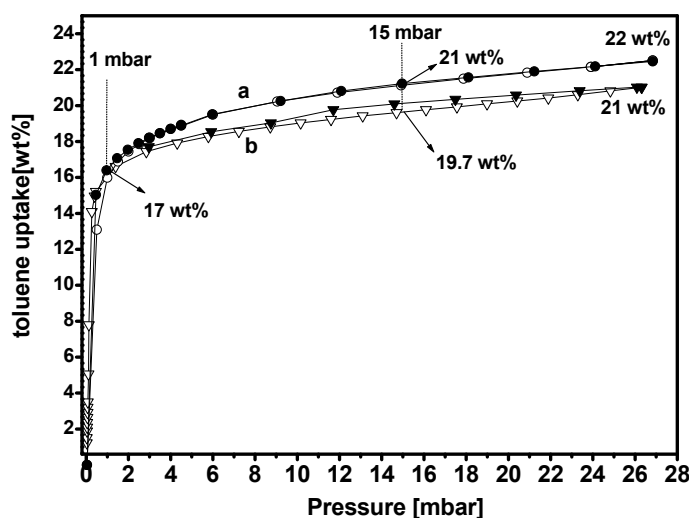


Figure 4.9: Gravimetric (curve a) and volumetric (curve b) of toluene adsorption (empty symbols) and desorption (full symbols) isotherms on HSZ-Y. Before the volumetric analysis, HSZ-Y was outgassed in vacuum conditions at 300 °C for 12 h.

As can be observed from the comparison of the gravimetric (Figure 4.9, curve a) and the volumetric (Figure 4.9, curve b) isotherms of toluene adsorbed on HSZ-Y, both types of quantitative analysis are comparable.

The molar absorption coefficients ε [cm mmol^{-1}] of the specific vibration modes at 1605 and 1380 cm^{-1} of toluene adsorbed on zeolites were determined by using the same methodology used to determine the molar absorption coefficient of *n*-hexane on the same zeolites (see paragraph 4.2). Therefore, the Beer-Lambert law for solids: Equation 4.1 was applied to calculate the value of the molar absorption coefficients of the specific IR bands. As in case of *n*-hexane, the IR analysis was repeated five times on each zeolite, each time on a different pellet, to reduce experimental errors. Each pellet was also weighed for each experiment, so that the density could be also calculated by using the equation 4.2.

Microgravimetric experiments allowed to obtain the number of toluene adsorbed molecules N [mmol g^{-1}] for each value of vapor pressure by using Equation 4.3. In this case of toluene M_r [g mol^{-1}] is the molecular mass of toluene (92.14 g mol^{-1}).

From each IR measurement it was possible to obtain the integrated absorption A [cm^{-1}] of the specific IR bands at 1605 and 1380 cm^{-1} for selected toluene pressure values. Then, for each adsorption band the average value of the integrated area was calculated.

These values are reported in Table 4.5 and are indicated as \bar{A} [cm^{-1}]. In the same table, the uptake of toluene (expressed as mmol g^{-1} and %) derived from microgravimetric isotherms (at selected toluene pressure values) are also reported.

Table 4.5: Toluene adsorbed on HSZ-Y and ZSM-5 zeolites. Pressures, integrated areas of the bands at 1605 and 1380 cm^{-1} (determined as an average of 5 repeated measurements), and uptake of toluene at increasing pressures (evaluated by microgravimetric analysis).

Microporous System										
HSZ-Y					ZSM-5					
P	\bar{A}_{1605}	\bar{A}_{1380}	Uptake		P	\bar{A}_{1605}	\bar{A}_{1380}	Uptake		
[mbar]	$[\text{cm}^{-1}]$	$[\text{cm}^{-1}]$	$[\text{mmol g}^{-1}]$	[%]	[mbar]	$[\text{cm}^{-1}]$	$[\text{cm}^{-1}]$	$[\text{mmol g}^{-1}]$	[%]	
0.50	2.10	1.24	1.63	15.03	0.50	0.80	0.30	0.44	4.09	
1.00	2.61	1.56	1.78	16.40	1.00	0.95	0.44	0.48	4.41	
2.00	3.21	1.88	1.90	17.54	2.00	1.14	0.62	0.52	4.78	
3.00	3.32	1.93	1.98	18.21	3.00	1.19	0.65	0.55	5.07	
4.00	3.40	1.98	2.03	18.70	4.00	1.22	0.68	0.58	5.33	
4.50	3.48	2.01	2.05	18.90	5.00	1.24	0.69	0.61	5.58	
6.00	3.52	2.03	2.12	19.52	6.00	1.26	0.70	0.69	6.37	
9.20	3.59	2.07	2.20	20.26	9.00	1.28	0.72	0.79	7.25	
12.10	3.64	2.10	2.26	20.81	12.20	1.30	0.73	0.85	7.82	
15.00	3.69	2.12	2.30	21.22	15.10	1.32	0.75	0.88	8.08	
18.10	3.76	2.16	2.34	21.57	18.00	1.35	0.77	0.90	8.27	
24.10	3.91	2.23	2.41	22.19	24.00	1.40	0.81	0.93	8.58	
26.80	4.03	2.29	2.44	22.46	26.90	1.41	0.82	0.94	8.70	

The molar absorption coefficients (ϵ) of toluene adsorbed on microporous systems were firstly determined over a specific range of pressures, where the correlation between the integrated absorption of 1605 and 1380 cm^{-1} bands (IA) and the amount of toluene adsorbed molecules $[\text{mmol g}^{-1}]$ is linear. These pressure ranges were determined experimentally by comparing the IA values of 1605 and 1380 cm^{-1} bands (average values) with the concentration of adsorbed toluene on both HSZ-Y and ZSM-5 zeolites (Figure 4.10A, B).

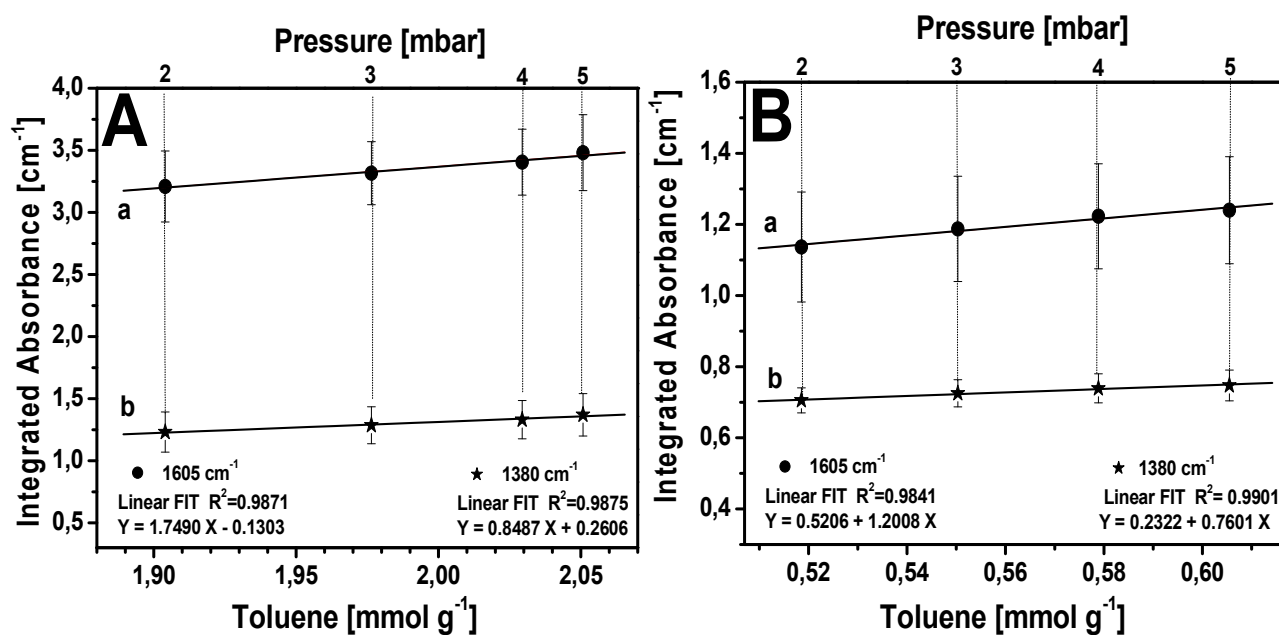


Figure 4.10: Dependence of the integrated absorbance (cm^{-1}) at 1605 cm^{-1} (fits a, *i.e.* the IR stretching mode of the monosubstituted ring C=C bond) and for the band at 1380 cm^{-1} (fits b, *i.e.* the IR in-phase deformations mode of the methyl of toluene) versus the amount of toluene adsorbed on HSZ-Y(A) and ZSM-5 (B).

Linear fitting for each experimental data set shows high coefficients of correlation (R^2), as reported in Figure 4.10. Error bars have been determined on the basis of the five repeated IR adsorption experiments for each zeolite. In Figure 4.10 is shown that for both zeolites that in the range between 2 and 5 mbar there is a linear trend between IA of the bands at 1605 cm^{-1} (fit a) and 1380 cm^{-1} (fit b) and toluene uptake [mmol g^{-1}]. These pressure ranges correspond to the formation of a statistical monolayer of toluene molecules on the two supports.

As in the case of *n*-hexane (see paragraph 4.2), by applying the linearized BET equation^[22] to the gravimetric isotherms reported in Figure 4.8, it was also possible to derive the range of pressure at which adsorption is mainly driven by host–guest interactions (zeolite/toluene). This allows the use of data of the pressure range at which the guest–guest interactions contribute to the overall uptake to be avoided.

The linearized BET equation shows that the monolayer of toluene molecules is formed between 2 and 5 mbar for HZS-Y and ZSM-5 (Fig. 4.11A, B, respectively). High values of the correlation coefficients (R^2) are obtained from linear curve-fitting procedures.

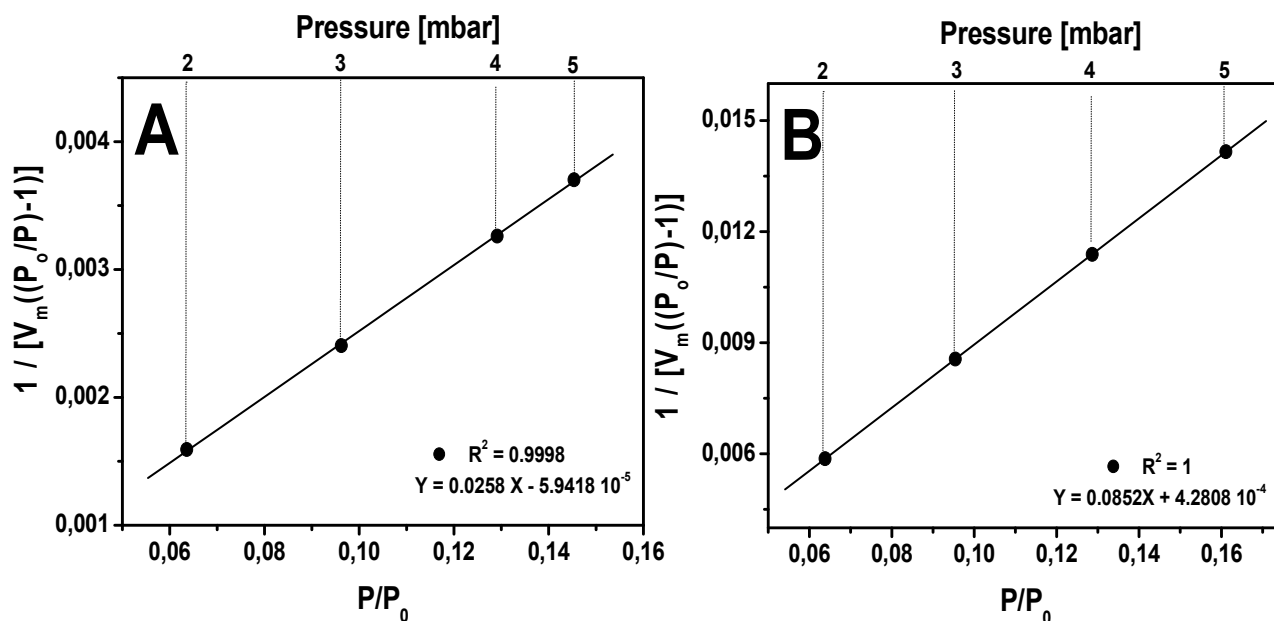


Figure 4.11. Linearized BET plot relative to the gravimetric/volumetric isotherm of toluene adsorption on HSZ-Y (A) and ZSM-5 zeolite (B).

These ranges of pressure are in good agreement with those found by the linear correlation between the values of IA of the bands at 1605 and 1380 cm^{-1} and toluene uptake (Figure 4.10); indicating that over this pressure range, the interactions between toluene molecules are not considered.

From the BET algorithm, the value of the C constant, which is a measure of the affinity of toluene for the surface, was also derived and reported in table 4.6.

Table 4.6: Values of C constants of toluene for the surface of both HSZ-Y and ZSM-5 zeolites; and their values of $\Delta H_{(\text{Ads1-Cond})}$ (difference in the heat of adsorption of the first layer and the heat of condensation)

Samples	C	$\Delta H_{(\text{Ads1-Cond})}$ [kJ mol ⁻¹]
HSZ-Y	429	15.53
ZSM-5	214	13.75

Values of C for HSZ-Y resulted higher than those of ZMS-5: this is an indication of the fact that toluene molecules have greater affinity to FAU framework respect to the MFI structure. These values of C are in full agreement with the results of the co-adsorption of equimolar mixture toluene/*n*-hexane (see Chapter III), where toluene is adsorbed preferentially on the HSZ-Y zeolite with respect to *n*-hexane and ZSM-5 has the opposite behaviour.

As in the case of *n*-hexane (see paragraph 4.2), by considering the values of *C* when toluene is adsorbed on both HSZY and ZSM-5, the difference in the heat of adsorption of the first layer and the heat of condensation $\Delta H_{(\text{Ads1-Cond})}$ [kJ mol⁻¹] were also calculated using the equation 4.7 and reported also on table 4.6.

The $\Delta H_{(\text{Ads1-Cond})}$ for the HSZ-Y is 15.53 kJ mol⁻¹, whereas for toluene adsorbed on ZSM-5 zeolite it corresponds to 13.75 kJmol⁻¹.

The calculated value is higher for HSZ-Y than the value calculated for ZSM-5, and this confirms again that HSZ-Y has high adsorption energies for toluene than ZSM-5 zeolite, as also derived by the previous results of the co-adsorption of equimolar mixture toluene/*n*-hexane (see Chapter III).^[24]

For toluene adsorption, a limited *P/P*₀ range is used because of the interactions that toluene forms with these solids (host–guest interactions). As also derived from gravimetric (see Figure 4.8), the plateau for supports is reached at low *P/P*₀ range ca. 0.14 and 0.16 for HSZ-Y and ZSM-5 zeolites, respectively, corresponding for both zeolites to ca. 5 mbar of toluene adsorbed. These data are also in agreement with intervals calculated by the BET method related to the formation of a pseudo monolayer of zeolites.

The average values of ϵ of the bands at 1605 and 1380 cm⁻¹, calculated by applying Equation 4.1 over the selected range of pressure for adsorbed toluene on solids are reported in Table 4.7.

Table 4.7: The average values of ϵ of the band at $\tilde{\nu} = 1605$ and 1380 cm⁻¹ of toluene adsorbed on supports with their standard deviations and experimental errors percentage.

Samples	ϵ_{1605} [cm μmol^{-1}]	ϵ_{1380} [cm μmol^{-1}]
HSZ-Y	0.224 ± 0.017 (7.6%)	0.130 ± 0.009 (7.1%)
ZSM-5	0.378 ± 0.030 (8.0%)	0.219 ± 0.019 (8.8%)

The calculated molar absorption coefficients of the bands at 1605 and 1380 cm⁻¹ of toluene adsorbed are different for the two microporous zeolites. This suggests that the pore architecture of zeolites influence the dipole moment of the adsorbed toluene in limited spaced of microporous solids, as it was already observed in the case of *n*-hexane.^[25]

Moreover, for comparison, the ϵ of the bands at 1605 and 1380 cm⁻¹ of toluene in gas phase were also determined by following the same methodology used for *n*-hexane (see Paragraph 4.2). For this, vapours of toluene were admitted into the same IR cell and spectra were recorded over the same range

of pressures as those adopted for the adsorption experiments. In Figure 4.12 is reported the plotting of the IA of bands at 1605 and 1380 cm^{-1} versus the gas-phase concentration of toluene, as determined from each pressure measurement and by applying the ideal gas law. [10,25]

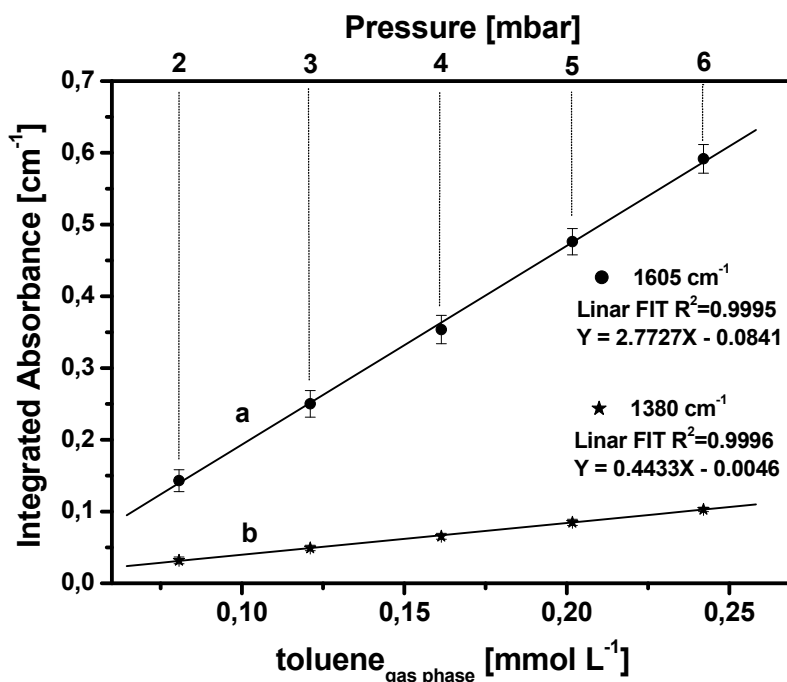


Figure 4.12. Dependence of the integrated absorbance [cm^{-1}] at 1605 cm^{-1} (fit a,) and for the band at 1380 cm^{-1} (fit b,)

The average value of the molar absorption coefficient of toluene in the gas phase was then calculated over the range of pressures at which there is a linear trend between IA and gas-phase concentration of toluene. The average value of the molar absorption coefficients of the bands at 1605 and 1380 cm^{-1} of gaseous toluene (considering six IR experiments) over the range of pressure between 2 and 6 mbar are 0.217 ± 0.012 and $0.041 \pm 0.003 \text{ cm } \mu\text{mol}^{-1}$ with 5.7 and 7 % of experimental error, respectively.

These values are slightly similar to the calculated coefficients of toluene adsorbed on HSZ-Y (see table 4.7): this suggests that at low coverages of toluene, the dipole moment of the adsorbed toluene is not influenced by the HSZ-Y cages. This behaviour also indicates that the interactions of toluene on HSZ-Y at low pressures are fairly weak interactions (van der Waals contributions), in agreement with our previous work. [14,25]

Whereas these values are lower than those calculated for ZSM-5 (see Table 4.7): this suggests that at low coverages of toluene, the dipole moment of the adsorbed toluene is influenced by the limited space of ZSM-5 channels.

The same approach as that applied above for the determination of the molar absorption coefficients in a specific range of pressure was also used to the full available pressure range (*i.e.* from 2 to 27 mbar) and as reported in Table 4.8.

Table 4.8. Molar Adsorption coefficients ϵ_i of the bands at $\tilde{\nu} = 1605$ and 1380 cm^{-1} of toluene on HSZ-Y and ZSM-5 zeolites.

Samples	$\epsilon_{1605} [\text{cm } \mu\text{mol}^{-1}] \text{ toluene}$			
	2 mbar	9 mbar	15 mbar	27 mbar
HSZ-Y	0.224±0.020	0.217±0.020	0.213±0.020	0.220±0.020
ZSM-5	0.412±0.056	0.305±0.038	0.282±0.034	0.281±0.036
Samples	$\epsilon_{1380} [\text{cm } \mu\text{mol}^{-1}] \text{ toluene}$			
	2 mbar	9 mbar	15 mbar	27 mbar
HSZ-Y	0.131±0.011	0.125±0.011	0.122±0.011	0.124±0.010
ZSM-5	0.226±0.020	0.172±0.018	0.160±0.017	0.162±0.017

Upon adsorption on the HSZ-Y support at 2 mbar, toluene has molar absorption coefficients of the bands at 1605 and 1380 cm^{-1} of 0.224 ± 0.020 and $0.131 \pm 0.011 \text{ cm } \mu\text{mol}^{-1}$; whereas increasing the pressure to 27 mbar the values continue slightly constant to 0.220 ± 0.020 and $0.124 \pm 0.010 \text{ cm } \mu\text{mol}^{-1}$. Regarding ZSM-5, the molar absorption coefficients of toluene change from 0.412 ± 0.056 and $0.226 \pm 0.020 \text{ cm } \mu\text{mol}^{-1}$ at 2 mbar to 0.281 ± 0.036 and $0.162 \pm 0.017 \text{ cm } \mu\text{mol}^{-1}$ at 27 mbar.

The different behaviours of the molar absorption coefficients of adsorbed toluene on both zeolites are probably due to their differences of the textural properties, as also observed for *n*-hexane adsorbed on the same zeolites (see paragraph 4.2). This effect is even more evident on ZSM-5 on which molar absorption coefficients at low pressures resulted affected because the molecules interact predominantly with the surface of ZSM-5 through host–guest interactions and the contribution of guest-guest interactions is reduced. Only increasing the pressure from 9 to 27 mbar and increasing the molecules inside the pores, the system becomes stabilized due the toluene-toluene interactions (guest-guest interactions) and the values of molar absorption coefficients keep constant.^[32]

4.4 Conclusions

The determination of the molar absorption coefficient (ϵ) can provide quantitative information about the adsorbed molecules thus spreading IR spectroscopy applications.

According to this, this chapter was focused on the description of the determination of the molar absorption coefficient of *n*-hexane and toluene adsorbed on microporous systems with different pore structure.

The molar absorption coefficients of *n*-hexane and toluene adsorbed on HSZ-Y and ZSM-5 zeolites were obtained by combining IR spectroscopy and microgravimetric analysis.

The microgravimetric measurements were used to evaluate the amount of adsorbed toluene and *n*-hexane at different specific pressures, whereas the optical absorbance of the specific band could be estimated through FTIR spectroscopy.

The coupling of the obtained data allowed to apply the Beer–Lambert law for the determination of the molar absorption coefficients (ϵ) of selected IR bands that are formed after adsorption of toluene and *n*-hexane singularly on the two microporous systems.

Notably, the experimental data indicated that the molecule experienced a different adsorption environment inside the solids; thus, resulting in very different values of the molar absorption coefficient of *n*-hexane and toluene adsorbed.

Indeed, the ϵ_{1380} of *n*-hexane values is $0.278 \pm 0.018 \text{ cm } \mu\text{mol}^{-1}$ for HSZ-Y and $0.491 \pm 0.032 \text{ cm } \mu\text{mol}^{-1}$ for ZSM-5. The difference on the calculated values means that the pore architecture property of the HSZ-Y and ZSM-5 zeolites affects the dipole moment of the adsorbed molecules.

These experimental data of *n*-hexane adsorbed microporous were also supported by computational modelling, which confirmed the effect of the different matrices on the IR absorption intensity.

Moreover, as observed in the case of *n*-hexane, the limited space of microporous solids also influences on the dipole moment of the adsorbed toluene, resulting different values of ϵ_{1605} and ϵ_{1380} of toluene: 0.224 ± 0.017 and $0.130 \pm 0.009 \text{ cm } \mu\text{mol}^{-1}$ for HSZ-Y whereas 0.378 ± 0.030 and $0.219 \pm 0.019 \text{ cm } \mu\text{mol}^{-1}$ for ZSM-5, respectively. Nevertheless, the established molar absorption coefficients for adsorbed toluene and *n*-hexane can be safely used for the quantitative determination of these molecules when they are adsorbed in a mixture of contaminants on similar supports; thus, providing a basis for environmentally relevant issues.

The values of the ϵ_{1605} and ϵ_{1380} of the gaseous phase of toluene and the value of ϵ_{1380} of the gaseous phase of *n*-hexane were also determined, in order to compare them with those when molecules are adsorbed. The value of ϵ_{1380} of the gaseous phase of *n*-hexane is $0.165 \pm 0.005 \text{ cm } \mu\text{mol}^{-1}$ which was

lower with respect to the calculated coefficients of *n*-hexane adsorbed on both zeolites, especially much lower than that calculated on ZSM-5. This behavior indicated that the interactions of *n*-hexane on ZSM-5 are greater than those on HSZ-Y zeolite.

Besides, the ϵ_{1605} and ϵ_{1380} of the gaseous phase of toluene are 0.217 ± 0.012 and 0.041 ± 0.003 cm μmol^{-1} , respectively. These values are slightly similar to the calculated coefficients of toluene adsorbed on HSZ-Y, this suggested the dipole moment of the adsorbed toluene (at low pressures) is not influenced by the HSZ-Y cages and the interactions of toluene on HSZ-Y are fairly weak interactions (van der Waals contributions). Whereas the values of ϵ_{1605} and ϵ_{1380} of the gaseous phase of toluene are lower than those calculated of toluene adsorbed on ZSM-5, this suggests that at low coverages of toluene, the dipole moment of the adsorbed toluene is influenced by the limited space of ZSM-5 channels.

References

- [1] T. Barzetti, E. Selli, D. Moscotti, L. Forni, *J. Chem. Soc. Faraday Trans.*, 1996, 92, 1401–1407.
- [2] H. H. Kung, *Transition Metal Oxides: Surface Chemistry and Catalysis*, Vol. 45, Elsevier, Dordrecht, 1991, p. 67.
- [3] I. S. Pieta, M. Ishaq, R. P. K. Wells, J. A. Anderson, *Appl. Catal. A*, 2010, 390, 127–134.
- [4] I. R. Subbotina, V. B. Kazansky, F. C. Jentoft, R. Schlegel, *Stud. Surf. Sci. Catal.*, 2008, 174, 849–852.
- [5] A. J. McCue, G. A. Mutch, A. I. McNab, S. Campbell, J. A. Anderson, *Catal. Today*, 2016, 259, 19–26.
- [6] C. A. Emeis, *J. Catal.*, 1993, 141, 347–354.
- [7] P. Bazin, A. Alenda, F. Thibault-Starzyk, *Dalton Trans.*, 2010, 39, 8432–8436.
- [8] A. I. McNab, T. Heinze, A. J. McCue, D. Dionisi, J. A. Anderson, *Spectrochim. Acta Part A*, 2017, 181, 65–72.
- [9] I. R. Subbotina, V. B. Kazansky, J. Krçhnert, F. C. Jentoft, *J. Phys. Chem. A*, 2009, 113, 839–844.
- [10] C. Sievers, A. Onda, R. Olindo, J. A. Lercher, *J. Phys. Chem. C*, 2007, 111, 5454–5464.
- [11] F. C. Jentoft, J. Krçhnert, I. R. Subbotina, V. B. Kazansky, *J. Phys. Chem. C*, 2013, 117, 5873–5881.
- [12] C. Morterra, G. Magnacca, V. Bolis, *Catal. Today*, 2001, 70, 43–58.
- [13] V. Sacchetto, *Silica Based Materials for Environmental and Energy Applications*, Doctoral thesis, University of Eastern Piedmont, Alessandria, 2017.
- [14] V. Sacchetto, C. Bisio, D. F. Olivas Olivera, G. Paul, G. Gatti, I. Braschi, G. Berlier, M. Cossi, and Leonardo Marchese, *J. Phys. Chem. C.*, 2015, 119, 24875–24886.
- [15] M. Che and J. C. Vedrine (Eds.), *Characterization of Solid Materials and Heterogeneous Catalysts: From Structure to Surface Reactivity*, Wiley-VCH, Weinheim, Vol. 1-2, 2012, p. 69.
- [16] N. B. Colthup, L. H. Daly, S. E. Wiberley, *Introduction to Infrared and Raman Spectroscopy*; Academic Press, San Diego CA, 1990.
- [17] E. Borello, A. Zecchina, C. Morterra, *J. Phys. Chem.*, 1967, 71, 2938–2945.
- [18] E. Baumgarten, R. Wagner, C. Lenters, C. Z. Wagner', *Anal. Chem.*, 1989, 335, 375–381.
- [19] C. Tan, J. F. Ni, *J. Chem. Eng. Data*, 1997, 42, 342–345.
- [20] O. Bortnovsky, Z. Melichar, Z. Sobal&k, B. Wichterlov, *Microporous Mesoporous Mater.* 2001, 42, 97–102.

- [21] K. L. Konan, C. Peyratout, A. Smith, J.-P. Bonnet, P. Magnoux, P. Ayrault, *J. Colloid Interface Sci.*, 2012, 382, 17–21.
- [22] S. Lowell, J. E. Shields, M. A. Thomas, M. Thommes, *Characterization of Porous Solids in Powders: Surface Area, Pore Size and Density*, Kluwer, Dordrecht, 2004.
- [23] K. D. Hammond, Jr., Wm. C. Conner, *Advances in Catalysis*, Vol. 56, Academic Press, San Diego, 2013, pp. 1–101
- [24] V. Sacchetto, D. F. Olivas Olivera, G. Paul, G. Gatti, I. Braschi, L. Marchese, and C. Bisio, *J. Phys. Chem. C*, 2017, 121, 6081–6089
- [25] G. Gatti, D. F. Olivas Olivera, V. Sacchetto, M. Cossi, Ilaria Braschi, L. Marchese, and C. Bisio, *ChemPhysChem*, 2017, 18, 2374 – 2380
- [26] A. D. Becke, *Phys. Rev. A*, 1988, 38, 3098–3105.
- [27] C. Lee, W. Yang, R. G. Parr, *Phys. Rev. B*, 1988, 37, 785–791.
- [28] D. Becke, *J. Chem. Phys.*, 1993, 98, 1372–1377.
- [29] P. C. Hariharan, J. A. Pople, *Theor. Chim. Acta*, 1973, 28, 213–222.
- [30] P. J. Hay, W. R. Wadt, *J. Chem. Phys.* 1985, 82, 270–279.
- [31] T. Schwabe, S. Grimme, *Phys. Chem. Chem. Phys.* 2006, 8, 4398–4401.
- [32] M. Choluż and W. Bartkowiak, *Chemical Physics Letters*, 2016, 663, 84-89

Chapter V

Silica-based Materials as Adsorbents for Groundwater Depollution

5.1 Introduction

Part of the research activities carried out during this Ph.D. work was focused to the study of the adsorption capacity of mesoporous silicas materials for groundwater depollution.

Special attention was devoted to mesoporous silica with different porosity, in particular two types of mesoporous silicas with irregular porosity (one from commercial origin the other one prepared in laboratory) and two ordered mesoporous silica with ordered arrays of pores.

Commercial FUMED silica, amorphous mesoporous silicas (AMSs) belonging to MSA family and two ordered mesoporous silicas (SBA-15 and MCM-41) were selected and characterized to be tested as sorbents for toluene adsorption (see Figure 5.1). Preliminary studies of *n*-hexane adsorption on the same supports have shown that this molecule is not significantly adsorbed on these materials.

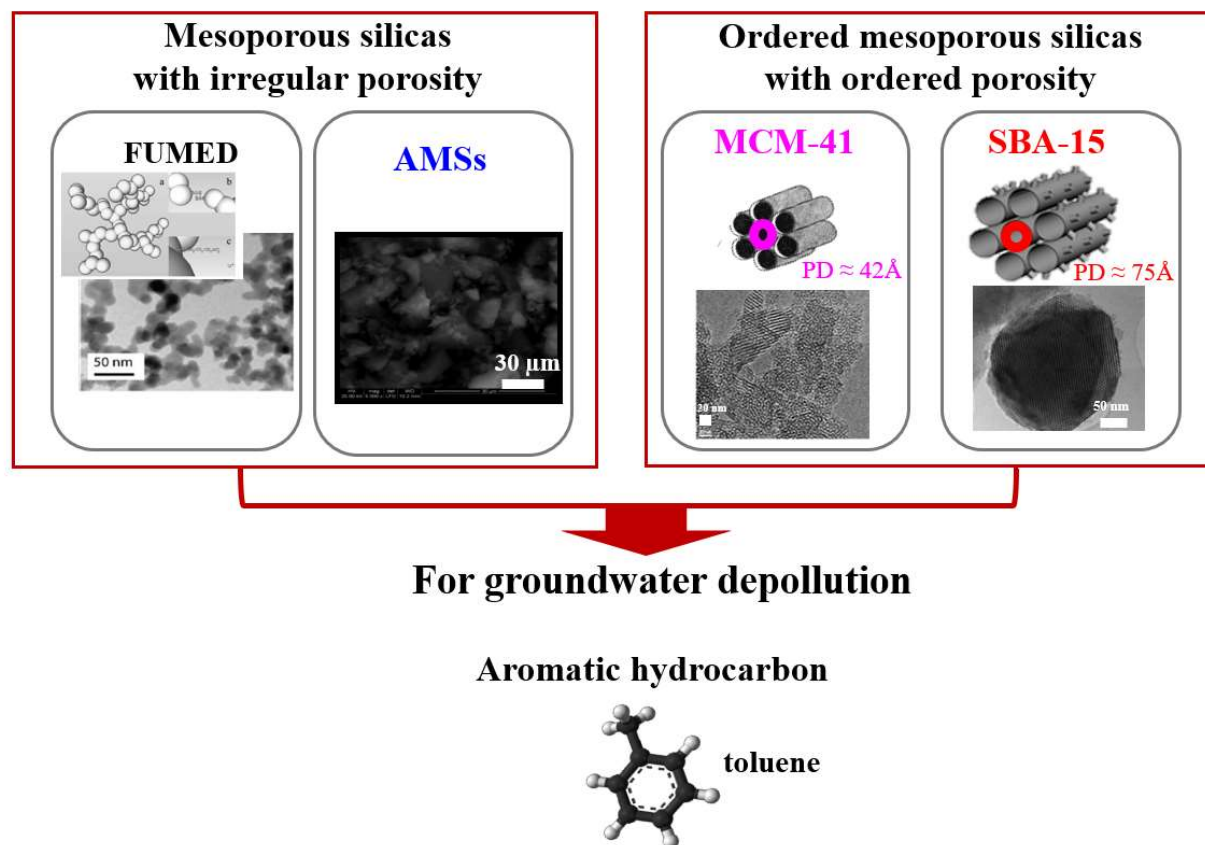


Figure 5.1: Solids investigated for the adsorption of toluene

Amorphous mesoporous silica (AMS) belonging to the mesoporous silica aluminas materials (MSA) family have been prepared by Eni S.p.A. Indeed, researchers from Eni S.p.A have successfully developed these amorphous mesoporous silicas whose interesting features can be exploited for adsorption purposes.^[1,2]

The selected silica samples have been studied through different experimental techniques such as N₂ adsorption, TGA, FTIR and SS-NMR spectroscopy in order to determine their physico-chemical properties. The capacity of toluene adsorption of these solid, together with the type and strength of the host-guest interactions between the molecules and the silica surface, has been studied by FTIR and volumetric analysis.

In particular, toluene adsorption volumetric analyses have been performed during a period of internship at the laboratories of the Department of Environmental and Chemical Engineering at the University of Calabria in Italy under the supervision of Prof. Giovanni Golemme.

Another aspect that was considered is the hydrothermal stability which is an important concern for researchers. This aspect is important because adsorbents are normally soaked in water during the adsorption of pollutants and in most cases thermal regeneration is required. For this, during my Ph.D. work, particular attention was given to the determination of the hydrothermal stability of the AMSs samples, since these kinds of materials are considered innovative with good performance for hydrocarbons removals.^[3]

The hydrothermal stability of the samples was studied by means of different experimental techniques and the overall toluene sorption capacity of hydrothermally treated mesoporous silicas was then tested and compared with those of fresh samples.

5.2 Amorphous silicas with non regular porosity

5.2.1 Fumed silica

Fumed silica is normally obtained by using a pyrolysis method in which SiCl₄ reacts with O₂ in a flame, and the SiO₂ seed grows in size or aggregates. Indeed, the morphology of the flame made silica nanoparticles in the aerosol consist of agglomerates, aggregates, and primary particles which determine the specific surface area(SSA).^[4] The SSA of Fumed can be varied over a large range between 50–500 m² g⁻¹ depending on the synthesis conditions as the temperature in the flame, the

flame length, the flow turbulence and velocity and the ratio of reactants.^[5] Aggregations are formed when the primary particles form larger, tightly bound tenth micrometer aggregates from which flake-like tertiary structures (agglomerates) arise on cooling. (5 to 30 nm, e.g. FUMED Aerosil).^[6,7] Fumed Aerosil 380 used in this work is from commercial origin (purchased from Evonik Industries, CAS Number 112945-52-5).

5.2.1.1 Physico-chemical characterization of fumed silica

FUMED Aerosil 380 has been studied using a multidisciplinary approach including scanning electron microscope (SEM), N₂ physisorption at liquid nitrogen temperature (77K) in the pressure range of 1.00×10^{-4} mbar to 1009 mbar (1 mbar = 100 Pa) using an Autosorb-1-MP (Quantachrome Instruments), FTIR spectroscopy and thermogravimetric analysis.

The morphology of FUMED Aerosil 380 was investigated by using scanning electron microscopy (SEM) and its images are reported in Figure 5.2.

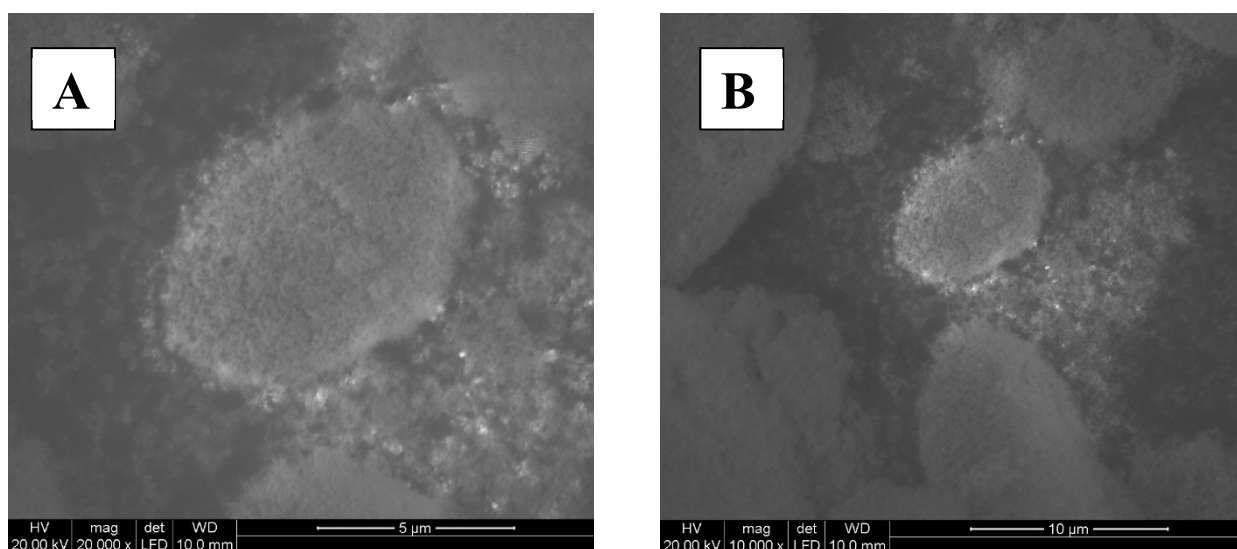


Figure 5.2: SEM micrographs of FUMED silica sample.

The SEM images of FUMED silica showed particles (see Fig. 5.2A) which dimensions vary from at 8–10 nm and agglomerates (see Fig. 5.2A) of larger diameters between 7-11 μm.

Specific surface area and pore size distribution of FUMED silica sample was determined by N₂ adsorption-desorption isotherms at 77K.

Prior to the adsorption, the sample was outgassed for 2 h at 80°C, 1 h at 140°C, 1 h at 180°C and finally at 10 h at 220°C under high-vacuum conditions (final pressure 7×10^{-4} mbar).

The specific area of the samples was determined by the Brunauer–Emmett–Teller (BET) equation in the range 0.1-0.25 p/p_0 of relative pressure. The pore size distribution was calculated by applying the cylindrical pore NLDFT kernel in the desorption branch isotherms.

In Figure 5.3 A,B the isotherm and pore size distribution of FUMED silica is reported.

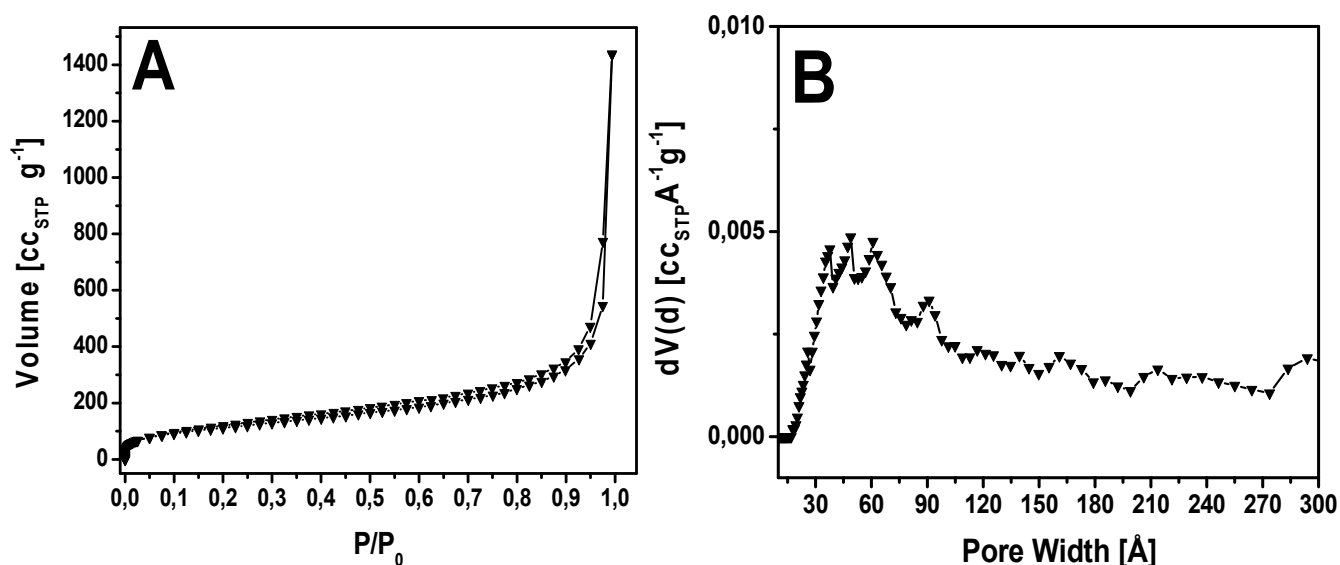


Figure 5.3: N₂ adsorption/desorption isotherms at 77K °C (A) and relative pore size distribution (B) of FUMED sample.

FUMED silica isotherm (Figure 5.3A) is of Type II following the IUPAC classification and present a hysteresis loop of H3 type.^[5,8] The narrow hysteresis loop suggests the presence of two kind of aggregation (*i.e.*, primary particles and smaller secondary particles).^[5] In fact, at low pressures of p/p_0 is possible to notice the completion of monolayer coverage, due the presence of porosity with small diameter given by aggregation of plate-like particles.^[9]

The textural properties of FUMED is reported in Table 5.1.

Table 5.1: Main Textural Properties of FUMED silica sample

Sample	SSA _{BET} ^a [m ² g ⁻¹]	V _T ^b [cm ³ g ⁻¹]	V _{<50 Å} ^c [cm ³ g ⁻¹]	V _{20-300 Å} ^d [cm ³ g ⁻¹]
FUMED	412	1.47	0.10	0.57

^aBrunauer–Emmet–Teller (BET) specific surface area (SSA); ^bTotal pore volume by NLDFT method; ^cVolume of mesopores NLDFT method.

From table 5.1, it can be derived that FUMED silica has a SSA of $412 \text{ m}^2 \text{ g}^{-1}$ with a total pore volume of $1.47 \text{ cm}^3 \text{ g}^{-1}$. The sample presents a heterogenous pore size distribution (Figure 5.3B) with pores in the range from 20 to 300 \AA and mesopores fraction of $0.57 \text{ cm}^3 \text{ g}^{-1}$.

For the sake of brevity, a short overview of the chemical composition (types of silanols species) of silica-based material is given in the Appendix I.

Surface properties of FUMED sample was studied by IR spectroscopy (Figure 5.4). The spectrum of FUMED was recorded after dehydration under vacuum at beam temperature (b.t.) for 30 minutes in order to remove water molecules from the samples surface.

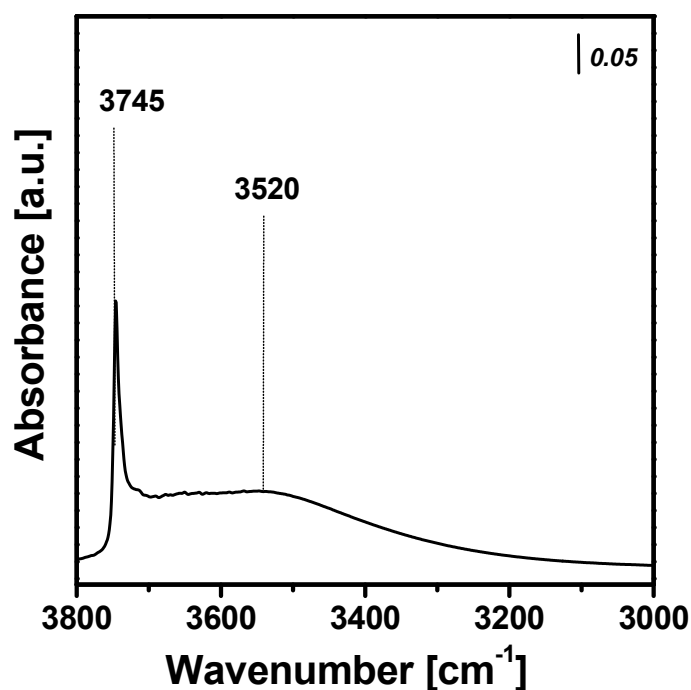


Figure 5.4: FTIR spectrum of amorphous mesoporous silica samples FUMED. The spectrum was recorded after outgassing the samples for 30 minutes at beam temperature (b.t.).

The IR spectrum of FUMED sample presents an evident narrow peak at *ca.* 3745 cm^{-1} that can be assigned to isolated silanols and a broad absorption extending from $3720\text{--}3200 \text{ cm}^{-1}$ with a maximum around at 3520 cm^{-1} that corresponds to hydrogen-bonded silanols.^[10,11]

Thermogravimetric analysis was also performed in order to quantify the amount of surface silanols, by considering the weight loss within the range $150\text{--}1100 \text{ }^\circ\text{C}$ and by following the equation given in Appendix II. The weight loss in the range $150\text{--}1000 \text{ }^\circ\text{C}$ of FUMED sample due to the condensation of silanols was approximately 1.82 wt%. From this, and the data of Table 5.1, the amount of silanol species of fumed silicas is normalized to 3.08 OH/nm^2 .

5.2.1.2 Toluene adsorption on FUMED silica

To investigate the interactions occurring between toluene and silica samples surface, IR spectroscopy analysis and volumetric measurements were performed.

The IR spectra collected after the adsorption of 30 mbar of toluene, and subsequent gradual decrease of pressure on FUMED silica are reported in Figure 5.5 together with the volumetric isotherms of toluene adsorbed on the same sample.

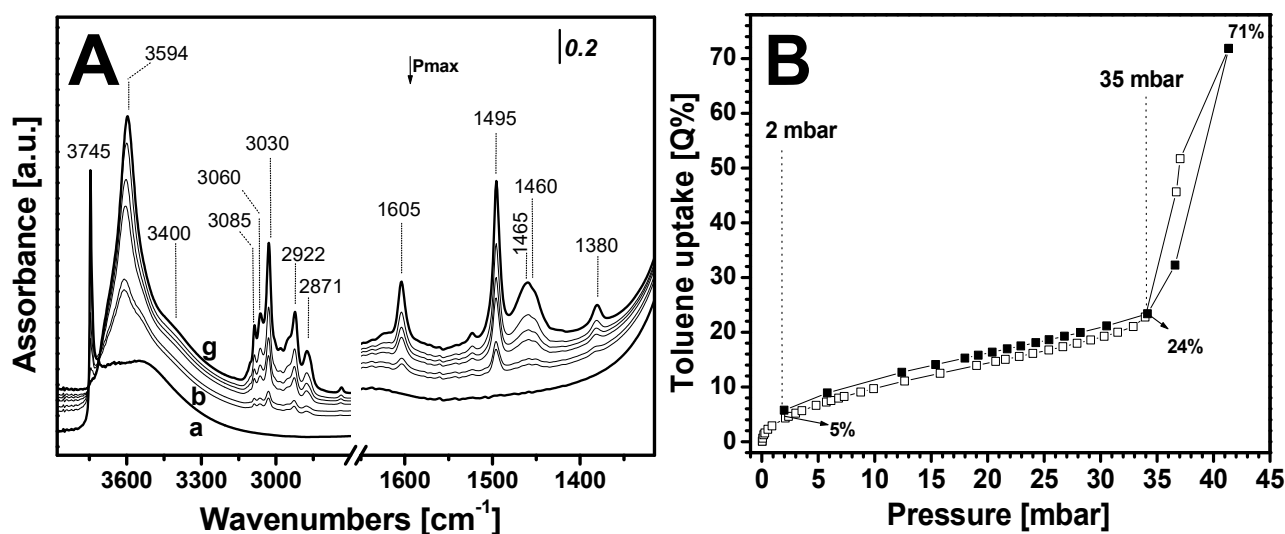


Figure 5.5: A FTIR spectra of toluene adsorbed at r.t. on FUMED sample. Spectrum a was recorded after outgassing the sample for 30 minutes at beam temperature (b.t.) before toluene adsorption; the spectra from g to b were collected during the progressive outgassing of toluene (30-0.1 mbar). B: Toluene volumetric adsorption (empty symbols) and desorption (full symbols) isotherms obtained at 35 °C on FUMED sample. Before the volumetric analysis, FUMED silica sample was outgassed in vacuum conditions at 220 °C for 12 h.

The IR adsorption experiments were carried out starting from high toluene pressure, however, for the sake of clarity, in the following text the IR spectra are described starting from low toluene pressure to high loading. It is evident from Figure 5.5A that the adsorption of small toluene doses from 0.1 to 4 mbar on FUMED (Figure 5.5A, curves b-e) led to the partial disappearance of the band related to isolated SiOH species at 3745 cm⁻¹ and to the consequent formation of a band at ca. 3594 cm⁻¹.

This behavior has been already observed in the case of toluene adsorption on dealuminated zeolites^[12]: the band at 3594 cm⁻¹ is due to the interaction of isolated silanols present on the silica surface with the aromatic ring of the toluene molecules (*i.e.*, O–H··· π interactions), the associated $\Delta\nu$ OH being ca. 150 cm⁻¹. The IR spectra of FUMED upon contact with toluene also show a broad

band with a maximum at ca. 3400 cm^{-1} , more evident at pressure higher than 15 mbar. This band is probable due to the interactions of toluene with the hydrogen-bonded silanol species present on the surface of FUMED.^[12]

Upon toluene admission, several absorptions are formed: the bands at 3085 , 3060 and 3030 cm^{-1} are related to C-H stretching modes of the toluene aromatic ring, whereas the signals at 2922 and 2871 cm^{-1} can be assigned to C-H stretching modes of the toluene methyl groups. The sharp signal at 1605 cm^{-1} is due to the quadrant stretching mode of the mono-substituted ring C=C bond whereas the band at 1495 cm^{-1} is associated to the semicircular stretching vibration of mono-substituted aromatic ring. Finally, the bands at 1460 and 1380 cm^{-1} correspond to the out-of-phase and in-phase deformations of the methyl group.^[12,13]

Increasing the toluene amount (till 30mbar, Figure 5.5, curve g), it is also possible to observe a slight increase of the intensity of the bands related to the toluene molecules. This indicates that the adsorption is likely driven by van der Waals interactions between the silica walls and the toluene molecules (host-guest interactions) and among toluene molecules (guest-guest interactions).

The toluene volumetric adsorption/desorption isotherms (Figure 5.5B) were obtained at $35\text{ }^{\circ}\text{C}$ and at standard temperature pressure (STP) on FUMED silica samples. Prior the adsorption, the samples were outgassed for 30 min at $50\text{ }^{\circ}\text{C}$, 30 min at $80\text{ }^{\circ}\text{C}$, 2h at 120°C , 2 h at $150\text{ }^{\circ}\text{C}$ and finally at 12 h at $220\text{ }^{\circ}\text{C}$ under high vacuum conditions (final pressure 7×10^{-4} mbar).

The volumetric isotherm of FUMED silica (Figure 5.5B) present a narrow hysteresis loop at high toluene pressure related to condensation in porosities given by the aggregation of the particles.

Three regimes can be observed on the isotherm (Figure 5.5B). The isotherm is indeed steep till 2 mbar and then the slope decreases up to ca.35 mbar when the slop increases again. The isotherms curves do not reach a plateau, thus suggesting that the pore saturation does not occur.

The uptake at 2 mbar is ca. 5 Q% (where Q represents the ratio between the amount adsorbed toluene (in mg) respect to 100 mg of solid sample). In the second regime of adsorption (between 2 and 35 mbar) the toluene uptake increases till 24 Q%. The third regimen at higher pressures of 35 mbar where the maximum of uptake is 71 Q%. This behaviour could be associated with the filling of heterogeneous porosity between 20-300 Å given by aggregation of plate-like particles (see pore size distribution on Figure 5.3B).^[9]

5.2.2 MSA-type silicas

In this Ph.D. work, two amorphous mesoporous silica (hereafter AMS) materials belonging to the amorphous mesoporous silica aluminas materials (named MSA) were selected as adsorbents for toluene adsorptions. The two samples were prepared by modifying the synthesis method of amorphous mesoporous silica-aluminas (MSA).^[14]

5.2.2.1 Preparation and physico-chemical characterization of amorphous mesoporous silicas (AMS)

The AMS materials were synthesized by^[2,15] using $\text{Si}(\text{OC}_2\text{H}_5)_4$ (TEOS, Dynasil-A, Nobel), tetrapropylammonium hydroxide (TPAOH, Sachem), 1-propanol (Sigma-Aldrich), via sol-gel synthesis in alkali-free medium, involving alkoxide hydrolysis and condensation, catalyzed by a proper basic organic gelling agent (TPAOH).

In a solution containing 280 g of 11.16 wt% TPAOH and 415.4 g of 1-propanol, a second solution of 360 g of TEOS and 415.4 g of 1-propanol was added at room temperature to get the molar gel composition of 1 TEOS:0.09 TPAOH:8 1-propanol :8 H_2O .

A monophasic clear solution was obtained then transformed in homogeneous opalescent gel without separation of phases. After 15 h of aging, the gel was dried under vacuum at 80°C for 24h, then in air at 120 °C for 48h.

Half of the gel was directly calcined at 550°C for 8 h. This first obtained material was named AMS-LSA due to its lower specific surface area (see below) whereas the rest of the gel was submitted to a further treatment in a boiling ethanol (1000 mL) for 2 h followed by room temperature water washing. The treatment was repeated twice, then the sample was calcined at 550°C for 8 h. This material showed higher specific surface area (see below) and was named AMS-HSA.

The two AMSs (AMS-HSA and AMS-LSA) have been studied using a multidisciplinary approach including scanning electron microscope (SEM), FTIR spectroscopy, solid state NMR, thermogravimetric analysis and nitrogen physisorption at 77K.

The morphology of AMS-HSA was investigated by using scanning electron microscopy (SEM) and its images are reported in Figure 5.6.

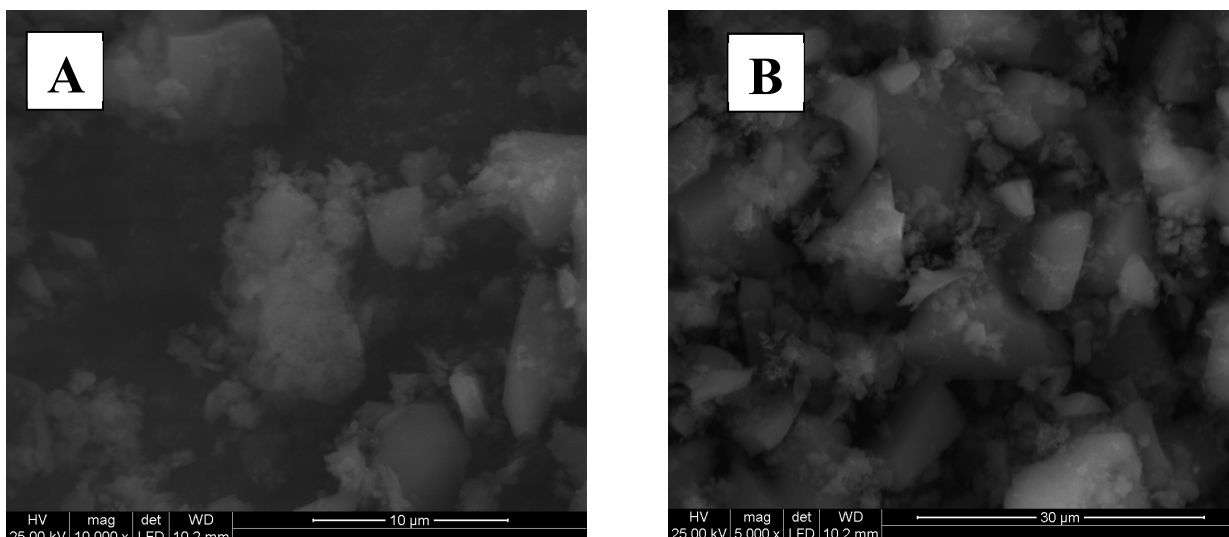


Figure 5.6: SEM micrographs of AMS-HSA silica sample.

The SEM images of AMS-HSA (Fig. 5.6A and B) showed polygonal particles with micrometric size with particle size between of 7-17 μm .

The specific surface area (SSA) of AMS samples were measured by means of N_2 adsorption-desorption isotherms at 77K to obtain information about textural properties.

Prior to adsorption, the samples were outgassed for 2 h at 80°C, 1 h at 140°C, 1 h at 180°C and finally at 10 h at 220°C under high-vacuum conditions (final pressure 7×10^{-4} mbar). In Figure 5.5 A,B are reported the isotherm and pore size distribution of both AMS samples.

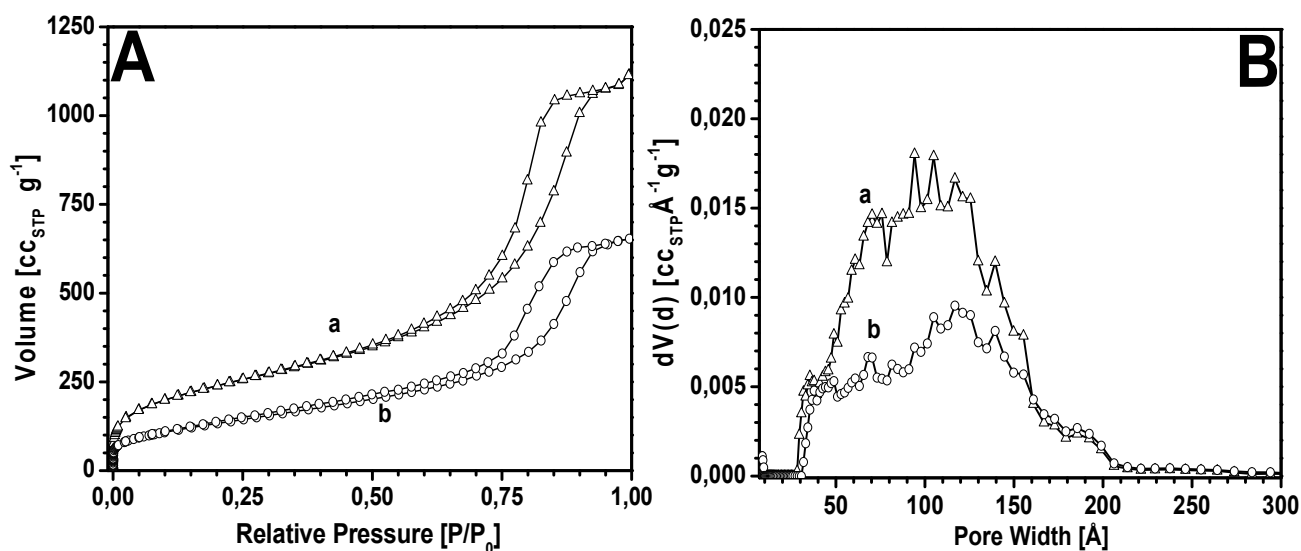


Figure 5.7: N_2 adsorption/desorption isotherms at 77K °C (A) and relative pore size distribution (B) of AMS-HSA (a) and AMS-LSA (b).

The N₂ adsorption isotherms of both porous materials (Figure 5.7A, curves a and b) are of type IVa following the IUPAC classification, thus indicating the presence of mesopores^[8]

The hysteresis loops are formed in the range 0.72-0.94 p/p_0 and can be classified as H2(b) types, following the extended IUPAC Technical Report of 2015, thus suggesting that adsorbents have large neck pores mainly generated by aggregation between the silica particles.^[8,16] At relative pressure below 0.72 p/p_0 in the desorption branch, the hysteresis is not completely closed (more evident for AMS-LSA sample): this behaviour suggests the presence of a fraction of small mesopores. Indeed, as evidenced by pore size distribution (Figure 5.7B), the samples have a heterogeneous pore size distribution between 30 to 200 Å. Moreover, a significant decrease of the volume for pores ranging from 50 to 150 Å is visible for the AMS-LSA sample (Figure 5.7B).

The textural properties of the AMS samples are reported in Table 5.2, where they are compared with those of FUMED silica. The AMS-HSA sample has higher specific surface area (SSA) and total pore volume than the AMS-LSA and FUMED samples.

Table 5.2: Main Textural Properties of AMS-LSA and AMS-HSA samples

Sample	SSA _{BET} ^a [m ² g ⁻¹]	V _T ^b [cm ³ g ⁻¹]	V _{<50 Å} ^c [cm ³ g ⁻¹]	V _{50-300 Å} ^d [cm ³ g ⁻¹]
AMS-HSA	870	1.66	0.12	1.48
AMS-LSA	496	0.99	0.08	0.85
FUMED	412	1.47	0.10	0.49

^aBrunauer–Emmet–Teller (BET) specific surface area (SSA); ^bTotal pore volume (V_T) by NLDFT method; ^cVolume of meso-pores <50 Å and d) between 50 and 300 Å.

The surface properties of AMS samples were studied by FTIR spectroscopy. The spectra reported in Figure 5.8 were recorded after dehydration under vacuum at beam temperature (b.t.) for 30 minutes in order to remove water molecules eventually adsorbed on the samples surface.

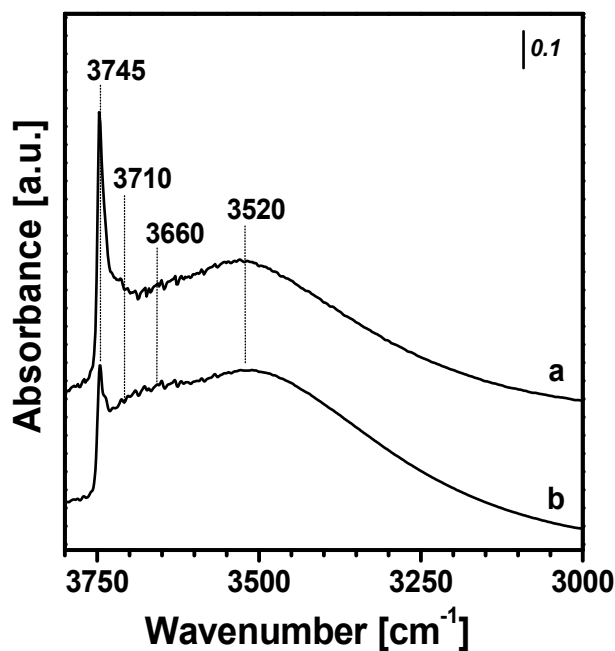


Figure 5.8: FTIR spectra of AMS -HSA (curve a) and AMS -LSA (curve b) samples. Spectra were recorded after outgassing the samples for 30 minutes at beam temperature (b.t.)

The spectra of both AMS samples (Figure 5.8) present an evident peak at ca. 3745 cm^{-1} that can be assigned to isolated silanols, and a broad absorption extending from 3720 to 3200 cm^{-1} that corresponds to H-bonded silanols.^[10,11] Interestingly, in the AMS-LSA sample (Fig. 5.8, curve b) the peak at 3745 cm^{-1} is less intense than for the AMS-HSA sample (Fig. 5.8, curve a), thus suggesting the presence of a lower amount of isolated SiOH species.

The concentration of silanol species in both samples was also determined by thermogravimetric analysis (TGA) and by following the equation given in Appendix II. The weight loss in the 150 - $1000\text{ }^{\circ}\text{C}$ range, due to the condensation of silanols, which are approximately 2.06 and 2.64% for AMS-LSA and AMS-HSA, respectively. From these data, and the data of Table 5.2, the amount of silanol species normalized for the SSA corresponds to 2.97 and 2.17 OH/nm^2 for AMS-LSA and AMS-HSA samples, respectively.

5.2.2.2 Monitoring the hydrothermal stability of AMS samples

To study the hydrothermal stability of the AMS samples, two aliquots of the solids (100 mg) were suspended in 10 mL of Milli-Q ultrapure water and heated at 50°C for 8 and 36 h , respectively. After that, samples were recovered by filtration and then dried at 60°C for 24 h . Samples recovered after

8h were named AMS-LSA-8H and AMS-HSA-8H, whereas the samples left 36 hours were coded AMS-LSA-36H and AMS-HSA-36H, respectively.

In this paragraph, the hydrothermal stability of the AMS samples and the possible modifications occurring to the samples after different contact times with warm water (50°C) have been studied by means of different experimental techniques (*i.e.* N₂ physisorption at 77K, FTIR, solid state NMR and TGA analysis).

Specific surface area (SSA) and pore size distribution of the treated materials are reported in Figure 5.9.

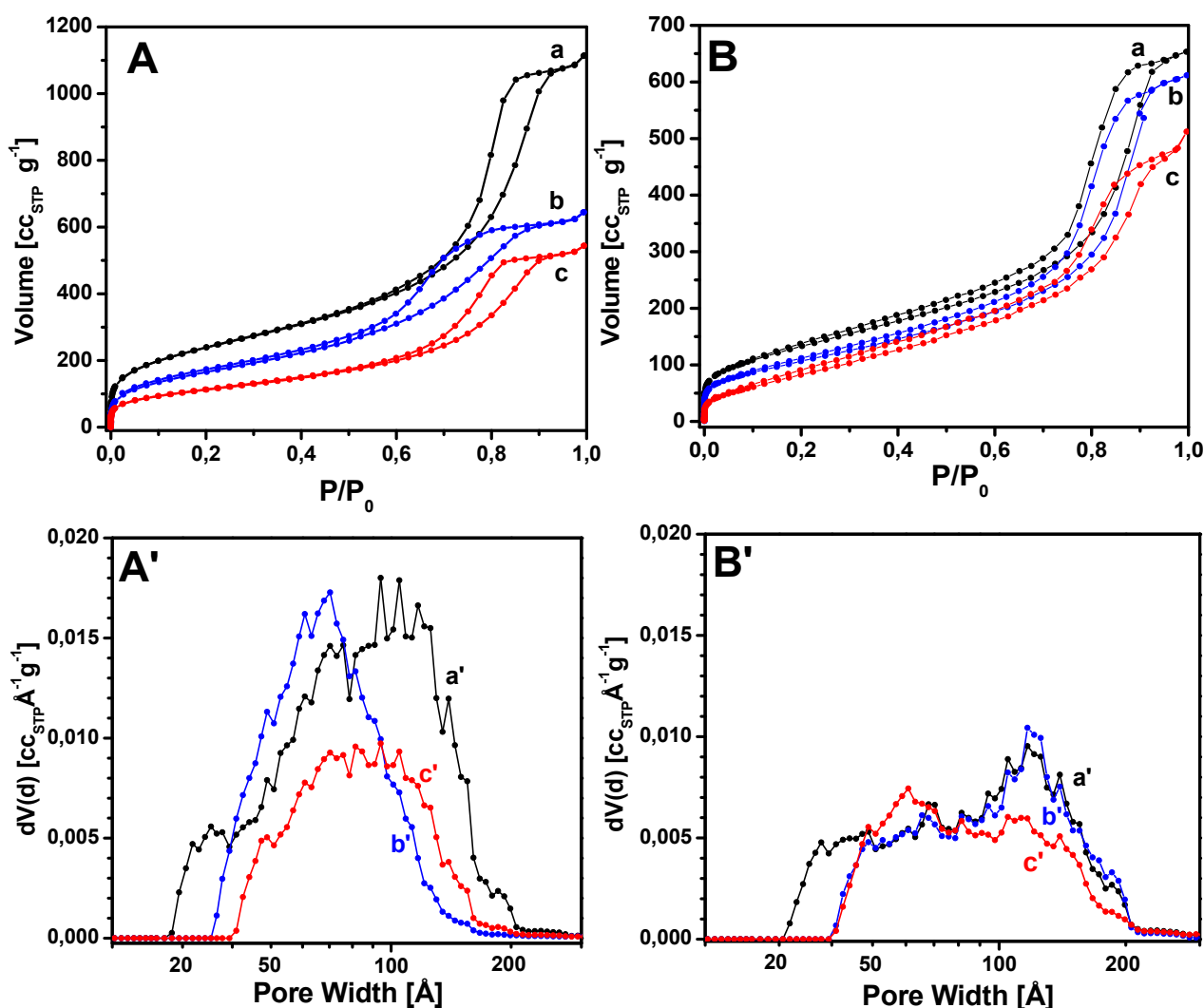


Figure 5.9: N₂ adsorption/desorption isotherms at 77K (A and B) and pore size distribution (A' and B') of AMS-HSA (A and A') and AMS-LSA (B and B') samples before (curves a, a') and after hydrothermal treatment at 50°C for 8 h (curves b, b') and 36 h (curves c, c') at 50°C.

As a general feature, for both samples the hydrothermal treatment does not substantially modify the shape of the isotherms even if a progressive decrease in the total N₂ adsorbed volume can be observed increasing the time of treatment. This is especially evident for AMS-HSA sample (Figure 5.9A). The overall textural properties of the AMS-HSA sample treated in water at 50°C are progressively modified with respect to the pristine sample: i) after 8 h the SSA decreases from 870 to 612 m² g⁻¹, and reaches the value of 409 m² g⁻¹ after 36 h; ii) the family of pores ranging from 100 to 200 Å, along with the small pores of ca. 30 Å, disappeared just after 8h treatment (Figure 5.9 A', b'). The modifications of the textural properties of this sample are probably associated to a partial dissolution-recondensation process leading to a pore deformation and then a pore clogging.^[17] It was indeed proposed that during the siloxane hydrolysis a Si-O-Si bond is broken with the formation of two silanol groups, and that this reaction accelerates upon formation of silanol groups because of their interaction with water molecules and hydroxyl groups.

Textural modifications also occur for AMS-LSA sample after treatment under hydrothermal conditions (Figure 5.9B and B'). Nevertheless, this sample appeared less sensible to water treatment with respect to the AMS-HSA.

After 8h treatment, SSA of the AMS-LSA sample decreases from 496 to 403 m² g⁻¹ this is due to a slight reduction of pores volume that passes from 0.99 to 0.92 cm³ g⁻¹ because of the disappearance of the smallest pores between 20 to 40 Å. The SSA of the sample becomes of 358 m² g⁻¹ with a further reduction of pore volume to 0.75 cm³ g⁻¹ after 36 h of treatment under hydrothermal conditions. As a result of the gradual collapse and partial dissolution of the AMS-LSA pore walls a limited reduction of the pores between 80 to 200 Å is observed after 36 h. The textural properties of the AMS samples hydrothermally treated are reported in Table 5.3.

Table 5.3: Main Textural Properties of AMS-LSA and AMS-HSA before and after hydrothermal treatment for 8 h and 36 h at 50°C

Sample	SSA _{BET} ^a [m ² g ⁻¹]	V _T ^b [cm ³ g ⁻¹]	V _{<50 Å} ^c [cm ³ g ⁻¹]	V _{50-300 Å} ^d [cm ³ g ⁻¹]
AMS-LSA	496	0.99	0.08	0.89
AMS-LSA-8h	403	0.92	0.04	0.87
AMS-LSA-36h	358	0.75	0.04	0.67
AMS-HSA	870	1.66	0.12	1.51
AMS-HSA-8h	612	0.95	0.11	0.82
AMS-HSA-36h	409	0.80	0.04	0.75

^aBrunauer–Emmet–Teller (BET) specific surface area (SSA); ^bTotal pore volume (V_T) by NLDFT method; ^cVolume of meso-pores <50 Å and ^dbetween 50 and 300 Å.

The modification of the silica surface as a consequence of the hydrothermal treatments was also followed by IR spectroscopy and analysis are reported in Figure 5.10.

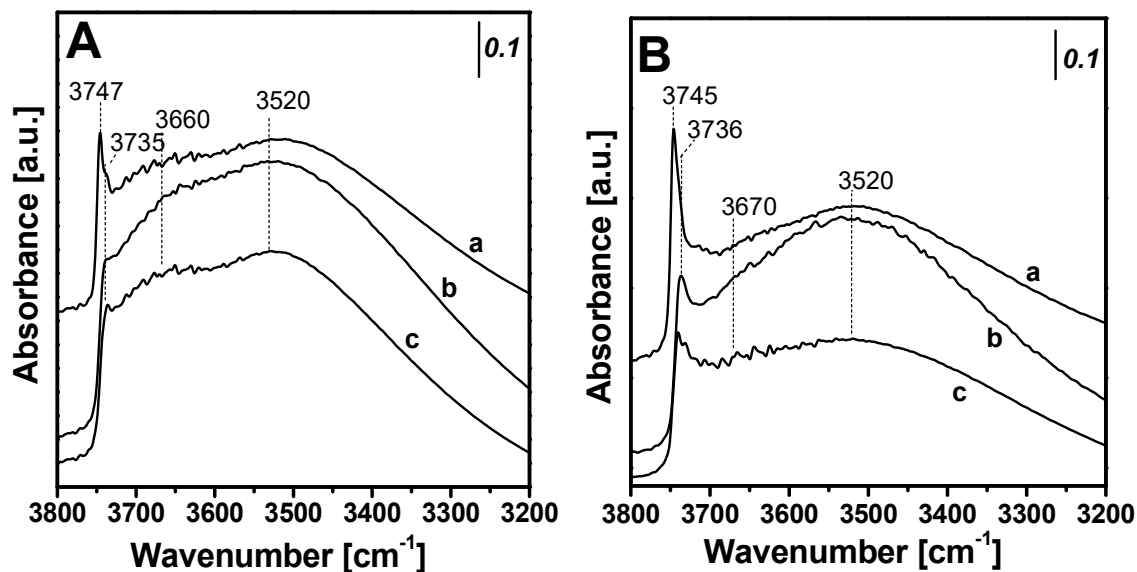


Figure 5.10: IR spectra of samples of AMS-LSA (A) and AMS-HSA (B). Curves a are related to fresh samples, curves b are associated with samples treated for 8 h and finally curves c indicates samples treated for 36 h, respectively.

The hydrothermal treatment leads to a modification of bands related to surface SiOH sites: for both samples a reduction of the band due to isolated silanols is visible together with a modification of the large band due to H-bonded species. This is another indication of the occurrence of a partial hydrolysis of weak Si-O-Si siloxanes, especially evident for AMS-HSA sample.^[11,18] The modification of the -SiOH concentration after hydrothermal treatments was determined by thermogravimetric analysis (Table 5.4) and by using the equation given in Appendix II.

The increasing amount of -OH groups per nm² is an indication of the progressive hydrolysis reactions on the AMS silica surface. After 8h of treatment, silanol species of the AMS-LSA sample increase from 2.97 to 5.62 OH/nm² and prolonging the time of treatment to 36 h, a further increasing to 7.49 OH/nm² was found. An even more extended hydroxylation was observed for AMS-HSA sample that after 36 h of contact with water shows an increase of the silanols density from 2.17 to 9.46 OH/nm².

Table 5.4: Amount of SiOH species of AMS-LSA and AMS-HSA before and after hydrothermal treatment for 8 h and 36 h at 50°C.

Sample	n° OH / nm ²		
	as-prepared samples	8h hydrothermal treatment	36h hydrothermal treatment
AMS-LSA	2.97	5.62	7.49
AMS-HSA	2.17	5.64	9.46

The modification of the silica surface as a consequence of the hydrothermal treatments was also followed by solid state NMR spectroscopy (ss-NMR). The SS-NMR spectra were acquired by using a Bruker Avance III 500 spectrometer with a wide-bore 11.7 T magnet with operational frequencies for ¹H and ²⁹Si of 500.13 and 99.35 MHz, respectively. A 4 mm triple-resonance probe with magic-angle spinning (MAS) was employed in all experiments. The samples were packed on a zirconia rotor and spun at a MAS rate between 10 kHz. Quantitative ²⁹Si MAS NMR data were recorded under ¹H decoupling conditions with the radio-frequency field of 42 kHz for $\pi/2$ pulse. The relaxation delay between accumulations was one minute. All chemical shifts are reported on the δ scale and were externally referenced to tetramethylsilane (TMS) at 0 ppm. All NMR spectra were fitted with DMFIT functions for quantitative deconvolution of overlapping peaks.

²⁹Si MAS NMR spectra of AMS-HSA and AMS-LSA before and after hydrothermal treatment, are shown in Figure 5.11. ²⁹Si population distributions were derived by deconvoluting the MAS NMR spectrum.^[19]

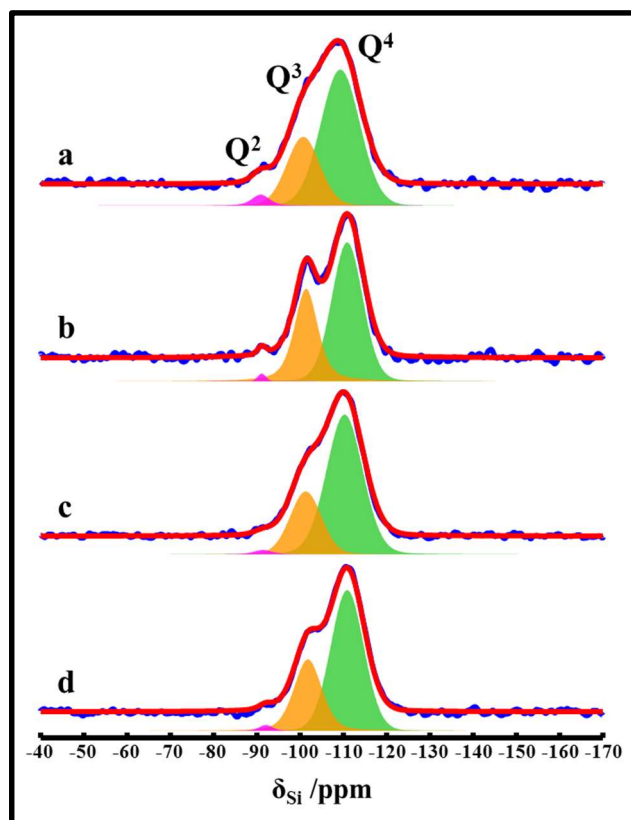


Figure 5.11: ^{29}Si MAS NMR spectra, recorded at a MAS rate of 10 kHz, of pristine AMS-HSA and AMS-LSA before (a, c) and after hydrothermal treatment at 50°C for 36 h (b, d), respectively. Each curve includes experimental and corresponding deconvoluted spectra with individual contribution from each type of ^{29}Si site.

The spectra of samples contain three broad peaks located at *ca.* -110, -101 and -91 ppm, corresponding to Q^4 , Q^3 and Q^2 Si sites, respectively. Such broad ^{29}Si NMR resonances are an indication of the amorphous nature of the AMS materials. The ^{29}Si MAS NMR spectra of AMS-HSA (Figure 5.11, curve a) and AMS-LSA (Figure 5.11, curve c) also show some differences. The $(\text{Q}^3+\text{Q}^2)/\text{Q}^4$ intensity ratios were 0.47 and 0.41 for AMS-HSA and AMS-LSA, respectively, reminiscent of a higher surface to bulk ratio for former sample. Furthermore, the textural modifications of samples under hydrothermal treatment were also monitored by ^{29}Si MAS NMR spectroscopy.

Spectra of powdered samples hydrothermally treated at 50°C for 36 hours are shown in Figure 5.11 curve b (AMS-HSA) and Figure 5.11 curve d (AMS-LSA). An overall improvement in the spectral resolution of samples treated hydrothermally was clearly evident. In addition, the new $(\text{Q}^3+\text{Q}^2)/\text{Q}^4$ intensity ratios were 0.61 and 0.49 for AMS-HSA and AMS-LSA, respectively. The significant increase in the $(\text{Q}^3+\text{Q}^2)/\text{Q}^4$ ratios, compared to pristine samples, specifies further the hydrolysis of the Q^4 units during hydrothermal treatment. Moreover, the difference in the values, between before

and after hydrothermal treatment, in two samples suggests that AMS-LSA is less susceptible to hydrothermal treatment.

In summary, the solid-state ^{29}Si MAS NMR studies demonstrated that the degree of hydrolysis under hydrothermal conditions is different for AMS-HSA and AMS-LSA. Therefore, there seems to be a correlation between the pore architecture/pore-wall thickness and the hydrothermal stability of AMS materials. Furthermore, the differences in the hydrothermal stability between samples are a very likely result of highly condensed silica produced upon extensive pre-treatment of synthesis gel prior to calcination (AMS-LSA).

5.2.2.3 Toluene adsorption on AMS samples

In order to investigate the interactions occurring between toluene and the surface of AMS samples IR spectroscopy and microgravimetric analysis were used (Figure 5.12 A, B).

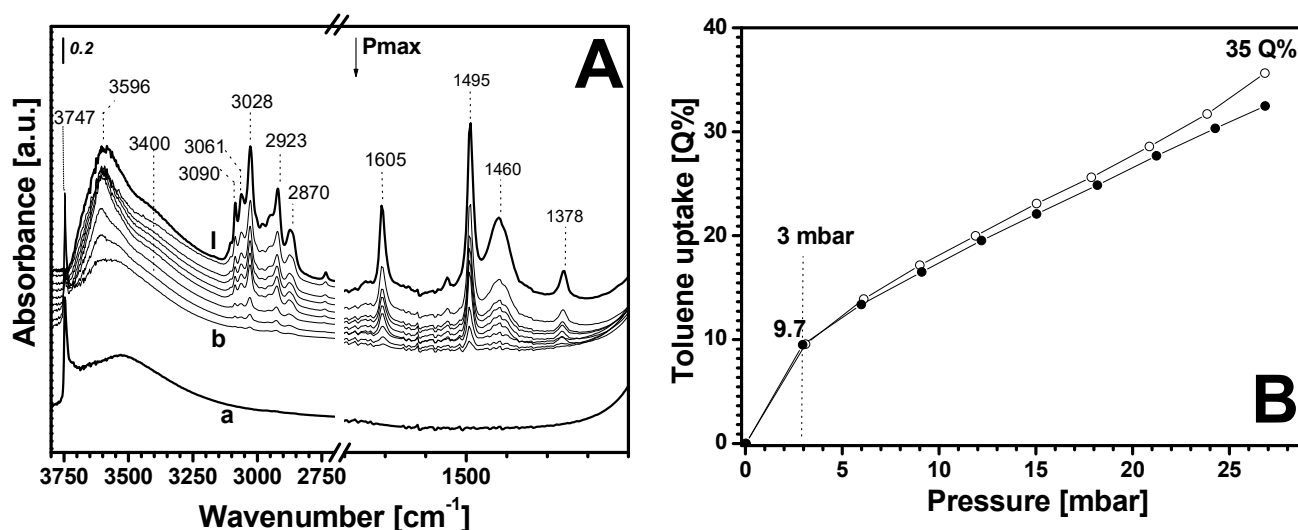


Figure 5.12: A: FTIR of toluene adsorbed at rt on AMS-HSA. Spectrum a was recorded after outgassing the sample for 30 minutes at beam temperature (b.t.) before toluene adsorption; the spectra from l to b were during the progressive outgassing of toluene (30-0.1 mbar). B: Toluene gravimetric adsorption (—o—) and desorption (—•—) isotherms obtained at 35 °C on AMS-HSA sample.

The IR spectra collected upon admission of 30 mbar of toluene, and subsequent gradual decrease of toluene pressure on AMS-HSA sample are reported in Figure 5.12A.

As in the case of the amorphous FUMED silica, the admission of small doses of toluene from 0.1 to 9 mbar (Figure 5.12, curves b-e) on AMS-HSA sample results in a progressive disappearance of the band related to isolated silanol species at ca. 3745 cm^{-1} and to the formation of an intense band at

3595 cm^{-1} likely due to $\text{O-H}\cdots\pi$ interactions between silanol species and toluene molecules, the associated $\Delta\nu\text{OH}$ being ca. 150 cm^{-1} . The IR spectra of AMS-HSA upon contact with toluene also show a broad band with a maximum at ca. 3400 cm^{-1} (more evident at pressure higher than 9 mbar), which is associated to the interactions of toluene with the hydrogen-bonded silanol species present on the surface of AMS-HSA.^[12]

Also, the bands of the characteristics modes of absorption of toluene are present, in particular, bands at 3028 cm^{-1} related to C–H stretching mode of the toluene aromatic ring, the signals at 2923 and 2870 cm^{-1} assigned to C–H stretching modes of the toluene methyl groups, the band at 1605 cm^{-1} associated to the quadrant stretching mode of the monosubstituted ring C=C and the bands at 1460 and 1378 cm^{-1} correspond to the out-of-phase and in-phase deformations of the toluene methyl group. The admission of toluene pressure higher than 9 mbar leads to a slight increase of the intensity of the bands due to toluene molecules and this indicates that the adsorption is likely driven by van der Waals interactions between the silica walls and the toluene molecules (host-guest interactions) and among toluene molecules (guest-guest interactions).

Microgravimetric analysis was also performed in order to determine the sorption capacity of AMS-HSA silica and its affinity with the pollutant (Figure 5.12B).

Two regimes can be observed on the gravimetric isotherm of toluene adsorbed on the sample AMS-HSA (Figure 5.12B). The isotherm is indeed steep at pressures lower than 3 mbar, then the slope decreases but does not reach a plateau, thus suggesting that the pore saturation does not occur.

The higher affinity observed at pressure below 3 mbar is likely due to the interaction of toluene with surface silanols of AMS sample. At high absolute pressure (27 mbar) the overall toluene uptake is ca. 35 Q% (where Q represents the ratio between the amount adsorbed toluene (in mg) respect to 100 mg of solid sample). This value is higher than those observed for microporous systems like HSZ-Y and ZSM-5 zeolites that at the same pressure adsorb ca. 22 and 8.8 Q% of toluene, respectively.^[12]

Similar IR experiments were carried out for AMS-LSA. In Figure 5.13A, selected IR spectra of toluene adsorbed on both AMS samples are reported.

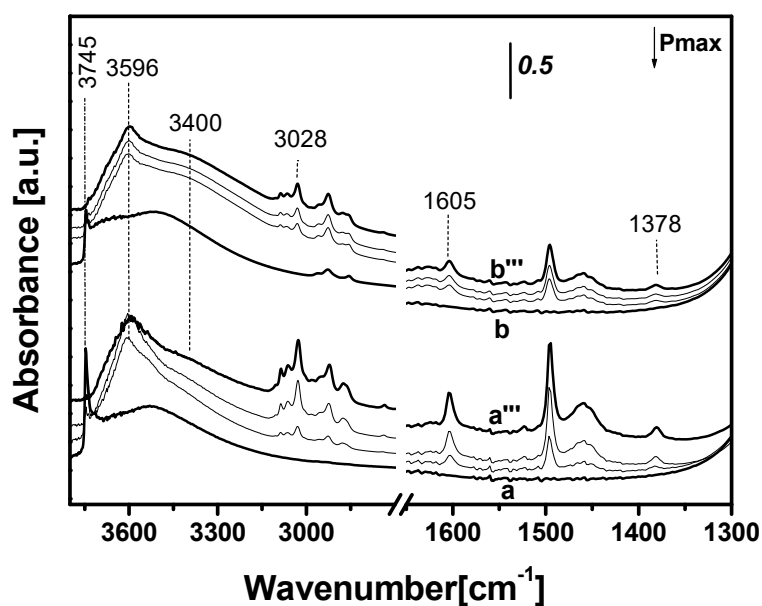


Figure 5.13: Comparison between IR spectra of toluene adsorption on both AMS samples: Spectra of AMS-HSA (curve a) and AMS-LSA (curve b) samples; both samples were outgassed at r.t. for 1 h before the adsorption experiments and spectra after dosage of toluene on both supports at pressure of 1 mbar (curves a' and b'); 5 mbar (curves a'' and b'') and 15 mbar (curves a''' and b''').

As can be observed from the comparison of the IR spectra (Figure 5.13), the adsorption of toluene lead to the formation of the same bands for both the supports. Nevertheless, the intensity of the bands are different thus suggesting that AMS-LSA sample is able to retain a lower amount of toluene with respect to AMS-HSA.

Optical adsorption isotherms of toluene adsorbed on the AMS-LSA sample were derived from FTIR data of the adsorbed molecule. Specifically, the spectroscopic data related to the adsorption of pollutant on AMS-LSA at controlled pressures have been used to quantify the toluene uptake. The estimation of concentration of toluene on AMS-LSA was calculated using the molar absorption coefficient (ϵ) of the 1605 cm^{-1} band related to the C=C stretching mode of the toluene ring.

The molar absorption coefficient (ϵ) of the band at 1605 cm^{-1} of toluene adsorbed on AMS with high specific surface area (AMS-HSA) was determined by combining FTIR and microgravimetric data.

The molar absorption coefficient of toluene adsorbed on AMS-HSA sample was determined following the same method related to the determination of the molar absorption coefficients of toluene and *n*-hexane adsorbed on different zeolites. In particular, it was obtained adapting the Beer-Lambert Law to adsorbent/substrate systems, described in the Chapter IV.

The average value of the molar absorption coefficient (ϵ) of the band at 1605 cm^{-1} of toluene adsorbed on AMS-HSA is $0.292 \pm 0.059\text{ cm } \mu\text{mol}^{-1}$.

The concentration of adsorbed toluene (C_{toluene}) on AMS-LSA defined as $\mu\text{mol g}^{-1}$ was obtained by using the formula:

$$C_{\text{toluene}} = \frac{A_{\text{MSA-LSA}}(1605)}{\epsilon_{\text{MSA-HSA-toluene}} \rho} \quad (5.1)$$

where $A_{\text{AMS-LSA}(1605)}$ is the integral absorption of the IR band at 1605 cm^{-1} of toluene adsorbed on AMS-LSA, $\epsilon_{\text{AMS-HSA-toluene}}$ is the molar extinction coefficient [$\text{cm } \mu\text{mol}^{-1}$] of toluene adsorbed on AMS-HSA, reported in Chapter VI and ρ [g cm^{-2}] is the density of the pellet that represents the path length. The calculated optical isotherms of toluene adsorbed on AMS-LSA sample is reported in Figure 5.14 and compared with the gravimetric isotherm of toluene adsorbed on the sample AMS-HSA.

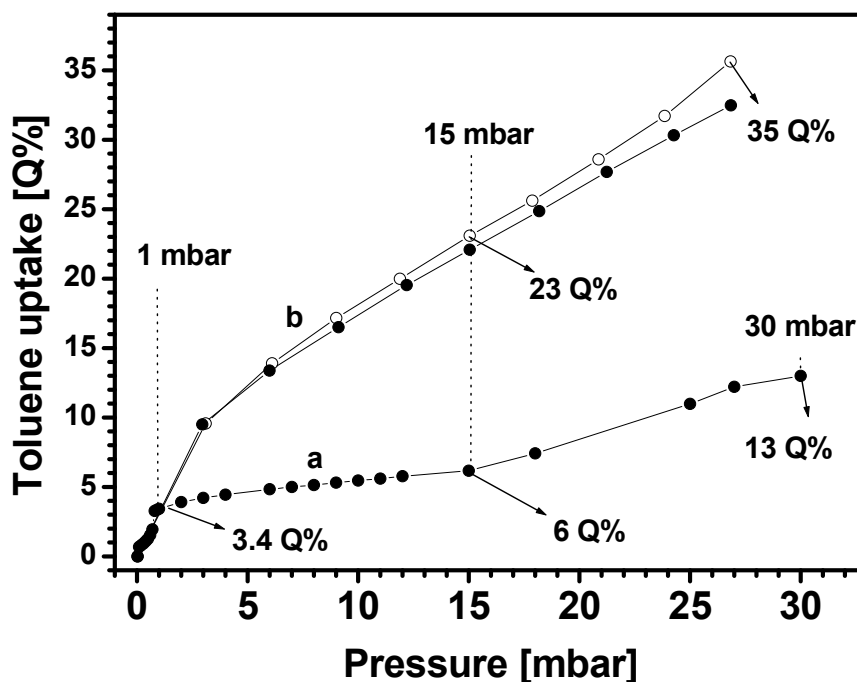


Figure 5.14: Optical isotherm (uptake vs pressure) for toluene derived from IR band (1605 cm^{-1}) formed upon adsorption as gaseous of toluene on AMS-LSA (curve a) and toluene gravimetric adsorption (—○—) and desorption (—●—) isotherms obtained at $35\text{ }^\circ\text{C}$ on AMS-HSA sample (curve b).

Three regimes can be observed on the volumetric isotherm of toluene adsorbed on the sample AMS-LSA (Figure 5.14, curve a). The rapid increase of toluene uptake until 1 mbar is mainly attributed to

the interaction of toluene with surface silanols of AMS-LSA which is characterized with a lower amount of isolated silanol species respect of the AMS-HSA sample (see IR part, Figure 5.6).

The second regime of adsorption between 1 and 15 mbar where the slope decreases, and the uptake reaches 6 Q%. The third regimen at higher pressures of 15 mbar where the maximum of uptake is 13 Q% and this confirms that this sample is less able to retain the aromatic molecule with respect to the other sample AMS-HSA (Figure 5.14, curve b) which adsorbs 35 Q%.

5.2.2.4 Toluene adsorption on AMS samples treated under hydrothermal conditions

The same adsorption experiments were carried out on both AMS samples after hydrothermal treatments.

In Figure 5.15A, selected IR spectra of toluene adsorbed on AMS-HSA samples before and after hydrothermal treatments are reported. In Figure 5.15B, microgravimetric analysis of the same sample treated in water for 36 h are compared to that collected on the untreated material.

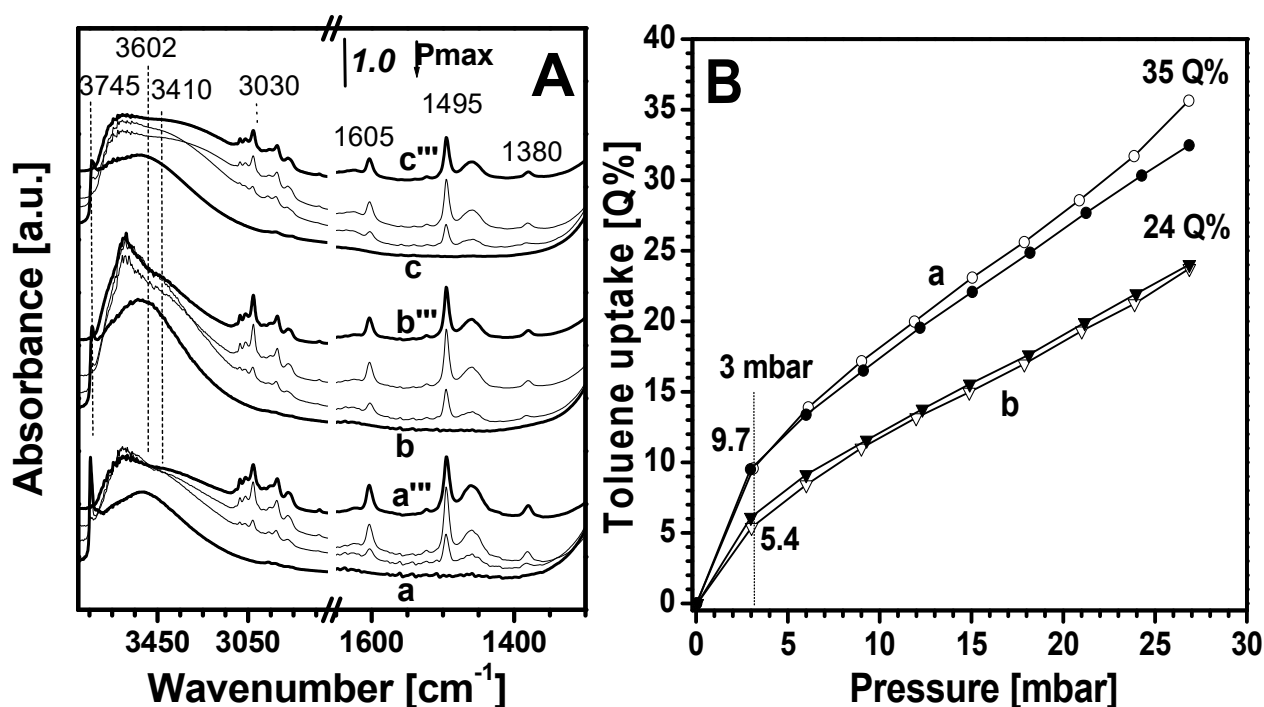


Figure 5.15: A: IR Spectra of AMS-HSA samples: before (curve a) and after hydrothermal treatment in water for 8 h, 36 h (curves b and c, respectively); all samples were outgassed at r.t. for 1 h before the adsorption experiments. Spectra after dosage of toluene at pressure of 1 mbar on the same supports (curves a', b' and c'); 5 mbar (curves a'', b'' and c'') and 15 mbar (curves a''', b''' and c''') are also displayed. B: toluene gravimetric adsorption (—o—) and desorption (—•—) isotherms at 35°C on AMS-HSA (curve a) and AMS-HSA treated in water for 36 h (curve b).

Upon toluene admission on the hydrothermally treated samples (Figure 5.15A), the same IR vibration already observed for the bare sample can be found (see above).

From the intensity of the bands of toluene at low frequencies (bands at 1605 and 1380 cm^{-1}) it is possible to notice that the AMS-HSA treated for 36 h shows a slight decrease of intensity respect to the untreated sample. Indeed, the microgravimetric analysis of toluene adsorbed on AMS-HSA before and after hydrothermal treatment for 36 h reported in Figure 5.15B, indicates a decrease of the capacity of toluene adsorption of 11 Q% after the hydrothermal treatment. This is probably associated to the loss of 53 % of the total pore volume, which passes from 1.66 to 0.8 $\text{cm}^3 \text{g}^{-1}$.

In Figure 5.16A, selected IR spectra of toluene adsorbed on AMS-LSA samples before and after hydrothermal treatments are reported. Optical adsorption isotherms of toluene adsorbed on AMS-LSA samples after hydrothermal treatments sample were also derived from gas adsorption followed by FTIR spectroscopy. The estimation of concentration of toluene on AMS-LSA after hydrothermal treatments were also calculated using ϵ of toluene of the 1605 cm^{-1} band on AMS-HSA and following the formula (5.1), see paragraph 5.2.2.3 and reported in Figure 5.16B.

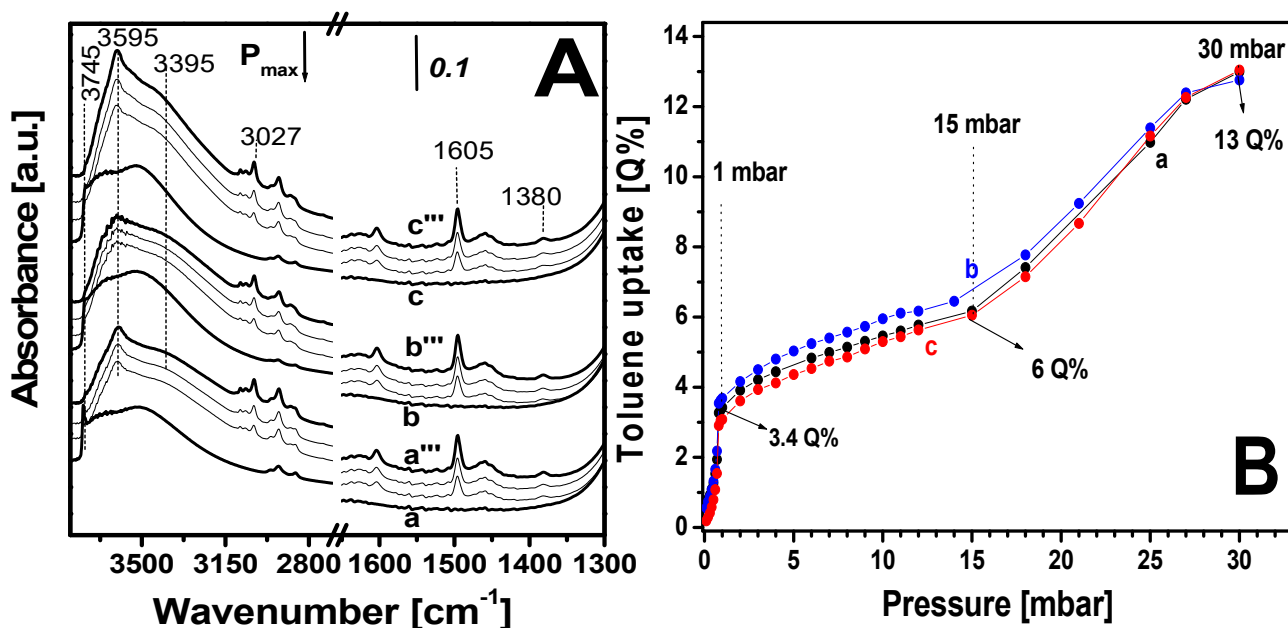


Figure 5.16: A: Spectra of AMS-LSA samples: before and after hydrothermal treatment in water for 8 h, for 36 h and outgassed at r.t. for 1 h (curves a, b and c respectively); spectra collected after dosage of toluene at pressure of 1 mbar on the same supports (curves a', b' and c'); 5 mbar (curves a'', b'' and c'') and 15 mbar (curves a''', b''' and c'''). B: Optical isotherms (uptake vs pressure) for toluene derived from IR band (1605 cm^{-1}) formed upon adsorption as gaseous of toluene on AMS-LSA samples before (curve a) and after hydrothermal treatment at 50°C for 8 h (curve b) and 36 h (curves c).

From the Figure 5.16A, B; it is possible to notice that the sorption capacity of AMS-LSA sample appeared less sensitive to the hydrothermal treatment with respect to the other sample. Indeed, the optical isotherms reported in Figure 5.16 indicate that a slight modification occurs in the toluene uptake after hydrothermally treating the sample for 8 and 36h. This sample appeared then more stable to hydrothermal treatments than the AMS-HSA one.

5.3 Monitoring the toluene adsorption capacities of ordered mesoporous silica

Besides mesoporous silicas with non regular porosity, ordered mesoporous MCM-41 and SBA-15 silicas were also tested as sorbent for toluene adsorption.

For the sake of brevity, a short overview of the general characteristic and synthesis methods of MCM-41 and SBA-15 ordered mesoporous silica is given in the Appendix I.

5.3.1 MCM-41 and SBA-15 silica samples

MCM-41 exhibits peculiar features such as highly ordered structure with regular hexagonal array (Figure 5.17A) of uniform pores with well-defined sizes with a diameter of *ca.* 30 Å (Figure 5.17B). The pore walls are constituted by amorphous silica and their thickness ranging between 10 and 20 Å. Furthermore, MCM-41 has high specific surface area (*ca.* 1000 m²/g) and narrow pore distribution centered at *ca.* 35-38 Å and these features allow high adsorption capacities.^[20]

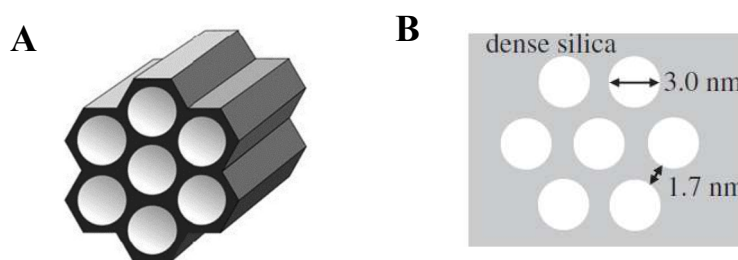


Figure 5.17: Pore structure of the MCM-41 A: Hexagonal arranged of mesoporous and B: Pore and thickness dimensions of the MCM-41. Adapted from Ref.^[17]

SBA-15 silica exhibits a highly ordered structure, high specific surface area (about 600-1000 m²/g) and a large uniform pore size (47-300 Å).^[21]

The porous structure of SBA-15 (Figure 5.18A) consists not only of large, uniform, and ordered channels (mesoporous channels) but also present smaller pores with of diameter between 10-20 Å (microporosity) which connect the ordered channels^[22] The presence of microporosity and the connectivity of the mesopores of silicas could have a significant impact on the potential applications of these materials.^[22]

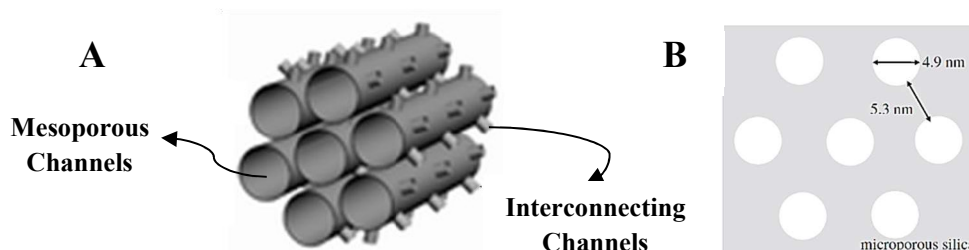


Figure 5.18: Pore structure of the SBA-15 A: Types of channels and B: Pore and thickness dimensions of the SBA-15. Adapted from Ref.^[17,23]

Moreover, it is known that SBA-15 has better performance of thermal and hydrothermal stability compared to MCM-41. This due to the fact that SBA-15 has greater wall thickness *ca* 53 Å (Figure 5.18B), respect to MCM-41 which has only *ca* 17 Å of wall thickness (see Figure 5.17B).^[24,25]

5.3.1.1 Preparation and physico-chemical characterization of ordered mesoporous silicas

MCM-41 was from commercial origin (Sigma Aldrich, CAS Number. 7631-86-9) whereas mesoporous silica SBA-15 was prepared in our laboratories following the synthesis method reported by Zhao.^[26] In detail, 4 g of P123 pluronic ((EO)₂₀ (PO)₇₀ (EO)₂₀ MW=5800, Aldrich) were dissolved in 30 mL of ultrapure water under magnetic stirring for 24 h, then mixed with 120 mL of a 2 M (37 wt%, Merck) HCl solution at 35 °C, the sol was stirred for 1 h at the same temperature. 8.5 g of tetraethoxysilane (TEOS 99 wt%, Sigma-Aldrich) were added, after the gel was placed under static conditions in a Teflon-lined autoclave at 100 °C for 24 h. The resulting white precipitate was filtered and washed using ultrapure water and dried for 24 h, finally the powder was calcined at 550 °C for 5 h (heating rate of 1 °C/min).

The morphology of MCM-41 (Fig.19A) and SBA-15 (Fig.19B) silica samples was investigated by transmission electron microscopy (TEM) and their images are reported in Figure 5.2

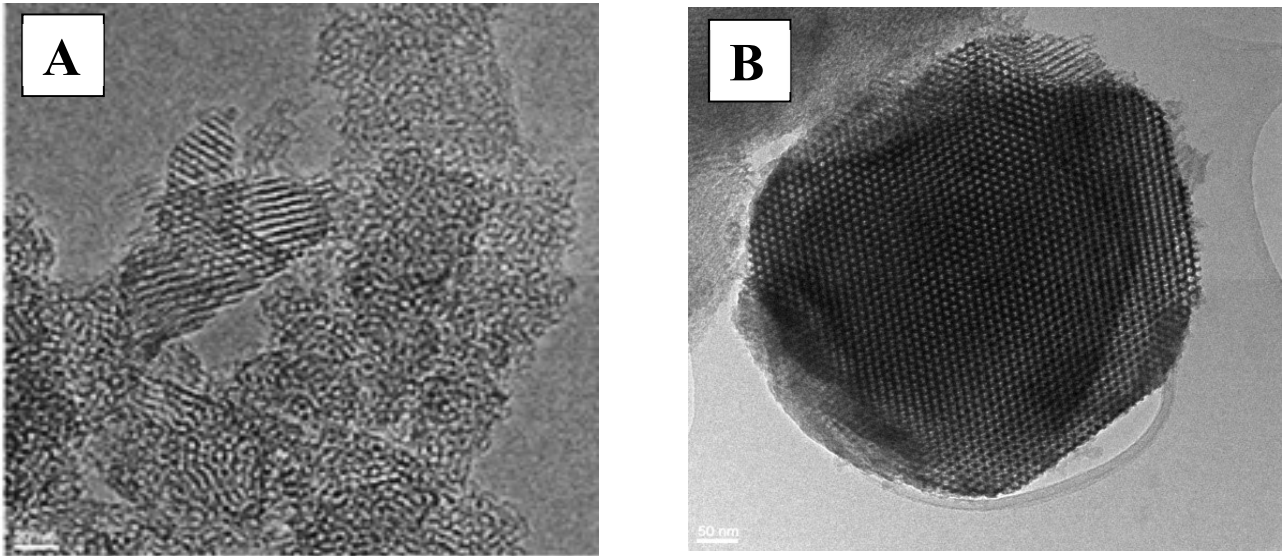


Figure 5.19: TEM micrographs of commercial MCM-41 (A) and SBA-15 (B) samples.

TEM analysis showed that commercial MCM-41 (Figure 5.19A) is a porous material with particle size between 760-1320 nm and which ordered arrays of pores can be observed. Whereas TEM analysis of SBA-15 sample (Figure 5.19A) showed that this sample have a round shape with a dimension of *ca.* 735 nm with a porous structure characterized by hexagonal pores of regular size, typical of 2D hexagonal mesostructures.

Specific surface area and pore size distribution of the two ordered mesoporous silica have been determined by N₂ adsorption isotherms at 77K and reported in Figure 5.20.

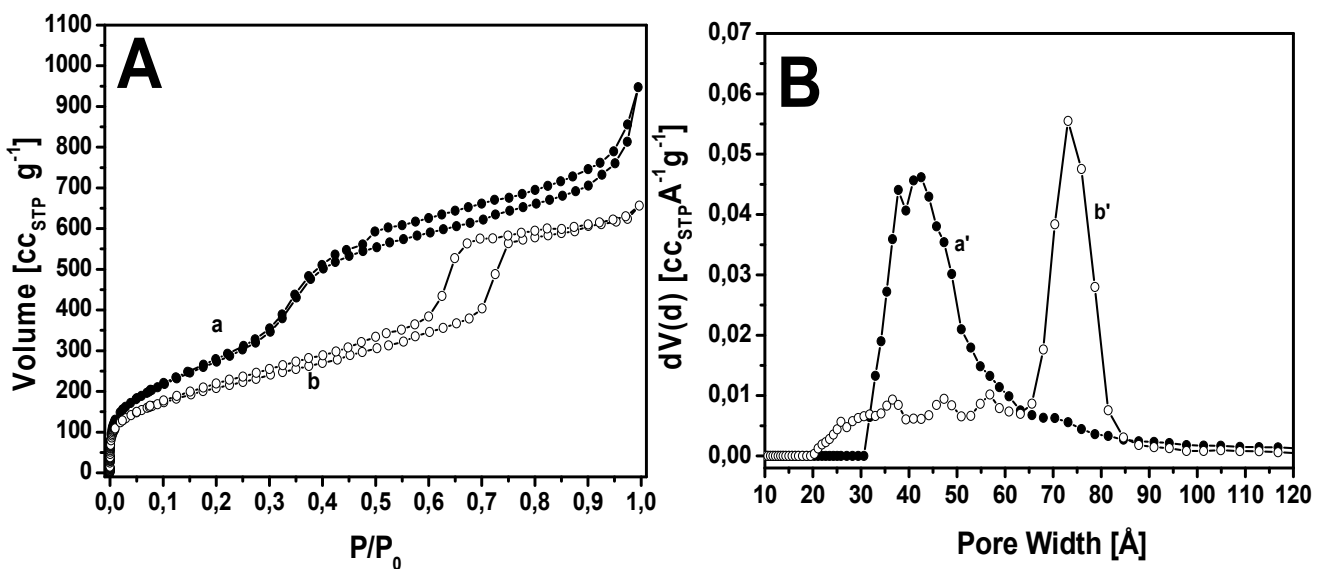


Figure 5.20: A: N₂ adsorption/desorption isotherms at 77K of MCM-41 and SBA-15 (curves a and b, respectively); B: pore size distribution of MCM-41 and SBA-15 (curves a' and b', respectively)

According to the IUPAC classification^[8], the N₂ adsorption isotherms of MCM-41 sample (Figure 5.20A, curve a) is of type IV(b) which is typical of mesoporous silicas with order of hexagonal arrays. This also indicates the presence of conical and cylindrical mesopores with small pore width.^[8,27] Moreover, MCM-41 exhibits a narrow hysteresis of type H4 formed in the 0.5–0.9 p/p_0 range, that suggests the presence of a fraction of cylindrical mesopores.^[28-30] Indeed, MCM-41 has a wide pore size distribution (see Figure 5.20B, curve a') between 30-80 Å, with a maximum centered at 42 Å, the associated mesopores volume being 0.90 cm³ g⁻¹.

SBA-15 sample (Figure 5.20A, curve b) presents an isotherm of type IV(a). The hysteresis loop of SBA-15 has two-step capillary condensation formed in the range 0.5-0.8 p/p_0 , can be classified of type H1 and H2, which suggests the co-presence of cylindrical and cage-like pores.^[31,32] At relative pressure below 0.5 p/p_0 in the desorption branch, the hysteresis is not completely closed: this behaviour suggests the presence of a fraction of small mesopores.

Indeed, this sample evidences two different family of pores (see Figure 5.20B, curve b'): one heterogenous family from 20 to 65 Å with a mesopores fraction of 0.31 cm³ g⁻¹ and one homogeneous family of pores between 65-100 Å with a maximum centered at 75 Å, with a related mesopores fraction of 0.55 cm³ g⁻¹.

The textural properties of MCM-41 and SBA-15 samples are reported in Table 5.5.

Table 5.5: Main Textural features of MCM-41 and SBA-15 silica.

Sample	SSA _{BET} ^a [m ² g ⁻¹]	V _T ^b [cm ³ g ⁻¹]	V _{mesop} ^c [cm ³ g ⁻¹] 30-80Å	V _{mesop} ^c [cm ³ g ⁻¹] 20-100Å	V _{mesop} ^c [cm ³ g ⁻¹]	
					20-65Å	65-100Å
MCM-41	1103	1.31	0.90	0.95	0.83	0.12
SBA-15	761	0.96	0.79	0.86	0.31	0.55

^aBrunauer–Emmet–Teller (BET) specific surface area (SSA); ^bTotal pore volume by NLDFT method; ^cVolume of mesopores NLDFT method.

As reported in Table 5.5, the commercial MCM-41 sample has a specific surface area (SSA) of 1103 m² g⁻¹ with a total pore volume 1.31 cm³ g⁻¹. The presence of pores between 30-80 Å has a related mesopores fraction of 0.90 cm³ g⁻¹.

Whereas SBA-15 sample has a SSA of 761 m² g⁻¹ and a total pore volume of 0.96 cm³ g⁻¹ associated to the two different family of pores between 20 to 65 and 65-100 Å with related mesopores fraction of 0.31 and 0.55 cm³ g⁻¹, respectively.

Surface properties of both MCM-41 and SBA-15 were studied by IR spectroscopy (Figure 5.21).

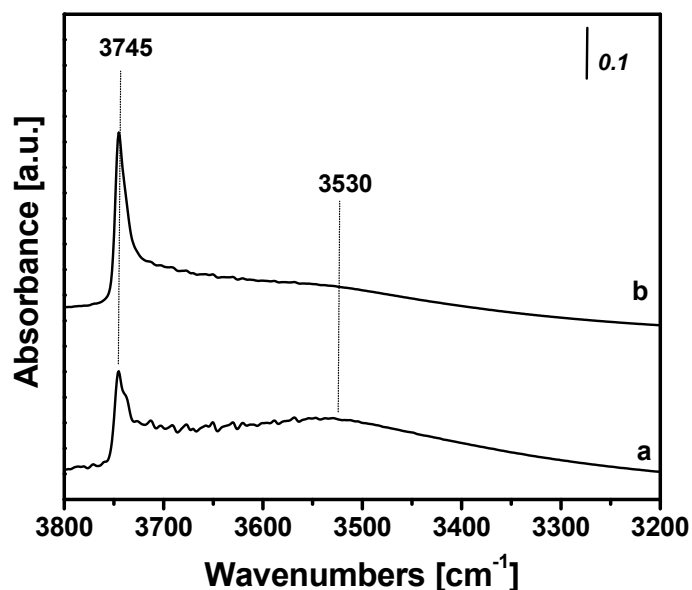


Figure 5.21: FTIR spectra of mesoporous silica materials MCM-41 (curve a) and SBA-15 (curve b).

Spectrum of MCM-41 (curve a) was recorded after outgassing the samples for 30 minutes at beam temperature (b.t.). Spectrum of SBA-15 (curve a) was recorded after outgassing the sample at 150 °C for 1 h to reduce the heterogeneity of surface -OH sites.

The spectra of both MCM-41 and SBA-15 samples (Fig. 5.21 curves a and b, respectively) present an evident narrow peak at ca. 3745 cm^{-1} that can be assigned to isolated silanols, and a broad absorption extending from 3720-3200 cm^{-1} with a maximum around at 3530 cm^{-1} that corresponds to hydrogen-bonded silanols.^[10,11]

In the MCM-41 sample, (Fig. 5.21, curve a), the peak at 3745 cm^{-1} appears less intense than for the SBA-15 (Fig. 5.21, curve b), thus suggesting that presence of a higher amount of isolated SiOH species on SBA-15.

To determinate the amount of silanol groups of the samples, thermogravimetric analysis was performed. As in the previous case, the amount of silanol species were determined considering the weight loss in the 150-1000 °C range and following the equation given in Appendix II. the weight loss in the 150-1000 °C range is approximately 3.12 and 3.10 and 1.82 %, corresponding to 2.03 and 3.09 OH/nm² for MCM-41 and SBA-15, respectively.

5.3.2 Monitoring the toluene adsorption capacities of MCM-41 and SBA-15

In Figure 5.22, a comparison of selected IR spectra of toluene adsorbed on silica supports (SBA-15 and MCM-41) is reported together with volumetric adsorption isotherms.

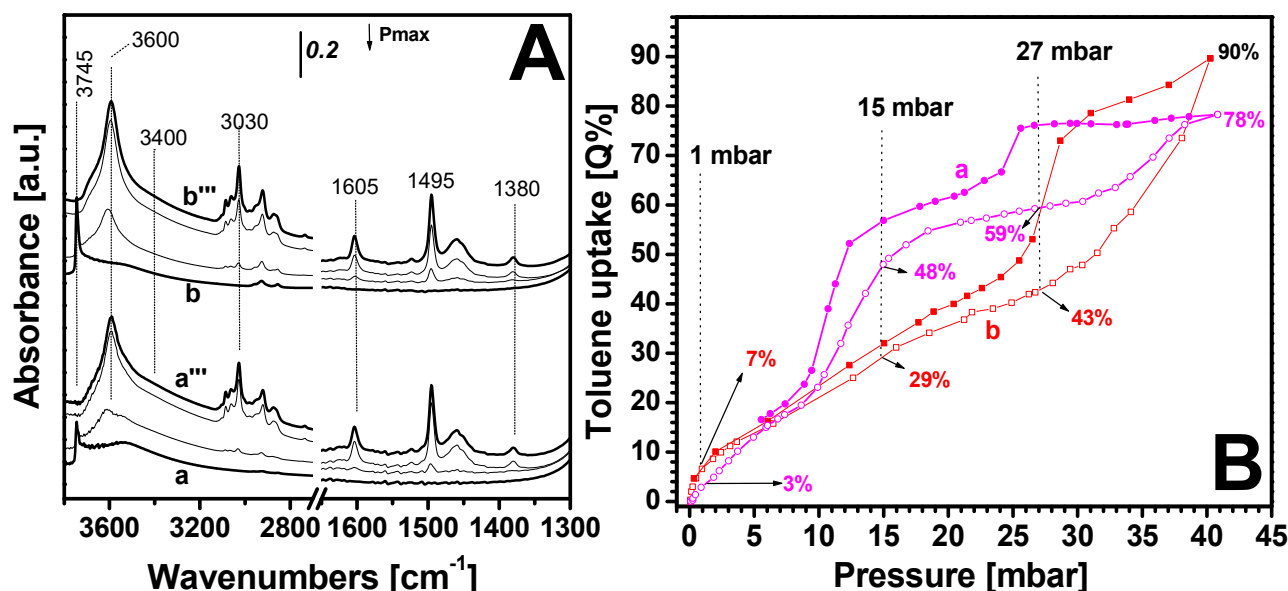


Figure 5.22: A: Comparison between IR spectra of toluene adsorption on SBA-15 and MCM-41: IR Spectra of MCM-41 (curve a) and SBA-15 (curve b) samples; both samples were outgassed at r.t. for 1 h before the adsorption experiments and spectra after dosage of toluene on both supports at pressure of 1 mbar (curves a' and b'); 5 mbar (curves a'' and b'') and 15 mbar (curves a''' and b'''). B: Toluene volumetric adsorption (empty symbols) and desorption (full symbols) isotherms measured at 35 °C of Toluene on MCM-41 (a) and SBA-15 (b). Before the volumetric analysis, samples were outgassed in vacuum conditions at 220 °C for 12h.

The admission of small toluene doses on MCM-41 and SBA-15 (Figure 5.22A, curves a' and b') results in a progressive disappearance of the band related to isolated silanol species at 3745 cm⁻¹ and to the formation of an intense band centered at 3600 cm⁻¹ which is associated to π interactions between silanol species and toluene molecules. The IR spectra of both samples upon contact with toluene also show a broad band with a maximum at ca. 3400 cm⁻¹, more evident at pressure higher than 15 mbar (Figure 5.22A, curves a''' and b'''), and it is related to the interactions of toluene with the hydrogen-bonded silanol species present on the surface of both samples. Moreover, upon toluene admission, all the bands related to the molecule vibrations (*i.e.*, of both the aromatic ring and the methyl group) are also observed.

In addition, as can be observed from the comparison reported in Figure 5.22A, is possible to notice that the bands of toluene on MCM-41 and SBA-15 at these pressures have similar intensity.

The toluene volumetric adsorption/desorption isotherms (Figure 5.22B) were obtained at 35 °C and at standard temperature pressure (STP) on both SBA-15 and MCM-41 by employing a volumetric analysis. Prior the adsorption, the samples were outgassed for 30 min at 50 °C, 30 min at 80 °C, 2h at 120°C, 2 h at 150 °C and finally at 12 h at 220 °C under high vacuum conditions (final pressure 7×10^{-4} mbar).

Different regimes can be observed by the analysis of the volumetric isotherms for both silicas.

The volumetric isotherm of toluene adsorbed on MCM-41 (Figure 5.22B, curve a) present three regimes of adsorption and a two hysteresis loops formed in the range 9-25 and 25-40 mbar due to a capillary condensation of the toluene molecules inside the pores.

The curve appears rapid till 9 mbar and then the slope increases up to *ca.* 15 mbar when gradually the adsorption curve tends to a first plateau at *ca.* 25 mbar. The rapid increase of toluene uptake until 9 mbar is probably mainly due to the interaction of surface silanols of MCM-41 samples with toluene, and the corresponding uptake is *ca.* 20 Q%. The first plateau at 25 mbar which uptake is *ca.* 59 Q% is associated with the filling of the fraction of mesopores with diameter lower than 40 Å (see pore size distribution in Fig. 5.20B, curve a').^[28] At pressures higher than 25 mbar the slope increases again and then progressively the curve tends to a second plateau at *ca.* 27 mbar till 45 mbar where the overall toluene uptake is *ca.* 78 Q%, this third adsorption step is probably associated with the filling of the fraction of mesopores with dimensions between 40-80 Å.

The volumetric isotherm of toluene adsorbed on SBA-15 (Figure 5.22B, curve b) present three regimes of adsorption and two hysteresis loops formed in the range between 9-25 and 25-40 mbar.

The isotherm is steep till 1 mbar and the corresponding uptake is 7 Q%. The toluene uptake of SBA-15 at 1 mbar is (+4 % higher) respect to MCM-41, this could be associated to the low amount of isolated silanol species (see IR part, Fig. 5.21) present on surface of MCM-41 respect to SBA-15, as also reported by thermogravimetric analysis where MCM-41 reported lower amount of -OH groups per nm² (2.03 OH/nm²) respect to SBA-15 (3.09 OH/nm²).

At higher pressures of 1 mbar the slope decreases up to *ca.* 27 mbar where uptake is *ca.* 43 Q%. This second adsorption step is probably associated with the filling of the heterogenous family pores from 20 to 65 Å (see pore size distribution in Fig. 5.20B, curve b'). At pressures higher of 27 mbar the slop

increases up to *ca.* 31 mbar then the slope decreases again progressively till 45 mbar where the overall toluene uptake is *ca.* 90 Q%, this third adsorption step is probably associated with the filling of the homogeneous family of pores between 65-100 Å with a maximum centered at 75 Å (see pore size distribution in Fig. 5.20B, curve b’).

Considering the previous IR data and the results coming from volumetric analysis, it is possible to propose that the volume and dimensions of pores is an important parameter for the adsorption of toluene on ordered mesoporous silicas.^[33]

5.4 Conclusions

In this chapter, the physico-chemical feature of mesoporous silicas samples (FUMED, AMSs, MCM-41 and SBA-15) were investigated by means of different experimental approaches (*i.e.* N₂ adsorption, FTIR, TGA and SS-NMR). These solids were tested for the adsorption of toluene, used as a representative molecule of aromatic by means of FTIR spectroscopy and volumetric/gravimetric analysis.

The textural properties of the mesoporous silicas studied in this Chapter are reported in Table 5.6.

Table 5.6: Main textural features of the mesoporous silicas studied in this Chapter.

Sample	SSA _{BET} ^a [m ² g ⁻¹]	V _T ^b [cm ³ g ⁻¹]	V<50 Å ^c [cm ³ g ⁻¹]	V _{mesop} ^c [cm ³ g ⁻¹] 20-300Å	V _{mesop} ^c [cm ³ g ⁻¹] 20-100Å	V _{mesop} ^c [cm ³ g ⁻¹]	
						20-65Å	65-100Å
FUMED	412	1.47	0.10	0.57	0.27	0.16	0.11
AMS-HSA	870	1.66	0.12	1.63	0.81	0.29	0.52
MCM-41	1103	1.31	0.66	1.13	0.95	0.83	0.12
SBA-15	761	0.96	0.20	0.92	0.86	0.31	0.55

^aBrunauer–Emmet–Teller (BET) specific surface area (SSA); ^bTotal pore volume by NLDFT method; ^cVolume of mesopores NLDFT method.

Both mesoporous silicas with irregular porosity (FUMED and AMS-HSA) have a heterogenous distribution pores between 20-300 Å (see Figure 5.23A, curves a and b).

MCM-41 showed a wide pore size distribution (see Figure 5.23B, curve a’) between 30-80 Å, with a maximum centered at 42 Å, the associated mesopores volume being 0.90 cm³ g⁻¹. SBA-15 showed two families of mesopores, one heterogeneous family of pores between 20 to 65 Å with a mesopores fraction of 0.31 cm³ g⁻¹ and another family of pores between 65-100 Å with a maximum centered at 75 Å and related mesopores volume of 0.55 cm³ g⁻¹.

In Figure 5.23B are reported the pore size distribution and toluene adsorption/desorption isotherms of all the solids studied in this Chapter.

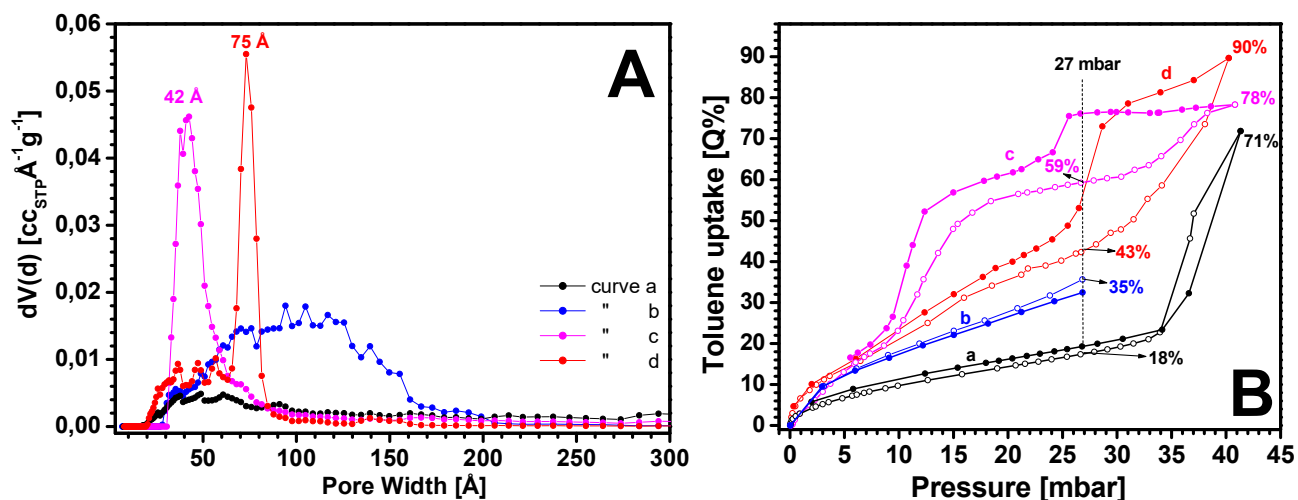


Figure 5.23: Pore size distribution (A) and toluene adsorption/desorption isotherms (B) of all the supports: FUMED (curve a), AMS-HSA (curve b), MCM-41 (curve c) and SBA-15 (curve d)

A comparison of the pore size distribution of the mesoporous materials used for toluene adsorption is recalled in Fig. 5.23, together with the volumetric adsorption isotherms. From these figures it is clear that textural properties, especially porosity, play an important role in determining the adsorption properties of used supports.

The most promising materials for this kind of application are ordered mesoporous materials, in which mesopores with dimensions in the 30-90 Å range seems to be important for the adsorption of significant amount of toluene.

It is possible to observe that at pressures of *ca.* 27 mbar, MCM-41 showed higher adsorption capacity (*ca.* +16 Q%) than SBA-15. This higher adsorption capacity of MCM-41 silica at this pressure was associated to the filling of the fraction mesopores between 20-65 Å (see Figure 5.23A, curve c) where the correlated mesoporous fraction volume resulted higher (+63%, compared to SBA-15), see table 5.6.

Contrarily, at higher pressures of 27 mbar, SBA-15 showed higher adsorption capacity (*ca.* +12 Q%) than MCM-41. This higher adsorption capacity of toluene of SBA-15 was associated with the filling of the second family of homogenous pores between 65 to 100 Å (see Figure 5.23A, curve d) where the correlated mesoporous fraction volume resulted higher (+78% compared to MCM-41), see table 5.6.

From these important results, it was possible to conclude that pore distributions play an important role on the adsorption properties of these ordered mesoporous silicas.

References

- [1] C. Rizzo, A. Carati, M. Tagliabue, C. Perego, *Stud. Surf. Sci. Catal.*, 2000, 128, 613.
- [2] G. Bellussi, C. Perego, A. Carati, S. Peratello, E. Previde Massara, G. Perego, *Stud. Surf. Sci. Catal.*, 1994, 84, 85-92.
- [3] M. Maretto, R. Vignola, C. D. Williams, R. Bagatin, A. Latini, M. Petrangeli Papini, *Microporous and Mesoporous Materials*, 2015, 203, 139–150.
- [4] H. Keskinen, S. Romakkaniemi, A. Jaatinen, P. Miettinen, E. Saukko, J. Jorma, J. M. Makela, A. Virtanen, J. N. Smith, and A. Laaksonen, *Aerosol Science and Technology*, 2011, 45,1441–1447.
- [5] V. M. Gun'ko, I. F. Mironyuk, V. I. Zarko, E. F. Voronin, V. V. Turov, E. M. Pakhlov, E.V. Goncharuk, Y. M. Nychiporuk, N. N. Vlasova, P. P. Gorbik, O. A. Mishchuk, A. A. Chuiko, T. V. Kulik, B. B. Palyanytsya, S. V. Pakhovchishin, J. Skubiszewska-Zieba, W. Janusz, A. V. Turov, R. Leboda, *Journal of Colloid and Interface Science*, 2005, 289, 427–445.
- [6] Wiley-VCH Verlag, Silica, amorphous, The MAK-Collection for Occupational Health and Safety, 2012 Vol 2, pp 157-179.
- [7] Wiley-VCH, Verlag Silica, amorphous, MAK Value Documentation, Published in the series Occupational Toxicants, Vol. 2 (1991)
- [8] M. Thommes, K. Kaneko, A.V. Neimark, J. P. Olivier, F. Rodriguez-Reinoso, J. Rouquerol, K. S.W. Sing, *Pure Appl. Chem.*, 2015, 87, 9-10, 1051–1069.
- [9] K.-M. Li, J.-G. Jiang, S.-C. Tian, X.-J. Chen, and F. Yan, *J. Phys. Chem. C*, 2014, 118, 2454–2462.
- [10] A. Burneau, O. Barrès, J. P. Gallas, J. C. Lavalley, *Langmuir*, 1990, 6, 1364-1372.
- [11] J.-P. Gallas, J.-M. Goupil, A. Vimont, J.-C. Lavalley, B. Gil, J.-P. Gilson, O. Miserque, *Langmuir*, 2009, 25, 5825–5834.
- [12] V. Sacchetto, C. Bisio, D. F. Olivas Olivera, G. Paul, G. Gatti, I. Braschi, G. Berlier, M. Cossi, L. Marchese. *J. Phys. Chem. C*, 2015, 119, 24875–24886.
- [13] N. B. Colthup, L. H. Daly, S. Wiberley, Introduction to Infrared and Raman Spectroscopy, Academic Press, San Diego CA, 1990.
- [14] C. Perego, S. Amarilli, A. Carati, C. Flego, G. Pazzuconi, C. Rizzo and G. Bellussi, *Microporous and Mesoporous Materials*, 1999, 27, 345–354.
- [15] A. Carati , G. Ferraris, M. Guidotti, G. Moretti, R. Psaro, C. Rizzo, *Catalysis Today*, 2003, 77, 315–323.
- [16] S. Lowell, J. E. Shields, M. A. Thomas, M. Thommes, Characterization of porous solids and powders: surface area, pore size and density, Kluwer Academic Publishers, USA, 2003.

- [17] B. Gouze, J. Cambedouzou, S. Parrès-Maynadié, D. Rébiscoul, *Microporous and Mesoporous Materials*, 2014, 183, 168-176.
- [18] M. W. Hahn, J. R. Copeland, A. H. van Pelt, C. Sievers, *ChemSusChem*, 2013, 6, 2304-2315.
- [19] D. Massiot, F. Fayon, M. Capron, I. King, S. Le Calve, B. Alonso, J.-O. Durand, B. Bujoli, Z. Gan, G. Hoatson. *Magn. Reson. Chem.*, 2002, 40 (1), 70-76.
- [20] X.S. Zhao, G. Q. Lu, and G.L. Millar, *Ind. Eng. Chem. Res.*, 1996, 35, 2075-2090.
- [21] F. Zhang, Y. Yan, H. Yang, Y. Meng, C. Yu, B. Tu, and D. Zhao, *J. Phys. Chem. B*, 2005, 109, 8723-8732.
- [22] R. Ryoo, C. H. and Ko, *J. Phys. Chem. B*, 2000, 104, 11465.
- [23] P. F. Fulvio, S. Pikus, M. Jaroniec, *J. Mater. Chem.*, 2005, 15, 5049-5053.
- [24] D. Zhao, Q. Huo, J. Feng, B. F. Chmelka, and G. D. Stucky, *J. Am. Chem. Soc.*, 1998, 120, 6024-6036.
- [25] A. Galarneau, M. Nader, F. Guenneau, F. Di Renzo, and A. Gedeon, *J. Phys. Chem. C*, 2007, 111, 8268-8277
- [26] D. Zhao, Q. Huo, J. Feng, B.F. Chmelka, and G.D. Stucky, *J. Am. Chem. Soc.*, 1998, 120, 6024-6036.
- [27] R. Atchudan, S. Perumal, T. Nesakumar, J. I. Edison and Y. R. Lee, *RSC Adv.*, 2015, 5, 93364-93373
- [28] A. Trouvé, I. Batonneau-Gener, S. Valange, M. Bonne, S. Mignard, *Journal of Hazardous Materials*, 2012, 201– 202, 107– 114
- [29] P. I. Ravikovitch, S. C. Domhnaill, A. V. Neimark, F. Schuth, and K. K. Unger, *Langmuir*, 1995, 11, 4765-4772.
- [30] M. Kruk and M. Jaroniec, *Adsorption*, 2000, 6, 47–51.
- [31] Y.-Q. Yeh, H.-P. Lin, C.-Y. Tang, C.-Y. Mou, *Journal of Colloid and Interface Science*, 2011, 362, 354–366.
- [32] K. Morishige and Y. Kanzaki, *J. Phys. Chem. C*, 2009, 113, 14927–14934.
- [33] W. Zhang, Z. Qu, X. Li, Y. Wang, D. Ma, J. Wu, *Journal of Environmental Sciences*, 2012, 24, 520–528

Chapter VI

Experimental Determination of the Molar Absorption Coefficient of Toluene on Mesoporous Silicas

6.1 Introduction

This chapter is focused to the determination of molar absorption coefficient (ϵ) of toluene adsorbed on mesoporous silicas with different textural properties (*i.e.* amorphous silica (FUMED) and ordered mesoporous MCM-41 and SBA-15 silicas). This was carried out by combining the results reported in the previous chapter (IR and volumetric analysis of adsorbed toluene) and adopting the method already described for the adsorption of toluene and *n*-hexane on microporous materials^[1] (see Chapter V).

For this purpose, the IR adsorption experiment of toluene on silica-based materials (FUMED, MCM-41 and SBA-15) were repeated five times, every time on different pellets of each solid, in order to reduce experimental errors.

6.2 Determination of molar absorption coefficient of toluene on mesoporous silica-based materials

The molar absorption coefficient ϵ [cm mmol^{-1}] of the vibrational modes at 1605 and 1380 cm^{-1} of toluene adsorbed on silica-based materials were determined by using the same experimental method used for the determination of the molar absorption coefficient of *n*-hexane captured in HSZ-Y and ZSM-5 zeolites,^[1] described in the Chapter IV (paragraph 4.2) by combining quantitative volumetric measures and IR spectroscopy data. Therefore, the Beer-Lambert law for solids was applied.

6.2.1 Experimental determination of molar absorption coefficient of toluene on FUMED amorphous silica

In Figure 6.1A the difference IR spectra of toluene adsorbed on FUMED silica at selected pressures (2, 15 and 27 mbar) in the range of frequency between 1700 to 1300 cm^{-1} is reported. The adsorption experiments followed by FTIR were performed on dehydrated solids. The dehydration under vacuum at BT for 30 min was sufficient to remove the water molecules from the mesoporous silica.

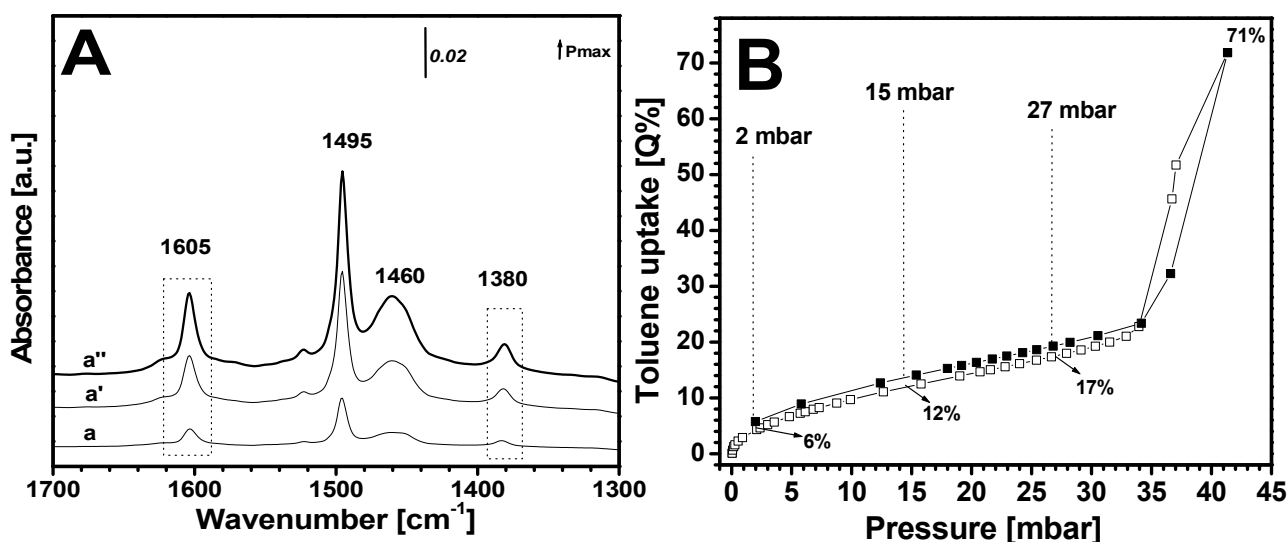


Figure 6.1: A: IR spectra in difference mode (after subtracting the bare solid) of toluene adsorbed on FUMED (b–b'') silica at pressures of 2 (a,b), 15 (a',b'), and 27 mbar (a'',b'') of toluene. B: toluene volumetric adsorption (empty symbols) and desorption (full symbols) isotherms on FUMED.

As previously reported, the band at 1605 cm^{-1} is due to the quadrant stretching mode of the monosubstituted ring C=C bond whereas the band at 1495 cm^{-1} is associated with the semicircular stretching vibration of monosubstituted aromatic ring. The bands at 1460 and 1380 cm^{-1} correspond to the out-of-phase and in-phase deformations of the methyl group.^[2] The single vibrational bands at 1605 and 1380 cm^{-1} were preferred for determination of the molar absorption coefficient of toluene adsorbed on both on FUMED silica due to that the bands at 1495 and 1460 cm^{-1} are heavily overlapped.

The integrated absorbances (IA) of the IR selected bands (at 1605 and 1380 cm^{-1}) were obtained by subtracting the spectrum of the bare materials outgassed from the spectra of adsorbed toluene, in order to avoid the contribution of absorbances of the materials.

The concentrations (uptake) of the adsorbed toluene on FUMED at definite pressure were obtained by means of volumetric analysis.

The average value of the five repeated IR measurements of the integrated area [\bar{A}] at $\tilde{\nu} = 1605$ and 1380 cm^{-1} and the uptakes% at a determined absolute pressure of toluene adsorbed on amorphous FUMED silica are reported in Table 6.1.

Table 6.1: Toluene adsorbed on FUMED non-porous silica. Pressures, integrated areas of the bands at 1605 and 1380 cm^{-1} (determined as an average of 5 repeated measurements), and uptake of toluene at increasing pressures (evaluated by volumetric analysis).

Non-Porous System				
FUMED				
P	\bar{A}_{1605}	\bar{A}_{1380}	Uptake	
[mbar]	[cm^{-1}]	[cm^{-1}]	[mmol g^{-1}]	[%]
0.50	0.41	0.15	0.23	2.27
1.00	0.47	0.18	0.33	3.01
2.00	0.68	0.25	0.46	4.26
3.00	0.84	0.31	0.57	5.22
4.00	0.97	0.36	0.65	6.03
5.00	1.10	0.41	0.73	6.75
6.00	1.20	0.45	0.80	7.39
7.00	1.30	0.48	0.87	7.99
8.00	1.40	0.53	0.93	8.54
9.00	1.48	0.56	0.98	9.07
10.00	1.58	0.60	1.05	9.68
11.00	1.66	0.63	1.09	10.02
12.00	1.73	0.66	1.14	10.46
13.00	1.81	0.70	1.20	11.07
14.00	1.89	0.73	1.23	11.30
15.00	1.95	0.76	1.27	11.70
18.00	2.20	0.87	1.39	12.82
21.00	2.45	0.97	1.59	14.66
23.00	2.59	1.04	1.69	15.57
24.00	2.66	1.06	1.75	16.12
25.00	2.77	1.10	1.82	16.76
27.00	2.97	1.20	1.88	17.35
30.00	3.09	1.26	2.09	19.25

In order to separate the different contributions, the molar absorption coefficients (ϵ) of toluene adsorbed on FUMED silica were first determined over a specific range of pressures, where the correlation between the integrated absorption (IA) bands at $\tilde{\nu} = 1605$ and 1380 cm^{-1} and the amount of toluene adsorbed molecules [mmol g^{-1}] was linear, as in the case for the determination of the molar absorption coefficient of *n*-hexane captured in zeolites (Chapter IV). These pressure ranges were

determined experimentally by comparing the IA values at $\tilde{\nu} = 1605$ and 1380 cm^{-1} with the concentration of adsorbed toluene on amorphous FUMED silica (Figure 6.2).

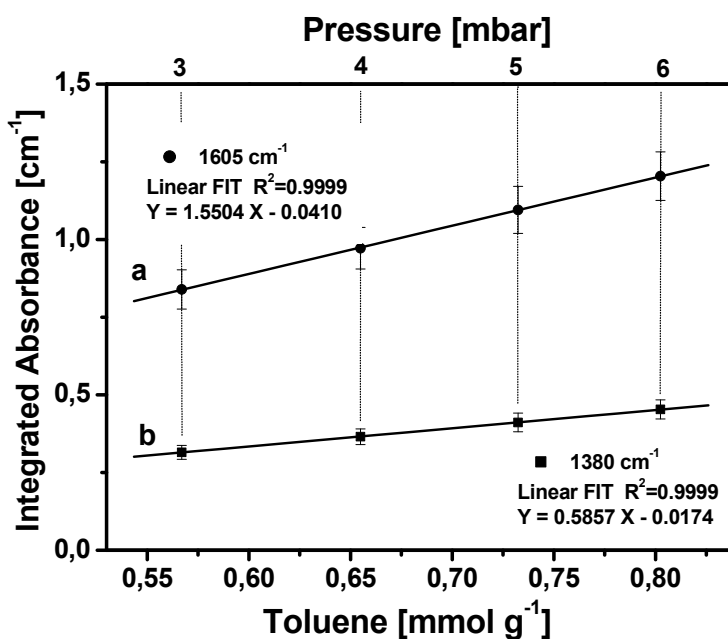


Figure 6.2: Dependence of the integrated absorbance (cm^{-1}) at 1605 cm^{-1} (fits a, i.e. the IR stretching mode of the monosubstituted ring C=C bond) and for the band at 1380 cm^{-1} (fits b, i.e. the IR in-phase deformations mode of the methyl of toluene) versus the amount of toluene adsorbed on FUMED.

Linear fitting for both experimental data sets shows high coefficients of correlation (R^2), as reported in Figure 6.2. Error bars have been determined on the basis of repeated experiments (5 repeated IR adsorption experiments for each support). This pressure range correspond to the formation of a statistical monolayer of toluene molecules on amorphous FUMED silica. Indeed, as in the case of *n*-hexane (see paragraph 4.2.), by applying the linearized BET equation^[3] to the volumetric isotherm reported in Figure 6.1B, it was also possible to derive the range of pressure at which the guest–guest interactions contribute are avoided.

The linearized BET equation shows that the monolayer is formed between 3-6 mbar for FUMED (Fig. 6.3). High coefficient of correlation (R^2), is reported in Figure 6.3 derived from linear curve-fitting procedures. This range is in good agreement with those found by the linear correlation between the experimental integrated absorption bands IA at $\tilde{\nu} = 1605$ and 1380 cm^{-1} and toluene uptake (Figure 6.2).

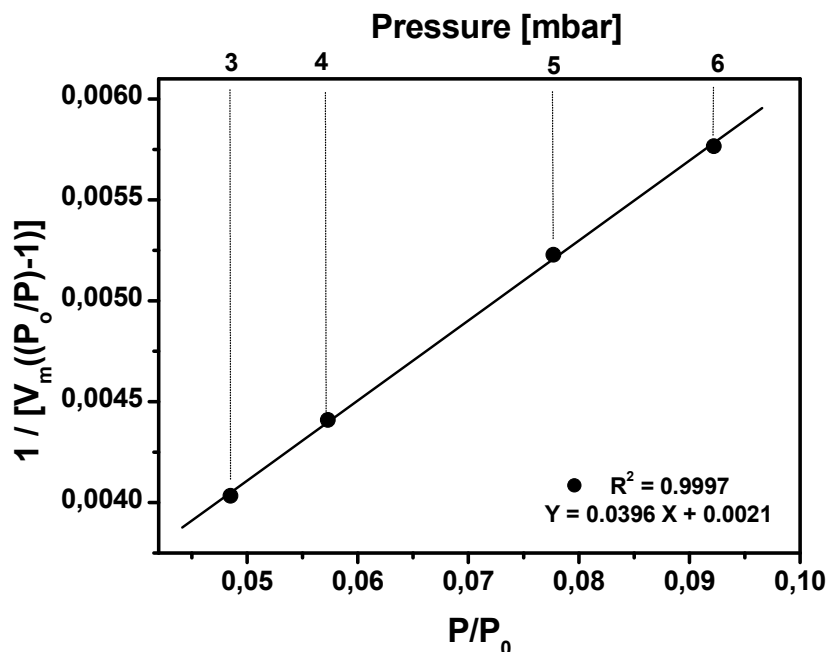


Figure 6.3: Linearized BET plot relative to the volumetric isotherms of toluene adsorption on FUMED.

As also calculated for toluene adsorbed on HSZ-Y and ZSM-5 zeolites (Chapter VI), the value of the C constant, which is a measure of the affinity of toluene adsorbed on the surface, was also derived from the BET algorithm and reported in table 6.2.

Table 6.2: Values of C constant of toluene for FUMED; and the value of $\Delta H_{(Ads1-Cond)}$ (difference in the heat of adsorption of the first layer and the heat of condensation)

Samples	C	$\Delta H_{(Ads1-Cond)}$ [kJ mol ⁻¹]
FUMED	20	7.68

The C value for amorphous FUMED silica is lower than those measured for HSZ-Y and ZSM-5 zeolites (C values of 429 and 214, respectively, as reported in the Chapter IV). This is an indication of the fact that toluene has greater affinity to zeolite structures, respect to FUMED.

These low values of C indicate that the heat of adsorption of the monolayer is not significative compared with the heat of adsorption of the subsequent layers (heat of condensation).^[4] Indeed, small value of the difference between the heat of adsorption of the first layer and the heat of condensation $\Delta H_{(Ads1-Cond)}$ [kJ mol⁻¹] was obtained for the FUMED (table 6.2). This value was calculated by considering the values of C as in the case of toluene on zeolites (see Chapter IV).

The $\Delta H_{(\text{Ads1-Cond})}$ for the FUMED is 7.68 kJ mol^{-1} . This calculated value for FUMED is lower than those measured for HSZ-Y and ZSM-5 zeolites (15.53 and $13.75 \text{ kJ mol}^{-1}$ for HSZ-Y and ZSM-5, respectively). This confirms that zeolites have higher adsorption energies due to the high affinity for toluene than amorphous silicas.

The average values of ϵ_i of the bands at $\tilde{\nu} = 1605$ and 1380 cm^{-1} , calculated by applying Beer-Lambert law for solids over the selected range of pressure for adsorbed toluene on amorphous FUMED silica are reported in Table 6.3.

Table 6.3: The average values of ϵ_i of the band at $\tilde{\nu} = 1605$ and 1380 cm^{-1} of toluene adsorbed on FUMED amorphous silica with their standard deviations.

Samples	$\epsilon_{1605} [\text{cm } \mu\text{mol}^{-1}]$	$\epsilon_{1380} [\text{cm } \mu\text{mol}^{-1}]$
FUMED	0.162 ± 0.010 (6.4%)	0.061 ± 0.004 (6.5%)

Interestingly, the ϵ_i of toluene adsorbed on FUMED resulted smaller than those measured for HSZ-Y and ZSM-5 zeolites —72% larger for ϵ_{1605} of toluene adsorbed on HSZ-Y (see the Chapter IV, paragraph 4.3), probably due that the dipole moment of adsorbed toluene is less influenced of the textural properties of FUMED.

The same approach for the determination of the molar absorption coefficients in a specific range of pressure was also used to the full available pressure range (*i.e.* from 2 to 27 mbar) and as reported in Table 6.4.

Table 6.4. Molar Adsorption coefficients ϵ_i of the bands at $\tilde{\nu} = 1605$ and 1380 cm^{-1} of toluene on FUMED amorphous silica at different pressures.

Samples	$\epsilon_{1605} [\text{cm } \mu\text{mol}^{-1}]$ toluene			
	2 mbar	9 mbar	15 mbar	27 mbar
FUMED	0.159 ± 0.010	0.163 ± 0.010	0.167 ± 0.011	0.171 ± 0.010
Samples	$\epsilon_{1380} [\text{cm } \mu\text{mol}^{-1}]$ toluene			
	2 mbar	9 mbar	15 mbar	27 mbar
FUMED	0.060 ± 0.004	0.062 ± 0.004	0.065 ± 0.004	0.069 ± 0.005

6.2.2 Experimental determination of molar absorption coefficient of toluene on SBA-15 and MCM-41 order mesoporous silica

As stated above, the determination of molar absorption coefficient (ϵ) of toluene adsorbed on ordered mesoporous SBA-15 and MCM-41 silicas were also calculated.

In Figure 6.4A is reported the difference IR spectra of toluene adsorbed on SBA-15 and MCM-41 silica at selected pressures (2, 15 and 27 mbar) in the range of frequency between 1700 to 1300 cm^{-1} . The adsorption experiments followed by FTIR were performed on dehydrated solids. The dehydration under vacuum at 150 °C for 1h for SBA-15 and at BT for 30 min were sufficient to remove the water molecules from both ordered mesoporous silicas.

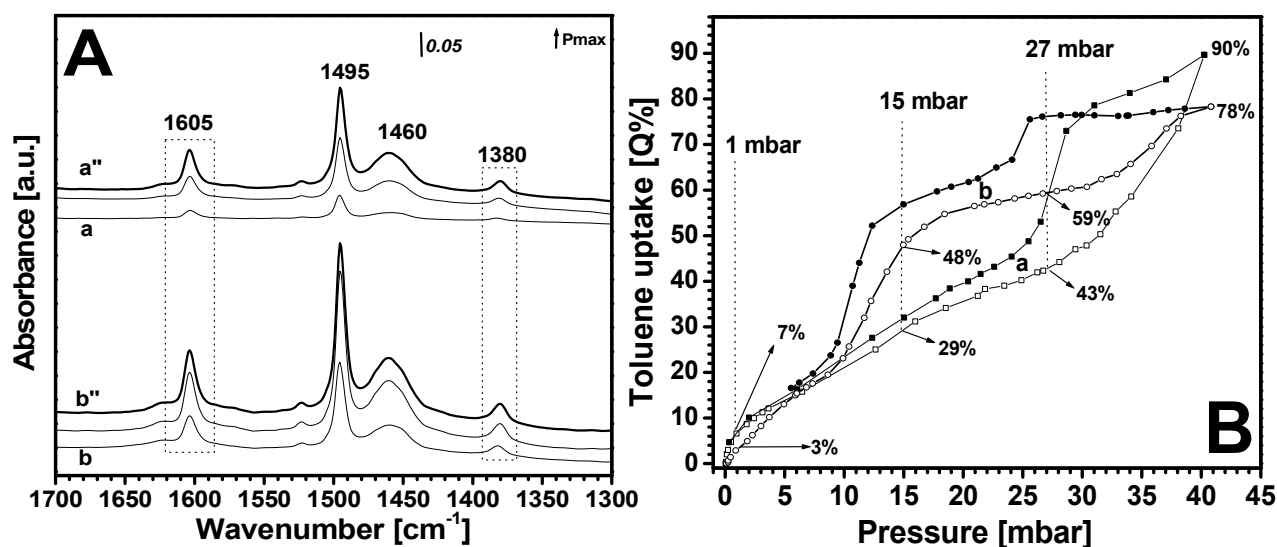


Figure 6.4: A: IR spectra in difference mode (after subtracting the bare solid) of toluene adsorbed on SBA-15 (a–a'') and MCM-41(b–b'') ordered mesoporous silica at pressures of 2 (a,b), 15 (a',b'), and 27 mbar (a'',b'') of toluene. B: Toluene volumetric adsorption (empty symbols) and desorption (full symbols) isotherms on SBA-15 (curve a) and MCM-41 (curve b).

As previously reported, the bands at 1605, 1495, 1460 and 1380 cm^{-1} are associated to related to the molecule vibrations (*i.e.*, stretching modes of the monosubstituted ring C=C bond and the monosubstituted aromatic and the deformations of the methyl group) at positions similar to those detected upon adsorption on amorphous silica (see above) and zeolites detailed in our previous work.^[2]

The concentrations (uptake) of the adsorbed toluene at definite pressure were obtained separately by means of volumetric analysis for both ordered mesoporous silica, reported in Figure 6.4Bcd.

The average value of the five repeated IR measurements of the integrated area [\bar{A}] at $\tilde{\nu} = 1605$ and 1380 cm^{-1} (obtained by subtracting the spectrum of the bare materials outgassed from the spectra of adsorbed toluene) and the uptakes% at a determined absolute pressure of toluene adsorbed on both SBA-15 and MCM-41 silica are reported in Table 6.5.

Table 6.5: Toluene adsorbed on SBA-15 and MCM-41 ordered mesoporous silica. Pressures, integrated areas of the bands at 1605 and 1380 cm^{-1} (determined as an average of 5 repeated measurements), and uptake of toluene at increasing pressures (evaluated by volumetric analysis).

Mesoporous System									
SBA-15					MCM-41				
P	\bar{A}_{1605}	\bar{A}_{1380}	Uptake		P	\bar{A}_{1605}	\bar{A}_{1380}	Uptake	
[mbar]	[cm^{-1}]	[cm^{-1}]	[mmol g^{-1}]	[%]	[mbar]	[cm^{-1}]	[cm^{-1}]	[mmol g^{-1}]	[%]
0.50	0.38	0.13	0.51	4.69	1.00	0.41	0.11	0.50	4.57
1.00	0.42	0.14	0.86	7.90	2.00	0.73	0.23	0.73	6.68
2.00	0.56	0.20	1.01	9.34	3.00	0.95	0.31	0.95	8.80
3.00	0.66	0.24	1.17	10.79	4.00	1.14	0.39	1.18	10.91
4.00	0.76	0.28	1.33	12.24	5.00	1.35	0.48	1.41	13.03
5.00	0.83	0.31	1.49	13.68	6.00	1.59	0.59	1.64	15.14
6.00	0.90	0.34	1.64	15.13	7.00	2.02	0.77	1.87	17.26
7.00	0.96	0.37	1.80	16.58	8.00	2.40	0.92	2.10	19.37
8.00	1.03	0.40	1.96	18.02	9.00	2.65	1.03	2.33	21.49
9.00	1.10	0.43	2.11	19.47	10.00	2.73	1.06	2.56	23.60
10.00	1.21	0.47	2.27	20.92	11.00	2.77	1.08	2.79	25.72
11.00	1.28	0.50	2.43	22.36	12.00	2.79	1.09	3.87	35.68
15.00	1.56	0.62	3.06	28.15	14.00	2.84	1.11	4.57	42.08
18.00	1.79	0.71	3.53	32.49	15.00	2.86	1.12	5.21	47.97
21.00	2.08	0.83	3.99	36.79	18.00	2.90	1.13	5.94	54.73
23.00	2.22	0.89	4.23	39.01	21.00	2.94	1.15	6.13	56.50
25.00	2.30	0.92	4.36	40.22	26.00	3.01	1.18	6.37	58.72
27.00	2.33	0.94	4.59	42.32	30.00	3.04	1.20	6.59	60.70
30.00	2.35	0.95	5.19	47.83					

Figure 6.5 shows that linear trends between the integrated absorption bands (IA) at $\tilde{\nu} = 1605$ and 1380 cm^{-1} and the amount of toluene adsorbed molecules [mmol g^{-1}] SBA-15 (Fig. 6.5A) and for MCM-41 (Fig. 6.5B) in the range between 2-7 and 2-6mbar, respectively. Linear fitting for both experimental data sets show high coefficients of correlation (R^2), as reported in Figure 5.9. Error bars have been determined on the basis of repeated experiments (5 repeated IR adsorption experiments for each support).

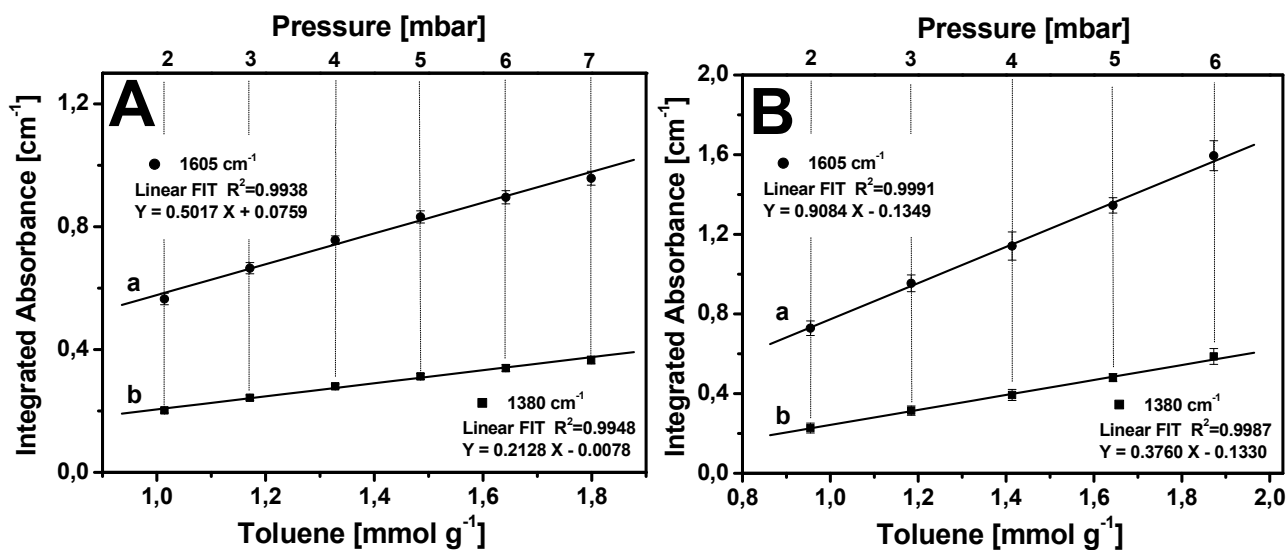


Figure 6.5: Dependence of the integrated absorbance (cm⁻¹) at 1605 cm⁻¹ (fits a, *i.e.* the IR stretching mode of the monosubstituted ring C=C bond) and for the band at 1380 cm⁻¹ (fits b, *i.e.* the IR in-phase deformations mode of the methyl of toluene) versus the amount of toluene adsorbed on SBA-15 (A) and MCM-41 (B).

The linearized BET equation shows that the monolayer is formed between 2-7 mbar for SBA-15 (Fig. 6.6B) and 4-7 mbar for MCM-41 (Fig. 6.6A). High coefficients of correlation (R^2), as reported in Figure 6.6 derived from linear curve-fitting procedures. These ranges are in good agreement with those found by the linear correlation between the experimental integrated absorption (IA) of the bands at $\tilde{\nu} = 1605$ and 1380 cm⁻¹ and toluene uptake (Figure 6.5 A,B).

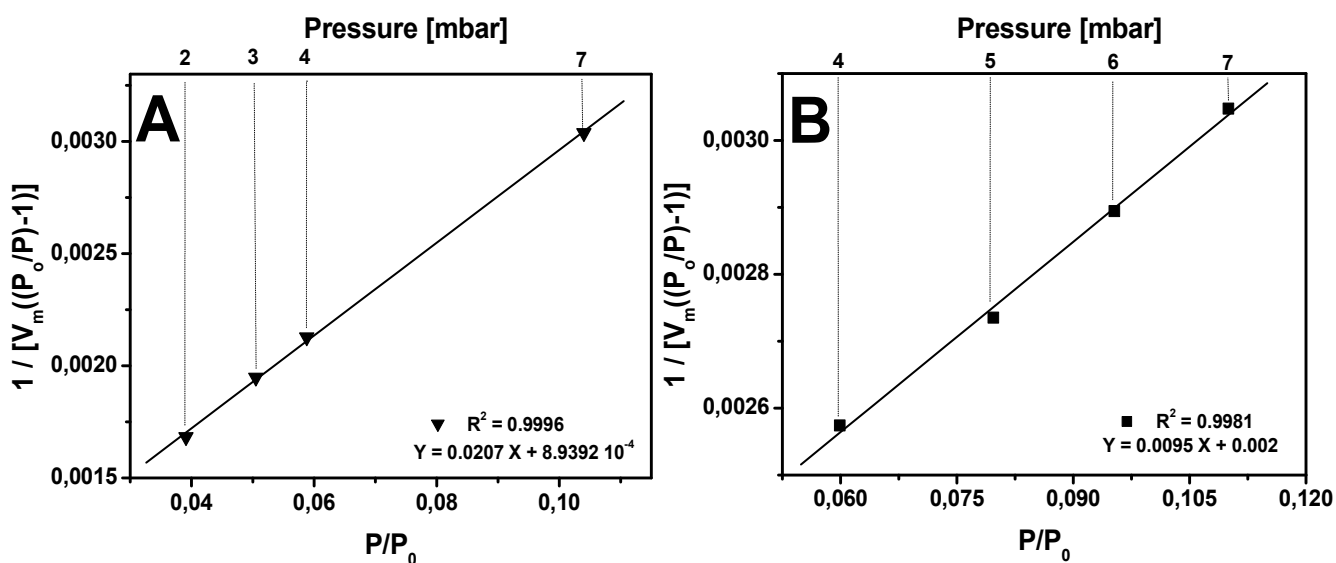


Figure 6.6: Linearized BET plot relative to the volumetric isotherm of toluene adsorption on SBA-15 silica(A) and MCM-41 (B).

The values of the C constants of toluene adsorbed on the ordered mesoporous surface, were also derived from the BET algorithm and reported in table 6.6.

Table 6.6: Values of C constants of toluene for both SBA-15 and MCM-41; and their values of $\Delta H_{(Ads1-Cond)}$ (difference in the heat of adsorption of the first layer and the heat of condensation).

Samples	C	$\Delta H_{(Ads1-Cond)}$ [kJ mol ⁻¹]
SBA-15	24	8.14
MCM-41	87	11.44

The values of C for order mesoporous silica (MCM-41 and SBA-15) were lower respect to those calculated for zeolites. This clearly confirms that toluene molecules have greater affinity to zeolite structures, respect to ordered mesoporous silica. In addition, low values of C for MCM-41 and SBA-15 silica gave small differences of the heat of adsorption of the first layer and the heat of condensation $H_{(Ads1-Cond)}$ [kJ mol⁻¹]^[4] which are 11.44 and 8.14 kJ mol⁻¹ for MCM-41 and SBA-15, respectively. These calculated values for both MCM-41 and SBA-15 are lower than those measured for HSZ-Y and ZSM-5 zeolites (15.53 and 13.75 kJ mol⁻¹ for HSZ-Y and ZSM-5, respectively). This confirms that zeolites have higher adsorption energies due to the high affinity for toluene than ordered mesoporous silica.

The average values of ϵ_i of the bands at $\tilde{\nu} = 1605$ and 1380 cm⁻¹, calculated by applying Beer-Lambert law for solids over the selected range of pressure for adsorbed toluene on both ordered mesoporous SBA-15 and MCM-41 silica are reported in Table 6.7.

Table 6.7: The average values of ϵ_i of the band at $\tilde{\nu} = 1605$ and 1380 cm⁻¹ of toluene adsorbed on MCM-41 and SBA-15 with their standard deviations.

Samples	ϵ_{1605} [cm μmol^{-1}]	ϵ_{1380} [cm μmol^{-1}]
SBA-15	0.256 ± 0.008 (3.3%)	0.095 ± 0.004 (3.7%)
MCM-41	0.296 ± 0.014 (4.9%)	0.101 ± 0.008 (8.1%)

Interestingly, the ϵ_i of toluene adsorbed are different for the ordered mesoporous SBA-15 and MCM-41) and higher than that calculated for FUMED —83% larger for ϵ_{1605} of toluene adsorbed on MCM-

41, and this means that the textural properties of ordered mesoporous silicas (in particular, their pore dimensions) influence the dipole moment of adsorbed molecules.

The same approach for the determination of the molar absorption coefficients in a specific range of pressure was also used to the full available pressure range (*i.e.* from 2 to 27 mbar) and as reported in Table 6.8.

Table 6.8. Molar Adsorption coefficients ϵ_i of the bands at $\tilde{\nu} = 1605$ and 1380 cm^{-1} of toluene on MCM-41 and SBA-15 ordered mesoporous silica at different pressures.

Samples	$\epsilon_{1605} [\text{cm } \mu\text{mol}^{-1}] \text{ toluene}$			
	2 mbar	9 mbar	15 mbar	27 mbar
SBA-15	0.256±0.009	0.240±0.005	0.236±0.005	0.233±0.023
MCM-41	0.304±0.015	0.343±0.027	0.170±0.018	0.141±0.013
Samples	$\epsilon_{1380} [\text{cm } \mu\text{mol}^{-1}] \text{ toluene}$			
	2 mbar	9 mbar	15 mbar	27 mbar
SBA-15	0.092±0.004	0.093±0.003	0.094±0.002	0.094±0.010
MCM-41	0.095±0.010	0.133±0.009	0.066±0.006	0.056±0.005

6.3 Conclusions

This Chapter was focused on the description of the determination of the molar absorption coefficient of the bands at $\tilde{\nu} = 1605$ and 1380 cm^{-1} (ϵ_{1605} and ϵ_{1380}) of toluene adsorbed on amorphous and ordered mesoporous materials with different structural and textural properties (*i.e.* the volume and dimensions of pores) by applying the same methodology already described for *n*-hexane and toluene adsorbed on zeolites (see Chapter IV).

In the Table 6.9 are reported the average values of ϵ_i of the bands at $\tilde{\nu} = 1605$ and 1380 cm^{-1} , calculated by applying Beer-Lambert law for solids over the selected range of pressure for adsorbed toluene on mesoporous materials studied in this Chapter compared with those calculated for both zeolites in the Chapter IV.

Table 6.9: The average values of ϵ_i of the band at $\tilde{\nu} = 1605$ and 1380 cm^{-1} of toluene adsorbed on silica-based materials with their standard deviations.

Samples	$\epsilon_{1605} [\text{cm } \mu\text{mol}^{-1}]$	$\epsilon_{1380} [\text{cm } \mu\text{mol}^{-1}]$
FUMED	0.162 ± 0.010 (6.4%)	0.061 ± 0.004 (6.5%)
HSZ-Y	0.224 ± 0.017 (7.6%)	0.130 ± 0.009 (7.1%)
ZSM-5	0.378 ± 0.030 (8.0%)	0.219 ± 0.019 (8.8%)
SBA-15	0.256 ± 0.008 (3.3%)	0.095 ± 0.004 (3.7%)
MCM-41	0.296 ± 0.014 (4.9%)	0.101 ± 0.008 (8.1%)

Interestingly, the calculated molar absorption coefficients of toluene are different for each material. The differences on the values of molar absorption coefficients of toluene adsorbed suggest that the adsorbed molecules experience different adsorption environments inside the solids. This confirms that the pore structure of solids affects the dipole moment of the adsorbed molecules and consequently on the molar absorption coefficients.^[1]

The ϵ_i of toluene adsorbed on ZSM-5 resulted higher than that calculated on SBA-15 and MCM-41, this because of the limited space of microporous solids influences on the dipole moment of the adsorbed molecules.^[1]

Whereas, the ϵ_i of toluene adsorbed on both SBA-15 and MCM-41 resulted higher than that calculated on FUMED, this because the differences on the textural properties of ordered mesoporous silicas such as pore size distribution and mesoporous volumes.

Moreover, the ϵ_i of toluene adsorbed on both SBA-15 and MCM-41 resulted higher to the ϵ_i of toluene in gas phase concentration (determined in the Chapter IV: 0.217 ± 0.012 for the band $\tilde{\nu} = 1605 \text{ cm}^{-1}$ and $0.041 \pm 0.003 \text{ cm } \mu\text{mol}^{-1}$ for the band $\tilde{\nu} = 1380 \text{ cm}^{-1}$). This confirms the dipole moment at low doses of adsorbed toluene on these materials is influenced by the textural properties.

In Table 6.10 are reported the average values of ϵ_i of the bands at $\tilde{\nu} = 1605$ and 1380 cm^{-1} calculated in full available pressure range (*i.e.* from 2 to 27 mbar) for adsorbed toluene on the mesoporous materials studied in this Chapter compared with those calculated on zeolites in the Chapter IV.

Table 6.10: The average values of ϵ_i of the band at $\tilde{\nu} = 1605$ and 1380 cm^{-1} of toluene adsorbed on silica-based materials with their standard deviations at different pressures.

Samples	$\epsilon_{1605} [\text{cm } \mu\text{mol}^{-1}] \text{ toluene}$			
	2 mbar	9 mbar	15 mbar	27 mbar
HSZ-Y	0.224±0.020	0.217±0.020	0.213±0.020	0.220±0.020
ZSM-5	0.412±0.056	0.305±0.038	0.282±0.034	0.281±0.036
FUMED	0.159±0.010	0.163±0.010	0.167±0.011	0.171±0.010
SBA-15	0.256±0.009	0.240±0.005	0.236±0.005	0.233±0.023
MCM-41	0.304±0.015	0.343±0.027	0.170±0.018	0.141±0.013
	$\epsilon_{1380} [\text{cm } \mu\text{mol}^{-1}] \text{ toluene}$			
	2 mbar	9 mbar	15 mbar	27 mbar
HSZ-Y	0.131±0.011	0.125±0.011	0.122±0.011	0.124±0.010
ZSM-5	0.226±0.020	0.172±0.018	0.160±0.017	0.162±0.017
FUMED	0.060±0.004	0.062±0.004	0.065±0.004	0.069±0.005
SBA-15	0.092±0.004	0.093±0.003	0.094±0.002	0.094±0.010
MCM-41	0.095±0.010	0.133±0.009	0.066±0.006	0.056±0.005

As indicated by the results in Table 6.10, the different behaviors of the molar absorption coefficients of adsorbed toluene on all solids are probably due to their differences on the textural properties.

This effect is even more evident on ZSM-5, SBA-15 and MCM-41 on which molar absorption coefficients at low pressures resulted affected because the molecules interact predominantly with the solids surface (host–guest interactions) and the contribution of guest-guest interactions is reduced.

Increasing the pressure from 9 to 27 mbar of toluene inside the pores, the contribution of toluene-toluene interactions (guest-guest interactions) make the values of molar absorption coefficients keep constant.^[5]

References

- [1] G. Gatti, D.F. Olivas Olivera, V. Sacchetto, M. Cossi, I. Braschi, L. Marchese, and C. Bisio, *ChemPhysChem*, 2017, 18, 2374 – 2380.
- [2] V. Sacchetto, C. Bisio, D. F. Olivas Olivera, G. Paul, G. Gatti, I. Braschi, G. Berlier, M. Cossi, and L. Marchese, *J. Phys. Chem. C.*, 2015, 119, 24875–24886.
- [3] S. Lowell, J. E. Shields, M. A. Thomas, M. Thommes, *Characterization of Porous Solids in Powders: Surface Area, Pore Size and Density*, Kluwer, Dordrecht, 2004.
- [4] K. D. Hammond, Jr. , Wm. C. Conner, *Advances in Catalysis*, Academic Press, San Diego, 2013, (56), 1–101.
- [5] M. Chołuj and W. Bartkowiak, *Chemical Physics Letters*, 2016, 663, 84-89.

Chapter VII

Monitoring the Adsorption of Glyphosate on Porous Materials

7.1 Introduction

As reported in Chapter I, in relation to their wide range of application, herbicides are a continuous source of contamination. In particular, glyphosate-based herbicides are currently among the most widely used and this can also result in a consequent pollution of groundwater. ^[1]

Part of the research activity was then devoted to the study of the glyphosate adsorption on different silicas. This was possible thanks to a collaboration with Prof. Maria del Rosario Sun Kou of the Department of Sciences, Section Chemistry, Pontifical Catholic University of Perú. This collaboration made possible the testing of selected solids for the adsorption of a pollutant molecule from aqueous media, near the real working conditions.

Particular attention was devoted to the use of the SBA-15 mesoporous material. Moreover, a sample of SBA-15 silica functionalized with amino groups was also used as adsorbent. The functionalization was needed to introduce on the surface of the SBA-15 specific functionalities able to increase the affinity of the material for the glyphosate molecules (see Chapter I, paragraph 1.3.1.3).

7.2 Physico-chemical properties of SBA-15 and SBA-15-PAPTS

SBA-15 was prepared in our laboratories following the synthesis procedure described in Chapter V, paragraph 5.3.1.1. Part of the SBA-15 sample was then functionalized in order to introduce amino groups on the surface by using a post-synthesis grafting procedure (see Figure 7.1). In particular; SBA-15 was functionalized with the 3-[2-(2-aminoethyl)aminoethyl]aminopropyltrimethoxysilane (PAPTS, see Figure 7.1).

One aliquot of 1.0 g of SBA-15 silica was treated under vacuum at 200 °C for 2 h to remove physisorbed water. After this treatment, the sample was kept under N₂ flow and then dispersed in 100 mL of anhydrous toluene before the addition of the organic silane. 0.48 mL of N-[3-(trimethoxysilyl)propyl]-diethylenetriamine(PAPTS) (H₂N(CH₂)₂NH(CH₂)₂NH(CH₂)₃Si(OCH₃)₃, Sigma-Aldrich, MW = 265.43 g mol⁻¹) were added drop-by-drop to the SBA-15 suspension that was

then left for 20 h at 50 °C under magnetic stirring. After this, the sample was recovered by filtering, and the powder was washed with toluene and ethyl ether to remove the unreacted silane, and finally dried for overnight at 80 °C. [2] This sample hereafter will be named as SBA-15-PAPTS.

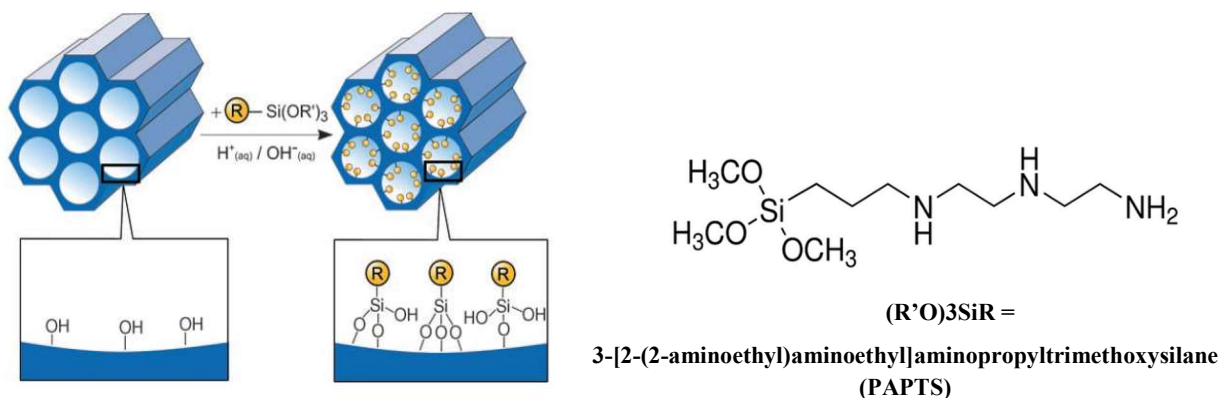


Figure 7.1: Scheme of the post-synthesis functionalization of pure ordered mesoporous silica with 3-[2-(2-aminoethyl)aminoethyl]aminopropyltrimethoxysilane (PAPTS). Adapted from reference.[3]

Specific surface area and pore size distribution of pure SBA-15 and the grafted SBA-15-PAPTS have been determined by N_2 adsorption at 77K. Adsorption/desorption isotherms and pore size distribution of both samples are reported in Figure 7.2.

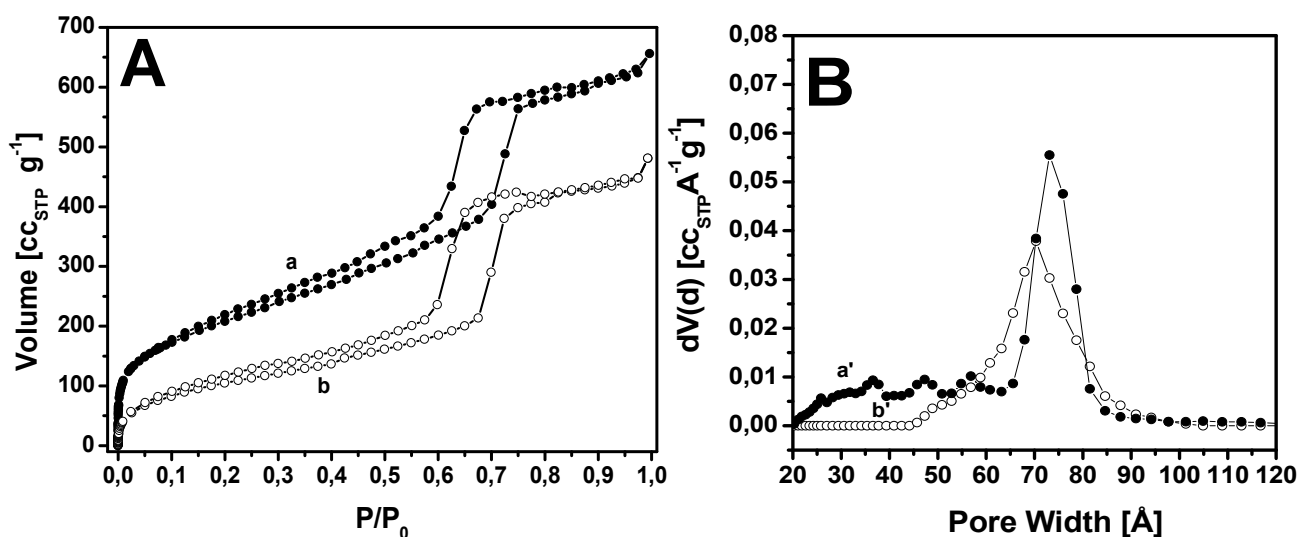


Figure 7.2: A: N_2 adsorption/desorption isotherms at 77K of SBA-15 and SBA-15-PAPTS (curves a and b, respectively); B: pore size distribution of SBA-15 and SBA-15-PAPTS (curves a' and b', respectively).

Adapted from Ref. [2]

According to the IUPAC classification ^[4], the N₂ adsorption isotherms of both SBA-15 samples (Figure 7.2A) is of type IV(a) which indicates the presence of mesoporosity. The hysteresis loop of both materials is of type H1 which is typical of samples with cylindrical pores.

The textural properties of SBA-15 samples are reported in Table 7.1.

Table 7.1: Main textural properties of SBA-15 and SBA-15-PAPTS

sample	SSA ^a _{BET} [m ² g ⁻¹]	SSA ^b _{mesop} [m ² g ⁻¹] 45-65Å	SSA ^b _{mesop} [m ² g ⁻¹] 65-100Å	V _p [cm ³ g ⁻¹]
SBA-15	761	114	295	0.96
SBA-15-PAPTS	236	79	145	0.41

^aBrunauer–Emmet–Teller (BET) specific surface area (SSA); ^bTotal pore volume and SSA_{mesop} by NLDFT method;

SBA-15 sample has a SSA of 761 m² g⁻¹ and a total pore volume of 0.96 cm³ g⁻¹. After the grafting procedure, SSA and total pore volume of the SBA-15 sample decrease to 236 m² g⁻¹ and the pore volume is reduced to 0.41 cm³ g⁻¹. The reduction of both SSA and pore volume is attributed to the presence of the organic species that limit the entrance of N₂ to the SBA-15 pores.^[2]

As observed in Figure 7.2B, pure SBA-15 (curve a') has a family of homogeneous pores between 65-100 Å with a maximum centered at 75 Å and a family of smaller pores from 20 to 65 Å. After the grafting procedure, the pore located at 75 Å shifts to ca. 70 Å (see Figure 7.2B, curve b'). In addition, the family of smaller pores located between 20 and 45 Å disappears. This is due to the fact that the introduction of long chain of the silanes into the pores of SBA-15 leads a reduction of pore size dimensions in favour of more disordered pore structures.^[2]

Surface properties of both SBA-15 samples were studied by IR spectroscopy.

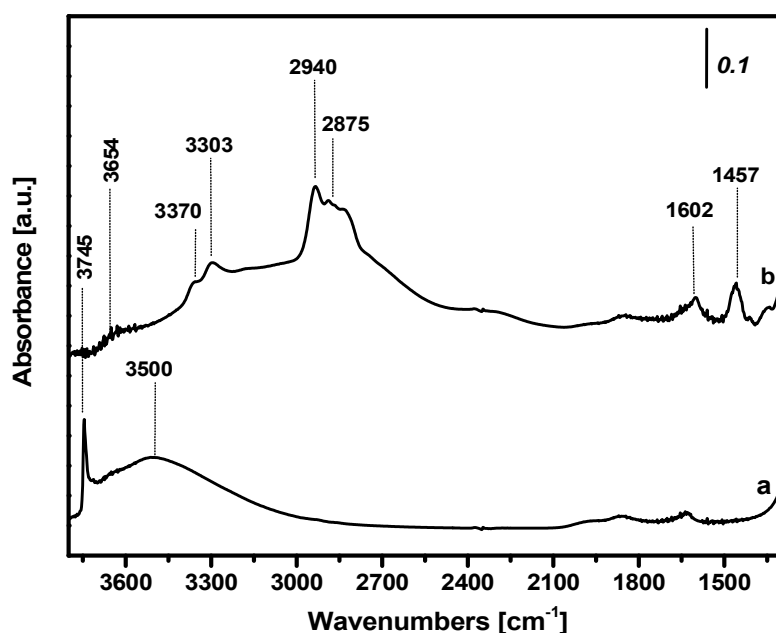


Figure 7.3: FTIR spectra of bare SBA-15 (curve a) and SBA-15-PAPTS(b), recorded after outgassing for 30 minutes at beam temperature (b.t.).

The IR spectrum of SBA-15 sample (Figure 7.3, curve a) presents an evident narrow peak at ca. 3745 cm^{-1} that can be assigned to isolated silanols, and a broad absorption extending from 3720-3200 cm^{-1} with a maximum around at 3500 cm^{-1} that corresponds to hydrogen-bonded silanols.

In the spectrum of grafted SBA-15-PAPTS sample (Fig. 7.3, curve b) present the bands related to SiOH species decrease of intensity due to the fact that they are used for the grafting procedure of PAPTS. Furthermore, it is also noticed the formation of a broad band in the 3600-2500 cm^{-1} with a maximum around at 3654 cm^{-1} which corresponds to the formation of hydrogen-bonding interactions between surface silanols and the amino groups of silane species introduced with the functionalization.^[2]

The IR spectrum of the SBA-15-PAPTS (Fig, 7.3, curve b) is also characterized by the presence of several absorption bands in the 3500–2500 cm^{-1} range. In particular, the absorption bands at 3370 and 3303 cm^{-1} are related to the asymmetric and symmetric stretching modes of NH_2 groups, respectively, whereas the bands at 2940 and 2875 cm^{-1} are assigned to the asymmetric and symmetric stretching modes of CH_2 moieties of the silane groups grafted onto the silica surface by the grafting procedure.^[2] The band at 1602 cm^{-1} is due to the scissoring mode of NH_2 groups, whereas the sharp band at 1457 cm^{-1} is associated to the bending modes of CH_2 groups.^[2]

It was estimated that the N content for SBA-15-PAPTS is ca. 3.5 mmol g^{-1} . In addition, concentration of silane molecules in SBA-15-PAPTS was also calculated by dividing the concentration of N by

three which is the number of nitrogen atoms present in the PAPTS chain, resulting of *ca.* 1.16 mmol g⁻¹.

It is known that the pH of the aqueous solution is a critical parameter affecting the adsorption process.^[5,6] The pH value determines the surface charge of the adsorbents, which will affect the interaction between with the glyphosate molecule.

The surface charges in a range of pH between 3 and 8 for SBA-15 and SBA-15-PAPTS were determined by Zeta potential (ξ) measurements (Figure 7.4). Before the analysis the silica samples were dispersed in ultrapure water (2 mg mL⁻¹) and the dispersions were sonicated for 10 min.

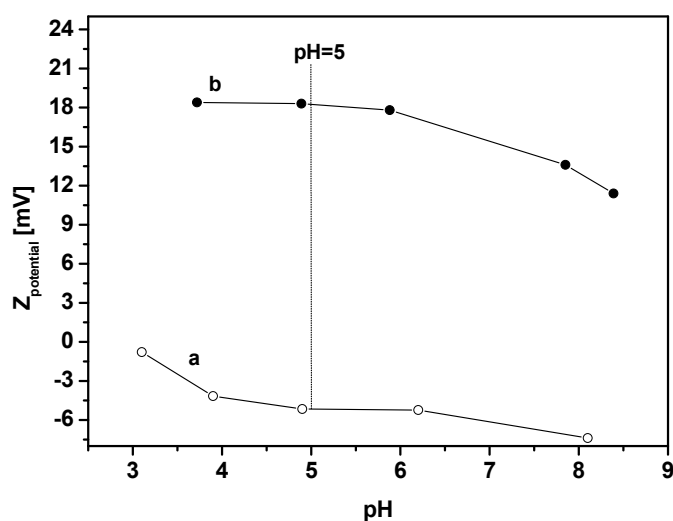


Figure 7.4: The Zeta potential of as SBA-15 and SBA-15-PAPTS as a function of pH at 25 °C.

As it can be seen from Fig. 7.4, at pH of adsorption conditions (pH=5), the SBA-15 shows a negative Z-potential (-5.12 mV) due to the presence of SiO⁻ species.^[7] In the presence of PAPTS the Z-potential becomes positive (18.17 mV) and this is a strong indication of the protonation of NH₂ groups in that conditions leading to the formation of NH₃⁺ species.

Table 7.2: Values of Z potential of SBA-15 and SBA-15-PAPTS at pH=5.0

sample	Z potential [mV] at pH=5
SBA-15	-5.12
SBA-15-PAPTS	18.17

7.3 Study of the adsorption of glyphosate from aqueous media

Few methods for the quantification of glyphosate such as gas-chromatography,^[8-10] GC/MS, ^[11,12] liquid-chromatography,^[13] HPLC,^[14] electrophoresis^[15] and current oscillographic titration^[16] are reported in the literature. Nevertheless, most of these analytical methods require expensive equipment.

In this Ph.D. thesis work the concentration of the glyphosate remaining in aqueous solutions after the adsorption experiments was determined by using UV–vis spectroscopy. This method was reported in the literature as a simple, fast, and accurate method for the determination of glyphosate.^[17]

Glyphosate molecule does not absorb in the UV–vis range due of the lack of a chromophore group in the molecule.^[18] For this reason, before the UV analysis, glyphosate must be derivatized as explained in the paragraph below.

The UV spectra were then recorded in the range of 190-900 nm and the concentrations of glyphosate after the adsorption experiments were obtained by using a calibration curve, which provided the linear relationship between maximum absorbances and the standard concentrations.

The Agilent UV–Vis spectrophotometer 8453 was used for this analysis.

7.3.1 Derivatization procedure

Chemical derivatization is an important procedure to modify the analytes into derivatives that can be more easily detected, improving the spectroscopic performance and sensitivity for trace analysis.^[19] Many reagents and conditions for derivatization of glyphosate have been proposed : 4-chloro-7-nitrobenzofurazan (NBD-Cl),^[20] 2,2-dihydroxy-1h-indene-1,3-(2h)-dione (Ninhydrin),^[21,22] 1-fluoro-2,4-dinitrobenzene (DNP),^[23] 9-fluorenylmethoxycarbonyl chloride (FMOC-Cl) ^[24-33]

The quantification of glyphosate was obtained by derivation with 9-fluorenylmethoxycarbonyl chloride (FMOC-Cl) in alkaline media. ^[17]

Glyphosate molecule has three functional groups: amine and carboxylate and phosphonate. In the derivatization reaction, the amine group reacts with FMOC-Cl to give the derivatized glyphosate (FMOC–glyphosate adduct) as reaction product, as shown in Figure 7.5, ^[34] which absorbs in the UV–vis of maximum absorbance at 265 nm (λ_{max}), due to the presence of two chromophores group (aromatic rings) in the FMOC molecule (see Figure 7.5). ^[28,16]

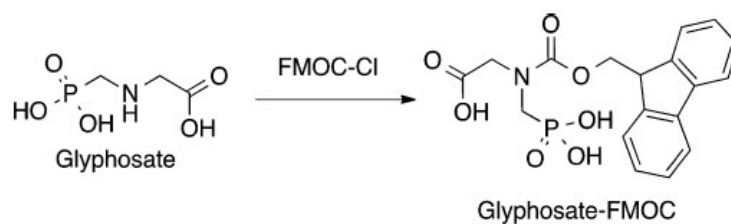


Figure 7.5: Reaction of Glyphosate with FMOC-Cl to the UV-Active Adduct. Adapted from reference. ^[34]

For the derivatization procedure of the aqueous glyphosate solutions, it was necessary to prepare a borate buffer solution at pH=9 by dissolving 1.5255 g of $\text{Na}_2\text{B}_4\text{O}_7 \cdot 10\text{H}_2\text{O}$ in 100 mL of Milli-Q water and a FMOC-Cl in acetonitrile solution with concentration of 1 g L^{-1} .

The procedure of the derivatization was performed directly in polypropylene centrifuge tubes by mixing 3 mL of the glyphosate solution with 0.5 mL of borate buffer and 0.5 mL of FMOC-Cl. The mixture was agitated and after 4 hours of reaction at room temperature was added 4 mL of dichloromethane. Finally, the mixture was centrifugated for 6 min at 1600 Rpm and the aqueous phase was separated. Dichloromethane was used to extract the excess of FMOC-Cl which could interfere with the spectrometric analysis. The aqueous phase, which contains the derivatization product, was quantified using UV-vis spectroscopy.

The glyphosate standard solutions were prepared by using analytical-standard purchased from Sigma-Aldrich. The borate buffer was prepared by using solution disodium tetraborate decahydrate ($\text{Na}_2\text{B}_4\text{O}_7 \cdot 10\text{H}_2\text{O}$) obtained from Merck. 9-fluorenyl methoxycarbonyl chloride (FMOC-Cl) was purchased from Sigma-Aldrich with a purity of 97%. Acetonitrile was purchased from J.T. Baker with HPLC grade. Dichloromethane of HPLC grade and KCl (analytical grade) were purchased from Merck.

7.3.2 Quantification of glyphosate by UV-vis analysis

Standard solutions with different glyphosate concentrations in the ranges of 1-10 and 1-30 mg L^{-1} for the kinetic and equilibrium adsorption experiments, respectively, in 0.1 M aqueous KCl (used as supporting electrolyte) solutions were prepared and used as references. The linearity of the concentration of the standard solutions and the experimental absorbances were evaluated by linear regression analysis, which was calculated by the least square regression method.

In Figure 7.6, the spectra of the standard glyphosate solutions in the range 1-10 mg L⁻¹ obtained after the derivatization procedure are reported.

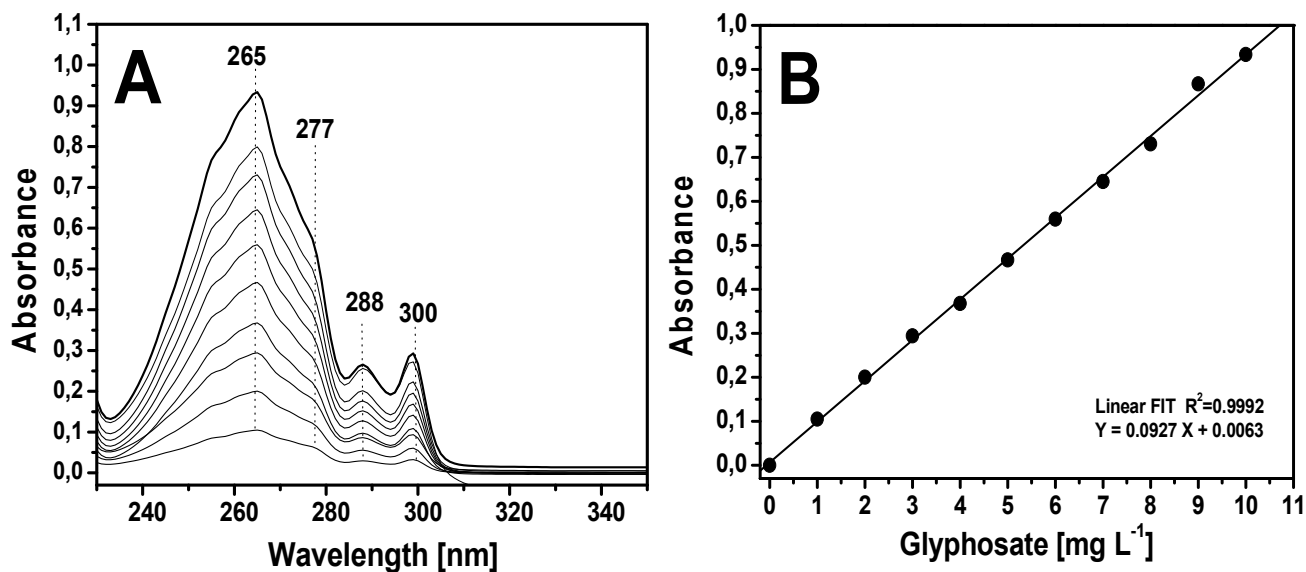


Figure 7.6: A: UV-vis spectra of derivatized glyphosate of different concentrations of the standard solutions [1-10 mg L⁻¹] of glyphosate. B: Dependence of maximum absorbance (λ_{max}) at 265 nm versus the concentration of the standard solutions.

As observed in the Figure 7.6A, the spectrum of the derivatized glyphosate presents four different bands; a broad band at 265 nm, a shoulder at 277 nm and two small bands located at 288 and 300 nm. All these bands are associated to (π - π^*) electronic transitions of aromatic rings present on the fluorenyl group.^[35] Linear fitting between the absorbance of the band at 265 nm and the concentration of glyphosate shows high coefficients of correlation (R^2), as reported in Figure 7.6B. A standard curve with fresh standard solutions, before each adsorption experiment.

7.4. Kinetic adsorption studies of glyphosate on SBA-15 silicas

Kinetics adsorption isotherms of glyphosate on SBA-15 and SBA-15-PAPTS were obtained from the adsorption measurements of glyphosate in contact with the selected solids in aqueous media. In order to reduce experimental errors associated with spectroscopic measurements, the batch adsorption experiments were replicated three times.

Batch kinetic experiments were carried out by using 20 mL standard solution of glyphosate [8 mg L⁻¹] and 50 mg of adsorbent, which were added to glass vials of 25 mL. The glass vials were subjected to shaking in ambient conditions by using Innova 2000 Platform Shaker at 300 RPM (see Figure 7.7A) at different adsorption contact times (t) ranging from 5 to 240 min.



Figure 7.7: A: Photography of the batch adsorption experiment of standard glyphosate solution in contact with each adsorbent. B: Photography of the filtering procedure after the contact time was completed

When the adsorption time of each glass vial was completed, the glyphosate solutions containing the adsorbents were filtered by using syringe filters of 0.45 μm and syringes (See Figure 7.7B). The liquid phase was then used for determination of the remaining concentrations of glyphosate (C_t) according the derivatization procedure and UV-vis analysis (standard curve prepared with standard solutions with concentrations in the ranges of 1-10 mg L^{-1} of glyphosate in 0.1 M aqueous KCl) explained in the paragraphs 7.3.1 and 7.3.2

The pH of the dispersions containing the glyphosate solution in contact with the selected solids was measured, resulting a value of 5.

The adsorption capacity q_t [mg g^{-1}] at contact time t [min] was determined according to equation 7.1

$$q_t = \frac{(C_o - C_t) V}{W} \quad (7.1)$$

Where C_o and C_t [mg L^{-1}] are the initial and the liquid-phase concentration of glyphosate at a contact time (t), respectively, V [L] is the volume of glyphosate solution used in the batch adsorption, and W [g] is the mass of dry adsorbent used. The percentage uptake of adsorption $q_t\%$ at contact time t was determined according to equation 7.2.

$$q_t\% = \frac{(C_o - C_t) 100}{C_o} \quad (7.2)$$

The kinetic adsorption isotherm of glyphosate on pure SBA-15 and on grafted SBA-15-PAPTS sample is reported in Fig. 7.8. Graphs are obtained by plotting the average value of adsorption capacity (q_t) in relation to the amount of adsorbed glyphosate (in mg) on 1 g di adsorbent (Frame A) and in terms of ratio amount of adsorbed glyphosate in 100 g di material (Frame B) $q_t\%$.

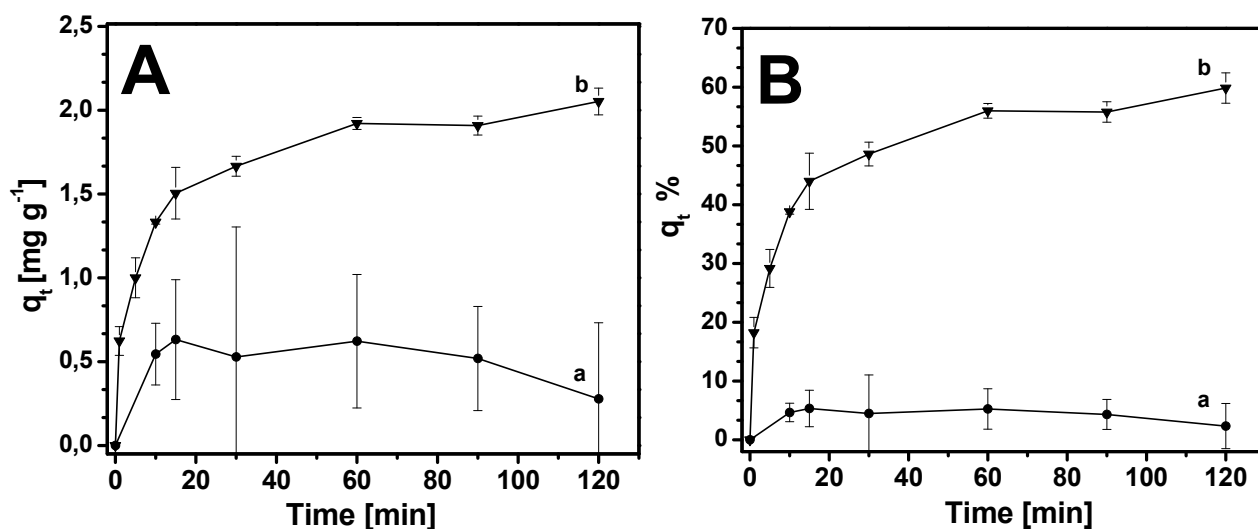


Figure 7.8: Kinetic isotherms of glyphosate adsorbed (q_t) on the bare SBA-15 (curves a) and the grafted SBA-15-PAPTS (curves b): in terms of mg per 1 g of adsorbent (A) and adsorption uptake q_t % (B). Batch experiments were performed with 50 mg of adsorbent in 20 mL of standard solution of glyphosate at 298K.

As observed from the Figure 7.8 A, B curves a, SBA-15 shows poor adsorption (*ca.* 5%) and high standard deviations values. Low adsorption capacities of bare SBA-15 was associated to the fact that repulsive ionic interactions do not allow adsorption,^[36] since glyphosate molecule at the pH of the adsorption batches (pH= 5) is ionized as monovalent or divalent anions (see forms in Chapter I, paragraph 1.3.1.3) and silica surface charge is negative due to the presence of SiO⁻ species, as confirmed by the Zeta potential analysis ($\xi = -5.12$ mV), see paragraph 7.2.1.

Therefore, SBA-15 will not considered as adsorbent for glyphosate since its poor adsorption performance.

The adsorption capacity of SBA-15-PAPTS (Figure 7.8 A, B curves b) is higher respect to the pure SBA-15: this is probably due to the introduction of the NH₂ species which at the pH of the adsorption batches (pH= 5) are protonated to NH₃⁺ species. These species provide a positive charge to the silica surface ($\xi = 18.17$ mV, see paragraph 7.2), that, thus favouring the ionic interactions with the phosphonate group of glyphosate molecules through the formation of monodentate and bidentate species.^[36]

Different regimes can be observed observing the kinetic adsorption isotherms of glyphosate on SBA-15-PAPTS. The kinetic isotherm of glyphosate adsorbed on SBA-15-PAPTS (Figure 7.8 A, curve b) is very steep until 15 min then the slope decreases up to *ca.* 60 min and then not significant variations

of uptake adsorption are found. In the range between 0-15 min, the adsorption uptake of SBA-15-PAPTS is 1.5 mg g⁻¹ corresponding *ca.* 44 q_t %. From 15 to 60 min the uptake increases to 1.92 mg g⁻¹ corresponding *ca.* 56 q_t %. The equilibrium adsorption capacity (q_e) on SBA-15-PAPTS is observed at 120 min which overall uptake is *ca.* 2.04 mg g⁻¹ corresponding *ca.* 60 q_t %.

7.4.1 Kinetic adsorption models

Kinetic adsorption process can be affected by different mechanism such as mass transfer, chemical reaction process, transport resistances and heterogeneity of the adsorbent (more than one type of adsorption sites whose could have different adsorption heats).^[37,38] Mass transfer comprises three steps: i) external diffusion of the adsorbate from the liquid phase (bulk) to the external surface of adsorbent, ii): intraparticle diffusion (IPD), that is the transport of adsorbate from the external surface into the pores of the adsorbent and iii) surface reaction, that is the attachment of adsorbates to the internal surface of the sorbent.^[37]

Taking account these previous considerations, the kinetic isotherm of glyphosate adsorbed on SBA-15-PAPTS was fitted with different kinetic models such as pseudo first and second order, Elovich and intraparticle diffusion to understand kinetic mechanism in the liquid adsorption system. A brief recall of these methods is given below.

7.4.1.1 Pseudo-first order model (Lagergren's equation)

In 1898, Lagergren described liquid–solid phase adsorption systems.^[39] Lagergren's first-order equation describes the adsorption rate based on the adsorption capacity.

Pseudo-first order model assumes that i) adsorption phenomenon only occurs on localized sites and involve non-dissociating molecular adsorption on the adsorbent, ii) the adsorption energy is not dependent on surface coverage, iii) equilibrium adsorption corresponds to the formation of a saturated monolayer of adsorbates on the adsorbent surface.^[40]

The linear form of the of pseudo-first order model is expressed as follow:^[42-43]

$$\log(q_e - q_t) = \log(q_e) - \frac{(k_1)}{2.303} t \quad (7.3)$$

where q_t is the adsorption capacity [mg g⁻¹] at contact time t [min], q_e is the adsorption capacity at equilibrium [mg g⁻¹] and k₁ is the first order rate constant [min⁻¹].

7.4.1.2 Pseudo-second order model

The Pseudo-second order model was introduced by Blanchard et al. in 1984.^[44]

The pseudo second order model assumes that the uptake rate is second order with respect to the available surface adsorption sites.^[37] This method describes the chemisorption involving valence forces through sharing or exchange of electrons between the adsorbent and the adsorbate. This model can be expressed as follows:

$$\frac{t}{q_t} = \frac{1}{k_2 q_e^2} + \frac{1}{q_e} t \quad (7.4)$$

where k_2 is the pseudo second order rate constant [$\text{g mg}^{-1} \text{min}^{-1}$].

7.4.1.3 Elovich model

In 1934, Zeldowitsch introduced this model which describes kinetics of heterogeneous chemisorption.^[45] This model is the most useful model for describing chemisorption and assumes that adsorption only occurs on specific sites through ionic interactions and the energy of adsorption increases linearly with the surface coverage.^[40]

It has commonly been called the Elovich equation which shows a linear correlation between q_t vs. $\ln(t)$ and can be expressed as:

$$q_t = \frac{1}{b} \ln(ab) + \frac{1}{b} \ln(t) \quad (7.5)$$

Where a [$\text{mg g}^{-1} \text{min}^{-1}$] is the initial adsorption rate and b [g mg^{-1}] is a constant related to the extent of surface coverage and activation energy for chemisorption. The slope $1/b$ and the intercept $[\ln(ab)]/b$ are the number of sites available for adsorption and the amount adsorbed in time $t = 1$ min, respectively.

7.4.1.4 Intraparticle diffusion model

Pseudo-first and second order and Elovich model are not able to identify the diffusion mechanism, thus intraparticle diffusion model was introduced in 1963 by Weber and Morris.^[46] Intraparticle diffusion model can be applied to adsorption process which are limited by intraparticle diffusion (IPD). This model is the third most common applied model for liquid adsorption kinetics in environmental remediation after the pseudo-first and second order models and describes the diffusion steps of species from the liquid phase (bulk) to inside the adsorbent pores^[35] and can be expressed as:

$$q_t = k_D \sqrt{t} + C_t \quad (7.6)$$

where k_D is the diffusion rate constant [$\text{mg g}^{-1} \text{min}^{-0.5}$] and C_t is the initial adsorption capacity [mg g^{-1}]. If the plot of q_t versus $t^{1/2}$ gives a straight line, then the sorption process is controlled by intraparticle diffusion only. However, if the data exhibit multi-linear plots, then two or more steps of diffusion influence the sorption process.^[47] k_D and the C_t can be calculated from the slope and the intercept of the plot q_t correlated to $t^{1/2}$ expressed also as $t^{0.5}$ [$\text{min}^{0.5}$].

7.4.2 Application of kinetic adsorption models to experimental data

The kinetic experimental values obtained from the adsorption of glyphosate on SBA-15 PAPTS were fitted with kinetic models described above in order to describe properly the kinetic mechanism of the adsorption of glyphosate on both materials and to compare the predicted adsorption values with the experimental data in different adsorbent/adsorbate systems.

Kinetic parameters such as the rate constants, equilibrium adsorption capacities and related correlation coefficients (R^2) and exact prediction of experimental data (the Nonlinear Chi-Square Test (χ^2)) were obtained by fitting of the experimental data to each kinetic model are reported in table 7.3.

Table 7.3: Kinetic parameters of the models for the adsorption of glyphosate on SBA-15-PAPTS

Pseudo-first order model	q_e [mg g ⁻¹]	k_1 [min ⁻¹] $\times 10^{-2}$	R^2	χ^2			
SBA-15-PAPTS	1.18	0.03	0.855	9.83			
Pseudo-second order model	q_e [mg g ⁻¹]	k_2 [g mg ⁻¹ min ⁻¹]	R^2	χ^2			
SBA-15-PAPTS	2.09	0.09	0.997	0.29			
Elovich model	$(1/b) \ln(ab)$ [mg g ⁻¹]	$1/b$ [mg g ⁻¹]	a [mg g ⁻¹ min ⁻¹]	b [g mg ⁻¹]	R^2	χ^2	
SBA-15-PAPTS	0.61	0.30	0.74	1.64	0.985	0.02	
Intraparticle diffusion model	k_{D1} [mg g ⁻¹ min ^{-0.5}]	k_{D2} [mg g ⁻¹ min ^{-0.5}]	k_{D3} [mg g ⁻¹ min ^{-0.5}]	R^2_1	R^2_2	R^2_3	χ^2
SBA-15-PAPTS	0.33	0.12	0.04	0.998	0.989	0.794	0.13

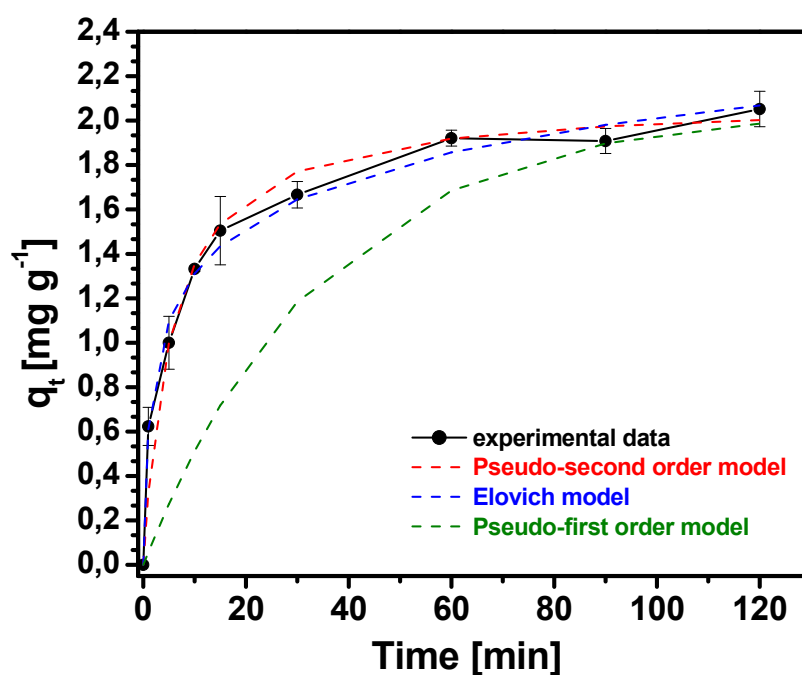


Figure 7.9: Comparison of experimental kinetics isotherms with kinetics models for glyphosate adsorption on SBA-15-PAPTS.

As it can be observed in Figure 7.9 and Table 7.3, the pseudo first order model was discarded for SBA-15-PAPTS because of the low accuracy in the prediction of experimental data (high values of χ^2 and low values of coefficients of correlation R^2).

The best kinetic fitting for SBA-15-PAPTS were obtained by using Pseudo-second order and Elovich models, which present $R^2 > 0.95$ and $\chi^2 < 10$ (see table 7.3 and Figure 7.9).

As reported in Table 7.3, SBA-15-PAPTS is described by the Pseudo-second order model (see table 7.3, $R^2= 0.997$ and $\chi^2=0.29$), which predicts a value of equilibrium adsorption capacity q_e of 2.09 mg g^{-1} very similar to that obtained experimentally (2.04 mg g^{-1}). This model suggests that the adsorption process on SBA-15-PAPTS is the result of a chemical interactions (chemisorption). The ionic interactions between glyphosate and SBA-15-PAPTS was expected due to the positive charged present on the surface of this materials related to the protonated amino groups (NH_3^+ species) and the negative charge of the functional groups of glyphosate molecules, as confirmed by the adsorption comparison between the bare SBA-15 and the grafted SBA-15-PAPTS (see Figure 7.8). In addition, low value of pseudo second order rate (k_2) $0.09 \text{ g mg}^{-1} \text{ min}^{-1}$, indicates that the adsorption for SBA-15-PAPTS in general is quite rapid, as can be confirmed on the experimental kinetic isotherm (Figure 7.8), where the functionalised mesoporous silica reaches the equilibrium after 2 h. This probably due to the textural properties of this material, where diffusion inside of the mesoporous is quite fast.

Elovich model also reported good fitting (see table 7.3, $R^2= 0.985$ and $\chi^2=0.02$) on the adsorption of glyphosate on SBA-15-PAPTS. This model confirms that the adsorption process on SBA-15-PAPTS is described by chemisorption on specific sites through ionic interactions. In addition, from the Elovich model (see table 7.3), the number of sites available for adsorption and the amount adsorbed at the first min for SBA-15-PAPTS were 0.30 and 0.61 mg g^{-1} , respectively. Whereas the constant related to the extent of surface coverage and activation energy for chemisorption (b) for SBA-15-PAPTS obtained from this model is $1.64 \text{ [g mg}^{-1}\text{]}$.

In the process of glyphosate adsorption on SBA-15-PAPTS, three particle diffusion steps of adsorption were identified by applying the intraparticle diffusion model suggesting different mechanisms for each step (Figure 7.10).

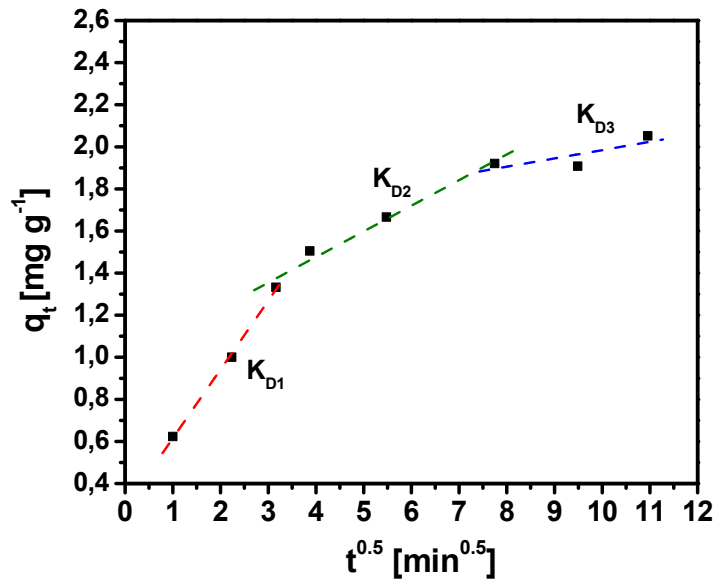


Figure 7.10: Linear fitting of the adsorption kinetic by the Intraparticle diffusion model for glyphosate adsorbed on SBA-15-PAPTS.

The process of adsorption of glyphosate on SBA-15-PAPTS (Figure 7.10), the first linear correlation in the range of $t^{0.5}$ was found in the range of 1-3.13 min^{0.5}, which according to the model would be associated with the instantaneous diffusion of the glyphosate molecules on the external surface of SBA-15-PAPTS. Low values of $t^{0.5}$ on the first linear behaviour should indicate that the mass transport through the liquid-SBA-15-PAPTS interface occurs rapidly and there is not a limiting stage in the process.^[48,49] The second stage at values of $t^{0.5}$ was found between 3.13-7.74 min^{0.5} for SBA-15-PAPTS which is associated with the mass transport of the adsorbate through the pores of the adsorbent (internal diffusion). The third step was found between 7.74-11 min^{0.5} for SBA-15-PAPTS which is the final equilibrium step where the intraparticle diffusion rate starts to decrease due to the remain low glyphosate concentration in the solution.

The diffusion rate of adsorption [mg g⁻¹ min^{-0.5}] (k_{1D} , k_{2D} and k_{3D}) are reported in Table 7.3.

For SBA-15-PAPTS, the first value of k_{1D} diffusion rate constant resulted the high values and then the value (k_{2D} and k_{3D}) decreases in the other steps: this behaviour suggests that the rate of adsorption is only limited by the external resistance (the mass transport through the liquid-SBA-15-PAPTS interface) and then progressively other diffusion mechanism affect with less effect to the adsorption process.^[50,51] The initial adsorption capacity of glyphosate on SBA-15-PAPTS (C_{t1}) was 0.289 mg g⁻¹ which was obtained from the intercept of the first linear correlation and is associated to the amount of glyphosate rapidly adsorbed on the external surface of SBA-15-PAPTS. This is related to the fact

that glyphosate is adsorbed first on the mesopores with large diameter between 65-100 Å. The SSA of SBA-15-PAPTS related to this range of mesoporous is 145 m² g⁻¹, as reported from Table 7.1.

7.5. Equilibrium adsorption studies of glyphosate on and SBA-15-PAPTS

Equilibrium adsorption isotherms were obtained from the adsorption measurements of different concentrations of glyphosate in contact at a specific equilibrium time in aqueous media. The batch equilibrium adsorption experiments were repeated in three different experimental batches to reduce experimental errors associated with spectroscopic measurements.

Batch equilibrium experiments were carried out by using 20 mL standard solution at different concentration of glyphosate ranging from 2-25 mg L⁻¹ which were placed in contact with 50 mg of the adsorbent inside to glass vials of 25 mL. The glass vials were subjected to shaking in ambient conditions (see Figure 7.7A) at each specific adsorption equilibrium time (t_e) obtained from the previous kinetic adsorptions studies which was 120 min for SBA-15-PAPTS.

When the t_e of each glass vial was completed, the glyphosate solutions containing the adsorbents were filtered by using syringe filters of 0.45 µm and syringes (See Figure 7.7B). The liquid phase was then used for determination of the glyphosate concentration remaining after equilibrium was reached (C_e) according the derivatization procedure and UV-vis analysis (standard curve prepared with standard solutions with concentrations in the ranges of 1-30 mg L⁻¹ of glyphosate in 0.1 M aqueous KCl), explained in the paragraphs 7.3.1 and 7.3.2.

The adsorption capacity q_e [mg g⁻¹] at equilibrium was determined according to equation 7.7:

$$q_e = \frac{(C_o - C_e) V}{W} \quad (7.7)$$

Where C_e [mg L⁻¹] is the equilibrium liquid phase concentrations of glyphosate. V [L] is the volume of glyphosate solution used in the batch adsorption, and W [g] is the mass of dry adsorbent used.

In Figure 7.11 the equilibrium adsorption isotherms with their standard deviation values of glyphosate adsorbed on the SBA-15-PAPTS silica at 298 K are reported.

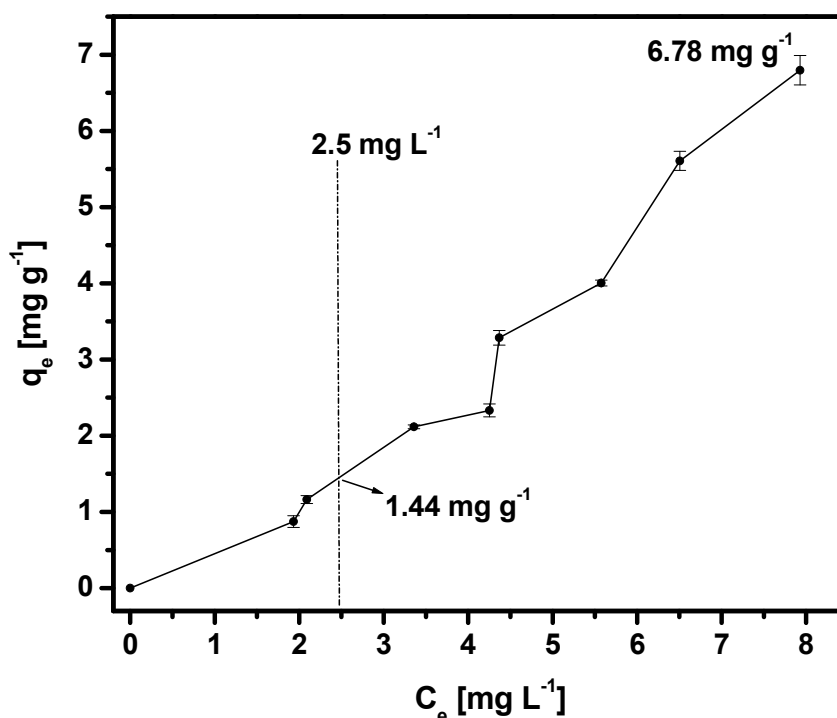


Figure 7.11: Equilibrium adsorption isotherms and their standard deviations of glyphosate on and SBA-15-PAPTS with $t_e = 2$ h, respectively, C_0 2–25 mg L⁻¹, ratio = 50 mg of adsorbent/20 mL glyphosate standard solution at $T = 298\text{K}$.

The isotherm has been classified according to the Giles classification.^[52] Giles have classified equilibrium adsorption isotherms in four main groups: L, S, H, and C.

According to the above classification, SBA-15-PAPTS (Fig. 7.11) shows C-type isotherm. In the C-type (Constant partition), the slope remains constant which means a constant affinity for a wide range of concentrations.^[53]

At low equilibrium concentrations $C_e = 2.5$ mg L⁻¹, SBA-15-PAPTS adsorbs 1.44 mg g⁻¹ and at maximum equilibrium concentrations (C_e), the SBA-15-PAPTS adsorbs $q_m = 6.78$ mg g⁻¹: The high adsorption capacity of this material can be associated to the fact that SBA-15-PAPTS material has a positive charge surface that is able to interact via electrostatic interactions with negatively charged glyphosate.

7.5.1 Equilibrium adsorption models

In order to optimize the adsorption mechanism pathways, to express the dependence of the surface properties of the adsorbent to the sorption results, to determine the adsorption capacities and design effectively the adsorption systems for the removal of glyphosate from effluents, it is important to

establish the most appropriate correlation for the equilibrium isotherms.^[54,55] The determination of adsorption parameters by applying adsorption models permits to describe the relationship between the amount of glyphosate adsorbed by the adsorbents (q_e) and the adsorbate concentration remaining in solution after equilibrium is reached (C_e).^[54]

Taking account these previous considerations, the equilibrium adsorption isotherms of glyphosate adsorbed on SBA-15-PAPTS were adjusted to different adsorption models such as Freundlich, Langmuir, Elovich, Temkin and Dubinin–Radushkevich (DR) to understand the mechanism in the liquid adsorption system.

7.5.1.1 Freundlich model

The Freundlich model empirically developed by Freundlich (1906)^[56] can be applied to describe adsorption of several compounds on heterogeneous surfaces or surfaces which possess different sites with varied affinities.

This model assumes that heterogeneous surface energy is a consequence that the sites with stronger affinities are occupied first and then the binding strength decreases with an increasing degree of site occupation^[57] and can be expressed as:

$$q_e = K_F C_e^{\frac{1}{n_F}} \quad (7.8)$$

where C_e is the concentration remaining in solution after equilibrium is reached [mg L^{-1}], q_e is the adsorption capacity at equilibrium [mg g^{-1}], K_F is the Freundlich constant related to the adsorption capacity of the adsorbent [$\text{mg g}^{-1} (\text{L mg}^{-1})^{1/n}$] and n_F is a constant indicative of the adsorption intensity of the adsorbent (dimensionless). K_F can be defined as the adsorption capacity or distribution coefficient and represents the adsorbed quantity of the adsorbate for a unit equilibrium concentration. The $1/n_F$ and $\log K_F$ can be calculated from the slopes and the intercepts, respectively by plot of $\log q_e$ versus $\log C_e$. The $1/n_F$ ranges between 0 and 1 is a measure of adsorption intensity or surface heterogeneity, becoming more heterogeneous as its value gets closer to zero. Whereas, $1/n_F < 1$ suggests chemisorptions process where $1/n_F > 1$ is an indicative of cooperative adsorption.^[58]

7.5.1.2 Langmuir model

Langmuir model proposed by Langmuir (1918) ^[59] which was primarily designed to describe gas-solid phase adsorption is also widely used to describe the adsorption occurred on homogenous surface by monolayer sorption with a finite number of identical sites.^[60] This model can be mathematically expressed as:

$$q_e = \frac{q_m C_e}{1 + K_L C_e} \quad (7.9)$$

where q_m is the maximum adsorption capacity per unit weight of the adsorbent [mg g^{-1}] and K_L is the Langmuir constant relating related to the free energy of adsorption (the affinity of the binding sites) [L mg^{-1}].

7.5.1.3 Elovich model

The equation was first developed to describe the kinetics of chemisorption of gas onto solids.^[61]

The Elovich model is based on a kinetic principle which assumes that adsorption sites increase exponentially with adsorption; this infers a multilayer adsorption.^[62,63] The Elovich equation is expressed as follows:

$$\frac{q_e}{q_m} = K_E C_e e^{-\frac{q_e}{q_m}} \quad (7.10)$$

where K_E is the Elovich equilibrium constant [L mg^{-1}] and q_m is the Elovich maximum adsorption capacity [mg g^{-1}]. If the adsorption follows Elovich equation, q_m and K_E can be calculated from the slopes and the intercepts, respectively of the plot of $\ln(q_e/C_e)$ versus q_e .

7.5.1.4 Temkin model

Temkin and Pyzhev model^[64] assumes that the heat of adsorption of all the molecules in the layer decreases linearly with coverage due to adsorbent-adsorbate interactions, considering a factor that explicitly takes into account of these interactions.^[65,66] This model assumes also that the adsorption is characterized by a uniform distribution of the binding energies, up to some maximum binding energy. The Temkin isotherm is expressed as:

$$q_e = \frac{RT}{b_T} \ln(K_T C_e) \quad (7.11)$$

Where b_T Temkin isotherm constant (dimensionless), RT/b_T [J mol⁻¹] is the Temkin constant related to the adsorption energy and K_T [L g⁻¹] is the Temkin equilibrium binding constant corresponding to the maximum binding energy. R (8.314 J mol⁻¹ K⁻¹) is the universal gas constant and T is the absolute solution temperature (298K). If the adsorption follows Temkin equation, the b_T and the K_T can be calculated from the slope and the intercept of the plot q_e versus $\ln(C_e)$.^[68]

7.5.1.5 Dubinin–Radushkevich model

Another popular equation for the analysis of isotherms of a high degree of rectangularity is that proposed by Dubinin and Radushkevich in 1947.^[69] This model is applied adsorption mechanism by discriminating between physical and chemical adsorption based on the potential theory assuming heterogeneous surface^[69] and is given by the following equation.

$$q_e = q_m e^{-B_{DR} \varepsilon^2} \quad (7.12)$$

where q_m is the maximum adsorption capacity per unit weight of the adsorbent [mg g⁻¹], B_{DR} (dimensionless) is the isotherm constant and ε values can be correlated as:

$$\varepsilon = RT \ln \left[1 + \frac{1}{C_e} \right] \quad (7.13)$$

where R is the gas constant (8.314 J mol⁻¹ K⁻¹) and T is the solution temperature (298K).

The free energy sorption per molecule of the sorbate when is transferred from the liquid phase (bulk) to the surface of the solid (E) can be calculated by using the constant B_{DR} by following relationship:

$$E = \left[\frac{1}{\sqrt{2B_{DR}}} \right] \quad (7.14)$$

A plot of $\ln(q_e)$ versus ε^2 allows to obtain the constants E and q_m from the slope and intercept, respectively.

7.5.2 Fitting the experimental adsorption data with models

The equilibrium experimental data obtained from the adsorption of glyphosate on SBA-15-PAPTS was adjusted to equilibrium adsorption models: Freundlich, Langmuir, Elovich, Temkin and Dubinin Radushkevich models, in order to describe properly the adsorption mechanism on the adsorption of glyphosate on both materials in a liquid adsorption system. The linearized forms of the equations were applied for all the models.

Adsorption parameters such as maximum adsorption capacity q_m per unit weight of the adsorbent at equilibrium adsorption, adsorption energies and related correlation coefficients (R^2) and exact prediction of experimental data (Chi-Square Test (χ^2)) were obtained by fitting of the experimental data to each adsorption model and are reported in table 7.4.

In Figure 7.12 are reported the fitting of the relevant models with best values of χ^2 , nevertheless the selection of the best fitting model was still evaluated in terms of both static values (χ^2 and R^2).

For SBA-15-PAPTS, Elovich, Temkin and Dubinin Radushkevich models were discarded because of the low accuracy in the prediction of experimental data ($R^2 < 0.95$ and $\chi^2 > 1$) for presenting a maximum adsorption capacity q_m (see table 7.4 and Figure 7.12), distant from that found experimentally ($q_m = 6.78 \text{ mg g}^{-1}$).

In conclusion, the best fittings for SBA-15-PAPTS sample (Figure 7.12B) were obtained by using a Freundlich and Langmuir model ($R^2 > 0.96$ and $\chi^2 < 0.6$).

Table 7.4: Isotherm parameters of the models for the adsorption for the adsorption of glyphosate on HSZ-Y zeolite and on SBA-15-PAPTS

Freundlich model	R^2	χ^2	$1/n_F$	$\log K_F$	n_F	K_F [$\text{mg g}^{-1} (\text{L mg}^{-1})^{1/n}$]
SBA-15-PAPTS	0.974	0.17	1.35	-0.40	0.74	0.37
Langmuir model	R^2	χ^2	$1/q_m$ [g mg^{-1}]	K_L/q_m [$\text{L mg}^{-2} \text{g}$]	q_m [mg g^{-1}]	K_L [L mg^{-1}]
SBA-15-PAPTS	0.986	0.16	0.15	0.01	6.77	0.07
Elovich model	R^2	χ^2	$-1/q_m$ [g mg^{-1}]	$\ln (K_E q_m)$	q_m [mg g^{-1}]	K_E [L mg^{-1}]
SBA-15-PAPTS	0.901	0.07	0.087	-1.25	7.12	0.04
Temkin model	R^2	χ^2	RT/b_T [J mol^{-1}]	$(RT/b_T) \ln K_T$ [J mol^{-1}]	b_T	K_T [L g^{-1}]
SBA-15-PAPTS	0.893	1.65	3.91	-2.19	624	0.57
Dubinin– Radushkevich model	R^2	χ^2	$\ln (q_m)$	B_{DR}	q_m [mg g^{-1}]	E [J mol^{-1}]
SBA-15-PAPTS	0.892	1.58	1.73	1.87×10^{-06}	5.65	517

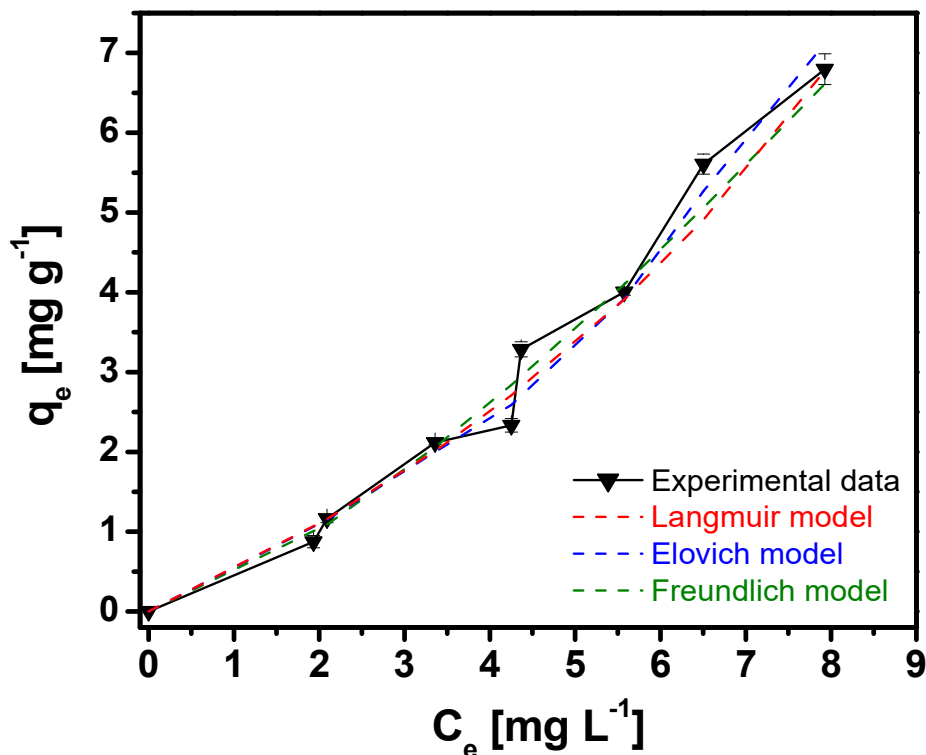


Figure 7.12: Comparison of experimental equilibrium adsorption isotherms with the equilibrium adsorption models of glyphosate on SBA-15-PAPTS.

The Langmuir isotherm is better fitted with experimental data with higher correlation coefficients ($R^2=0.986$) than that of the Freundlich isotherm ($R^2=0.974$). This means that the adsorption process of glyphosate on SBA-15-PAPTS is better described by the Langmuir model than Freundlich model. Langmuir model suggests that the surface of SBA-15-PAPTS as homogenous surface (equal affinity) with well distributed active sites that interact with the glyphosate molecules through chemical interactions (chemisorption). Therefore, the active sites present on the surface of SBA-15-PAPTS described by this model are related to the protonated amino groups (NH_3^+ species) which interact through ionic interactions with negative charge of the functional groups of glyphosate molecules, in accordance with the kinetic analysis.

The Langmuir constant K_L which relates the free energy of adsorption (the affinity of the binding sites) for SBA-15-PAPTS is 0.07 L mg^{-1} .

7.6 Conclusions

In this chapter, data related to glyphosate adsorption from aqueous solution on SBA-15 and SBA-15-PAPTS collected during a period of internship at the laboratories of the Department of Sciences, Section Chemistry, Pontifical Catholic University of Perú are reported. Kinetic and equilibrium studies were obtained from batch adsorption of glyphosate solutions in contact with the SBA-15 and SBA-15-PAPTS in aqueous media.

UV-vis spectroscopy was used to obtain the concentration of glyphosate of the aqueous solutions, after the adsorption experiments. A derivatization procedure was necessary for the detection of glyphosate, by using 9-fluorenylmethoxycarbonyl chloride (FMOC-Cl) as derivative reagent. The UV spectra of the product of the derivatization (FMOC-glyphosate adduct) allowed to obtain the absorbances at 265 nm (λ_{max}). The concentrations of glyphosate after the adsorption experiments were calculated by using a calibration curves prepared with standard solutions of glyphosate at different concentrations.

Kinetic adsorption isotherms of glyphosate on bare SBA-15 and on grafted sample (SBA-15-PAPTS) revealed the importance of functionalization to improve the adsorption capacities. Indeed, the presence of positive amino groups on SBA-15-PAPTS surface improves the adsorption performances respect to the bare SBA-15. This is due to the fact that the introduction of amino groups promotes ionic interactions with the negative charge of the functional groups of glyphosate molecules.

Kinetic and equilibrium studies of SBA-15-PAPTS for the adsorption of glyphosate had a best fit towards pseudo-second order and Langmuir models, which showed the prevalence ionic interactions between the surface and the adsorbed species

References

- [1] D. R Van Stempvoort, J. Spoelstra, N. D Senger, S. J Brown, R. Post and J. Struger, *Pest Manag Sci*, 2016, 72, 1862–1872.
- [2] G. Gatti, D. Costenaro, C. Vittoni, G. Paul, V. Crocella`, E. Mangano, S. Brandani, S. Bordiga, M. Cossi, L. Marchese and C. Bisio, *Phys.Chem.Chem.Phys.*, 2017, 19, 14114-14128.
- [3] F. Hoffmann, M. Cornelius, J. Morell, and M. Fröba, *Angew. Chem. Int. Ed.*, 2006, 45, 3216 – 3251.
- [4] M. Thommes, K. Kaneko, A.V. Neimark, J. P. Olivier, F. Rodriguez-Reinoso, J. Rouquerol, K. S.W. Sing, *Pure Appl. Chem.*, 2015, 87 (9-10) 1051–1069.
- [5] L. H. da Cruz; H. de Santana; C. Thaïs Bussamra V. Zaia; D. Augusto M. Zaia, *Brazilian Archives of Biology and Technology an International Journal*, 2007, 50, 385-394.
- [6] Y. Sun, C.-X. Lin, M.-H. Liu and Yi-Fan Liu, *BioResources*, 2011, 6(1), 631-640.
- [7] Z. Wu , H. Xiang, T. Kim, M.-S. Chun, K. Lee, *J. Colloid Interf. Sci.*, 2006, (304), 119–124.
- [8] R. A. Guinivan, N. P. Thompson, W. B. Wheeler, *J. Assoc. Off. Anal. Chem.*, 1982, 65, 35-39.
- [9] H. Kotaoka, K. Horii, M. Makita, *Agric. Biol. Chem.*, 1991, 55, 195-198.
- [10] H. A. Moye, C. L. Deyrup, *J. Agric. Food. Chem.*, 1984, 32, 192-195.
- [11] E. Bçrjesson, L. Torestenesson, *J. Chromatogr. A*, 2000, 886, 207-216.
- [12] P. S. Magadati, J. B. Couis, J. D. Rosen, *J. Assoc. Off. Anal. Chem.*, 1996, 79, 157.
- [13] M. J. Lovdahl, D. J. Pietrzyk, *J. Chromatogr. A*, 1992, 602, 197.
- [14] M. P. Abdullah, J. Daud, K. S. Hong, C. H. Yew, *J. Chromatogr. A*, 1995, 697, 363-369.
- [15] S. V. Chang, C. H. Ciao, *J. Chromatogr. A*, 2002, 959, 309-315.
- [16] J. Xiiao, Q. Zhau, B. Yang, Z. Wang, *Anal. Sci.*, 2004, 20, 1415-1418.
- [17] C. V. Waiman, M. J. Avena, M. Garrido, B. Fernández Band and G. P. Zanini, *Geoderma*, 2012, 170, 154–158.
- [18] K. Qian, T. Tang, T. Shi, F. Wang, J. Li, Y. Cao, *Analytica Chimica Acta*, 2009, 635, 222–226.
- [19] B. Sahasrabuddhey, A. Jain and K. K. Verma, *Analyst*, 1999, 124, 1017–1021.
- [20] I. D. Merás, T. G. D'iaz, M. A. Franco, *Talanta*, 2005, 65, 7–14.

- [21] D. G. Thompson, J. E. Cowell, R. J. Daniels, B. Staznik, L. M. MacDonald, *J. Assoc. Off. Anal. Chem.*, 1989, 72, 355-360.
- [22] B.L. Bhaskara, P. Nagaraja, *Helv. Chim. Acta*, 2006, 89, 2686-2693.
- [23] L. N. Lundgren, *J. Agric. Food Chem.*, 1986, 34, 535-538.
- [24] C. J. Miles, H. A. Moye, *J. Agric. Food Chem.*, 1988, 36, 486-491.
- [25] J. V. Sancho, F. J. López, F. Hernández, E. A. Hogendoorn, P. V. Zoonen, *J. Chromatogr. A*, 1994, 678, 59-67.
- [26] E.A. Hogendoorn, F.M. Ossendrijver, E. Dijkman, R.A. Baumann, *J. Chromatogr. A*, 1999, 833, 67-73.
- [27] C. Hidalgo, C. Rios, M. Hidalgo, V. Salvadó, J. V. Sancho, F. Hernández, *J. Chromatogr. A*, 2004, 1035, 153-157.
- [28] T. V. Nedelkoska and G. K-C. Low, *Analytica Chimica Acta*, 2004, 511, 145–153.
- [29] M. P. Garcia de Llasera, L. Gómez-Almaraz, L. E. Vera-Avila, A. Pena-Alvarez, *J. Chromatogr. A*, 2005, 1093, 139-146.
- [30] M. Ibáñez, O.J. Pozo, J.V. Sancho, F.J. López, F. Hernández, *J. Chromatogr. A*, 2005, 1081, 145-155.
- [31] I. Freuze, A. Jadas-Hecart, A. Royer, P.Y. Communal, *J. Chromatogr. A*, 2007, 1175, 197-206.
- [32] B. Li, X.J. Deng, D.H. Guo, S.P. Jin, *Chin. J. Chromatogr.*, 2007, 25, 486-490.
- [33] P. J. Peruzzo, A. A. Porta, A. E. Ronco, *Environ. Pollut.*, 2008, 156, 61-66.
- [34] D. E. Felton, M. Ederer, T. Steffens, P. L. Hartzell, and K. V. Waynant, *J. Chem. Educ.*, 2018, 95, 136–140.
- [35] D. D. Nguyen, J. Trunk, L. Nakhimovsky and J. Spanget-Larsen, *Journal of Molecular Spectroscopy*, 2010, 264, 19–25.
- [36] L. Rivoira, M. Appendini, S. Fiorilli, B. Onida, M. Del Bubba and M. C. Bruzzoniti, *Environ Sci Pollut. Res.*, 2016, 23, 21682–21691.
- [37] K. L. Tan and B.H. Hameed, *Journal of the Taiwan Institute of Chemical Engineers*, 2017, 74, 25–48.
- [38] Y. S. Ho and G. McKay, *Water, Air, and Soil Pollution.*, 2004, 158, 77–97.
- [39] S. Lagergren, About the Theory of so-Called Adsorption of Soluble Substances, *Kungliga Svenska Vetenskapsakademiens Handlingar*, 1898, 24, 1-39.
- [40] L. Largetitte and R. Pasquier, *Chemical engineering research and design*, 2016, 109, 495–504.

- [41] Yuh-Shan Ho, *Journal of Hazardous Materials B*, 2006, 136, 681–689.
- [42] V. K. Gupta, M. Gupta and S. Sharma, *Wat. Res.*, 2001, 35, 1125–1134.
- [43] A. Syafiuddin, S. Salmiati, J. Jonbi and M. Ali Fulazzaky, *Journal of Environmental Management*, 2018, 218, 59-70.
- [44] G. Blanchard, M. Maunaye, G. Martin, *Water Res.*, 1984, 18, 1501–1507.
- [45] J. Zeldowitsch, *Acta Physicochim. URSS*, 1934, 1, 364–449.
- [46] W.J. Weber and J.C. Morris, *J Sanit Eng Div*, 1963, 89, 31–60.
- [47] V. Fierro, V. Torne-Fernandez, D. Montane, A. Celzard, *Microporous and Mesoporous Materials*, 2008, 111, 276–284.
- [48] Tan, I.A.W. Ahmad, A.L. Hameed, B.H, *Journal of Hazardous Materials*, 2009, 164, 473–482.
- [49] R. Beltran-Suito, A. Pinedo-Flores, F. Bravo-Hualpa, J. Ramos-Munoz, G. Picasso-Escobar and M. del Rosario Sun-Kou, *Adsorption*, 2015, 21, 577–587.
- [50] G. Yang, H. Chen, H. Qin, Y. Feng, *Appl Surf Sci.*, 2014, 293, 299–305.
- [51] W. Yang, P. Ding, L. Zhou, J. Yu, X. Chen, F. Jiao, *Appl Surf Sci*, 2013, 282, 38–45.
- [52] C.H. Giles, D. Smith, *J. Colloid Interf. Sci.*, 1974, 47, 755–765.
- [53] Christoph Hinz, *Geoderma*, 2001, 99, 225–243.
- [54] E.C. Lima, M.A. Adebayo, F. M. Machado, Chapter 3- Kinetic and Equilibrium Models of Adsorption in Carbon Nanomaterials as Adsorbents for Environmental and Biological Applications, C.P. Bergmann, F.M. Machado editors, Springer 2015, pp.33-69.
- [55] S. Rengaraj, Y. Kim, C.K. Joo, K. Choi, J. Yi, Korean, *J. Chem. Eng.*, 21, 2004, 187–194.
- [56] H. Freundlich, *J. Phys. Chem.*, 1906, 57, 1100-1107.
- [57] S.M. Silva, K.A. Sampaio, R. Ceriani, R. Verbe, C. Stevens, W. De Greyt, A.J.A Meirelles, *J. Food Eng.*, 2013, 118, 341-349.
- [58] K.Y. Foo and B.H. Hameed, *Chemical Engineering Journal*, 2010, 156, 2–10.
- [59] I. Langmuir, *J. Am. Chem. Soc.*, 1918, 40, 1361-1403.
- [60] A. Syafiuddin, S. Salmiati, J. Jonbi and M. Ali Fulazzaky, *Journal of Environmental Management*, 2018, 218, 59-70.

- [61] S.Y. Elovich, and O.G. Larinov, Theory of Adsorption from Solutions of Non Electrolytes on Solid (I) Equation Adsorption from Solutions and the Analysis of Its Simplest Form, (II) Verification of the Equation of Adsorption Isotherm from Solutions. *Izvestiya Akademii Nauk SSSR, Otdelenie Khimicheskikh Nauk*, 1962, 2, 209-216.
- [62] N.Ayawei, A. Newton Ebelegi, and D. Wankasi, *Hindawi Journal of Chemistry*, 2017, 1-12.
- [63] A. Akolo and A. C. Sanni Kovo, *Journal of Encapsulation and Adsorption Sciences*, 2015, 5, 21-37.
- [64] M. I. Temkin, Adsorption Equilibrium and the Kinetics of Processes on Nonhomogeneous Surfaces and in the Interaction between Adsorbed Molecules, *Zhurnal Fiziche- skoi Khimii*, 1941, 15, pp. 296-332.
- [65] M. Temkin, and V. Pyzhev, *Acta Physicochimica U.R.S.S.*, 1940, 12, 327-356.
- [66] I. A. W. Tan, A. L. Ahmad, B. H. Hameed, *Journal of Hazardous Materials*, 2009, 164, 473–482.
- [67] O. Hamdaoui and E. Naffrechoux, *Journal of Hazardous Materials*, 2007, 147, 381–394.
- [68] S. Rengaraj, Y. Kim, C.K. Joo, K. Choi, J. Yi, *J. Chem. Eng.*, 2004, 21, 187–194.
- [69] M. M. Dubinin and L. V. Radushkevich, *Chem. Zentr.* 1947, 1, pp 875.

General Conclusions

In this Ph.D. thesis, siliceous materials with different porosity degree for potential application in groundwater depollution have been studied.

In this respect, solids with different pore dimensions and architecture, particle size and textural properties have been selected and tested as sorbents for hydrocarbon adsorption, with particular attention to toluene and *n*-hexane (used as model molecules of aromatic and aliphatic fuel-based pollutants, respectively).

First at all, microporous solids such as zeolites have been selected as adsorbents and the effect of their physico-chemical properties on the adsorption capacity were studied. Particular attention has been paid to the use of two dealuminated high silica HSZ-Y and ZSM-5 zeolites (with a SiO₂/Al₂O₃ ratio of 200 and 280, respectively) with commercial origin, that were selected on the basis of their pore dimension, hydrophobicity, and textural properties.

HSZ-Y zeolite belonging to Faujasite family (FAU) is characterized by the presence of large supercages (of ca. 13 Å of diameter) whereas ZSM-5, with framework type MFI, is characterized by two types of intersecting straight channels of ca. 5 Å x diameter. The specific surface area (SSA) of the zeolite HSZ-Y is of 991 m² g⁻¹, more than half of which is due to the presence of micropores (710 m² g⁻¹); whereas ZSM-5 zeolite has a SSA of 550 m² g⁻¹, and the presence of micropores is related to a SSA_{micro} of 355 m² g⁻¹.

In order to improve the adsorption capacities, the interest was then devoted to the use of mesoporous silicas with different porosity. In particular, two types of mesoporous silicas with irregular porosity (*i.e.*, FUMED and AMSs silicas) and two types of mesoporous silicas with ordered porosity (*i.e.*, SBA-15 and MCM-41) were studied.

The physico-chemical feature of these solids (FUMED, AMSs, HSZ-Y, ZSM-5, MCM-41 and SBA-15) were investigated by means of different experimental approaches (*i.e.* N₂ adsorption, FTIR, TGA and SS-NMR).

Amorphous silica samples FUMED and AMS sample have SSA of 412 and 870 m² g⁻¹. FUMED has a heterogenous pore size distribution with pores in the range from 20 to 300 Å whereas AMSs sample has heterogeneous pore size distribution between 30 to 200 Å.

Mesoporous ordered SBA-15 and MCM-41 silicas have a SSA of 761 and 1103 m² g⁻¹, respectively. MCM-41 has a wide pore size distribution between 30-80 Å, with a maximum centered at 42 Å.

Whereas, SBA-15 has two different family of pores: one heterogenous family from 20 to 65 Å and one homogeneous family of pores between 65-100 Å with a maximum centered at 75 Å.

The textural properties of the silica-based solids studied in this Ph.D. are summarised in Table 1.

Table 1: Main textural features of silica-based solids studied in this Ph.D.

Sample	SSA _{BET} ^a [m ² g ⁻¹]	V _{microp} ^c (≤ 20 Å) [cm ³ g ⁻¹]	V _T ^b [cm ³ g ⁻¹]	V<50 Å ^c [cm ³ g ⁻¹]	V _{mesop} ^c [cm ³ g ⁻¹] 20-300Å	V _{mesop} ^c [cm ³ g ⁻¹] 20-100Å	V _{mesop} ^c [cm ³ g ⁻¹]	
							20-65Å	65-100Å
HSZ-Y	991	0.28	0.68	0.37	0.29	0.13	0.09	0.04
ZSM-5	550	0.02	0.52	0.20	0.46	0.39	0.28	0.11
FUMED	412	-	1.47	0.10	0.57	0.27	0.16	0.11
AMS-HSA	870	-	1.66	0.12	1.63	0.81	0.29	0.52
MCM-41	1103	-	1.31	0.66	1.13	0.95	0.83	0.12
SBA-15	761	-	0.96	0.20	0.92	0.86	0.31	0.55

^aBrunauer–Emmet–Teller (BET) specific surface area (SSA); ^bTotal pore volume by NLDFT method; ^cVolume of mesopores NLDFT method.

The first part of this Ph.D. thesis was focused to the understanding of the competition of organic contaminants for a specific adsorbent. This important issue is relevant from the environmental point of view in that, under real conditions, pollutants are generally present in groundwater as complex mixtures. As stated before, dealuminated HSZ-Y and ZSM-5 zeolites (with a SiO₂/Al₂O₃ ratio of 200 and 280, respectively) have been selected as adsorbents for the co-adsorption of toluene and *n*-hexane equimolar mixture. From FTIR analyses it was possible to observe that the two zeolites behave differently in the presence of the toluene/*n*-hexane mixture: indeed, the HSZ-Y zeolite preferentially retains toluene, whereas *n*-hexane is preferentially adsorbed on ZSM-5.

This information has been obtained thank to the determination of the molar absorption coefficient of specific IR bands of *n*-hexane and toluene adsorbed on microporous systems (HSZ-Y and ZSM-5) that are derived by coupling IR and microgravimetric data. SS-NMR spectroscopy provided more insight on the on the local environment that the pollutants experience inside the zeolites pores and revealed that the adsorption and diffusion of toluene and *n*-hexane adsorbed as mixture are significantly influenced by the pore/channel architecture and volume availabilities in zeolites.

In Figure 1 (A,B), a comparison of the volumetric adsorption isotherms of toluene adsorbed on the different materials studied in the frame of the thesis work is reported together with the pore size distribution of the used solids.

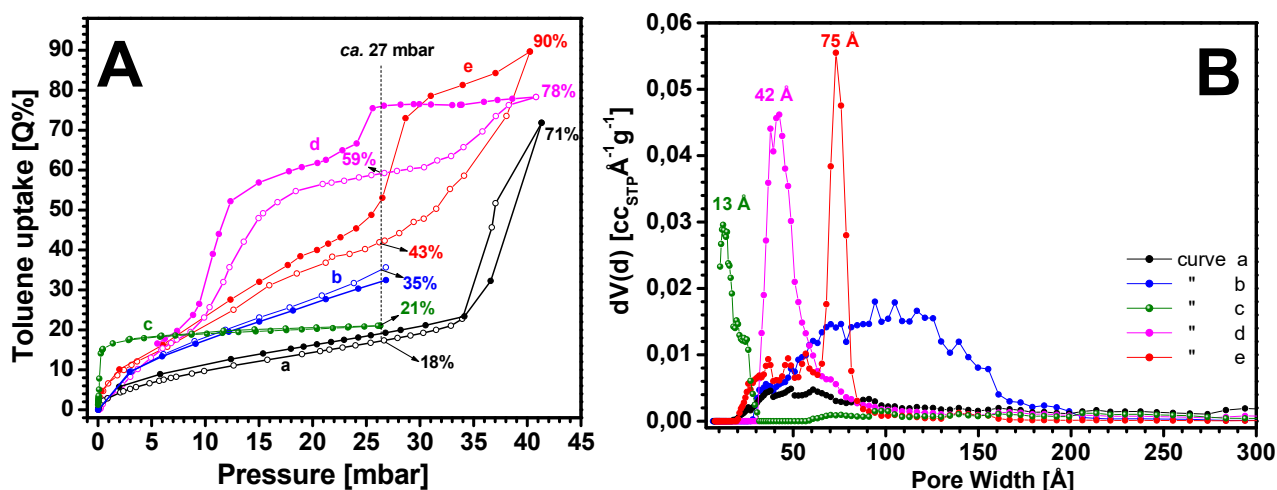


Figure 1: Toluene adsorption/adsorption isotherms (A) and pore size distribution (B) of all the supports: FUMED (curve a), AMS-HSA (curve b), HSZ-Y (curve c), MCM-41 (curve d) and SBA-15 (curve e)

From these figures, it is clear to observe that at low pressures (0-5 mbar), microporous HSZ-Y zeolite has higher adsorption capacities towards toluene respect to the mesoporous silicas.

This behaviour should be related to the presence of micropores able to entrap toluene molecules.

The high affinity of HSZ-Y for toluene at low pressures is partially related to the O-H $\cdots\pi$ interactions between silanol species and toluene molecules. These results suggest that at low pressures of toluene, the surface silanols play a key role in driving toluene adsorption capacity. Nevertheless, HSZ-Y has an adsorption limit at low pressures (*ca.* 5 mbar) in which HSZ-Y reaches the saturation (monolayer). The overall adsorption capacity for HSZ-Y at 27 mbar is *ca.* 21 Q%.

The use of mesoporous silicas allowed to increase significantly the toluene uptake.

When amorphous silicas with non regular porosities (*i.e.* FUMED and AMS silicas) are used as supports, the toluene uptake increases with respect to the performances of HSZ-Y zeolite. Nevertheless, at relatively high toluene pressure (*i.e.* *ca.* 25 mbar), FUMED silica is able to adsorb *ca.* 20 Q% of toluene (similarly to that occurring for the HSZ-Y zeolite) and at *ca.* 40 mbar the toluene uptake is strongly increased to 71 Q%, probably in relation to the condensation of the aromatic molecules in the intraparticles porosities. As indicated by microgravimetry, at pressure of *ca.* 30 mbar, AMS silica is able to adsorb more toluene than FUMED silica (*ca.* 35 Q%).

Ordered mesoporous silicas have a completely different adsorption behaviour. As it can be derived from Fig. 1A, even if at low toluene pressure (below 5 mbar) the toluene uptake is lower than HSZ-

Y zeolite, both supports displayed an interesting increase of the toluene uptake in the region between 5 and 25 mbar. In this region of pressure, MCM-41 is able to adsorb more toluene than SBA-15 and this is probably related to the fact that in these conditions the mesopores with diameter in the 20-65 Å range are filled. As it can be seen from Table 1, for MCM-41 these pores have a total volume of $0.82 \text{ cm}^3 \text{ g}^{-1}$, whereas in SBA-15 the volume of this family of pores is only $0.31 \text{ cm}^3 \text{ g}^{-1}$. At higher toluene pressure, the overall adsorption capacity is 90 Q% for SBA-15 and 78 Q% for MCM-41. This is probably to the partial filling of pores in the 65-100 Å range, available especially in SBA-15 material.

This collection of data suggests that porosity and confinement effects play a key-role in driving toluene adsorption capacity.

The volumetric data, together with FTIR analysis of adsorbed toluene, were also used for the determination of molar absorption coefficients of toluene adsorbed on mesoporous silicas (FUMED and ordered mesoporous MCM-41 and SBA-15 silicas).

The last part of this Ph.D. was devoted to the study of glyphosate (N-(phosphonomethyl)-glycine) adsorption on porous SBA-15 solid, also functionalized with amino groups.

In particular, SBA-15 was functionalized with the aminopropyltrimethoxysilane (PAPTS) in order to introduce specific functionalities able to increase the affinity of the material for the glyphosate molecules. SBA-15 and SBA-15 PAPTS have been studied in order to evaluate their physico-chemical properties.

The surface charge of SBA-15 and SBA-15-PAPTS at pH of adsorption conditions (pH=5) were determined by Zeta potential (ξ) measurements. SBA-15 showed a negative Z-potential (-5.12 mV), due to the presence of SiO^- species, whereas SBA-15-PAPTS showed positive Z-potential (+18.17 mV) due to the introduction of NH_2 species which at the pH of the adsorption batches (pH= 5) are protonated to NH_3^+ species.

Kinetic and equilibrium studies were obtained from batch adsorption of glyphosate solutions in contact with SBA-15 and SBA-15-PAPTS in aqueous media.

The concentration of the glyphosate after the adsorption experiments was determined by using UV-vis spectroscopy. Before the UV analysis, glyphosate was derivatized to another molecule by using a derivative reagent (fluorenylmethoxycarbonyl chloride (Fmoc-Cl)).

Kinetic adsorption isotherms of glyphosate on bare SBA-15 and on SBA-15-PAPTS revealed that the presence of amino groups on SBA-15-PAPTS surface improves the adsorption performances respect to the bare SBA-15. This is related to the fact that the NH_3^+ species present at the silica surface are able to interact with the phosphonate group of glyphosate molecules through ionic interactions.

The kinetic and equilibrium data obtained from the adsorption of glyphosate on SBA-15 PAPTS were fitted with different models, in order to understand the adsorption mechanisms and the kinetic process.

List of Publications

1. **2017**: “Experimental Determination of the Molar Extinction Coefficient of *n*-hexane adsorbed on High Silica Zeolites”: V. Sacchetto, **D. F. Olivas Olivera**, G. Gatti, C. Cossi, I. Braschi, C. Bisio, and L. Marchese, *ChemPhysChem*, 2017, *18*, 1 – 8.
2. **2017**: “On the adsorption of gaseous mixtures of hydrocarbons on high silica zeolites”. V. Sacchetto, **D. F. Olivas Olivera**, G. Paul, G. Gatti, I. Braschi, L. Marchese and C. Bisio. *J. Phys. Chem. C*, 2017, *121*, 6081–6089.
3. **2015**: “Interactions of Toluene and *n*-Hexane on High Silica Zeolites: An Experimental and Computational Model Study. Vittoria Sacchetto, Chiara Bisio, **Diana F. Olivas Olivera**, Geo Paul, Giorgio Gatti, Ilaria Braschi, Gloria Berlier, Maurizio Cossi, and Leonardo Marchese. *J. Phys. Chem. C*, 2015, *119*, 24875–24886.

Acknowledgements

Finally, one of the most important episodes of my life become reality. And I would like here to thank all the people involved.

Firstly, I would like to express my sincere gratitude to my supervisor *Prof. Chiara Bisio* and to the *Prof. Leonardo Marchese* for giving me the opportunity to work on this Ph.D. project.

In particular, *Prof. Chiara Bisio* for her continuous support during my Ph.D., for her patience, motivation, and immense knowledge. Her supervision helped in every time of this period of research of writing this thesis. I also want to thank her for all the motivation to continues in every difficult moment that I passed during my Ph.D. I want to say that without her motivation and supporting it would have been impossible to finish. I am very grateful.

I would also like to thank all the (current and past) members of the Physical Chemistry group: *Dr. Giorgio Gatti, Dr. Geo Paul, Dr. Fabio Carniato, Dr. Daniele Costenaro, Dr. Mina Errahali, Dr. Chiara Vittoni, Prof. Enrica Gianotti, Dr. Ivana Miletto, Ms. Chiara Ivaldi, Ms. Federico Begni, Mr. Stefano Marchesi, Dr. Marta Corno, Prof. Maurizio Cossi, Dr. Alberto Fraccarollo and Dr. Lorenzo Canti*. My sincere thanks also go to *Dr. Vittoria Sacchetto*, with whom I started to work since my thesis of Master degree: Thanks for enlightening me the first glance of research and a special thanks for your personal support also in my difficult moments during this Ph.D.: You will always be in my heart and you have my eternal thanks.

I would also like to thank *Prof. Giovanni Golemme, Dr. Enrico Catizzone* and all the members from the Department of Environmental and Chemical Engineering of the University of Calabria for giving me the opportunity to work their laboratories. I greatly appreciate the support received through the collaborative work. In Particular, *Prof. Giovanni Golemme*: thank you very much for your hospitality and the precious teachings.

My thanks also go out to the *Prof. Maria del Rosario Sun Kou* and *Ms. Angela Pinedo, Miss. Fabiola Bravo Hualpa, Mr. Jorge Trevejo* of the Department of Sciences, Section Chemistry of the Pontifical Catholic University of Perú, for giving me the opportunity to work their laboratories on a long period of internship. Thanks a lot for your hospitality and the precious teachings, you will always be in my heart.

To conclude the "working" section I would like to thank *Dr. Marco Tagliabue* with whom my research group collaborated for this Ph.D. work through the ENI-Donegani Research Center.

I would also thank my friends: *Ms. Elisa Cala, Ms. Andrea Lombardo, Ms. Manuel Striani* for being always.: Our friendship will continue always. I would like to thank my family: my mother *Eva Olivera* to which this thesis is devoted, my father *Marco Olivas* and to my sister *Jessica Olivas* for their continuous and unparalleled love, help and support. I am grateful to my sister for always being there for me as a friend. I am forever indebted to my parents for giving me the opportunities and experiences that have made me who I am. I would like to thank the rest of my family, aunt *Ana Olivera*, my uncles *Humberto Olivera and Jose Enrrique Quintana*, my dear cousins *Adriana Quintana and Alejandra Quintana*.

And last, but obviously not least, I would like to thank *Lorenza Priano e Carlo Olivieri* for their kindness motivation to continue in every difficult moment that I passed during my Ph.D. I want to say that without your motivation and help it would have been impossible to finish. I am very grateful. You will always be in my heart.

Appendix I

Microporous Materials: Introduction to Zeolites

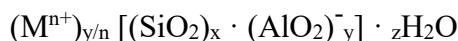
One of the oldest members of the microporous materials family are zeolites.

Zeolite is a Greek word ζεω (*zeo*) means ‘to boil’ and λιθος (*lithos*) means ‘stone’ and together mean “boiling stone”. This is because when the Swedish mineralogist (Baron) Friedrich Axel Cronstedt discovered a natural zeolite for the first time in 1756, he observed a “stilbite” which is currently famous zeolite, lost huge quantities of steam upon heating.^[1]

1. Structure and chemical composition of zeolites

Structurally, zeolites are crystalline polymers based on a three-dimensional arrangement of TO₄ tetrahedra (T = Si or Al) linked through their oxygen atoms to form subunits and finally large lattices by repeating identical building blocks (unit cells), producing a network containing channels and cavities of molecular dimensions.^[2]

Zeolites are composed of an aluminosilicate framework which general formula is:



where n is the valence of the cation M and (x+y) is the number of tetrahedra per crystallographic unit cell and x/y is the framework silicon/aluminium ratio n_{Si}/n_{Al} (or simply Si/Al).^[3,4]

The ways of combining each TO₄ (Si, Al) tetrahedra are many and this leads to the possibility of obtaining different regular rings that also take the name of Secondary building units, SBUs (Figure 1). The most common rings are formed by 4-T, 6-T, 8-T, 10-T, and 12-T; however, zeolitic structures containing 14, 18, and 30-member rings have been also obtained.^[5]

Each zeolite is recognized with a three-letter code that identifies the type of lattice (connectivity, pore size, etc.). The typical rings of the zeolitic structures can generate polyhedra, one of the most common is the polyhedron called the truncated octahedron cube, in which there are 24 primary structural units (tetrahedra), has a surface defined by 6 rings formed by 4-T and 8 rings formed by 6-T [4⁶6⁸]. This structure is highly symmetrical and also known as the *sodalite unit* cage β (Figure 3.1, top line). These units can be connected to each other thus forming different three-dimensional structures (Figure 1). Some of the most typical three-dimensional structures of zeolites are shown in Figure 1. Adapted from ref.^[4]

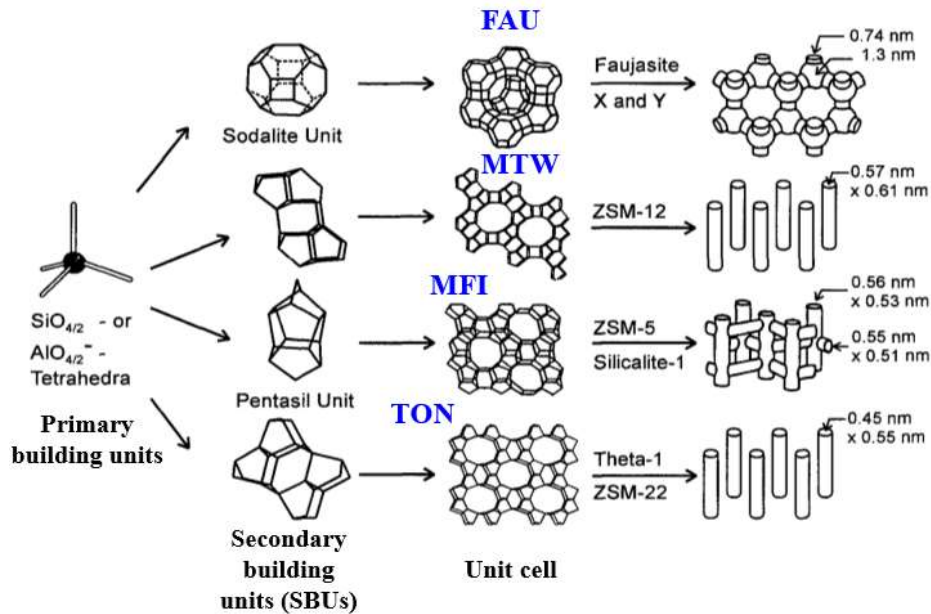


Figure 1: Structures of four selected zeolites (from top to bottom: faujasite or zeolites X, Y; zeolite ZSM-12; zeolite ZSM-5 or silicalite-1; zeolite Theta-1 or ZSM-22) and their micropore systems and dimensions.

Adapted from ref.^[4]

The size of the micropores of the zeolite varies depending on the number of members in the rings, between 4 and 12 Å. On rings, T-O-T angles vary mostly in the range 130°–180°. The Flexibility of this angle is one of the most important factors determining the huge variety of zeolites frameworks. (Figure 2).^[5]

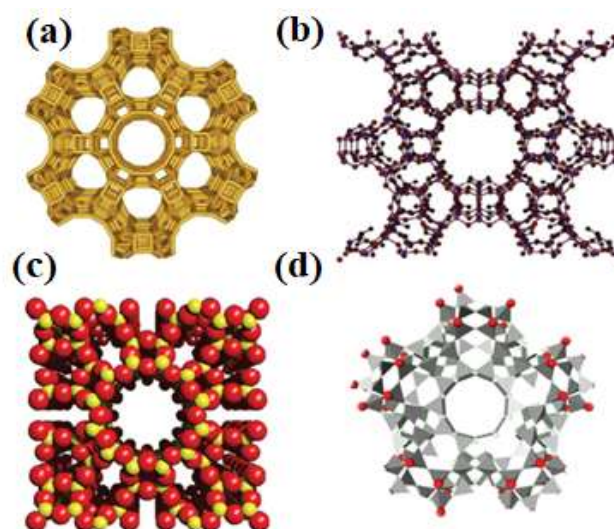


Figure 2: Framework structure of zeolites; (a) T-site bonding only, (b) ball and stick, (c) space filling, and (d) (Si, Al)O₄ tetrahedra. Adapted from ref.^[5]

The term silicon/aluminum ratio (Si/Al) is used to define the composition of a zeolite. The concentration of silicon and aluminum is important to explain the chemical characteristics of zeolites. Silicon (Si^{4+}) and aluminium (Al^{3+}) cations bounded by four oxygen anions (O^{2-}). The presence of trivalent Al atoms in the framework results negatively charged an anionic framework (AlO^{2-}) which can be neutralised by the extra framework cations such as sodium (Na^+), calcium (Ca^{2+}) and magnesium (Mg^{2+}).^[6] Heavy metal cations in solution can be exchanged for these extra framework cations via ion exchange mechanism, which is, in certain cases, found to be the primary mechanism of heavy metal sorption employed by zeolite.^[7-9]

There is an avoidance of the formation of Al-O-Al linkages known as “Loewenstein rule” in honor of the Loewenstein who first rationalized this observation. This rule explains that two tetrahedra are linked by one oxygen bridge, the center of only one of them can be occupied by aluminium; the other center must be occupied by silicon.^[10]

Likewise, whenever the maximum of Si by Al may be 50% and therefore the minimum rate of Si/Al is 1. Furthermore, for a replacement equal to 50%, a strict alternation of Si and Al in the tetrahedra is necessary^[10]

As explain above, the presence of Al^{3+} produces the formation of a negative charge of the framework that must be neutralized by counterions positive. Usually, the negative charge is compensated by additional non-framework cations like sodium (Na^+). However, sodium ions are mostly replaced by protons (H^+) that form a bond with the negatively charged oxygen anions of the zeolite (this results in Brønsted OH acid sites)^[11] The zeolites surface plays important roles on the adsorption properties (*i.e.*, hydrophobicity, hydrophilicity and binding to reactant with molecules). In fact, it is well known that the many relevant properties of zeolites are based on the concentration, distribution, and nature of surface species (*silanols*) present on the internal and external surface inside the porous as explained in Figure 3 (Schematic description of the surface species of zeolites. Adapted from ref.)^[12,13]

These species silanols on zeolites has been identified as (Figure 3): *isolated silanols* Si-OH situated at the external surface, where the possibility of interaction with surrounding groups is not possible.

Vicinal Silanols (or bridged silanols), silanols situated on the inner surfaces of the zeolite, where interaction of them with the surrounding is possibly. *Terminal silanols* consisting of an OH group bonded to an external Si atom. *Geminal silanols*, which are formed by two OH groups linked to an external Si atom. And Silanols belonging to the Si-(OH)-Al bridges (Brønsted sites).

The Brønsted acid sites can be described by the resonance structures I and II (Figure 3) where the structure I has the weak bound between the oxygen and proton (H^+) and the structure II is a weak interaction between OH group which with the proton Al^{3+} (Lewis acid).

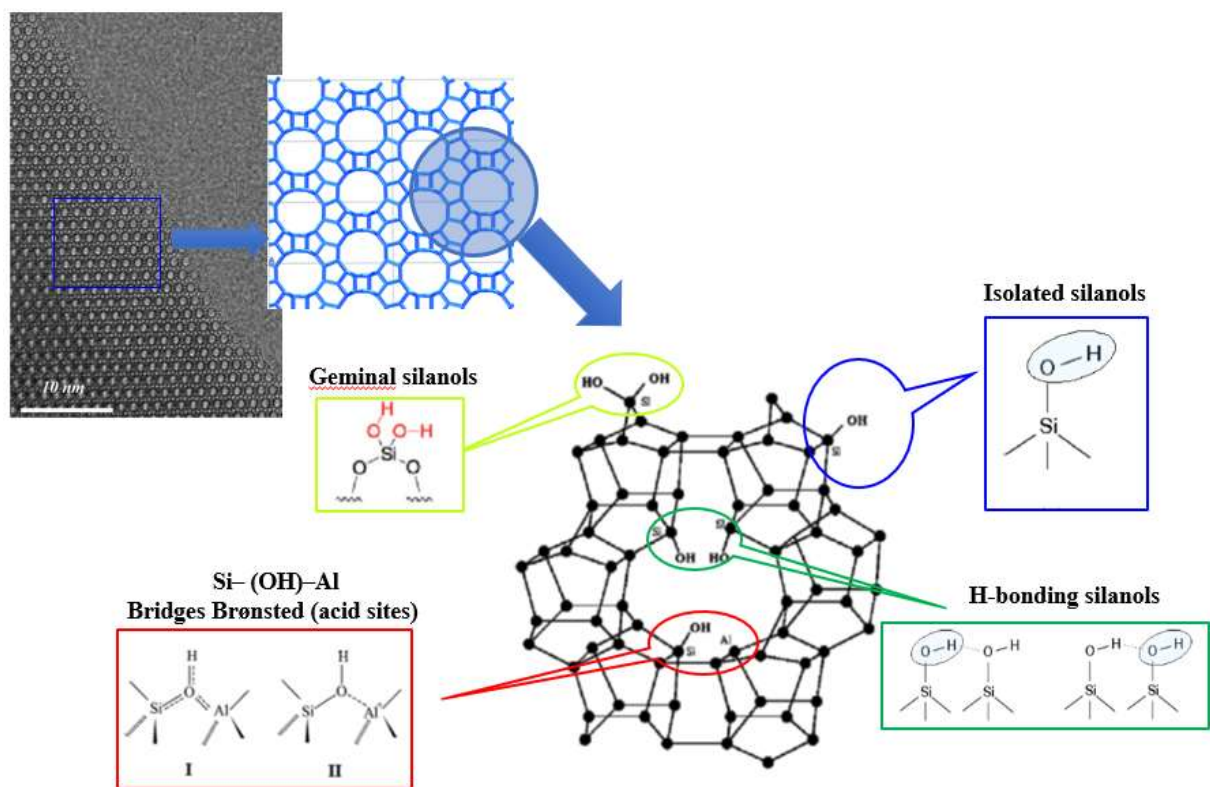


Figure 3: Schematic description of the surface species of zeolites. TEM image of zeolite beta together to Structural model of a ZSM-5 zeolite indicating the configuration of the different silanols. Adapted from ref.^[12,13]

Several zeolites have a prominent role because of its application in various important catalytic processes, including the oligomerization of light olefins, fluid catalytic cracking, and the alkylation of aromatics.^[14-23] The catalytic behaviours of zeolites are mainly determined by the number and nature of their acid sites (Brønsted sites), the location and distribution of which affects the effective diffusion paths of the reactant molecules. However, as illustrated above, the key challenge for the development of efficient adsorbents for organic pollutants is adjusting the hydrophobic/hydrophilic character of zeolites. Furthermore, some literatures show that the stability of zeolite in hot liquid water is strongly associated with the density of Brønsted and Lewis acid sites^[24], which in turn is correlated by the Si/Al ratio in their framework. Nevertheless, increasing the Si/Al ratio makes the zeolite structure last longer in aqueous environment due it increases the hydrophobicity character of the zeolite. For this purpose, it is possible to removal the acid sites (Brønsted silanols) by eliminating Al atoms from the framework through dealumination process.

2. The dealumination process of zeolites

Dealumination is a method of chemical and structural modification of zeolites by a post-synthesis treatment in which the Al atoms are removed from the zeolite lattice.

Dealumination can be accomplished by thermal or hydrothermal treatments, acids leaching, and chemical treatments with hexafluorosilicate (AHFS) or silicon tetrachloride (SiCl₄). Among these methods, hydrothermal treatment is the most frequently used one.^[25-30]

It is well known that dealumination through hydrothermal treatment consists of hydrolysis of Al-O bonds with formation of neutral and cationic aluminium species.^[31,32] Then the defect sites created by dealumination are filled by silicon atoms with a consequent stabilization of the zeolite framework. Wang et. al. explained the mechanism of dealumination of NH₄NaY zeolite by hydrothermal Treatment and is illustrated in Figure 4.^[33]

In this mechanism, the reactions 1 to 4 explain the dealumination during the period of steaming. The step 1 denominated deammoniation begins at low temperature leads to a protonic zeolite in equilibrium with the hydroxyl form. Steps 2 to 4 correspond to the hydrolysis of the various Si-O-Al bonds and the migration of the Al species, consequently the formation defective sites (Si-OH). The following step 5 is the filling of the created vacancies (Si-OH) by Si atoms, leading to the stabilization of the framework.

It is also possible to observe a loss of crystallinity during the dealumination, this because the amount of water is relatively small, the migration of the Si species occurs slowly to fill the hydroxylated species (defective sites).^[33]

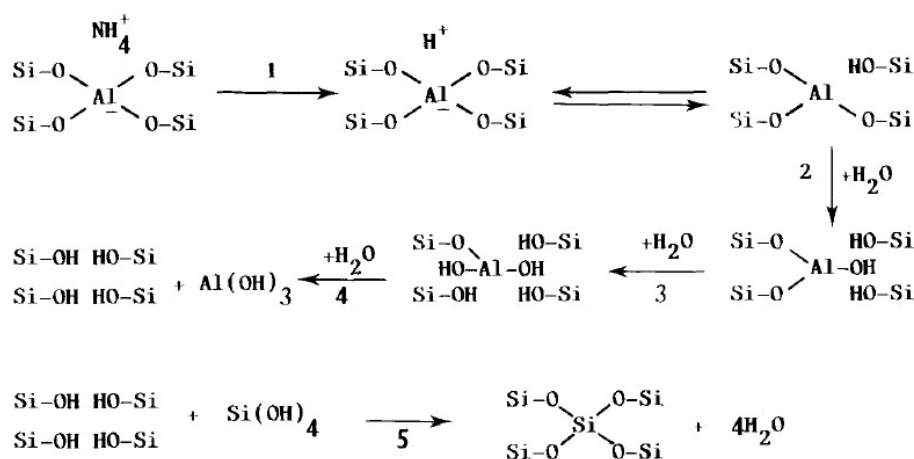


Figure 4: Mechanism of dealumination of a NH₄Y zeolite by hydrothermal treatments. Adapted from ref. ^[33]

As reported in the literature dealumination of zeolites through hydrothermal (steaming) treatment promotes the formation of a mesoporous system at the expense of the original micropores of the

samples.^[34,35] In this way the one-dimensional zeolite micropores are interconnected by mesopores so that a two or three-dimensional structure is obtained. The presence of these mesopores is decisive because they help to overcome problems of diffusion in microporous zeolites and they allow shorter diffusion paths.^[36]

3. *Zeolites applications*

Originally zeolites were useful as adsorbents for drying and separation process. Since the development of the first concepts of acid zeolite catalyst, to date many business processes based on zeolites as catalysts have been implemented. In 1938 Houdry et al. used them in catalytic cracking of hydrocarbons.^[37,38] Later, in 1986, Pop et al. developed two ZSM-5 zeolites with different Si/Al ratios as catalysts for BTX synthesis by a selective methanol conversion.^[39]

Both natural and synthetic zeolites are extensively used in the fields of adsorption, ion-exchange, heterogeneous catalysis (nowadays most of gasoline is produced by zeolitic catalytic processes), energy storage, and more recently in several emerging fields such as health and medicine.^[40]

Zeolites are excellent support of catalysts and adsorption due to their physic-chemical features, such as: High surface area, Molecular dimensions of the pores, high adsorption capacity, partitioning of reactant/products, possibility of modulating the electronic properties of the active sites, possibility for pre-activating the molecules when in the pores by strong electric fields and molecular confinement.

The research and knowledge of zeolites have grown so much that it was founded in 1973 the International Zeolite Association (IZA). This association aims to promote and encourage the scientific and technological development of zeolites and porous materials.^[5,41]

Ordered Mesoporous Silicas

Meso, the Greek prefix, meaning—in between, has been adopted by IUPAC to define porous materials with pore sizes between 2.0 and 50.0 nm. Mesoporous materials are characterized by high specific surface areas ($>1000 \text{ m}^2 \text{ g}^{-1}$), and large pores dimensions with large pore volumes. These characteristics allow to use such materials to overcome the limitations imposed by the reduced space of zeolite channels for interactions with larger molecules.^[42]

The synthesis of the M41S family developed by the Mobil Oil Company in 1992.^[43,44] This class of materials are characterized by very large specific surface areas, ordered pore systems, and well-defined pore radius distributions, in spite of these materials are amorphous materials but with ordered mesoporosities (Ordered mesoporous materials), in other words the framework of these materials is not crystalline but mesopores are arranged periodically within the structure.

Three main subgroups of M41S materials were first reported by Mobil's group. They include of a hexagonal phase referred to as MCM-41, a cubic phase known as MCM-48, and a nonstable lamellar phase known MCM-50 (Figure 5).^[45,46]

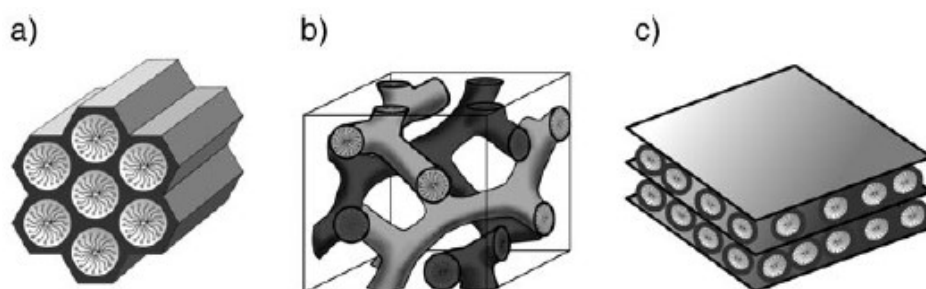


Figure 5: Structures of mesoporous M41S family: a) MCM-41 (2D hexagonal), b) MCM-48 (cubic), and c) MCM-50 (lamellar, space group p2). Adapted from ref.^[46]

The discovery of these materials represented a turning point in the research of materials and has led to an evolution of methods to develop new mesoporous solids similar to M41S silicas. Varying the conditions of synthesis, the silica precursor and the type of surfactant used to create the porous structure, many mesoporous materials have been established including:

- ✓ Hexagonal Mesoporous Silicones (HMS);
- ✓ Korea Advanced Institute of Science and Technology Silicas (KIT);
- ✓ Santa Barbara Amorphous silicas (SBA);
- ✓ Folded Sheets Mesoporous Material (FSM), for example the mesoporous silica FSM-16.^[47,48]

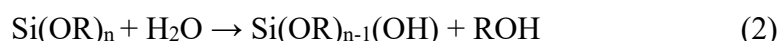
Typically, the synthesis of M41S materials takes place under mild conditions, typically below 120 °C, in the presence of anionic, cationic or neutral surfactants, under either basic or acidic conditions.

Synthesis procedures generally include the use of sol-gel methods. Sol-gel methods provide metal alkoxide molecular precursors to produce a metal oxide according to the overall reaction 1:

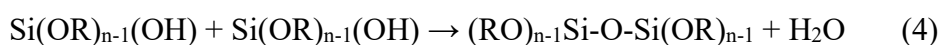
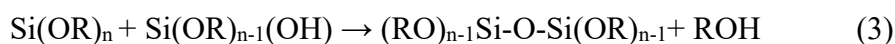


where R is an alkyl group and the metal in this case is Si.^[49,50]

The sol-gel method initially provides for the formation of a solution called SOL, which is generated by the following hydrolysis reaction (2):



The second reaction is that of condensation which leads to the formation of colloidal evolution called GEL. This reaction involves dealcoholisation reactions (3) and condensation (4):



The continuation of these reactions increases the number of bonds $\equiv\text{Si-O-Si}\equiv$, and therefore there is a reduction in the flexibility of the lattice and consequently an increase in viscosity. Even after gelation (gel aging) the number of bonds $\equiv\text{Si-O-Si}\equiv$ continues to increase causing the contraction of the gel and the expulsion of the solvent from the pores for which the gel becomes more and more rigid.

In the case of the synthesis of mesoporous systems, the sol-gel synthesis procedure is modified by the introduction of surfactants which are used as templates to allow formation of the porous structure. In Figure 6 is shown how surfactants, in the form of a lyotropic liquid-crystalline phase, lead to the assemblage of micelles generating an ordered mesostructured composite during the condensation of the silica precursors. After this, the mesoporous materials are obtained by subsequent removal of the surfactant by extraction or calcination.^[46,51]

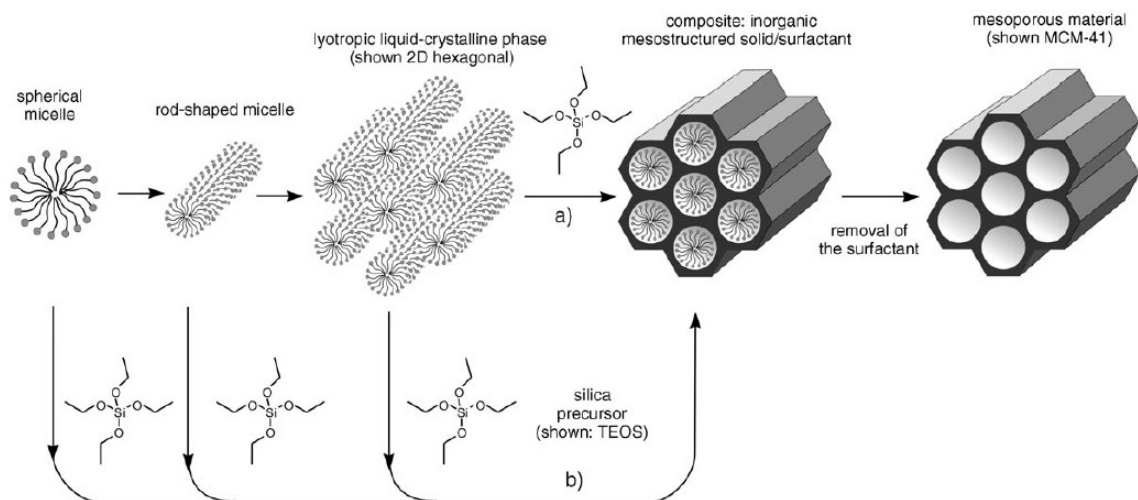


Figure 6: Formation of mesoporous materials by structure-directing agents: a) true liquid-crystal template mechanism, b) cooperative liquid crystal template mechanism. Adapted from ref.^[46]

1. Chemical composition of silicas

It is known that the SiO_2 chemical composition comprises *silanol* groups ($\equiv \text{Si-OH}$) and *siloxane* ($\equiv \text{Si-O-Si}$) groups.^[52,53] In fact, the surface properties of silica, which is considered to be an oxide adsorbent, in many cases depend on the presence of silanol groups. Silanols are OH groups that are covalently bound to Si atoms on the silica surface.^[54]

Silanol groups are formed on the surface by two main processes.^[54] In detail, silanols groups are formed while silica synthesis, during the condensation/polymerization process of the Si(OH)_4 (Figure 7, a). In this step, the supersaturated solution of the acid becomes converted into its polymeric form, which then changes into spherical colloidal particles containing $\equiv \text{Si-OH}$ groups on the surface. Upon drying, the hydrogel yields xerogel (the final product) which retains some or all the silanol groups on its surface.

The second process which can form silanols OH groups is by rehydroxylation of dehydroxylated silica when it is treated with water or aqueous solutions. The surface silicon atoms tend to have a complete tetrahedral configuration, and in an aqueous medium their free valence becomes saturated with hydroxyl groups (Figure 7, b).

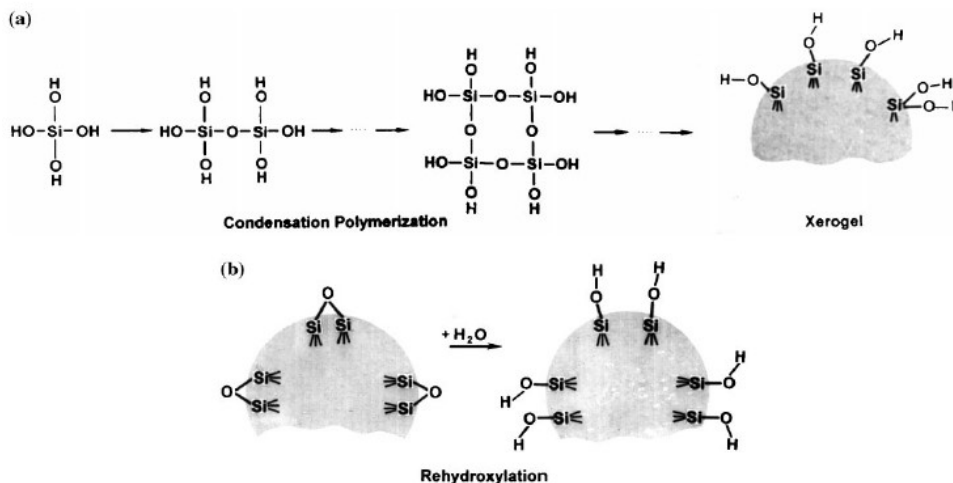


Figure 7: The formation of silanol groups on the silica surface: (a) Condensation polymerization; (b) Rehydroxylation. Adapted from ref.^[54]

The silanols can be divided into *isolated groups* (or free silanols), where the surface silicon atom has three bonds into the bulk structure and the fourth bond attached to a single OH group (Figure 8, a), and *vicinal silanols* (or bridged silanols), where two single silanol groups, attached to different silicon atoms, are close enough to hydrogen bond (Figure 8, b). A third type of silanols, *geminal silanols*, consist of two hydroxyl groups, that are attached to one silicon atom (Figure 8, c). The geminal silanols are too close to hydrogen bond each other, whereas the isolated silanols are too far separated.^[55]

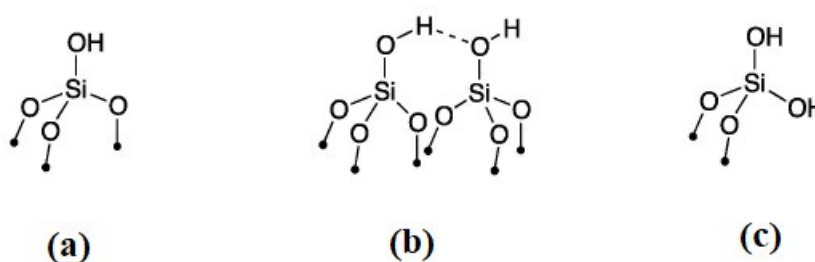


Figure 8: Silanols present on the silica surface, (a) isolated silanols, (b) vicinal silanols and (c) geminal silanols. Adapted from ref.^[56]

References

- [1] H. van Bekkum, E.M. Flanigen, P.A. Jacobs and J.C. Jansen, Eds. 2nd edition, Elsevier Science, Amsterdam, 2001.
- [2] B. Jha and D.N. Singh, Chapter 3 Basics of Zeolites, Fly Ash Zeolites, Advanced Structured Materials 78, Springer Science Business Media, Singapore 2016, pp. 5.
- [3] M. Guisnet and J.P. Gilson, Introduction to Zeolite Science and Technology, Zeolites for Cleaner Technologies Catalytic Science Series, Imperial College Press, London, 2002, 3, pp. 4
- [4] J. Weitkamp, *Solid State Ion*, 2000, 131, 175-188.
- [5] A. Chica, Review Article Zeolites: Promised Materials for the Sustainable Production of Hydrogen, Hindawi Publishing Corporation ISRN Chemical Engineering, 2013, pp. 1-19.
- [6] H. Ghobarkar, O. Schäf, and U. Guth, *Progress in Solid State Chemistry*, 1999, 27, 2-4, 29-73.
- [7] A. M. Ziyath, P. Mahbub, A. Goonetilleke, M. O. Adebajo, S. Kokot, A. Oloyede, *Journal of Water Resource and Protection*, 2011, 3, 758-767.
- [8] K. S. Hui, C. Y. H. Chao, and S. C. Kot, *Journal of Hazardous Materials*, 2005, 127, 1-3.
- [9] B. Biškup and B. Subotic, *Separation and Purification Technology*, 2004, 37, 1, 17-31.
- [10] W. Loewenstein, *American Mineralogist*, 1954, 39, 92-9.
- [11] S. Van Donk, Adsorption, Diffusion and Reaction Studies of Hydrocarbons on Zeolite Catalysts. Doctoral thesis, Utrecht University, Netherlands, 2002.
- [12] P. Hoffmann, J. A. Lobo, *Microporous and Mesoporous Materials*, 2007, 106, 122-128.
- [13] S. Inagaki, I. Kawamura, Y. Sasaki, K. Yoshida, Y. Kubota and A. Naito, *Phys Chem Chem. Phys*, 2013, 15, 13523-13531.
- [14] L. R. Aramburo, L. Karwacki, P. Cubillas, S. Asahina, D. A. Matthijs de Winter, M. R. Drury, I. L. C. Buurmans, E. Stavitski, D. Mores, M. Daturi, P. Bazin, P. Dumas, F. Thibault-Starzyk, J. A. Post, M. W. Anderson, O. Terasaki, and B. M. Weckhuysen, *Chem. Eur. J.*, 2011, 17, 13773 – 13781.
- [15] A. Corma, *Chem. Rev.*, 1995, 95, 559.
- [16] A. Corma, A. Martinez, *Adv. Mater.*, 1995, 7, pp. 137.
- [17] J. M. Thomas, *Sci. Am.*, 1992, 266, pp. 112.
- [18] M. A. den Hollander, M. Wissink, M. Makkee, J. A. Moulijn, *Appl. Catal. A.*, 2002, 223, 85.
- [19] R. J. Quann, L. A. Green, S. A. Tabak, F. J. Krambeck, *Ind. Eng. Chem. Res.*, 1988, 27, 565.

- [20] X. C. Wu, R. G. Anthony, *J. Catal.*, 1999, 184, 294.
- [21] J. M. Thomas, R. Raja, G. Sankar, R. G. Bell, *Nature*, 1999, 398, pp. 227.
- [22] B. M. Weckhuysen, *Angew. Chem.*, 2009, 121, pp. 5008.
- [23] VCH Wiley, Weinheim, *Zeolites and Catalysis*, Eds.: J. Čejka, A. Corma and S. Zones, 2010.
- [24] R. M. Ravenelle, F. Schübler, A. D'Amico, N. Danilina, A. J. Van Bokhoven, J. A. Lercher, C. W. Jones, and C. Sievers, *J. Phys. Chem. C.*, 2010, 114, 19582–19595.
- [25] F. Lonyi, J. H. Lunsford, *J. Catal.*, 1992, 136, 566.
- [26] C. S. Triantafillidis, N. P. Evmiridis, *Ind. Eng. Chem. Res.*, 2000, 39, 3233.
- [27] P. A. Jacobs, M. Tielen, J. B. Nagy, G. Debras, E.G. Derouane, Z. Gabelica, In Proceedings of the 6th International Zeolite Conference, D. Olson and A. Bisio (Eds.), London, 1984, pp. 783.
- [28] S. Han, D. S. Shihabi, C. D. J. Chang, *Catal.*, 2000, 196, 375.
- [29] M. R. Apelian, A. S. Fung, G. J. Kennedy, T. F. Degnan, *J. Phys. Chem.*, 1996, 100, 16577
- [30] Y. Fan, X. Bao, X. Lin, G. Shi, and H. Liu, *J. Phys. Chem. B*, 2006, 110, 15411-15416
- [31] Th. Gross, U. Lohse, G. Engelhardt, K. H. Richter, and V. Patjelova, *Zeolites*, 1984, 4, pp.25
- [32] P. K. Maher, F. D. Hunter, and J. Scherzer, "Molecular Sieve Zeolites-I", *Adv. Chem. Ser.*, Vol. 101, Am. Chem. Soc., 1971, Washington, DC, p. 266.
- [33] Q. L. Wang, G. Giannetto, M. Torrealba, G. Perot, C. Kappenstein, and M. Guisnet, *Journal of Catalysis*, 1991, 130, 459-470.
- [34] L. Teyssiera, M. Thomasa, C. Bouchya, J. Martensb and E. Guillon, *Zeolites and Related Materials: Trends, Targets and Challenges Proceedings of 4th International FEZA Conference (2008)*.
- [35] M. Brotas de Carvalho, A.P. Carvalho, F. Ramô, Ribeiro, A. Florentino, N.S. Gnep and M. Guisnet, *Zeolite*, 1994, 14, 217-224
- [36] V. Sacchetto; *Silica Based Materials for Environmental and Energy Applications*; Doctoral thesis, University of Eastern Piedmont, Alessandria, 2017
- [37] E. Houdry, W. F. Burt, A. E. Pew, and W. A. Peters, "The houdry process," *Oil and Gas Journal*, Engineering and Operating Section, 1938, 37, pp. 40–45.
- [38] E. M. Flanigen, "Zeolites and molecular sieves. An historical perspective," *Introduction To Zeolite Science and Practice*, H. van Bekkum, E. M. Flanigen, and J. C. Jander, Eds., *Studies in Surface Science and Catalysis*, Elsevier, 2nd Completely Revised and Expanded Edition, Amsterdam, 1991, pp. 11–37.

- [39] G. Pop, G. Musca, G. Maria, S. Straja and R. Mhall, *Ind. Eng. Chem. Prod. Res. Dev.*, 1986, 25, 2 pp. 209.
- [40] S. Yang, M. Lachhab, I. I. Vaisman, E. Blaisten-Barojas, X. Li and V. L. Karen, Framework-Type Determination for Zeolite Structures in the Inorganic Crystal Structure Database, *J. Phys. Chem. Ref. Data*, 2010, 39(3).
- [41] The International Zeolite Association (IZA), Welcome to the IZA Website, last updated: 15-August-2017 Available: <http://www.iza-online.org/>
- [42] A. Matsumoto, H. Chen, K. Tsutsumi, M. Gruen, K. Unger, *Microporous and Mesoporous Materials*, 1999, 32, 55–62.
- [43] C. T. Kresge, M. E. Leonowicz, W. J. Roth, J. C. Vartuli, J. S. Beck, *Nature*, 1992, 359, 710 – 712.
- [44] J. S. Beck, J. C. Vartuli, W. J. Roth, M. E. Leonowicz, C. T. Kresge, K. D. Schmitt, C. T.-W. Chu, D. H. Olson, E. W. Sheppard, S. B. McCullen, J. B. Higgins, J. L. Schlenker, *J. Am. Chem. Soc.* 1992, 114, 10834 – 10843.
- [45] A. Sayari, *Chem. Mater.*, 1996, 8, 1840.
- [46] F. Hoffmann, M. Cornelius, J. Morell, and M. Friba, *Angew. Chem. Int. Ed.*, 2006, 45, 3216 – 3251
- [47] Matsumoto, T. Sasaki, N. Nishijima, and K. Tsutsumi, *Colloids and Surfaces A. Physicochem. Eng. Aspects*, 2002, 203, 185–193.
- [48] Y. Tozuka, T. Oguchi, and K. Yamamoto, *Pharmaceutical Research*, 2003, 20 (6), 926-930.
- [49] J. E. Lofgreen and G. A. Ozin, *Chem. Soc. Rev.*, 2014, 43, 911-933.
- [50] C. J. Brinker and G. W. Scherer, Academic Press, San Diego, 1990, 97–234
- [51] A. Monnier, F. SchEth, Q. Huo, D. Kumar, D. Margolese, R. S. Maxwell, G. Stucky, M. Krishnamurty, P. Petroff, A. irouzi, M. Janicke, B. Chmelka, *Mesostructures Science*, 1993, 261, 1299 – 1303.
- [52] A. M. Schrader, J. I. Monroe, R. Sheil, H. A. Dobbs, T. J. Keller, Y. Li, S. Jain, M. S. Shella, J. N. Israelachvili, and S. Han, *PNAS*, 2018, 115, 2890–2895
- [53] J. Nordstrom, A. Matic, J. Sun, M. Forsyth and D. R. MacFarlane, *Soft Matter*, 2010, 6, 2293–2299
- [54] L. T. Zhuravlev, *Colloids and Surfaces A: Physicochemical and Engineering Aspects*, 2000, 173, 1–38
- [55] E. F. Vansant, P. Van Der Voort, K.C. Vrancken, *Studies in Surface Science and Catalysis*, 1995, 93, 1995, 59-77
- [56] M. P. Conley, A. J. Rossini, A. Comas-Vives, M. Valla, G. Casano, O. Ouari, P. Tordo, A. Lesage, L. Emsley and C. Copereet, *Phys. Chem. Chem. Phys.*, 2014, 16, 17822-17827.

Appendix II

Instrumental Parameters

1. N₂ Physisorption Analysis

N₂ physisorption analyses were carried out at 77K in the relative pressure range from 10⁻⁷ to 1 *p/p*₀ by using a using an Autosorb-iQ (Quantachrome Instruments). Prior to adsorption, the zeolites HSZ-Y and ZSM-5 under high vacuum conditions (final pressure 7 × 10⁻⁴ mbar) for 1 h at 90 °C, 1 h at 130 °C, and finally 16 h at 300 °C. All other silica samples were outgassed for 2 h at 80°C, 1 h at 140°C, 1 h at 180°C and finally at 10 h at 220°C.

The specific surface areas of the samples were determined by the Brunauer–Emmett–Teller (BET) equation in particular, using the 0.005-0.01 *p/p*₀ range for the HSZ-Y zeolite and the 0.15-0.30 *p/p*₀ range for ZSM-5. The specific area of other silica samples was determined by the Brunauer–Emmett–Teller (BET) equation in the range 0.1-0.25 *p/p*₀ of relative pressure. The pore size distributions of all the samples were calculated by applying the cylindrical pore NLDFT kernel in the desorption branch isotherms.

2. Thermogravimetric Analysis (TGA)

TGA analyses were made using a SETSYS Evolution TGA-DTA/DSC thermobalance. TG analysis were collected in a heating rate of 2 °C/min under oxygen (100 mL/min). Samples were heated from ambient temperature to 1100 °C.

To know the amount of surface silanol species present on the surface of all the samples was considered the weight loss of the samples in the temperature range between 150-1000 ° C and following the Equation 1:

$$\frac{n(OH)}{nm^2} = \frac{wt\% \times N.A \times 2(OH)}{(100 - wt\%) \times M.W._{H_2O} \times SSA_{BET}} \quad (1)$$

where: wt% is the weight loss due to the condensation of silanols group, N.A is the Avogadro number 6.023x10²³, 2(OH) is the number of SiOH needed to form a water molecule by condensation, M.W._{H₂O} is the molecular weight of water (18 g mol⁻¹), SSA_{BET} is the specific surface area of the sample [m² g⁻¹], estimated by N₂ Physisorption Analysis.

3. Elemental Analysis.

C–H–N elemental contents were determined using an EA 3000 elemental analyser (EuroVector). Helium and oxygen at 120 and 35 kPa pressures were used, respectively. For each material, three measurements were done.

4. Fourier Transform Infrared Spectroscopy (FTIR)

Infrared spectra were collected on a Thermo Electron Corporation FT Nicolet 5700 spectrometer with 4 cm^{-1} resolution.

Zeolites samples: self-supporting pellets of HSZ-Y and ZSM-5 samples were obtained by using a mechanical press at ca. 7 tons cm^{-2} and placed into an IR cell equipped with KBr windows permanently attached to a vacuum line (residual pressure $\leq 1 \times 10^{-4}$ mbar), allowing all treatments and pollutants adsorption/desorption experiments to be carried out in situ. Spectra of pollutants adsorbed on zeolites have been collected at beam temperature (ca. $35\text{ }^\circ\text{C}$) on samples previously dehydrated under vacuum at beam temperature for HSZ-Y and ZSM-5 zeolites.

- other silica samples (FUMED, AMSs, MCM-41 and SBA-15, SBA-15-PAPTS silica sample): self-supporting pellets were placed into an IR cell with KBr windows permanently connected to vacuum line (residual pressure $\leq 1 \times 10^{-4}$ mbar), allowing all treatments and adsorption-desorption experiments to be carried out in situ. Before the analysis samples were outgassed in vacuum at $150\text{ }^\circ\text{C}$ for SBA-15 whereas for the other samples at r.t. for 30 min.

For the figures of comparisons, the IR spectra of the various samples were normalized taking as reference the density ρ [g cm^{-2}]. In this way, differences of the bands intensity among different samples related to intrinsic oscillators of the materials can be associated to actual differences in the amount of such species in the samples. As a consequence of the normalization, the absorbance values are reported as arbitrary unit (a.u.).

5. Solid state NMR (SS-NMR) Spectroscopy

All spectra were acquired on a Bruker Avance III 500 spectrometer and a wide bore 11.7 T magnet with operational frequencies for ^1H and ^{13}C of 500.13 and 125.77 MHz, respectively. A 4 mm triple resonance probe with MAS was employed in all of the experiments.

The binary mixture of pollutants was adsorbed directly on dehydrated zeolites (HSZ-Y and ZSM-5) powder. After waiting for an appropriate time (ca. 30 min) for reaching equilibrium, the rotor was packed in a glovebox and submitted for solid state NMR experiments. The Zirconia rotor was spun at a MAS rate between 10 and 15 kHz. The magnitude of the radio frequency field was 100 kHz for ^1H MAS NMR, and the relaxation delay, d_1 , between accumulations was 5 s. For the $^{13}\text{C}\{^1\text{H}\}$ CPMAS experiments, the rf fields $\nu_{\text{rf}}^{\text{H}}$ of 55 and 28 kHz were used for initial excitation and decoupling, respectively. During the CP period, the ^1H RF field $\nu_{\text{rf}}^{\text{H}}$ was ramped using 100 increments, whereas the ^{13}C RF field $\nu_{\text{rf}}^{\text{C}}$ was maintained at a constant level. During acquisition, the protons are decoupled from the carbons by using a TPPM decoupling scheme. A moderate ramped

RF field ν_{rf}^H of 62 kHz was used for spin locking, while the carbon RF field ν_{rf}^C was matched to obtain optimal signal, and a variable CP contact time was used. All chemical shifts are reported using the δ scale and are externally referenced to TMS at 0 ppm.

The ^{29}Si MAS NMR spectra of AMSs before and after hydrothermal treatment acquired by using the same Bruker Avance III 500 spectrometer with a wide-bore 11.7 T magnet with operational frequencies for ^1H and ^{29}Si of 500.13 and 99.35 MHz, respectively. A 4 mm triple-resonance probe with magic-angle spinning (MAS) was employed in all experiments. The samples were packed on a zirconia rotor and spun at a MAS rate between 10 kHz. Quantitative ^{29}Si MAS NMR data were recorded under ^1H decoupling conditions with the radio-frequency field of 42 kHz for $\pi/2$ pulse. The relaxation delay between accumulations was one minute. All chemical shifts are reported on the δ scale and were externally referenced to tetramethylsilane (TMS) at 0 ppm. All NMR spectra were fitted with DMFIT functions for quantitative deconvolution of overlapping peaks.

6. Theoretical Calculations

Theoretical calculations were performed with Gaussian09 program at the Density Functional Theory (DFT) level, with hybrid functional B3LYP, using Poples's 6-31G(d,p) basis set, including polarization functions on all the centers, for light atoms, and LANL2DZ effective core potentials and basis set for silicon. The atom-atom pairwise algorithm proposed by Grimme and implemented in Gaussian09 was used to estimate the contribution from dispersion (van der Waals) forces to energies, geometrical structures and harmonic frequencies and intensities.

7. Gravimetric Analysis

Toluene adsorption isotherms on AMS-HSA samples were obtained at 35°C by using an Intelligent Gravimetric Analyzer (IGA-002, Hiden Analytical Ltd., U.K.), with integrated temperature and pressure controllers. The former consists of a thermos stated water bath/circulator, employing a 50% water: 50% antifreeze (inhibited ethylene glycol) mixture. The latter is based on two pressure sensors, working in the 0–10 mbar (Baratron capacitance manometer, accuracy ± 0.05 mbar) and 10–1000 mbar (strain gauge, accuracy ± 1 mbar) ranges. IGA is an ultra-high-vacuum (UHV) microbalance (weighing resolution = 0.2 μg), specifically designed to study vapor sorption, which allows isotherms and the corresponding kinetics of adsorption and desorption to be determined. Buoyancy corrections were carried out using the weights and densities of all the components of the sample and counterweight sides of the balance and the measured temperature. Prior the analysis, samples were outgassed for 4 h at 35°C. Buoyancy corrections were carried out using the weights and densities of

all the components of the samples and counterweight sides of the balance and the measured temperature.

8. Volumetric Analysis

The toluene volumetric adsorption isotherms on the SBA-15, MCM-41 and FUMED silicas were obtained at 35 °C by employing a volumetric analysis of vaporsorption Autosorb-iQ (Quantachrome Instruments). Prior to adsorption, the samples were outgassed for 30 min at 50 °C, 30 min at 80 °C, 2h at 120°C, 2 h at 150 °C and finally at 12 h at 220 °C under high vacuum conditions (final pressure 7×10^{-4} mbar).

9. UV-vis Analysis

The UV spectra of glyphosate solutions were recorded by using The Agilent UV–Vis spectrophotometer, 8453 which is located at the laboratories of the Department of Sciences, Section Chemistry, Pontifical Catholic University of Peru. The spectra were recorded in the range of 190 - 900 nm. And the maximum absorbances (λ_{\max}) were obtained at 265 nm.

10. Zeta Potential (ζ)

The Zeta potential of SBA-15 and SBA-15-PAPTS samples was evaluated by using a Zetasizer NANO ZS (Malvern Instruments). Before the analysis the silica samples were dispersed in ultrapure water (2 mg/mL) and the dispersions were sonicated for 10 minutes.

11. ZHigh-Resolution Transmission Electron Microscopy (HRTEM)

HRTEM micrographs were recorded on a JEOL 3010-UHR microscope, available at the Università degli Studi di Torino, operating at 300 kV. Before the analysis, samples were ultrasonically dispersed in isopropanol and a drop of the suspension was deposited on a copper grid covered with a lacey carbon film.

12. Scanning Electron Microscopy (SEM).

SEM images were recorded on a Quanta 200 FEI scanning electron microscope equipped with EDAX EDS attachment, using a tungsten filament as the electron source at 20 keV. Samples were prepared by sonicating the sample in isopropanol and by depositing a drop of the suspension on metal stub and then covered with 20 nm of gold.